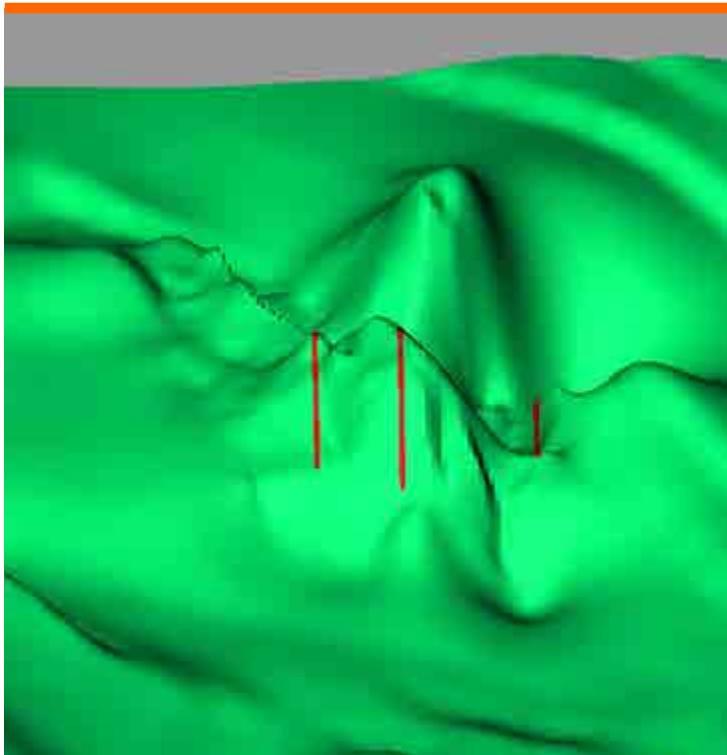# Assessment of Dynamic Flow, Pressure and Geomechanical Behaviour of a CO2 Storage Complex

Ernest Ncha Mbia

PhD Thesis

Department of Civil Engineering
2014

DTU Civil Engineering Report R-310 (UK)
May 2014

DTU Civil Engineering
Department of Civil Engineering

Ernest Ncha Mbia

Assessment of Dynamic Flow, Pressure and Geomechanical Behaviour of a CO2 Storage Complex

Report R-310

Assessment of dynamic flow, pressure and geomechanical behaviour of a CO$_2$ storage complex

Ernest Ncha Mbia

PhD Thesis, 2014

Address: Department of Civil Engineering
            Technical University of Denmark
            Brovej, building 119
            DK-2800 Kgs. Lyngby
            Denmark
            http://www.byg.dtu.dk

I

Preface

This PhD thesis entitled "Assessment of dynamic flow, pressure and geomechanical behaviour of a CO_2 storage complex" is based on the research carried out as part of the CO_2-GS project (**http://co₂gs.geus.net/**) funded by the Danish Strategic Research Council (DSF-09-067234) and Vattenfall AB. The work was supervised by Professor Ida Lykke Fabricius at the Department of Civil Engineering, Technical University of Denmark (DTU) and co-supervised by senior reservoir geologist Peter Frykman at the Geologic Survey of Denmark and Greenland (GEUS). As Vattenfall employee, I was co-supervised by senior research geologist Finn Dalhoff at Vattenfall Vindkraft A/S. This research has been accomplished in collaboration with Vattenfall Vindkraft, the Geological Survey of Denmark and Greenland (GEUS) and the Danish Geotechnical Institute (GEO). The laboratory experiments in this thesis were carried out at DTU, GEO and GEUS. Five weeks external research (reservoir simulation with Eclipse-Schlumberger tool) was performed at the Heriot-Watt University under the supervision of senior lecturer Dr. Gillian Pickup at the Institute of Petroleum Engineering Heriot-Watt University Riccarton Edinburgh EH14 4AS Scotland, UK. As Vattenfall employee, the knowledge generated in this project was distributed within Vattenfall through a number of internal presentations. Similarly presentations and discussions were done at international conferences and EU-project technical meetings to secure that forefront knowledge forms the base of the research made in this project.

The thesis consists of four main chapters (2-5) constituting journal papers (a-d) of which two (a & c) are published in Journal of Petroleum Science and Engineering and International Journal of Greenhouse Gas Control, and the other two are submitted to Journal of Petroleum Geosciences and International Journal of Greenhouse Gas Control. In addition, five peer read extended abstracts (I-V), which were converted into the four journal papers have been included. Only the published manuscripts and peer read extended abstracts are enclosed as appendices (chapter 8) to this thesis.

a) Mbia E. N., Fabricius I.L., Collins, O., 2013. Equivalent pore radius and velocity of elastic waves in shale. Skjold Flank-1 Well, Danish North Sea. Journal of Petroleum Science and Engineering, 109 (2013) 280–290.

b) Mbia E. N., Fabricius I.L., Krogsbøll A., Frykman P., Dalhoff, D., 2013. Permeability, compressibility and porosity of Jurassic shale from the Norwegian-Danish Basin. In Press. 2014, Journal of Petroleum Geoscience.

c) Mbia E. N., Fabricius I.L., Frykman P., Bernstone C., Pickup G., Nielsen, C. M., 2014. Caprock Compressibility and Permeability and the Consequences for Pressure Development in CO_2 Storage sites. International Journal of Greenhouse Gas Control 22, 139–153.

d) Mbia, E. N., Frykman P., Nielsen, C. M., Fabricius I.L., Pickup G., Sørensen T., 2014. Modelling of the pressure propagation due to CO_2 injection and the effect of fault permeability in a case study of the Vedsted structure. (In Press. 2014, International Journal of Greenhouse Gas Control).

I) Mbia, E. N., Fabricius, I.L., Frykman, F., Krogsbøll, A., Dalhoff, F., 2014. Quantifying Porosity, Compressibility and Permeability in Shale. Extended abstract and presentation at the Fourth EAGE Shale Workshop 6–9 April 2014, Porto, Portugal.

II) Mbia, E. N., Fabricius, I.L., Frykman, F., Nielsen, C.M, Bernstone, C., Pickup, G., 2013. Caprock compressibility and the consequences for pressure development in CO_2 storage sites. Extended abstract and presentation at the 7th Trondheim CCS Conference (TCCS-7), 04–06 of June 2013 in Trondheim, Norway.

III) Mbia, E.N., Fabricius, I.L. & Krogsbøll, A. Different Methods of Predicting Permeability in Shale. Extended abstract and presentation at the third EAGE Shale Workshop Shale Physics and Shale Chemistry, 4–7 June 2012, Copenhagen, Denmark.

IV) Mbia, E. N. & Fabricius, I. L, 2012. Pore Radius and Permeability Prediction from Sonic Velocity. Extended abstract and presentation at the 3rd EAGE Shale Workshop, 23–25 January 2012 in Barcelona, Spain.

V) Mbia, E.N & Fabricius, I.L., 2011. Petrophysics of Shale Intervals in the Skjold Field, Danish North Sea. Extended abstract and presentation at the 73rd EAGE Conference & Exhibition incorporating SPE EUROPEC, 23–26 May 2011 in Vienna Austria.

Summary

The increasing global temperature is of much concern to the present and future society and is drawing much attention to climate change causes and consequently, significant efforts are being made to mitigate global emissions of greenhouse gases from the atmosphere as one of the main causes. Carbon dioxide (CO_2) is the primary greenhouse gas emitted through human activities. Over 7,500 large CO_2 emission sources (above 0.1 million tons CO_2 year^{-1}) have been identified (IPCC, 2005). These sources are distributed geographically around the world but four clusters of emissions can be observed: in North America (the Midwest and the eastern freeboard of the USA), North West Europe, South East Asia (eastern coast) and Southern Asia (the Indian sub-continent). One of the ways in which global emission of CO_2 can be reduce is by capturing large volumes of CO_2 from point sources (carbon emitters such as coal-fired power plants) and injecting it into deep formations (e.g., saline aquifers, oil and gas reservoirs, and coalbeds) for storage. This process has drawn increasing consideration as a promising mitigation method that is economically possible. Deep saline aquifers offer the largest storage potential of all the geological CO_2 storage options and are widely distributed throughout the globe in all sedimentary basins. CO_2 storage cannot have a significant impact on reducing atmospheric levels of greenhouse gases if the amounts of CO_2 injected and sequestered underground is not extremely large. However, there is concern that storing extremely large amounts of supercritical CO_2 in deep formations will introduce additional fluids that may cause pressure changes and displacement of native brines thereby affecting subsurface volumes that can be significantly larger than the CO_2 plume itself. If this happens it will be of great environmental concern especially to the ground water and other subsurface resources implying that quantifying pressure changes in CO_2 sites is very important for monitoring purposes in order to prevent this phenomenon.

Large scale CO_2 storage has previously been considered for the Vedsted structure located in the Northern part of Jylland in Denmark. In the Vedsted site the primary caprock is the 530 m thick Fjerritslev Formation sealing the Gassum Formation. The Fjerritslev Formation extends from the Norwegian-Danish Basin to the Northeast and North Sea Central Graben to the Southwest. The magnitude of pressure buildup and transmission from the reservoir into the surrounding formations will depend on the properties (compressibility and permeability) and thickness of the sealing rock

and presence of faults. Pressure buildup in the Gassum reservoir and transmission to the shallower Chalk Group where the brine-fresh water interface resides need to be investigated and quantified through simulation studies as part of site qualification, as overpressure can push brine into the fresh water zone and thereby affecting aquifer performance.

In order to estimate the sealing potential and rock properties, samples from the deep wells, Vedsted-1, in Jylland and Stenlille-2 and -5 on Sjælland were studied and compared to samples from Skjold Flank-1in the Central North Sea. Mineralogical analysis based on X-ray diffractometry (XRD) of shale cuttings samples obtained from the three different locations show a clear trend in composition from the Northeast presently onshore of the Norwegian-Danish Basin where we encounter a more silty shale with up to 50% quartz content to less silty shale of about 30% quartz content in the Southwest, offshore section of the Central Graben. Illite and kaolinite dominate the clay fraction.

The equivalent pore radius that links permeability and porosity of a porous medium was calculated from specific surface and porosity data measured in the laboratory. In this study we demonstrate that elastic moduli as calculated from bulk density and velocity of elastic waves relate to equivalent pore radius of the studied shales. This relationship establishes the possibility of calculating equivalent pore radius from logging data. We found exponential relationships between equivalent pore radius and elastic moduli, and these empirical relationships were used to calculated equivalent pore radius for the Cenozoic, Cretaceous and Jurassic shale sections in Skjold Flank-1 well from elastic moduli, calculated from sonic velocity and density logs. The calculated equivalent pore radius logs vary from 27 nm at 500 m to 13 nm at 2000 m within Cenozoic shale and from 12 nm to about 6 nm in the deeper Cretaceous and Jurassic shale intervals.

Porosity of shale was measured from three independent methods including helium porosimetry-mercury immersion (HPMI), mercury injection capillary pressure (MICP) and nuclear magnetic resonance (NMR) and the results on same material show that MICP porosity is 6% to 10% points lower than HPMI or NMR porosity. Compressibility from uniaxial loading and velocity of elastic waves were measured simultaneously on saturated samples under drained condition at room temperature. Uniaxial loading causes both elastic and plastic deformation at low stress, but

unloading at stress corresponding to in situ stress gives stiffer material with high elastic moduli close to values calculated from mass density and velocity of elastic waves. This result indicates that shale is significantly stiffer in situ than normally assumed in geotechnical modelling. Permeability can be predicted from elastic moduli and from combined MICP and NMR data. The predicted permeability from BET specific surface using Kozeny's formulation for these shales being rich in silt and kaolinite fall in the same order of magnitude as measured permeability from constant rate of strain (CRS) experiments, but is two to three orders of magnitude higher than the predicted permeability from the Yang and Aplin model, which is based on clay fraction and average pore radius. We also found that taking Biot's coefficient into account when interpreting CRS data has a significant and systematic influence on resulting permeability of deeply buried shale.

The second part of this project is focused on assessing two scenarios including sensitivity of caprock permeability and compressibility on pressure development and transmission to the shallower Chalk Group where the brine-fresh water interface resides due to large scale CO_2 storage in Vedsted structure when faults are ignored and when faults are considered. The measured compressibility for the Fjerritslev Formation is $0.5 \times 10^{-5}\ \mathrm{bar}^{-1}$, which is an order of magnitude lower than the standard compressibility ($4.5 \times 10^{-5}\ \mathrm{bar}^{-1}$) normally used for reservoir simulation studies. The consequences of this lower compressibility are investigated in a simulation case study by injecting 60 million tons (Mt) of CO_2 at a rate of 1.5 Mt/year into the Gassum Formation for 40 years. The results indicate that overpressure difference of about 5 bar is created in the reservoir and the caprock between the case with measured and the standard compressibility case. Overestimating caprock compressibility can therefore underestimate overpressure within the storage and sealing formations and this can have significant implication in the presence of highly permeable fractures and faults. The sensitivity of pressure development for the caprock permeability has been studied by varying from one to three orders of magnitude higher and one to two orders of magnitude lower than the measured permeability value of 0.1 μD. The results show that with permeability above 1.0 μD which is higher than the measured value, overpressure can be transmitted through the 530 m thick Fjerritslev Formation caprock and further up into the overburden layers.

Seismic profiling of the structure shows the presence of Northwest-Southeast trending faults of which some originate in the upper layer of the Gassum reservoir and some reach the base Chalk Group layer. Two faults in the upper Gassum reservoir have been interpreted to be connected to the

base Chalk Group. In order to evaluate potential risks associated with vertical pressure transmission via the faults through the caprock, a number of simulation cases have been run with various fault permeabilities spanning orders of magnitude to represent both the worst and best case scenarios. Fault rock permeability data were obtained from a literature study and range from 1000 mD (common in crystalline rock environment) for the worst case scenario down to 1.0 µD (common in sedimentary rock environment) for the best case scenario. The results show that after injecting 60 million tons (Mt) of CO_2 at a rate of 1.5 Mt/year for 40 years, overpressure is developed in the reservoir and about 5 bar is transmitted to the base Chalk Group for the 1000 mD fault permeability (worst) case, while for the 1.0 µD (best) case the pressure buildup was confined within the primary caprock. The results also show that, approximately 0.3 to 5.0 bar overpressure can be transmitted to the base Chalk Group when the fault permeability is above 1.0 mD. The evaluation of Vedsted site from this work has been based on pressure development and CO_2 plume distribution 40 years after injecting 60 Mt of supercritical CO_2 into the Gassum Formation. The results based on both best and worst case scenarios show no potential short term threat to CO_2 storage in Vedsted site. This work underscores the importance of obtaining site specific data for simulation study of potential CO_2 storage sites. Laboratory data generated and methodology employed during this study can be useful for other simulation work and scientific investigations.

Dansk sammendrag

Den globale temperaturstigning har skabt bekymring i samfundet, og opmærksomheden er henledt på drivhusgasser og deres mulige indvirkning på klimaet. Carbondioxid (CO_2) regnes for en væsentlig drivhusgas og atmosfærens indhold af CO_2 øges gennem menneskelig aktivitet. IOCC (2005) har identificeret over 7500 store CO_2 kilder, der udleder mere end 0.1 millioner ton CO_2 om året. Disse kilder findes over hele verden, men de ligger særlig tæt i fire områder: Nordamerika (midtvesten og østkysten), Nordvesteuropa, Sydøstasien (østkysten) og Sydasien (Indien). En mulig måde at nedbringe CO_2-belastningen på er at samle gassen op ved punktkilden og injicere den dybt ned i jorden, for eksempel ind i saline akviferer, kulbrintereservoirer eller kullag. Denne strategi regnes for teknisk og økonomisk mulig. Dybtliggende saline akviferer kan have stor lagerkapacitet og findes i alle Klodens sedimentære bassiner, og der kræves netop meget stor lagerkapacitet for at CO_2 lagring kan have målelig effekt på indholdet i Atmosfæren. Imidlertid kan der være grund til bekymring for, om store mængder superkritisk CO_2 i dybtliggende lag vil forårsage trykændringer og forskydninger af det oprindelige porevand og dermed påvirke volumener, der er væsentlig større end den injicerede CO_2. Dette kunne have konsekvenser for miljøet specielt i relation til grundvandet, og det er derfor nødvendigt at kvantificere de mulige trykændringer og deres rumlige fordeling i forbindelse med CO_2 lagerpladser, så at vidtrækkende konsekvenser kan undgås.

Det har været planlagt at lagre CO_2 i Gassumformationen i Vedstedstrukturen i Nordjylland. Den primære forseglende bjergart over Gassumformationen i Vedstedstrukturen er den 530 m tykke Fjerritslevformation. Fjerritslevformationen dækker et stort geografisk område fra det Norsk-danske Bassin i nordøst til Centralgraven i Nordsøen i sydvest. Hvor meget trykket vil vokse og hvor meget tryk, der transmitteres fra lagerbjergarten til de omkringliggende formationer afhænger at den forseglende bjergarts kompressibilitet, permeabilitet og tykkelse, samt den mulige tilstedeværelse af åbne sprækker eller forkastninger. Det er derfor hensigten gennem numeriske simuleringer at undersøge, hvor meget tryk der vil kunne bygges op i Gassumformationen og hvor meget af trykket, der vil kunne transmitteres til den overliggende Kalkgruppe, hvor grænsen mellem fersk og salt grundvand befinder sig, og hvor grundvandsakviferen kan blive påvirket.

For at undersøge effektiviteten af den forseglende bjergart, blev der indsamlet skylleprøver fra følgende dybe boringer: Vedsted-1 i Jylland, Stenlille-2 og -5 på Sjælland, samt Skjold Flanke-1 i

den centrale del af Nordsøen. Prøvernes mineralogiske sammensætning blev undersøgt ved hjælp af røntgendiffraktion (XRD), og det viser sig, at der mod nordøst i det Norsk-dansk Bassin er en højere siltholdighed (op til 50% kvarts) end i Centralgraven mod sydvest (omkring 30% kvarts). Lerfraktionen domineres af mineralerne illit og kaolinit. Ud fra laboratoriemålinger af specifik overflade og porøsitet kan den ækvivalente poreradius beregnes, og vi vil her vise, at for de undersøgte lerbjergarter kan den ækvivalente poreradius udtrykkes som en exponentialfunktion af elastisk modulus som beregnet ud fra massefylde og hastigheden af elastiske bølger. -Egenskaber som typisk bliver målt med geofysiske borehulssonder. Ved hjælp af det fundne udtryk, kan vi således konstruere logs for ækvivalent poreradius i lerbjergartslagene fra Kænozoikum, Kridttiden og Jura i boringen Skjold Flanke-1. Den beregnede ækvivalente poreradius i de kænozoiske lerbjergarter varierer fra 27 nm ved 500 meters dybde til 13 nm på 2000 meters dybde, mens den for de dybereliggende kretassiske og jurassiske lerbjergarter varierer fra 6 nm til 12 nm. Skylleprøvernes porøsitet blev målt på 3 uafhængige måder: He-ekspansion kombineret med kviksølvimmersion (HPMI), Kviksølvskapillærtrykskurver (MICP) og kernemagnetisk ressonnansspektrometri (NMR). MICP metoden giver typisk værdier der er 6-10 procentpoint lavere end HPMI og NMR. Ved hjælp af enaksede geotekniske deformationsforsøg (CRS) ved stuetemperatur på kerneprøver fra Stenlille kunne kompressibiliteten måles direkte samtidig med at densiteten blev beregnet og den elastiske bølgehastighed blev målt, så der derudfra kunne beregnes en uafhængig kompressibilitet. Under de enaksede deformationsforsøg skete der ved lav spænding både plastisk og elastisk deformation. Ved aflastning fra spænding svarende til det niveau hvor prøven stammer fra, har prøverne stor stivhed og tæt på den man beregner ud fra massefylde og bølgehastighed. Det betyder at lerbjergarten nede i Jorden er betydeligt stivere end normalt antaget ved geoteknisk modellering. Permeabiliteten kan estimeres ud fra elastiske moduli i kombination med porøsiteten fra MICP og NMR data. Den kan også estimeres fra specifik overflade målt med BET og porøsiteten ved hjælp af Kozenys ligning. Endelig kan den estimeres ud fra trykopbygning under de geotekniske CRS-forsøg. De to sidste metoder giver værdier i samme størrelsesorden; men resultatet for de undersøgte lerbjergarter, der jo er rige på kvarts, illit og kaolinit, er to til tre størrelsesordner større end forudsagt ud fra Yang og Aplins model, som er baseret på poreradius og indholdet af lerfraktion i smectitdomineret ler. Ved tolkningen af CRS forsøgene fandt vi yderligere, at det har en signifikant effekt at tage Biots koefficient med i beregningen af permeabilitet.

I anden del af projektet blev det lagt vægt på at modellere CO_2-lagringsscenarier for Vedstedstrukturen af to typer: med og uden ledende forkastninger i den forseglende bjergart. Modellerne for trykopbygning og tryktransmission blev undersøgt for følsomhed med hensyn til varierende kompressibilitet og permeabilitet.

Den målte kompressibilitet for Fjerritslevformationen (0.5×10^{-5} bar^{-1}) er en størrelsesorden mindre end standardværdien (4.5×10^{-5} bar^{-1}), som mange bruger ved reservoirsimulering. Den lavere kompressibilitet betyder at efter injektion af 60 Megaton CO_2 over 40 år med en rate på 1.5 Mt/år opnås et 5 bar højere poretryk i reservoir og forseglende bjergart med den lave kompressibilitet end med den høje. Ved at bruge for høj kompressibilitet af den forseglende bjergart vil man således kunne undervurdere det mulige overtryk. Det har især betydning når permeable sprækker og forkastninger er til stede. Den modellerede trykopbygnings følsomhed med hensyn til permeabilitet blev undersøgt ved at bruge en til tre størrelsesordner højere og en til to størrelsesordner lavere permeabilitet end den målte (0.1 µD). Resultaterne viser at permeabiliteten skal være højere end 1.0 µD, altså højere end den målte, før overtryk kan transmitteres gennem den 530 m tykke Fjerritslevformation og op i de overliggende lag.

På seismiske profiler gennem Vedstedstrukturen kan man se sydvest-nordøst løbende forkastninger, hvoraf nogle har udspring i den øvre del af Gassumformationen og andre når den nedre del af Kalkgruppen. Det skønnes at to forkastninger forbinder Gassumformationen med Kalkgruppen, og for at vurdere den potentielle risiko for tryktransmission via forkastningerne, udførte vi modellering med varierende permeabilitet af forkasningerne, så at både et værst tænkelige scenarie med høj permeabilitet (1000 mD svarende til sprækker i krystalline bjergarter) og et bedst tænkelige scenarie med en flere størrelsesordner lavere permeabilitet (1.0 µD –svarende til lavpermeable sedimentære bjergarter). Resultaterne viser at efter injektion af 60 millioner ton (Mt) CO_2 over 40 år med en rate på 1.5 Mt/år er der opbygget overtryk i reservoiret og når permeabiliteten af sprækkerne er højest tænkelig, er der transmitteret 5 bar overtryk op til Kalkgruppen, mens der ved lavest tænkelige sprækkepermeabilitet ikke transmitteres tryk gennem den forseglende bjergart. Når sprækkepermeabiliteten er over 1.0 mD kan der transmitteres et tryk på 3-5 bar Kalkgruppen.

Vores evaluering af Vedstedstrukturen med henblik på CO_2-lagring i Gassumformationen har således taget udgangspunkt i situationen efter 40 års injektion af i alt 60 Mt superkritisk CO_2.

Resultaterne baseret på både værst tænkelige og bedste scenarie viser ikke nogen umiddelbar trussel mod grundvandskvaliteten. Undersøgelsen demonstrerer også, hvordan evalueringen af et potentielt lager bør bygge petrofysiske data, der passer til på det pågældende sted. Vi mener dog at den beskrevne procedure og de indsamlede laboratoriedata bør være af interesse for andre mulige CO_2-akviferlagre.

Acknowledgement

TABLE OF CONTENT

1 Introduction

1.1 Statement of problem

Increasing global warming is drawing much attention to climate change and efforts to mitigate global emissions of greenhouse gases from the atmosphere, and one of the ways in which this can be done is by capturing large volumes of CO_2 from point sources (carbon emitters such as coal-fired power plants) and injecting it into deep formations (e.g., saline aquifers, oil and gas reservoirs, and coalbeds) for storage. This process has drawn increasing consideration as a promising method to mitigate the adverse impacts of climate change (Holloway, 1996; Gale, 2004; IPCC, 2005; Hepple and Benson, 2005). Deep saline aquifers offer the largest storage potential of all the geological CO_2 storage options and are widely distributed throughout the globe in all sedimentary basins. CO_2 storage cannot have a significant impact on atmospheric levels of greenhouse gases if the amounts of CO_2 injected and sequestered underground is not extremely large (Holloway, 2005).

However, there is concern storing extremely large amount of supercritical CO_2 in deep formations. The concern can be positive or negative, positive in that the storage process can stimulate reservoir oil during enhanced oil recovery (EOR) in some depleted reservoirs with very low matrix permeability (Gozalpour et al., 2005; Darvish et al., 2006; Ferguson et al., 2009; Alam, 2011). On the other hand, it can be negative in that storing extremely large amount CO_2 will introduce additional fluids in the formation that may cause pressure changes and displacement of native brines thereby affecting subsurface volumes that can be significantly larger than the CO_2 plume itself (Birkholzer et al., 2009). If this happens it will be of great environmental concern especially to the ground water and other subsurface resources. Previous investigations have been focused on evaluating under which hydrogeological conditions the injected volumes of CO_2 can be safely stored over a long time (hundreds or thousands of years). Some of these investigations include; long-term efficiency of structural trapping of CO_2 under sealing layers, mineral trapping, solubility trapping and residual CO_2 trapping (Han et al., 2010). Thus, even if the injected CO_2 itself is safely trapped in suitable geological structures, pressure changes and brine displacement may affect shallow groundwater resources, for example, by increasing the rate of discharge into a lake or stream, or by mixing of brine into drinking water aquifers (Bergman and Winter, 1995).

Less emphasis has been placed on evaluating the large-scale pressure changes caused by industrial-scale injection of CO_2 into deep saline formations or understanding the fate of the native brines that are being displaced by the injected fluids (Van der Meer, 1992; Holloway, 1996; Gunter et al., 1996). Although a number of studies on pressure buildup due to CO_2 storage has been carried out lately (Birkholzer et al., 2009; Buscheck et al., 2012; Zhou et al., 2008), they are based on conceptual models and not site specific. Consequently, CO_2 storage based on conceptual models will inherently embody much uncertainty regarding the input parameters which will result in weak decisions in the site specific risk assessment process. Many potential deep saline formations which can be use for CO_2 storage often have limited data and experience.

The Vedsted structure located in the Northern part of Jylland is among a number of onshore potential units for CO_2 storage in Denmark. The site comprises of the Gassum Formation which forms the primary reservoir and is about 1900 m below mean sea level. Sealing the primary reservoir is the 530 m thick low permeable shale of the Fjerritslev Formation overlying the entire sequence constituting a flow barrier due to the high capillary pressure and very low permeability. The reservoir is underlain by the Skagerrak Formation with uncertain properties. Overlying the primary caprock is the Haldager Sand Formation forming an upside storage potential with excellent reservoir properties. This formation has a net thickness of about 80 m with porosity of about 17 % and permeability of 200-300 mD. The geologic setting of Vedsted structure and its proximity to the Nordjyllandsværket coal power station at Aalborg has lead to (in the period 2007–2012) the consideration of a Carbon Capture and Storage (CCS) demonstration project. The project would involve the post-combustion capture of CO_2 from the Nordjyllandsværket coal power station at Aalborg followed by geological storage of the CO_2 in a nearby onshore saline aquifer (Gassum reservoir) within the Vedsted structure (Christensen et al. 2012). The project was temporarily stopped in 2011. The investigation license was active during 2011 and as a part of that, research activities were initiated related to key technical issues, one being to gain better understanding of formation pressure buildup and pressure transmission through the caprock Fjerritslev shale formation to the base Chalk Group hosting the brine-fresh water interface. Pressure buildup and CO_2 leakage are quick events that can occur during the storage process. The pressure buildup in the base Chalk Group may push brine water into fresh water aquifer thereby affecting the fresh water quality which is of great environmental concern to the surrounding communities.

The core of this research study is to predict how the overpressure created by injection of supercritical CO_2 in the Gassum reservoir, possibly can be transmitted up to the base chalk Group

via the Fjerritslev (shale) caprock, and at what magnitude this pressure rise is recorded at the base Chalk Group with groundwater interests. The pressure transmission can arise by at least two mechanisms: 1) vertically through the caprock with low compressibility and high permeability 2) through fault-zones connecting the reservoir layer with the shallower zone, i.e. a combination of horizontal and vertical pressure propagation.

The first effect is related to the tensile strength and the vertical permeability of the caprock overlying the reservoir layer. Seal compressibility and permeability have been investigated (Birkholzer et al., 2009) to have a significant impact on pressure buildup and brine displacement behaviour within the storage formation. Seal with relatively high permeability but still suitable for long-term trapping of CO_2 allow for considerable brine leakage out of the formation vertically upward and/or downward. As a result, the pressure buildup in the storage formation can be strongly reduced compared to a perfect seal with zero or close-to-zero permeability. In such cases, one needs to ensure that vertical pressure propagation and brine migration have no negative impact on freshwater aquifers. The second effect is governed by the pressure wave reaching a fault-zone with potential permeability, which can transmit the pressure. The timing, the velocity and the magnitude of this are governed by parameters like tensile strength and fault permeability.

Accurate quantification of these parameters that describe the geologic system are fundamental to the quality of the simulation and prediction. Parameter quantification will rely on laboratory measurements on formation core samples, theoretically derived values and availability literature data.

Regardless of the quantification method, uncertainty is frequently associated with parameters describing natural systems, resulting from both the difficulty to quantify a parameter and the variability exhibited by many parameters. Sensitivity analysis will be carried out for parameters that have significant influence on pressure development in the Vedsted site to provide insight into the impact of this uncertainty on the predictions.

Caprock properties and fault permeability that are responsible for pressure propagation in CO_2 storage sites have been addressed in this project by conducting laboratory experiments on Jurassic shale material from the Fjerritslev Formation. Prediction on some of the properties has been made from laboratory. Finally for the case of fault permeability, available literature data have been used. The aim of this project is to provide input parameters for the caprock lithology required for reservoir simulations and the sensitivity of the fault permeability in predicting and quantifying pressure propagation in CO_2 storage sites.

1.2 Scope of study

CO_2 sequestration in saline aquifers requires the understanding of the properties of the sealing layers in order to evaluate the potential risk associated with storage site. Petrophysical and geomechanical data of the caprock sealing the reservoir in a specific site will give information as to whether the caprock is a good seal or not. For example if information on permeability is known, high caprock permeability which allows CO_2 to leak through or overpressure to propagate through will of course act as a poor seal. In order to consider a site for the potential industrial scale CO_2 storage, the caprock must be studied and characterized since it is the caprock that confine the CO_2 and pressure within the storage formation. Characterising shale caprocks can be time consuming and sometimes in situ material of the deep caprock formations may be scarce and more so determining some of the properties (porosity, permeability, compressibility, etc) may be more difficult than for sandstone or chalk formations. Available conceptual models for pressure propagation in storage sites have used literature data for caprocks in their simulations (Birkholzer et al., 2009; Buscheck et al., 2012; Zhou et al., 2008) which are not site specific and even use data (compressibility) from other lithologies (sandstones).

Pressure development due to CO_2 in Gassum Formation and the potential transmission through the sealing shale layers to the overburdens in Vedsted site can be investigated through simulation studies. In order to carry out reservoir simulation studies of the Vedsted site we need to know the input parameters of the various formations with our primary concern on the sealing formations. The characterisation of the deep Jurassic shale (primary caprocks) through laboratory experiments constitutes the first part of this project.

This study contain 4 main chapter or papers: a.) Equivalent Pore Radius and velocity of elastic waves in shale Skjold Flank-1 Well, Danish North Sea, b.) Permeability, compressibility and porosity of Jurassic shale from the Norwegian-Danish Basin, c.) Caprock compressibility and permeability and the consequences for pressure development in CO_2 storage sites, d.) modelling of the pressure propagation due to CO_2 injection and the effect of fault permeability in a case study of the Vedsted structure, Northern Denmark. Chapters 2 and 3 describe petrophysical and geomechanical properties of shale in the Norwegian-Danish basin but with more emphasis on the Jurassic shales which form the primary caprock. The caprocks properties have been quantified through laboratory experiments and some of the quantified properties are related to each other and

these relations have been used to form empirical relations (Chapter 2). Chapter 3 also deals with laboratory measurements and modelling of the caprock prosity, compressibility and permeability. Chapters 4 and 5 deals the usage of the measured caprock properties as input parameters for the simulation study of pressure propagation in the Vedsted site and the movement of CO_2 front from the injection well during and after end of CO_2 injection into the Gassum reservoir. The simulation studies have been carried out using conventional software (Schlumberger Eclipse-100).

Chapter 2: This study deals with the study of equivalent pore radius which links permeability and porosity of a porous medium. This property is easily predicted from the laboratory data of BET specific surface, grain density and porosity and not from field data. Laboratory data measured on shale material from Skjold Flank-1 well in the North Sea, and synthetic material of kaolinite and smectite have been used to demonstrate that elastic moduli as calculated from bulk density and velocity of elastic waves relate to equivalent pore radius of the shale. This relationship establishes the possibility of calculating equivalent pore radius from elastic data which can be obtained from laboratory or field measurements.

Chapter 3: This study focuses mainly on Jurassic shale, mainly the Fjerritslev Formation in an attempt to evaluate the caprock properties including mineralogy, porosity, compressibility and permeability. Jurassic shale material from the deep wells from the Norwegian-Danish Basin including Vedsted-1, in Jylland and Stenlille-2 and Stenlille-5 on Sjælland were studied and compared to samples from Skjold Flank-1in the Central North Sea in order to estimate the sealing potential and rock properties.

Mineralogical analysis of the caprock material was carried out based on X-ray diffractometry in order to identify and quantify both the clay and non-clay minerals present in Jurassic shale and their distribution from the onshore to the offshore materials. The composition of Jurassic shale mineralogy influences how permeable, compressible and to some extent how porous the caprock can become.

Shale porosity values reported in the literature vary significantly (Howard 1991; Yang & Aplin 2007) depending on its solid properties and stress condition but also on the method used in the quantification process. This part focuses on the shale porosity measurements from three independents methods; Firstly, the Helium porosimetry method which is one of the most reliable methods used for determining porosity in this case the Helium Porosimetry-Mercury Immersion

(HPMI) technique is used in determining porosity for cuttings samples. Secondly, the Mercury Intrusion Capillary Pressure (MICP) method was carried out on cleaned dry cuttings samples. Porosity was determined from cumulative fraction of the pores intruded as mercury is forced into the samples as a function of increasing pressure. Thirdly, Nuclear Magnetic Resonance (NMR) was used to determine porosity. In this method we used fully saturated core samples to measure the total porosity. We then compared the porosity results from these three methods.

Laboratory measurements were also carried out on centimeter-scale core plug samples from analogue onshore wells to determine shale compressibility. The experiments were performed under drained conditions. A series of uniaxially confined loading and unloading stress paths were applied up to the in situ stress level. Static compressibility was determined from the loading and unloading stress paths. The loading experiments were undertaken with continuous ultrasonic recording of compressional and shear wave velocities. At reservoir conditions, dynamic compressibility is similar to the static compressibility at the beginning of the unloading stress path corresponding to elastic deformation. The analysis of both data sets indicates that compressibility might be order of magnitude lower than the standard values (Buschet et al. 2012; Birkholzer et al. 2009; Zhou et al. 2008 etc) normally used for shale compressibility in reservoir simulation studies.

Permeability prediction was made from three independent approaches; from 1) measured BET specific surface, grain density and porosity, from 2) combined BET specific surface and nuclear magnetic resonance (NMR) data, and from 3) elastic data. Further experiments were carried out on centimeter-scale core plug samples from analogue onshore wells to measured shale permeability in the vertical and the horizontal (permeability anisotropy, an input parameter in simulation studies) direction based on excess pore pressure buildup using geotechnical approach of constant rate of strain experiments (Wissa et al., 1971). The samples were loaded uniaxially to their in situ stress condition. This method of permeability measurements is found to be comparable with the flow through method (Mondol et al. 2008; Daigle & Hugan, 2009). The predicted permeability was compared with the measured permeability in order to evaluate the certainty of the predictions.

Chapter 4: This study deals with simulation cases involving injection of large volume of supercritical CO_2 in Gassum Formation to investigate and quantify pressure buildup and propagation in Vedsted site as a result of the caprock permeability and compressibility data from section 3. The sensitivity of caprock permeability and compressibility to pressure build up and CO_2 migration are investigated. In order to carry out the simulation studies, a 3D geologic model is build

from seismic data that was obtained in 2008 using Schlumberger Petrel modeling tool. Even though the storage capacity for CO_2 in this case is dependent on the compressibility and permeability of the caprock, the properties of the reservoir and the other layers in the storage site are also important. The assessment is carried out by injecting 60 million tons (Mt) of CO_2 into the Gassum reservoir over a period of 40 years at constant injection rate of 1.5 Mt/year and 100 years after the end of injection period using Schlumberger Eclipse 100. The simulation results of the caprock compressibility value measured in the laboratory is compared with the standard compressibility of 4.5×10^{-5} bar^{-1} (was measured for unconsolidated reservoir rocks by Newman (1973) normally used for caprocks in reservoir simulation studies (Birkholzer et al., 2009; and Buscheck et al., 2012; Jin et al., 2012; Pruess et al., 2002; Zhou et al., 2008). The sensitivity of permeability was also carried out by varying caprock permeability in several orders of magnitudes higher and lower than the measured value. Sensitivity study on caprock compressibility and permeability is carried out to evaluate possible worst and best care scenarios for pressure development in the base Chalk Group hosting brine-fresh water interface.

Chapter 5: This paper deals with modelling of the pressure propagation due to CO_2 injection and the effect of fault permeability in a case study of the Vedsted structure, Northern Denmark. Seismic profiling of the structure shows the presence of Northwest-Southeast trending faults of which some originate in the upper layer of the Gassum reservoir and some reach the base Chalk Group layer. Two faults in the upper Gassum reservoir have been interpreted to be connected to the base Chalk Group. In order to evaluate potential risks associated with vertical pressure transmission via the faults through the caprock, a number of simulation cases have been run with various fault permeabilities spanning orders of magnitudes to represent both the worst and best case scenarios. We obtained fault rock permeability data from a literature study and evaluated vertical pressure transmission plus the migration of CO_2 within the reservoir based on changing fault permeability orders of magnitudes from the upper to the lower range. Quantification of the pressure buildup in the Vedsted site especially in the base Chalk Group was carried out. Base Chalk Group pressure data is very important input for hydrogeologic study of ground water movement but this is beyond the scope of this work.

2 Equivalent Pore Radius and Velocity of Elastic Waves in Shale Skjold Flank-1 Well, Danish North Sea

2.1 Summary

Equivalent pore radius links permeability and porosity of a porous medium. This property can be calculated from specific surface and porosity data measured in the laboratory. We can obtain porosity information from logging data but specific surface information can only be obtained from laboratory experiments on cuttings or core samples. In this study we demonstrate that elastic moduli as calculated from bulk density and velocity of elastic waves relate to equivalent pore radius of the studied shale intervals. This relationship establishes the possibility of calculating equivalent pore radius from logging data.

We used cuttings samples and available well logs to characterize Cenozoic, Cretaceous and Jurassic shale sections in the Skjold Flank-1 well of Danish North Sea. Logging data and well reports were used to select 31 shale cuttings samples and experimental data for porosity, grain density and BET specific surface were obtained from these samples using kaolinite and smectite as reference. The cuttings samples were also characterized with respect to mineralogical composition, content of organic carbon and cation exchange capacity.

Equivalent pore radius was calculated from porosity and BET data. It varies from 5 nm for some Cretaceous and Jurassic shale samples to about 25 nm in some Cenozoic samples. Pore radius is controlled by shale mineralogy and the degree of compaction.

We found exponential relationships between equivalent pore radius and elastic moduli, and these empirical relationships were used to calculated equivalent pore radius for the Cenozoic, Cretaceous and Jurassic shale sections in Skjold Flank-1 well from elastic moduli, calculated from sonic velocity and density logs. The calculated equivalent pore radius logs vary from 27 nm at 500 m to 13 nm at 2000 m within Cenozoic shale and from 12 nm to about 6 nm in the deeper Cretaceous and Jurassic shale intervals. Cross plots of the equivalent pore radius with neutron porosity and gamma ray data separate the Cenozoic shale section with high equivalent pore radius from Cretaceous and Jurassic sections.

2.2 Introduction

Equivalent pore radius links permeability and porosity when modeling flow through porous media, but it is not straight forward to predict this property for shale. In gas shale plays, gas flow occurs mainly through interconnected fracture network systems which is constantly recharged by gas flowing through the shale matrix which is dominated by micropores ($\leq$ 2 nm) and mesopores ranging from 2 nm to 50 nm (Kuila et al. 2011). Gas flow in nanometer pores may be a combination of Knudsen diffusion and slip flow while larger pores are dominated by Darcy-like flow. Modelling this flow requires knowledge of pore radius and pore-size distribution (Kuila et al. 2011).

Shale is known to forms source rocks for hydrocarbon generation and seals to hydrocarbon reservoirs and aquifers. Shale can be rich in organic matter ($\geq$ 2 % weight fraction Total Organic Carbon (TOC)) and contain huge estimated gas reserves of about 1000 TCF in North America and 200 TCF in Europe (Jaffe, 2010). Recently the term ''reservoir'' is being used for shales with huge gas potentials. In shale clay minerals typically constitute the load bearing framework containing sub-micrometer pore size resulting in low permeability (Pearson, 1990). Several authors have discussed the inter-relationship between clay mineralogical composition and petrophysical properties of shale and have shown that change in temperature and effective stress causes diagenetic transformation of clay minerals as reflected in other petrophysical properties (Bjørlykke, 1998; Colten-Bradly 1987; Dypvik 1983; Hall et al. 1986; Howard & Roy 1985; Hower et al. 1976; Marcussen et al. 2009; Peltonen et al. 2008, 2009; and Pollastro 1985).

Prasad (2003) used a collection of velocity, porosity, and permeability data from limestone and sandstone and showed that, by grouping the data in different hydraulic units based on pore space properties, a positive correlation between velocity and permeability can be established. For synthetic clay samples an exponential relationship was found between equivalent pore radius and elastic moduli (Fabricius, 2011, partly based on data from Mondol, 2007).

The objective of this work is to predict equivalent pore radius from elastic moduli as calculated from density and sonic logs. Shape factor determination in shale is beyond the scope of this study. We base the work on cuttings data for porosity, specific surface and density. Secondly, we will then assess relationships between the predicted equivalent pore radius and other logging data. We have used logging data and available reports to select cuttings samples from Cenozoic, Cretaceous and Jurassic shale sections in Skjold Flanke-1 well. Skjold Flank-1 is located in the Central Graben of the North Sea Basin (Figure 2.1). The well penetrated five litho-stratigraphical units including

shale-dominated Cenozoic Post Chalk group (73–2128 m), the chalk-dominated primarily Cretaceous Chalk Group (2128–2773 m), the Cretaceous shale rich Cromer Knoll Group (2773–2857 m), the shale-dominated Jurassic (2857–4411 m) and Triassic units (4411–4599 m). The Chalk Group and the Triassic units are not included in this work, so we will group the data into "Cenozoic shale", "Cretaceous shale" and "Jurassic shale".
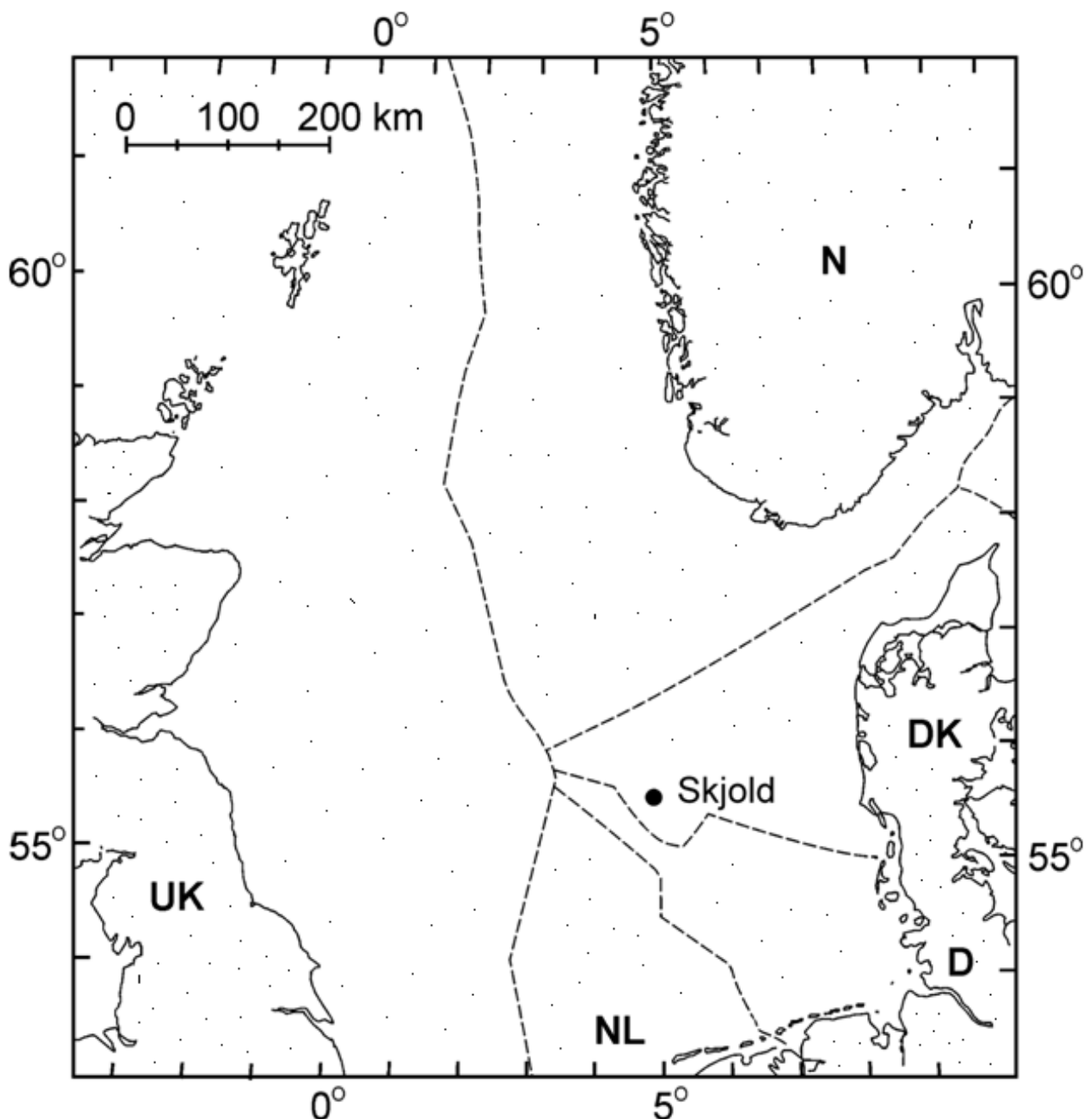
Figure 2.1 Skjold Flank-1 well is located near the Skjold field, Danish North Sea (Modified after Fabricius et al., 2007).

2.3 Methodology

2.3.1 Logging data

The logs used for this study include; mud log, caliper, resistivity, gamma ray, density, neutron, as well as P-wave and S-wave velocity logs (Figure 2.2). The mud log was compiled during drilling operation and records the lithology. The caliper log tool measures the hole-diameter. Resistivity logs measure the formation's resistivity to the passage of an electric current. The following resistivity tools were recorded: Micro-spherically-focused Resistivity (MSFL), Laterolog Deep Resistivity (LLD) and Laterolog Shallow Resistivity (LLS).
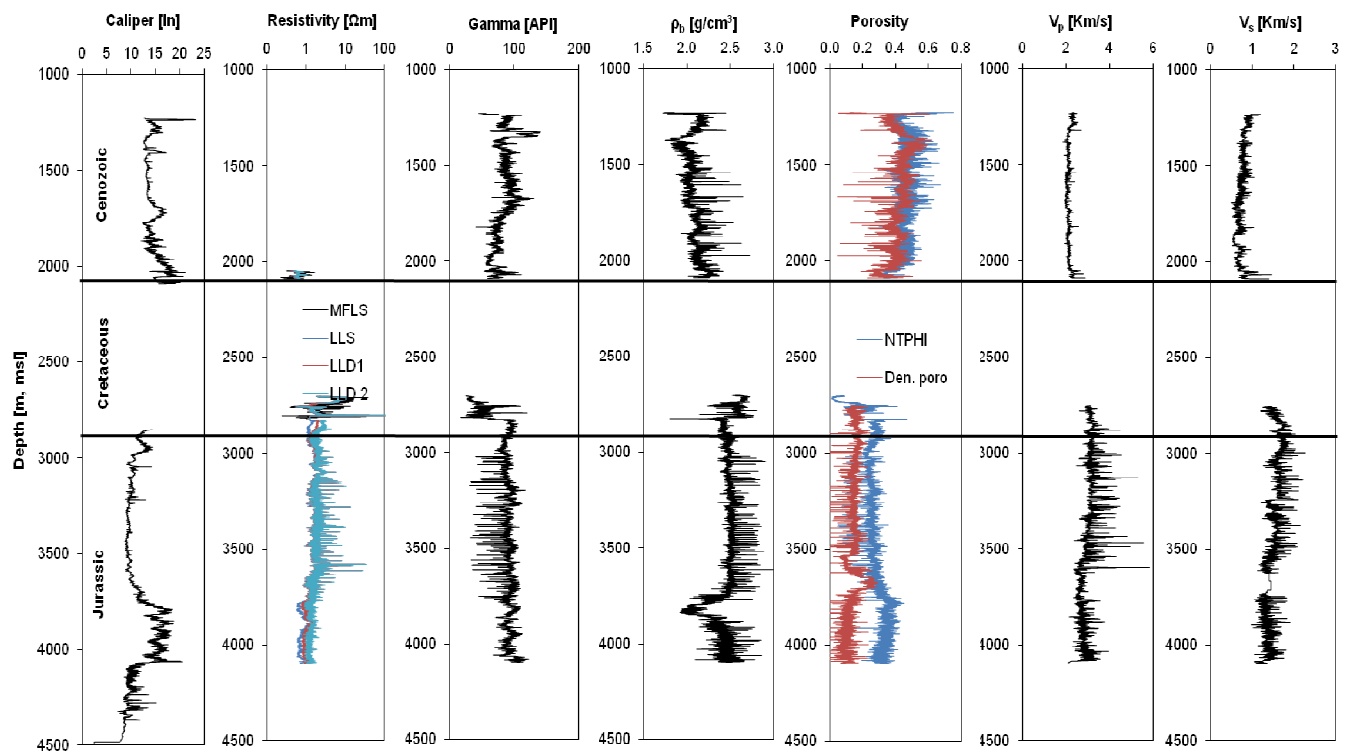
Figure 2.2 Petrophysical well logs showing Cenozoic, Cretaceous and Jurassic shale sections in Skjold Flank-1 well. Cretaceous chalk section is shown as blank. The NTPHI is limestone calibrated porosity from neutron log and Den. poro is porosity from density log assuming 100% water saturation and a grain density of 2.71 g/cm³.

The natural gamma ray log records the gamma radioactivity of the formation. The radiation originates from the radioactive decay of naturally occurring Uranium, Thorium and Potassium. The radioactivity is measured in API units. The density log records bulk density (ρ_b). Porosity is calculated from the bulk density log data by considering the average grain density of the solids from

laboratory data as shown in Table 1. All sections were assumed to be saturated with brine with average density of 1.18 g/cm^3. The neutron porosity log is used as an indicator of porosity and lithology in combination with the density log. The neutron density log is given in porosity as calibrated in 100% water saturated limestone.

Table 2.1 Cuttings data. Semi-quantitative mineralogy based on X-ray diffractometry (XRD) of bulk and <2µm fractions). In Cenozoic and two youngest Cretaceous shale samples, smectite and illite are semi-quantified as separate phases, although they may occur as inter-layered phases.

Period	Depth	Non-clay minerals [%]						Clay minerals [%]			
	(m, msl)	Quartz	K-feldspar	Plagioclase	Calcite	Dolomite	Pyrite	Smectite	Illite	Kaolinite	Chlorite
CENOZOIC	552	37	6	10	2			9	16	14	6
	707	38	2	7	1		2	8	31	6	5
	863	41	4	3	4		2	10	23	9	4
	872	34	3	3	2		14	11	19	9	5
	1009	31	11	9	2		10	9	13	11	4
	1164	34	4	5	1		12	10	14	16	4
	1338	28	1	1			9	9	32	17	3
	1484	24	1	1			10	10	33	19	2
	1622	22	2	1	2		7	11	35	15	5
	1768	23	2				10	8	36	11	10
	1923	21	2	2			4	11	39	12	9
	2070	20	1	1			4	10	38	20	6
CRETACEOUS	2691	20	1		19		9	12	27	10	2
	2719	22			28		5	11	25	6	3
	2746	13		3	34		6		30	9	5
	2774	25			35		7		23	6	4
	2807	26			33		5		27	4	5
	2829	13			33		4		35	7	8
	2850	29	2	3	10		8		31	14	3
	2871	28	2	3	10	3	5		33	13	3
JURASSIC	3051	24	2	7	17	10	4		33	4	2
	3200	27	1	3	7	10	9		30	10	3
	3353	24	2	3	3	3	7		40	15	3
	3520	22	1	7	4	6	5		39	11	5
	3658	16	5	6	3	8	4		48	10	
	3810	22	2	3		11	6		36	13	7
	3959	21	1	2		6	7		47	9	7
	4115	18	2	3		5	7		45	11	9
	4270	20	2	2		5	8		43	12	8
	4420	23	3	2		3	8		42	11	8
	4572	24	1	5		4	9		38	11	8

The sonic data were obtained by the SDT log. It does not have a separate shear source, so we are dependent on shear waves that were refracted back only when larger than the mud velocity. The recorded shear is thus sometimes uncertain when recorded with this log. The sonic log records velocity of elastic waves in the formation as expressed in travel time, quoted as *Δt*, which is the inverse velocity. We recalculated travel times to P-wave and S-wave velocities (V_p and V_s). Cross plots of gamma ray with bulk density, neutron porosity, compressional and shear wave velocities

(Figure 2.3a–d) split Cretaceous and Jurassic shale sections from the Cenozoic shale section, which show higher gamma ray response in some intervals, higher neutron porosity, lower bulk density, as well as lower compressional and shear wave velocity.
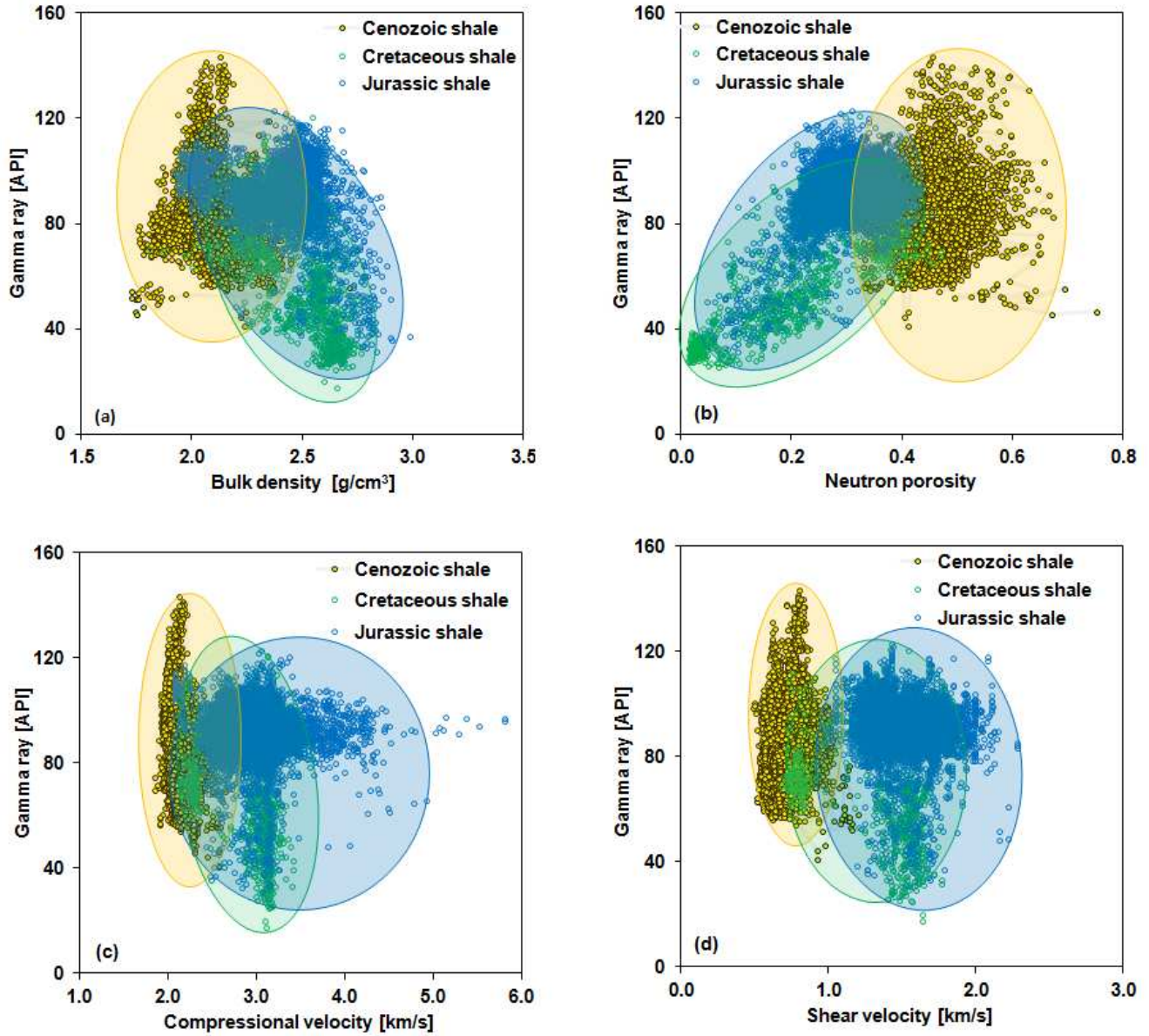
Figure 2.3 Cross plots of gamma ray log versus other logging data from Skjold Flank-1. The data are split according to geological age: Cenozoic, Cretaceous and Jurassic. (a) Gamma ray versus bulk density. (b) Gamma ray versus neutron porosity. (c) Gamma ray versus P-wave velocity (d) Gamma ray versus S-wave velocity.

2.3.2 Cuttings-data

The sample material consisted of unwashed cuttings. Well logs and final well reports were used to develop a sampling strategy for the well, and cuttings samples were taken at approximately 50–100 m spacing in shale intervals, so as to represent changes in the petrophysical logs. The well is vertical with only minor deviation and all depths are given as vertical depth, in meters from sea level. Thirty-one shale cuttings samples were collected for this study, 12 samples from the Cenozoic section, 8 samples from Cretaceous shale, and 11 samples from the Jurassic. The samples were carefully washed with deionized water several times to remove all the drilling mud and left in methanol for two weeks to dissolve salts. Silver nitrate was used to check for the presence of salts. It is worth noting the difficulty involved in cleaning shale samples with very low permeability which may prevent methanol from getting into the micro pores to dissolve all the salts. The cleaned samples were then dried in an oven at about 60°C for three days. Upon completion of this cleaning process, each sample was handpicked for cavings. The final samples weigh from 55 to 95 grams, and the following parameters were determined and the results are presented in Tables 2.1 and 2.2.

2.3.2.1 Mineralogy from X-ray diffractometry

Bulk samples were ground in an agate mortar and pressed into a sample holder for X-ray dffraction (XRD) analysis. For analysis of the clay fraction, approximately 0.5 g samples were shaken with distilled water for 15 minutes, mixed with 10 ml of 1M NaCl, and then repeatedly dispersed and centrifuged to recover the <2 μm fraction. This suspension was treated with acetic acid to remove carbonate minerals. The <2 μm clay fraction (using the Navier Stoke's equation) was extracted with a pipette to a frosted glass slide. Then the water was allowed to evaporate overnight to achieve basal orientation of the clay minerals for XRD analysis. For identification of clay minerals four X-ray diffractograms were taken: air-dried, ethylene glycol-solvated at 60°C for 2 days, subsequently heated to 350°C/2h and 550°C/2h. The XRD pattern was obtained by Cu-Kα X-ray radiation by using Ni filter with variable divergence slit through 2° to 65° 2θ. The XRD data and intensities versus angle of diffraction were used to calculate lattice distances (*d*-values) by using Bragg's law, and minerals were identified. The bulk mineral composition was assessed semi-quantitatively according to method used at University of Aarhus by O. Bjørslev. On bulk samples net peak height, h was measured on the following peaks where a correction factor was applied: Quartz: 0.25 h(100); K-feldspar 0.10 h(220); Plagioclase: 0.10 h(002); Calcite: 0.076 h(104); Dolomite: 0.076 h(104); Pyrite: 0.085 h(200); Clay minerals 1 h(020). Semi-quantification was then done from the relative corrected peak height. Clay mineral groups were then semiquantified from the glycolated oriented

samples. The peak area of the 17Å, 10Å, and 7Å peaks were measured and corrected by factors 1, 3 and 1.15 respectively. This allows an estimate of contents of Smectite, Illite, and combined Chlorite and Kaolinte. Chlorite and Kaolinite were then semi-quantified from the ratio of the height of the 14Å peak after heating to 550°C to the height of the 7Å peak corrected by a factor 1.5 on the untreated oriented sample.

2.3.2.2 Determination of porosity by He-porosimetry and mercury immersion

We first measured the grain volume V_g, of each sample by helium porosimetry. To get grain density, ρ_{grain} we divided sample weight with sample volume. Since we could not measure the bulk volume of the cuttings samples by caliper, we had to employ a mercury immersion method. In order to carry out this measurement a special set-up was designed which includes weighing balance with a swing arm and perforated steel basket. The basked has a lid and is attached to the swing arm. A beaker glass was filled with mercury to an expected level.

The following steps were taken to obtain the volume of the sample: (1) The weight of the empty basket was measured in air and in mercury. (2) The weight of the basket plus the sample is measured in air and in mercury. (3) Actual sample weight is equal to weight of the basket plus the sample in air minus weight of empty basket in air. (4) Actual sample weight in Hg is equal to weight of the basket plus the sample in Hg minus weight of empty basket in Hg. To get the dry bulk volume (V_{dry}) we divided actual sample weight in mercury by the density of mercury. To get dry density (ρ_{dry}) we divide actual sample weight by dry bulk volume. Porosity (ϕ) is then derived as

$$\phi = (V_{dry} - V_g)/V_{dry} \tag{2.1}$$

For calibration, similar cuttings were obtained by crushing a plug with known porosity, and we found a relative error of ±2 %.

2.3.2.3 BET specific surface

The specific surface of the samples (BET) was determined by nitrogen adsorption according to the method developed by Brunauer, Emmet and Teller (1938). A Gemini III 2375 surface area analyzer apparatus (Micrometrics Instruments Corp.) was used. To preserve the sample mineralogy, we degassed samples for 4 hours at 70°C on a FlowPrep060 degasser (Micrometrics Instruments Corp.) using nitrogen as a carrier gas. The determination of specific surface area was achieved in two

steps: 1) evaluation of the adsorbed monolayer volume, and 2) conversion of this quantity to specific surface area by means of the molecular area, (a_m). The test was carried out in duplicate. The specific surface, S, with respect to bulk volume was calculated as;

$$S = BET * \rho_{dry} \tag{2.2}$$

2.3.2.4 Cation exchange capacity (CEC)

The CEC was measured by Ba-ion exchange. First 0.1M $BaCl_2$ (pH = 5.8) solution was added to each sample so that Ba^{2+} ions replace the bases such as Ca^{2+}, K^+, Mg^{2+} and Na^+. Afterwards the concentration of the bases was measured with Inductively Coupled Plasma – Optical Emission Spectrophotometry (ICP-OES). To analyze the cation-exchange capacity which is known as the effective CEC, the samples were next immersed in a dilute 0.1 M $BaCl_2$ (pH=5.8) solution with an ionic strength of about 0.01M. Then the Ba^{2+} which replaced the bases was removed with an excess of $MgSO_4$. The Mg lost for the exchange with Ba^{2+} is measured with the ICP-OES to determine the effective CEC.

Measurement of CEC on shale samples with carbonate gave significantly higher CEC exchangeable bases than expected. Analysis showed that calcium carbonate in shale samples increases the CEC exchangeable bases which gave exaggerated values of effective CEC. We normally expect that the effective CEC is higher than the CEC exchangeable bases but that was not the case.

We measured the carbonate content of each sample and realized that the higher the percentage of carbonate in shale sample, the higher the contribution of calcium cations. In a sample with 72% carbonate content, the contribution of calcium cations from carbonate is about 78% of the CEC exchangeable bases. While shale samples with low carbonate content of about 8%, contributes only 1% of calcium cations to the CEC exchangeable bases. In order to correct for this error we treated selected carbonate bearing shale samples with CH_3COOH acid at pH = 2, to remove the carbonate before carrying out renewed CEC measurements. From these CEC results it was possible to apply a correction factor to obtain the effective CEC for the remaining carbonate containing shale samples by plotting the ratio of CEC and CEC carbonate free against carbonate content. During the removal of carbonate, also cations from shale supposed to contribute to the CEC exchangeable base were leached out and replaced by the acid cations (H_3O^+).

Table 2 Cuttings data from well Skjold Flank-1. ρ_g is grain density, ϕ is mercury porosity, R_p is equivalent pore radius, BET is specific surface by N_2 adsorption, CEC is cation exchange capacity, $CaCO_3$ is carbonate presented as equivalent calcium carbonate; TOC is total organic carbon, Th is Thorium, U is Uranium and K is Potassium identified by spectral gamma radiometry, V_p and V_s are compressional and shear velocities obtained by averaging ten data points from corresponding depths in the logging data. Experimental errors are: for $\rho g < 0.03$ g/cm^3; for CEC < 5%; for BET < 0.3 m^2/g; for ϕ <2 %; for $CaCO_3$< 0.2%; for TOC < 0.2 %; for Th < 0.5 ppm; for U < 0.2 ppm; for K < 0.02%. Data for kaolinite and smectite are given for reference.

Sample	Depth	ρ_g	CEC	BET	ϕ	CaCO$_3$	TOC	Th	U	K	V$_p$	V$_s$
	m	g/cm^3	mEq/100g	m^2/g		%	%	ppm	ppm	%	km/s	km/s
Kaolinite		2.61		11	0.55						1.25	0.28
Kaolinite		2.61		11	0.45						1.36	0.34
Kaolinite		2.61		11	0.30						1.50	0.45
Kaolinite		2.61		11	0.32						1.56	0.47
Kaolinite		2.61		11	0.17						1.98	0.77
Kaolinite		2.61		11	0.11						2.18	0.90
Smectite		2.62		25	0.55						1.54	0.32
Smectite		2.62		25	0.49						1.62	0.37
Smectite		2.62		25	0.45						1.67	0.40
Smectite		2.62		25	0.39						1.88	0.51
Smectite		2.62		25	0.36						1.98	0.59
Cenozoic	552	2.65	38	30	0.35	6	0.6	14.40	4.98	1.87	2.32	0.81
Cenozoic	707	2.65	26	30	0.39	6	0.9	12.90	4.38	1.74	2.25	0.77
Cenozoic	863	2.65	22	30	0.35	4	1.1	11.60	4.58	1.63	2.29	0.93
Cenozoic	872	2.74	27	31	0.35	5	1.1	12.90	5.38	1.68	2.35	0.97
Cenozoic	1009	2.65	36	30	0.34	4	0.9	13.90	4.38	1.66	2.50	0.97
Cenozoic	1164	2.68	48	28	0.45	4	0.9	12.80	5.88	1.81	1.97	0.72
Cenozoic	1338	2.68	55	28	0.45	2	0.8	9.40	5.98	1.77	2.01	0.61
Cenozoic	1484	2.68	46	28	0.49	3	2.6	8.10	3.58	1.90	1.99	0.57
Cenozoic	1622	2.65	43	30	0.46	2	3.5	7.40	6.48	1.85	2.10	0.73
Cenozoic	1768	2.65	48	30	0.52	4	1.4	7.30	5.68	2.22	1.95	0.71
Cenozoic	1923	2.65	29	30	0.47	2	1.0				1.85	0.71
Cenozoic	2070	2.67	39	23	0.30	5	0.7				2.65	1.15
Cretaceous	2691	2.75	9	23	0.27	56					2.50	1.12
Cretaceous	2719	2.71	22	18	0.16	27					3.20	1.55
Cretaceous	2746	2.71	7	18	0.20	72					3.13	1.33
Cretaceous	2774	2.69	8	18	0.15	44					2.90	1.68
Cretaceous	2807	2.72	15	18	0.15	52		2.30	4.68	0.69	3.30	1.43
Cretaceous	2829	2.74	10	18	0.15	66					4.06	1.60
Cretaceous	2850	2.73	22	18	0.17	10					3.24	1.52
Cretaceous	2871	2.74	20	24	0.20	11					2.93	1.38
Jurassic	3051	2.75	9	18	0.21	28	2.0	7.70	4.68	1.86	2.44	1.20
Jurassic	3200	2.73	14	24	0.23	15	2.4	4.70	3.48	1.42	2.61	1.41
Jurassic	3353	2.74	17	24	0.26	13	2.5	7.10	2.38	1.34	2.53	1.22
Jurassic	3520	2.75	14	24	0.26	13	2.3				2.55	1.22
Jurassic	3658	2.76	12	24	0.25	11	2.4	7.80	2.88	1.68	2.64	1.20
Jurassic	3810	2.75	13	24	0.24	7	2.6				2.55	1.27
Jurassic	3959	2.75	15	19	0.16	5	1.4	9.60	3.68	1.78	3.20	1.55
Jurassic	4115	2.76	14	18	0.14	7	1.4	9.00	4.98	2.17	3.21	1.57
Jurassic	4270	2.75	15	18	0.15	6	1.7	8.20	5.18	2.15	3.06	1.71
Jurassic	4420	2.76	13	16	0.14	6	2.2				3.16	1.75
Jurassic	4572	2.76	16	16	0.14	5	1.2	10.30	4.38	1.94	3.26	1.85

2.3.2.5 Carbonate content and total organic carbon (TOC)

The carbonate content was obtained by means of dissolution with 1M HCl followed by titration with 1M NaOH. The error is ± 0.2%. Data are presented as equivalent $CaCO_3$. The total organic carbon content (TOC) was measured by combustion in a LECO (CS-200) Carbon/Sulfur Analyzer – oven with an error of ± 5%.

2.3.2.6 Gamma spectrometry

The concentrations of U, Th and K were measured on powdered samples by a NaI-crystal gamma spectrometer with an error for U: < 0.2 ppm, for Th: < 0.5 ppm, and for K: < 0.02 %

2.3.2.7 Equivalent pore radius prediction

Experimental data obtained in this work together with data from Fabricius (2011) on pure kaolinite and smectite were used to model the relationship between elastic moduli and equivalent pore radius. The experimental data used includes porosity (ϕ), BET specific surface, grain density (ρ_g), compressional and shear wave velocities in the water saturated state. For the Skjold Flank-1 shale, velocity data was collected by averaging sonic velocity log data in 5 m intervals from the same cuttings depths which gives approximately the same resolution. For the pure kaolinite and smectite laboratory velocity data from Mondol et al. (2007) were used. The frequency of elastic waves while logging differs from frequency of laboratory measurements, but we expect only insignificant dispersion of wave velocity due to small pore size and consequent high critical frequency.

The bulk density, ρ_b, is calculated as; $\qquad \rho_b = \rho_g \,(1 - \phi) + \rho_{fl}\,\phi$ $\qquad\qquad$ (2.3)

where ρ_{fl} is fluid density

Elastic compressional modulus, M, is given as: $\qquad M = \rho_b V_p^{\,2}$ $\qquad\qquad\qquad$ (2.4)

Elastic shear modulus, G, is given as: $\qquad G = \rho_b V_s^{\,2}$ $\qquad\qquad\qquad$ (2.5)

Elastic bulk modulus, K, is calculated as: $\qquad K = M - 4/3\,G$ $\qquad\qquad\qquad$ (2.6)

For modeling pore radius, we need information on ϕ, and the specific surface of the bulk sample S.

The equivalent pore radius, R_p, is defined as: $\qquad R_p = 2\,\phi S = 2/S_p$ $\qquad\qquad$ (2.7)

where S_p is the specific surface relative to pore space.

2.4. Results

2.4.1 Mineralogical composition

Results from XRD analysis is shown in Figure 2.4 and Table 2.1. The non-clay fraction consists mainly of quartz. Quartz content decreases from about 40% in the younger Cenozoic sediments to about 20% in the deeper Cenozoic. In Cretaceous and Jurassic shales the quartz content varies stratigraphically between 15% and 30%. Feldspar (K-feldspar and plagioclase) is most prevalent in younger Cenozoic sediments and in the Jurassic (5–15%), whereas it is sparser in older Cenozoic and Cretaceous shale. Calcite content is below 5% in the Cenozoic and Jurassic shale samples, whereas in Cretaceous samples up to about 35% calcite was found. Dolomite was not detected in Cenozoic and Cretaceous samples (save the oldest), whereas 5–10% dolomite was identified in the Jurassic shale samples. Pyrite is also identified in these geologic intervals and varies stratigraphysically in Cenozoic shale from 2% to about 14% and from 4% to about 9% in Cretaceous and Jurassic shales.

The main clay minerals identified include smectite, illite, kaolinite and chlorite. Smectite (10–15%) is present in the Cenozoic and in the youngest Cretaceous samples (deepest smectite bearing sample is from 2719 m, msl). Below this depth no smectite was identified. Although Smectite and Illite are partly interlayered, thery are semiquantified as separate phases (Figure 2.4). Illite is the dominating clay mineral throughout, and most prevalent in older Cenozoic (30–40%) as well as oldest Cretaceous and Jurassic (30–50%) samples. The content of kaolinite and chlorite does not vary much with depth and constitute 5–10% for chlorite and 6–20% for kaolinite.

2.4.2 Petrophysical properties

The results of grain density, porosity, equivalent pore radius, BET specific surface, CEC, equivalent carbonate content, TOC, spectral gamma data, and elastic wave velocities, are summarized in Table 2. Plots of these petrophysical properties as a function of burial depth are shown in figures 2.5a–2.5l. Grain density

(Figure 2.5a) show no significant depth trend for Cenozoic shale samples but varies between 2.65 and 2.75 g/cm^3.
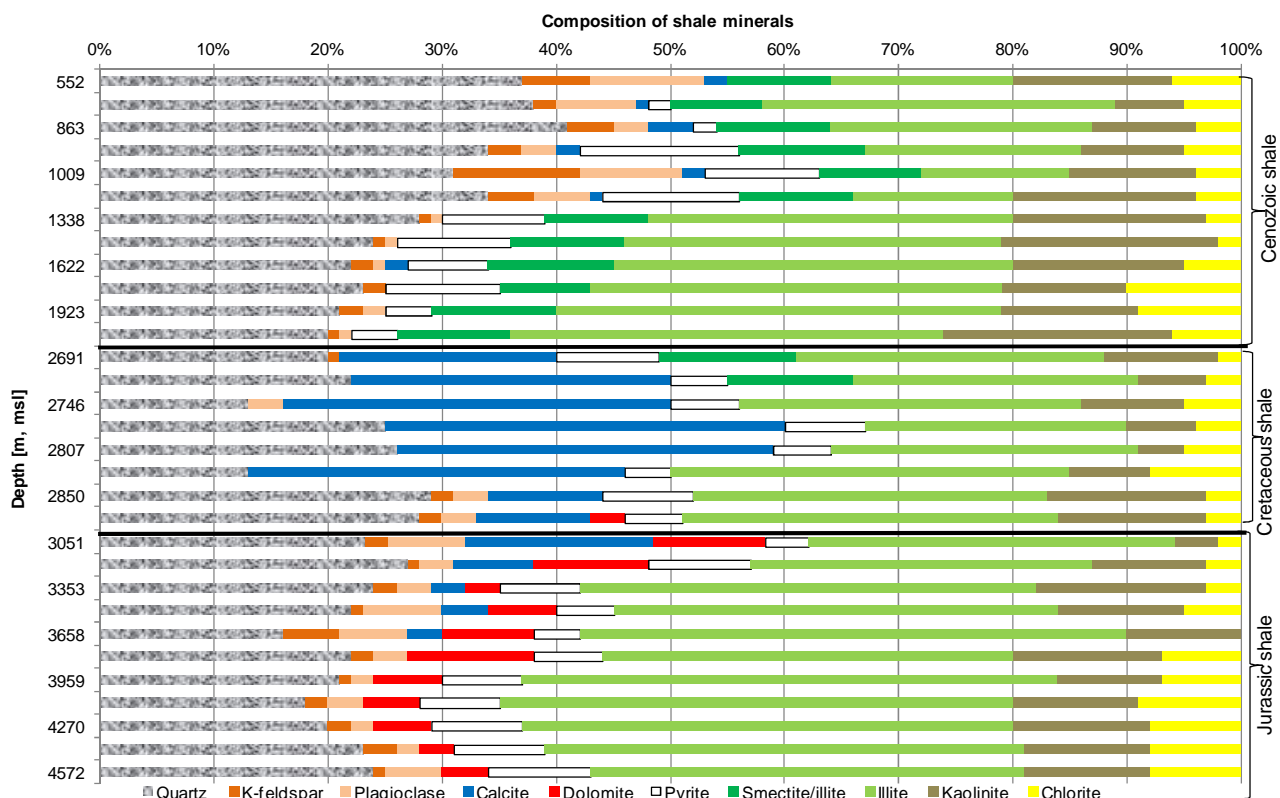
Figure 2.4 Mineralogical composition of cuttings samples based on X-ray diffractometry.

There is significant increase in grain density with depth from 2.69 g/cm^3 in Cretaceous shales samples to about 2.76 g/cm^3 in Jurassic samples. Porosity (0.3–0.5) and equivalent pore radius (10–27nm) show higher values in Cenozoic shale samples (Figure 2.5b and 2.5c) which reduces with depth to about 0.15 for porosity and 7 nm for equivalent pore radius in the deeper Jurassic sediments. Porosity and pore radius show opposite depth trend to that seen in grain density.

BET specific surface and cation exchange capacity show higher values for the Cenozoic shale samples in comparison with the low values obtained for the Cretaceous and Jurassic samples. The BET specific surface decreases with depth from 30 m^2/g in Cenozoic samples to <20 m^2/g in deeper Jurassic samples (Figure 2.5d). Cation exchange capacity vary from 25 to 55 mEq/100g in Cenozoic shale, while it is significantly lower (10–20 mEq/100g) in Cretaceous and Jurassic shale (Figure 2.5e). Carbonate content is low in Cenozoic and older Jurassic shales as compared to Cretaceous and younger Jurassic shale. This reflects the content of carbonate minerals by XRD (Figure 2.4 and 2.5f). The total organic carbon content (TOC) is generally lower in Cenozoic samples (0.6–1.4%) than in Jurassic samples (1.2%-2.6%), but Cenozoic samples at 1484 m and 1622 m, msl have relatively high TOC of 2.6% and 3.5% (Figure 2.5g).

The variation in TOC is not reflected in the radioactivity of these shale samples (Figure 2.5h, i, & j). The most conspicuous trends are the decreasing depth trend of Th in Cenozoic shale (From 15 ppm to 5 ppm), and the more modest increasing depth trend in Jurassic shale from 5 ppm to 10 ppm (Figure 5h). P-wave and S-wave velocity (Figure 2.5k) show similar depth trend behaviour as grain density but opposite to that of porosity and equivalent pore radius from Cenozoic to Jurassic shale samples which increases from 0.8 to 1.6 km for S-wave and from 2.3 to 3.3 km/s for P-wave velocity.
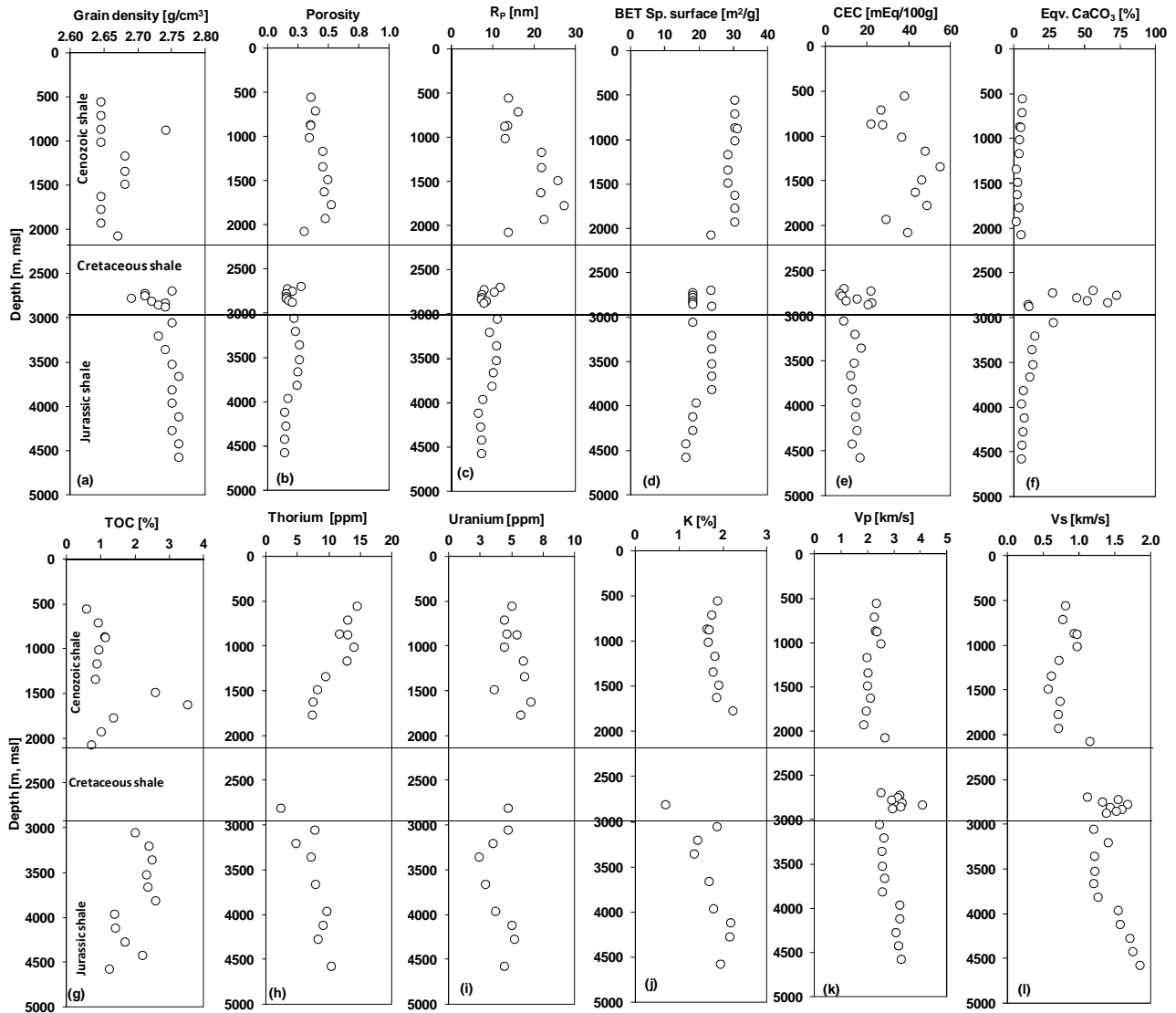
Figure 2.5 Depth plots of cuttings data: (a) Grain density, (b) Porosity, (c) Calculated equivalent pore radius, (d) BET specific surface, (e) Cation Exchange Capacity (CEC), (f) Carbonate content, (g) Total Organic Carbon (TOC), (h) Thorium content, (i) Uranium content,(J) Potassium content, (k) Compressional wave velocity and (l) Shear wave velocity.
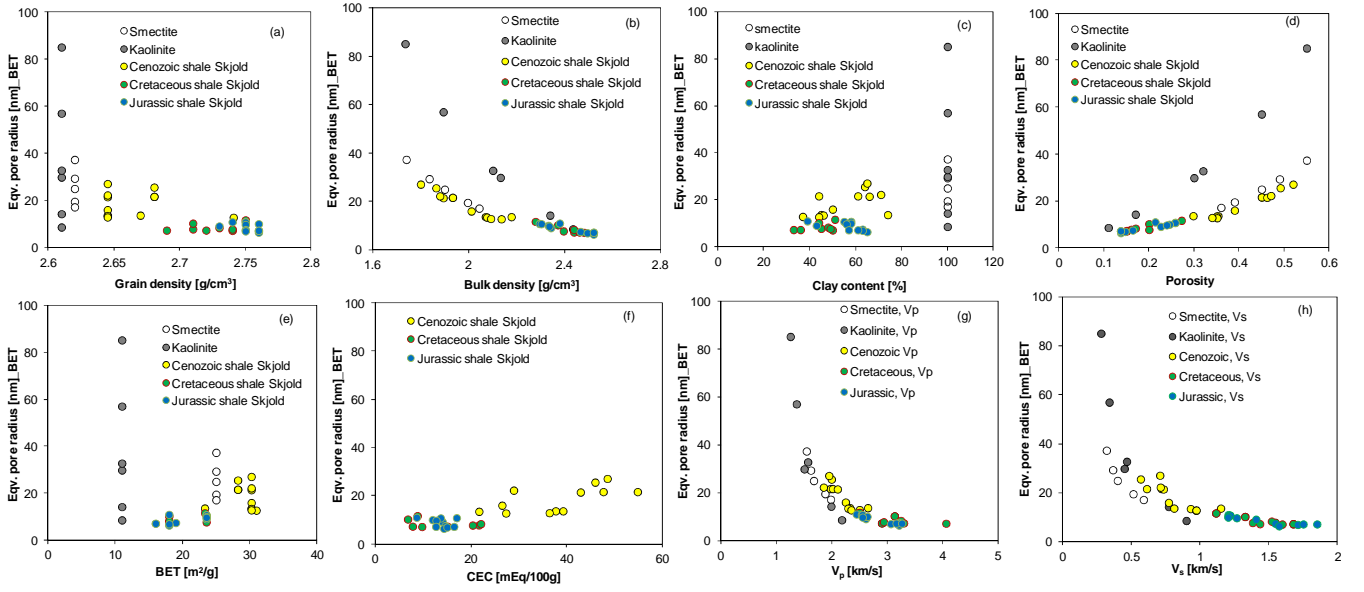
Figure 2.6 Cross plots of cuttings data: pore radius calculated from BET and porosity versus: (a) grain density, (b) Bulk density (c) Clay content, (d) porosity, (e) specific surface from BET, (f) Cation Exchange Capacity, (g) Compressional wave velocity, (h) Shear wave velocity. Data for pure smectite and kaolinite are shown for reference.

2.4.3 Equivalent pore radius

We investigated the relationships between the equivalent pore radius and the other petrophysical parameters as shown in figure 2.6 (a–h) and found clear relationships between pore radius and acoustic velocity as well as pore radius and bulk density implying that we can possibly predict pore radius from elastic properties. Elastic moduli were calculated from experimental data from Cenozoic, Cretaceous and Jurassic shales of Skjold Flank-1 well and from artificially compacted kaolinite and smectite (Mondol et al, 2007) (Figure 2.7a–c). Compressional modulus vary from 4 to about 30 GPa, shear modulus from 0.1 to 9 GPa and bulk modulus from 4 to 24 GPa. For pure kaolinite, the equivalent pore radius from BET specific surface and porosity vary from 86 nm to 9 nm with increasing compaction. For pure smetite equivalent pore radius varies from 37 nm to 17 nm with increasing compaction. The cross plots of the calculated pore radius with elastic moduli (Figure 2.7a–7c) combine the data set into an exponential relationship independent of the mineralogy.
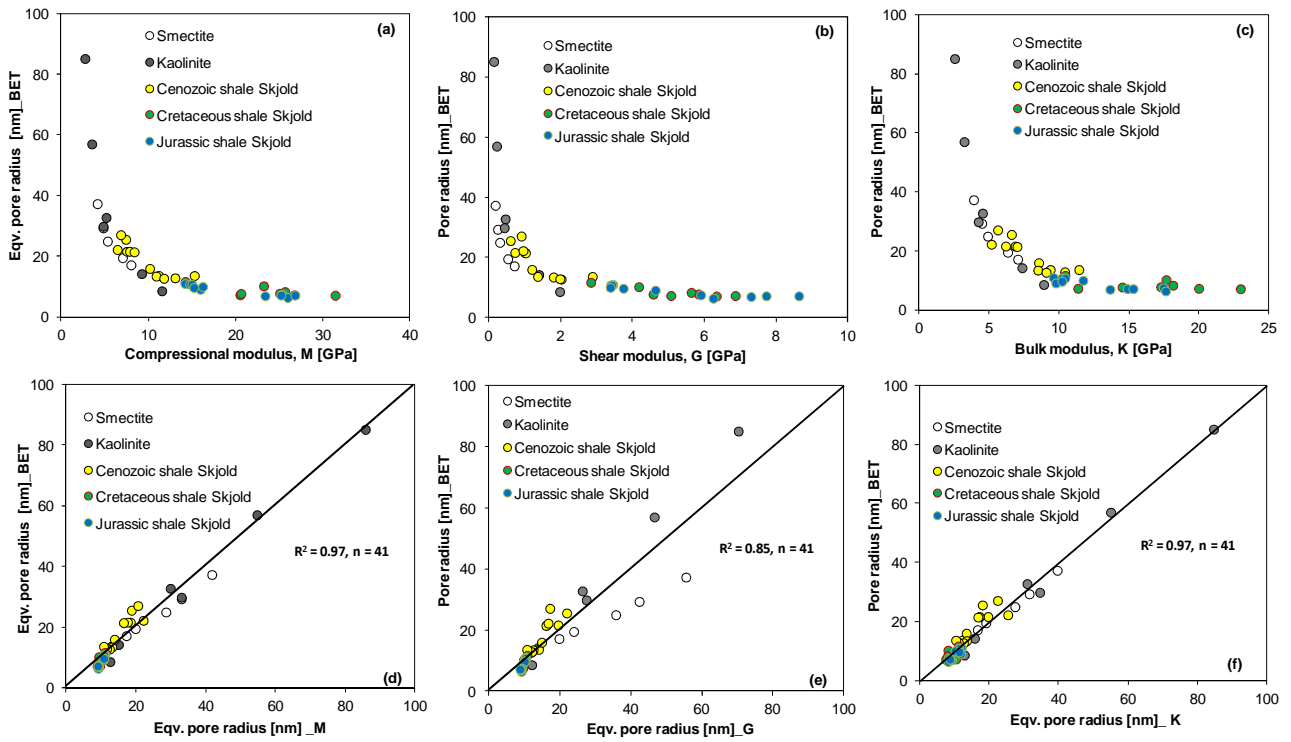
Figure 2.7 Cross plots of cuttings data: pore radius calculated from BET and porosity versus: (a) Compressional modulus, M, (b) Shear modulus, G, (c) Bulk modulus, K, (d) Pore radius estimated from M, (e) Pore radius estimated from G, (f) Pore radius estimated from K. Data for pure smectite and kaolinite are used as reference.
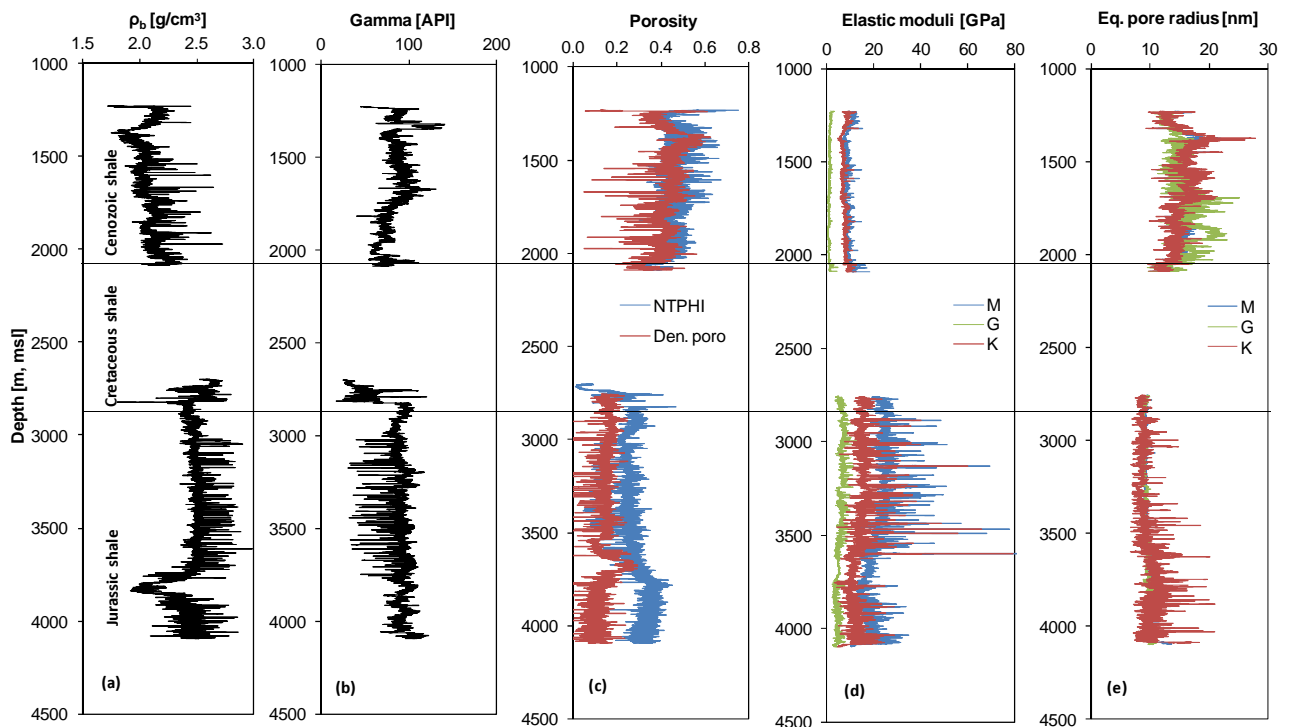
Figure 2.8 Depth plots of logging data: (a)–(c) Bulk density, gamma ray and porosity, (d) Elastic moduli (M, G and K), (e) Pore radius estimated from M, G and K.

23

2.5 Discussion

2.5.1 Cenozoic shale

The younger Cenozoic sediments, above 1200 m, msl are silty shales with high quartz and relatively high feldspar content. A low content of calcite is reflected in low carbonate content and also relatively high pyrite content is noticed. The clay minerals in order of abundance are illite, kaolinite, smectite and chlorite. These younger Cenozoic shales have a relatively low porosity of 0.35–0.40 probably reflecting poor sorting caused by the high silt content. A relatively high detrital content is indeed reflected in a relatively high content of Thorium. A relatively high specific surface (BET) and low grain density probably reflect interlayered clays dominated by smectite and stratigraphical variation in pyrite content. Poor sorting and smectite dominated clay thus result in low porosity and high BET and consequent modest equivalent pore radius of c. 15 nm.

The older Cenozoic shales are poorer in quartz and tend to have higher porosity (up to 0.5) than the younger Cenozoic sediments. The older Cenozoic shales are dominated by illite-dominated mixed layered clays, so in spite of the higher clay content, specific surface is similar to that of the younger section. The resulting equivalent pore radius is consequently high: 20–25 nm. The equivalent pore radius is well predicted from bulk modulus and compressional modulus, and less well predicted from the shear modulus (Figure 2.7d–f). Nevertheless it is the shear modulus-based prediction of equivalent pore radius in combination with the neutron log which gives the most effective separation of Cenozoic data points from older data points (Figure 2.9d–e). In spite of a high content of feldspar and Thorium the younger Cenozoic sediments with moderate pore radius only causes a small bias towards higher radioactivity for Cenozoic sediments (Figure 2.9a–c).

2.5.2 Cretaceous shales

Cretaceous shales form a relatively thin section below the thick Chalk Group. Calcite, quartz and pyrite constitute a total of 40–50% of each sample, with the abundance of calcite declining with depth. The clay minerals identified comprise mixed layered smectite respectively illite dominated clays, as well as kaolinite and chlorite. Below 2719 m, msl (corresponding to around 85°C) no smectite was found. Depositional smectite may have transformed to illite by diagenesis. A diagenetic transformation of mixed layered illite-smectite is known as illitization and described in

the North Sea shales by several authors (Hower et al. 1976; Dypvik 1983; Howard & Roy 1985; Pollastro 1985; Hall et al. 1986; Colten-Bradly 1987, Bjørlykke, 1998; Peltonen et al. 2008; Marcussen et al. 2009). The transition to smectite free clay is reflected in the increased grain density and lower specific surface and cation exchange capacity.

In spite of the lower specific surface, the predicted equivalent pore radius in Cretaceous shale is small: around 10 nm. This is caused by a low porosity (0.15–0.20). Relatively high velocities of elastic waves and relatively low specific surface relative to the overall depth trends indicate a relatively high degree of diagenetic cementation (Figure 2.5d, k & l). On cross plots of equivalent pore radius versus gamma ray and neutron porosity log Cretaceous shale tends to overlap Jurassic shale (Figure 2.9).

2.5.3 Jurassic shales

The Jurassic shale section is inter-bedded with thin layers of sandstone or dolomite stringers as indicated by low GR and high density log peaks (Figure 2.2). XRD analysis indicates that quartz occurs as the main non-clay mineral, that plagioclase and dolomite are present in all samples, while calcite significantly reduces as we get to lower Jurassic shale. This is also reflected in a depth-wise decreasing content of carbonate (Figure 2.4, 2.5f). Clay minerals generally constitute 60% of the solids. . The clay minerals identified comprise primarily illite, but also kaolinite and minor amounts of chlorite (Figure 2.4). An increasing maturation of illite is indicated by a depth-wise increasing K-content (Figure 2.5j) which is consistent with other Jurassic samples from the Central Trough studied by Lindgreen & Hansen (1999).

The predicted equivalent pore radius in the Jurassic shale tends to decrease with depth from 10 to 7 nm. This is a reflection of decreasing porosity which counteracts a decreasing specific surface (Figure 2.5b, d). Cretaceous and Jurassic shale intervals tend to overlap in the cross plots of equivalent pore radius versus gamma ray and neutron porosity log data (Figure 2.9). The best separation is obtained from equivalent pore radius predicted from compressional modulus, where a relatively well defined trend of equivalent pore radius versus neutron porosity is found for Jurassic shale (Figure 2.9d).
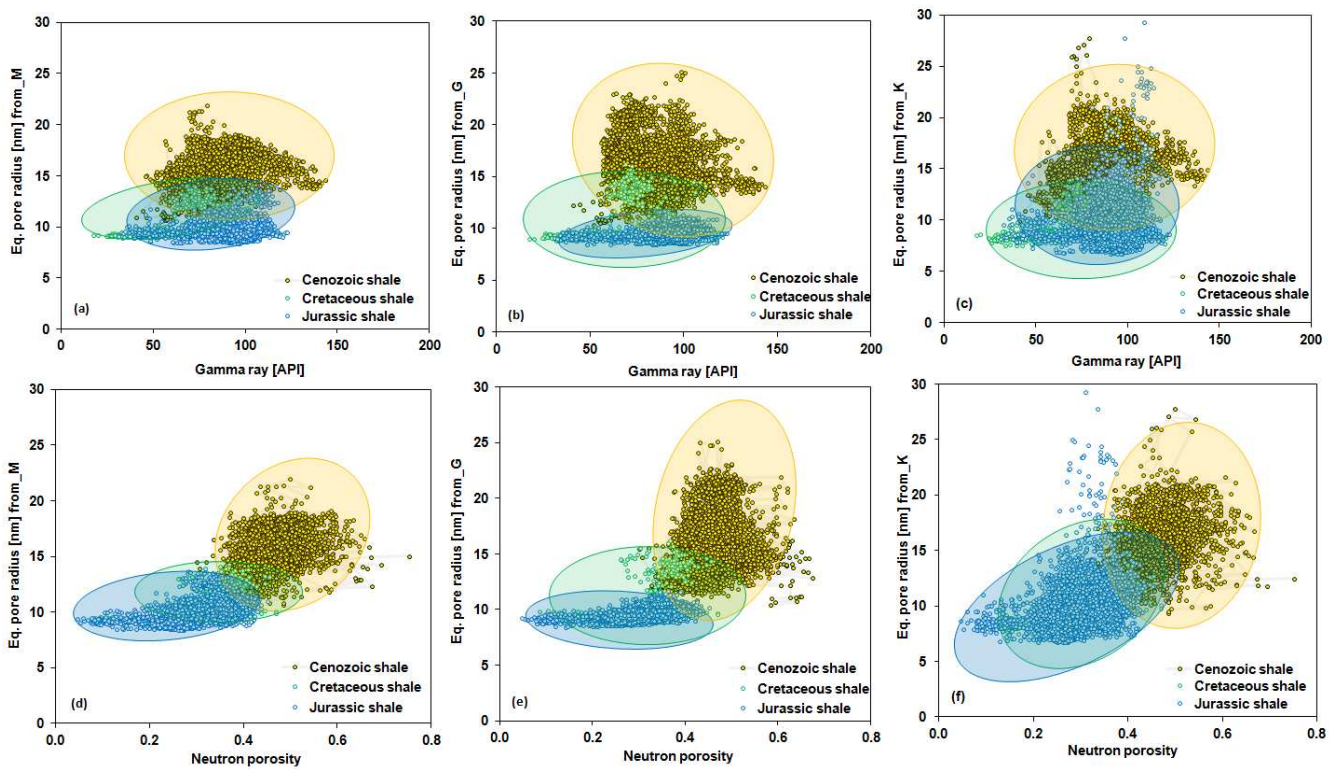
Figure 2.9 Cross plots of logging data: pore radius estimated from elastic moduli versus (a)–(c) Gamma ray and (d)–(f) neutron porosity. The data are split according to geological age: Cenozoic, Cretaceous and Jurassic. (a) and (d) Pore radius estimated from compressional moduldus M, (b) and (e) Pore radius estimated from shear moduldus, G, (c) and (f) Pore radius estimated from bulk modulus, K.

2.6 Conclusions

Petrophysical well logs and well cuttings were used to characterize Cenozoic, Cretaceous and Jurassic shale sections in Skjold Flank-1 well of the Danish North Sea. The data were supplemented with data from artificially consolidated samples of kaolinite and smectite. Equivalent pore radius can be calculated from porosity and specific surface of all samples. This forms a basis for predicting equivalent pore radius from logging data.

Cuttings were used to establish empirical relationships between equivalent pore radius and elastic moduli. The relationships are independent of mineralogical composition and give a correlation coefficient (R^2) of 0.97 for bulk modulus and compressional modulus and a correlation coefficient of 0.85 for shear modulus based on 41 data points.

These empirical equations were used to predict equivalent pore radius from the elastic moduli calculated from sonic velocity and bulk density logs from the Skjold Flank-1. The predicted

equivalent pore radius show an overall depth-wise decrease, but is highest in the lower part of the Cenozoic shale sections (20 nm) and decreases to 8 nm in the deeper Jurassic shale section. A relatively modest equivalent pore radius of around 15 nm in the youngest sediments is related to the relatively low porosity of these silty shales. The overall reduction in the equivalent pore radius with depth can be correlated with the changing mineralogical composition of the shale from smectite rich Cenozoic shale to illite rich Jurassic shale causing a decrease in specific surface.

3 Permeability, Compressibility and Porosity of Jurassic Shale from the Norwegian-Danish Basin

3.1 Summary

The Fjerritslev Formation in the Norwegian-Danish Basin forms the main seal to Upper Triassic¬– Lower Jurassic sandstone reservoirs. In order to estimate the sealing potential and rock properties, samples from the deep wells, Vedsted-1, in Jylland and Stenlille-2 and Stenlille-5 on Sjælland were studied and compared to samples from Skjold Flank-1in the Central North Sea. Mineralogical analysis based on X-ray diffractometry (XRD) show that onshore shales from the Norwegian-Danish Basin are siltier than offshore shales from the Central Graben. Illite and kaolinite dominate the clay fraction. Porosity from helium porosimetry-mercury immersion (HPMI), mercury injection capillary pressure (MICP) and nuclear magnetic resonance (NMR) measurements on the shale samples show that MICP porosity is 6% to 10% points lower than HPMI or NMR porosity. Compressibility from uniaxial loading and velocity of elastic waves were measured simultaneously on saturated samples under drained condition at room temperature. Uniaxial loading causes both elastic and plastic deformation at low stress, but unloading at stress corresponding to in situ stress gives stiffer material with high elastic moduli close to values calculated from mass density and velocity of elastic waves. This result indicates that shale is significantly stiffer in situ than normally assumed in geotechnical modelling. Permeability can be predicted from elastic moduli and from combined MICP and NMR data.The predicted permeability from BET specific surface using Kozeny's formulation for these shales being rich in silt and kaolinite fall in the same order of magnitude as measured permeability from constant rate of strain (CRS) experiments, but is two to three orders of magnitude higher than the predicted permeability from the Yang and Aplin model, which is based on clay fraction and average pore radius. We also found that taking Biot's coefficient into account when interpreting CRS data has a significant and systematic influence on resulting permeability of deeply buried shale.

3.2. Introduction

Shale and mudstone are important sedimentary rocks and together with other fine-grained clastic sediments, fill the majority of the world's sedimentary basins. Shales may act as source rocks and seals to hydrocarbon and CO_2 in reservoirs and in context of shale gas exploration and exploitation can also be referred as reservoir rocks. Important petrophysical properties of shale include porosity, permeability and compressibility, and quantifying these properties is relevant in assessing its sealing efficiency to fluid movement and the possibility of pore pressure propagation or overpressure development in sedimentary basins. These properties have been studied extensively in different places and, and their variation has been shown to depend on composition and the history of compaction which may differ from basin to basin. Quantifying these properties is necessary to evaluate the sealing potential of Jurassic shale from the Norwegian-Danish basin.

3.2.1 Porosity

Shale porosity values reported can range from 2% to more than 80% (Howard 1991; Yang and Aplin 2007), but measuring shale porosity is difficult and the derived values depend on the method used. The Helium porosimetry method which is one of the most reliable methods used for determining porosity has been speculated to overestimate porosity in shale because of He-adsorption on clay minerals (Cui et al. 2009). Even if porosity were to be measured accurately, it may include porosity from microcracks which then adds to an overestimate of the porosity. The Helium Porosimetry-Mercury Immersion (HPMI) technique can be used in determining porosity for cuttings samples (Mbia et al. 2013). Estimating shale porosity from the Mercury Intrusion Capillary Pressure (MICP) method can underestimate total porosity because mercury cannot fill the entire pore space. Nuclear Magnetic Resonance (NMR) porosity determination is based on saturation state of the sample, and if 100% saturated it will give the total porosity measurement of the sample but may also overestimate porosity in the presence of micro-cracks. In this study we will compare these methods to determine the porosity.

3.2.2 Compressibility

Compressibility of shale is essential in several engineering tasks such as investigation of pressure propagation through caprocks, predicting caprock and well bore stability as well as predicting regional subsidence. Uniaxial static and dynamic compressibility in different directions with respect to bedding of a rock material can be obtained from consolidation experiments and continuous

elastic wave propagation which is routinely recorded during drilling operation and also may be recorded during geotechnical testing. Elastic constants and anisotropic parameters (Thomsen 1986) can also be computed from velocity and bulk density data (Thomsen 1986; Dewhurst et al., 2006; and Yenugu, 2010).

Unlike the situation for reservoir rocks and shallower mudstones available in the geotechnical literature, there are not so much experimental data available for uniaxial compressibility of deeply buried shale. For example Jizba and Nur (1990) did hydrostatic measurements on dry mudstone samples and reported static and dynamic compressibility data to be similar at higher stress level of 75 – 125 MPa and to range from 0.5 x 10^{-10} Pa^{-1} to 0.3 x 10^{-10} Pa^{-1}. Sandstone compressibility of 4.5 x 10^{-10} Pa^{-1} and above has been used in several occasions also as a value for shale compressibility for reservoir simulation studies (Zhou et al. 2008; Birkholzer et al. 2009; Buscheck et al. 2012). Zhou et al. (2008) suggested that compressibility of up to 10^{-6} or 10^{-7} Pa^{-1} order of magnitude can be achieved as indeed shown by the data of Hendron et al. (1970). Compressibilities obtained under hydrostatic loading condition are used in several reservoir engineering studies, but differ from uniaxial compressibilities (Teeuv 1971; Lachance and Anderson 1983; Anderson and Jones 1985; Rhet and Teufel 1992), and will in many cases not represent true reservoir conditions of stress, whereas uniaxial compressibilities measured under uniaxial strain conditions are known to best represent true reservoir conditions although only few data are available (Khatchikian 1995; Ong et al. 2001; Yi et al. 2005). We are presenting experimental compressibility data for shale samples from the fairly deeply buried Fjerritslev Formation in Stenlille-2 and 5 wells and will compare the static and dynamic compressibility.

3.2.3 Permeability

Permeability (k) is a measure of the rate of fluid flow through a porous material under a pressure gradient and it is usually determined by measuring the steady state flow rate through a sample under a constant pressure gradient as (Darcy 1856)

$$k = -\frac{Q\mu}{A}\left(\frac{\delta P}{\delta x}\right)^{-1} \qquad (3.1)$$

where Q is the volume of fluid discharge per unit time, A is the cross-section area, μ is the dynamic viscosity of fluid, and $\delta P/\delta x$ is the pressure gradient in flow direction x. Permeability is one of the most important but least predictable physical properties of shale. Due to low permeability, shale plays a dominant role in controlling fluid flow and the occurrences of abnormal pore pressures in

sedimentary basins (Dickinson 1953; Dickey et al. 1968; Magara 1971; Chapman 1972, 1994; Schmidt 1973; Berg and Habeck 1982; Freed and Peacor 1989; Bigelow 1994; Mondol et al. 2007; Peltonen et al. 2008, 2009). Shale permeability varies widely in order of magnitude from microdarcy to nanodarcy with values well above and below those required for pressure seals over characteristic geologic and reservoir production times (Young et al. 1964; Magara 1971; Lin 1978; Bredehoeft et al. 1983; Katsube et al. 1991; Dewhurst et al. 1998, 1999; Kwon et al. 2001). Shale permeability has been reported to depend on porosity, clay mineralogy and clay content, grain size distribution, grain shape, grain packing, specific surface area of the clay minerals and viscosity of the pore fluids (Macey 1942; Michaels and Lin 1954; Leonards 1962; Mesri and Olson 1971; Olsen 1972; Katsube et al. 1991; Dewhurst et al. 1998, 1999; Revil and Cathles, 1999; Kwon et al., 2004; Yang and Aplin 1998, 2007), all of which may change with increasing temperature linked to a high geothermal gradient (Hower et al. 1976; Lee et al. 1985; Dzevanshir et al. 1986; Kim et al. 1999). Clay aggregates with a high content of smectite exhibit extremely low permeability to the flow of fluids due to the smaller pore throat sizes in smectite and because the aggregates are susceptible to clay swelling (Scott and Smith 1966; Norrish 1972; Van Olphen 1977; Moore et al. 1982; Sparks 1995; Sposito et al. 1999; Faulkner and Rutter 2000). Hydration and expansion of smectitic clays may be affected by changing fluid composition, as interlayer cations are replaced by solutes of the pore fluid. Correspondingly, permeability of clay aggregates may also depend on electrolytes in the pore fluid (Mesri and Olson 1971; Olsen 1972; Whitworth and Fritz 1994). Permeability of deeply buried shale, with abundant illite and little or no smectite, are expected to show less chemical sensitivity than permeability of shallow mudstones with higher smectite contents. Yet, transport properties may continue to depend on fluid composition if cation exchange occurs at intergranular clay-fluid interfaces, and pores are affected by changing dimension of the diffuse double layer (Kwon et al. 2004). Knowledge of shale permeability is required in lots of engineering tasks yet this parameter remain very difficult to determine, especially for deeply buried mudstones with sub micro-darcy values (Katsube et al. 1991; Neuzil 1994; Schlömer and Krooss 1997; Dewhurst et al. 1998, 1999; Hildenbrand et al. 2004; Kwon et al. 2004; Mallon et al. 2005).

Measuring fluid flow directly from shale to calculate permeability is very difficult and time consuming. An indirect approach has been proposed by Wissa et al., (1971) to measure permeability from excess pore pressure build up when a shale sample is compressed under increasing uniaxial strain condition during constant rate of strain experiments. This technique is relatively efficient and less expensive and often results in permeability values similar to those

measured directly from flow rate (Mondol et al. 2008; Daigle and Dugan 2009). The influence of Biot's coefficient has not been tested in this method and it is often assumed to be 1.0 even for deeply buried shale that might have undergone some degree of cementation. Alam et al. (2012) showed that Biot's coefficient can be estimated from uniaxial confined tests because it is related to the mechanical strain in the elastic stress regime. Besides measuring shale permeability directly from flow through tests or indirectly from geotechnical tests on core samples, there exists a variety of capillary tube models that could estimate permeability from more easily measured physical properties such as porosity, grain density and specific surface area data (Kozeny 1927); from mercury injection capillary pressure (MICP) data (Leonards 1962; Scheidegger 1974; Garcia-Bengochea et al. 1979; Pittman 1992; Yang and Aplin 1998, 2007); from NMR and MICP data (Daigle and Dugan 2011). FIB-SEM (Focused Ion Beam - Scanning Electron Microscopy) 3D imaging at high resolution can be used to model permeability from porosity and pore network connectivity (Zhang et al. 2011) but this will not be discussed further. Permeability may also be predicted from elastic data and has been discussed for the case of synthetic shale and for Skjold Flank-1 shale from the Central North Sea (Fabricius 2011; Mbia and Fabricius 2012, Mbia et al., 2013). In this study we compare different methods for estimating shale permeability and also discuss the mechanisms that may be used to explain the discrepancy between the different methods used in determining porosity and compressibility of Jurassic shale from the Norwegian-Danish Basin.

3.3 Materials and methods

The ideal situation would be to use Fjerritslev Formation core samples from Vedsted-1 well for this study, but because of the lack of core materials in this location, cuttings samples were used. For establishing analogy between the different localities, core material and well-log data were combined with cuttings samples from three other wells penetrating the same formation (Stenlille-2, Stenlille-5 and Skjold Flank-1). The locations of the wells are shown in Figure 3.1. Preserved cores are available from Stenlille-2 and Stenlille-5. Well logs and final well reports were used to develop a sampling strategy for the cuttings samples which were taken in a 30–100 m maximum spacing interval that could show effects of changes in mineralogy. The wells are vertical with only minor deviation and all depths are given as vertical depth, in meters from sea level.
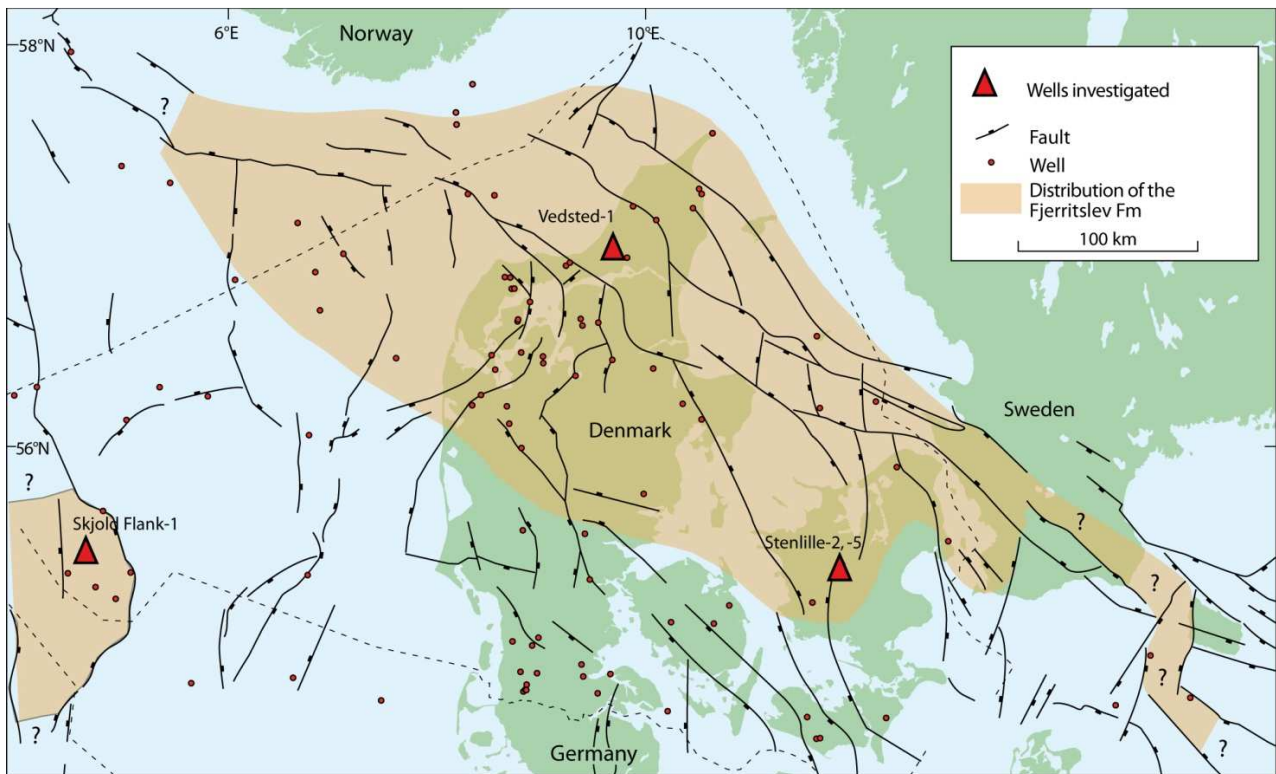
Figure 3.1 Map showing location of the three studied sites and the outline of the Fjerritslev Formation in the Norwegian-Danish Basin to the Northeast and North Sea Central Graben to the Southwest (Modified after Petersen et al., 2008).

Forty-two Jurassic shale cuttings samples, 31 from the three onshore wells (Vedsted-1 and Stenlille-2 & 5) and 11 samples from the Skjold Flank-1 offshore well were used for this study. The sampled material consists of unwashed cuttings. In the Vedsted-1 well, two samples were taken from each of Børglum, Flyvbjerg and Haldager Sand Formations overlying the Fjerritslev Formation, three samples from Gassum Formation and seven samples from the Fjerritslev Formation; all twenty nine samples from Stenlille-2, Stenlille-5 and Skjold Flank-1 are from Fjerritslev Formation. The Fjerritslev Formation is divided into four members and constitutes the main stratigraphic intervals that are widespread in the Jurassic of Norwegian-Danish Basin and the Danish Central Graben sealing most of the Lower to Upper Triassic reservoirs. Previous studies have shown that the lower member of the Fjerritslev Formation is regionally widely spread over much of the basin but not all the members have been preserved due to Middle Jurassic uplift and erosion (Andsbjerg et al. 2001; Nielsen 2003). For a detailed review of the Permian–Cenozoic depositional evolution of the basin and a comprehensive account of the basin evolution and stratigraphy, the reader is referred to Michelsen et al. (2003), Nielsen (2003) and Petersen et al. (2008). Figure 3.2 shows a simplified stratigraphical correlation of the wells used in the present study.
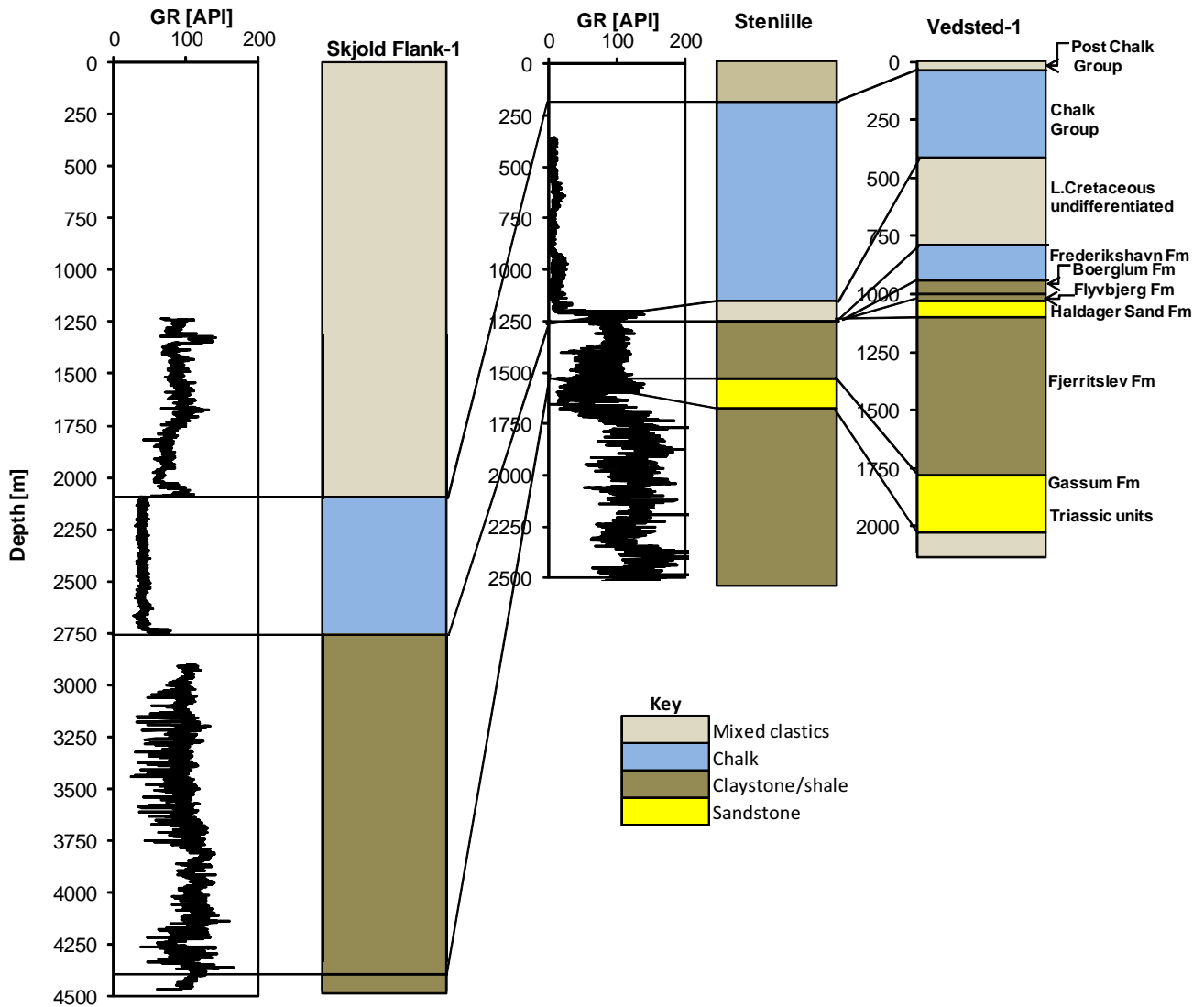
Figure 3.2 Simplified lithostratigraphic correlations of Vedsted-1, Skjold Flank-1 and Stenlille wells where Gamma Ray well logs data and well reports were available.

The cuttings samples were carefully washed with deionized water several times to remove all the drilling mud and were left in methanol for two weeks to dissolve any salt present. Silver nitrate was added to the extracted solution from the samples after each cleaning step to make sure that there is no salt present in the methanol solution. It is worth noting the difficulty involved in cleaning shale samples with very low permeability that may prevent methanol from getting into the entire pore space to dissolve all the salts. The cleaned samples were then dried in an oven at 60°C for three days. Upon completion of the cleaning process, each sample was handpicked to remove irrelevant cavings material. The final samples weigh from 55 to 95 grams and mineralogy was determined by XRD, texture was evaluated by scanning electron microscopy of polished section by applying the backscatter technique (BSEM), grain density analysis was done by He-porosimetry, grain size

distribution was done using the SediGraph method which is based on well-established physical phenomena of gravitational sedimentation, specific surface area was measured by the BET method, cation-exchange capacity (CEC) was measured by Ba-ion exchange and Inductively Coupled Plasma–Optical Emission Spectrophotometry (ICP-OES). For detailed sample preparation and procedure see Mbia et al. (2013). Results are summarized in Table 3.1.

Preserved shale cores are scarce and the ones from deep boreholes are difficult to handle due to the low permeability and sensitivity to contacting fluids (Chenevert et al. 1991; Katsube et al. 1991 and Best et al. 1995). The fact that these samples have been retrieved from kilometers of depth adds to complexity because unloading the shale from in situ pressure and temperature, may cause damage and alteration by several processes such as: expansion, creation of micro-cracks, and reduced saturation (the samples may not be 100% saturated under atmospheric conditions, even if the pore water is contained in the sample). This makes laboratory testing susceptible to artifacts unless special procedures are applied (Forsans et al.1994 & Horsrud et al. 1998). In this study two preserved core samples were taken from the Fjerristlev Formation in Stenlille-2 and Stenlille 5 wells at 1484 m and 1576 m respectively. The core had been preserved in the native brine in sealed core barrel. Plug samples of 38.2 mm (1.5 inch) diameter and 24 mm (0.95 inch) long were drilled at three different orientations; normal to the apparent geologic bedding plane (V), diagonal to the bedding plane (D) and parallel to the bedding plane (H) in order to enable us to determine velocity and permeability anisotropy. Drilling was done with prepared synthetic brine (189 g/l) equivalent to in situ concentration to prevent dehydration of the samples. The drilled plugs were immediately immersed in the synthetic native brine solution to prevent desiccation of the samples and were then stored in the refrigerator at 15 ^{0}C. Ten shale samples were taken from the dry and non-preserved cores in the same depth range as the wells with the preserved cores. Although these samples have been dried naturally after being placed in the core boxes, they still contain salts in their pore spaces. In order to remove salt formed during drying and any drilling mud we washed the samples in deionized water and Soxhlet cleaned the samples in methanol for two weeks. Silver nitrate was used to test for any salt that may be present before drying in an oven at about 60°C for two weeks to remove any pore fluid. Since the samples contain only little smectite we assumed that there is no shrinkage effects, even if it would be very small and not affect our results.

3.3.1 Quantification of shale porosity

Three independent methods have been used to quantify shale porosity from both cuttings and core material and these include; helium porosimetry-mercury immersion (HPMI), mercury injection capillary pressure (MICP) and nuclear magnetic resonance (NMR).

The HPMI method is used to measure porosity in cuttings samples, we first measured the grain volume, V_g of each sample by helium porosimetry. To get grain density, ρ_{grain} we divided sample weight with V_g. Since we could not measure the bulk volume of cuttings samples by caliper, a mercury immersion technique was used. In order to carry out this measurement a special set-up was used as shown by a simplified diagram in Figure 3.3, which includes a weighing balance where the beaker is placed, a perforated steel basket that can be opened in the middle to insert the samples. The basket is then attached to a swing arm through the lid of the beaker in order to keep the basket steady in the mercury. The beaker glass is filled with mercury to an expected level before the basket is immersed in it.
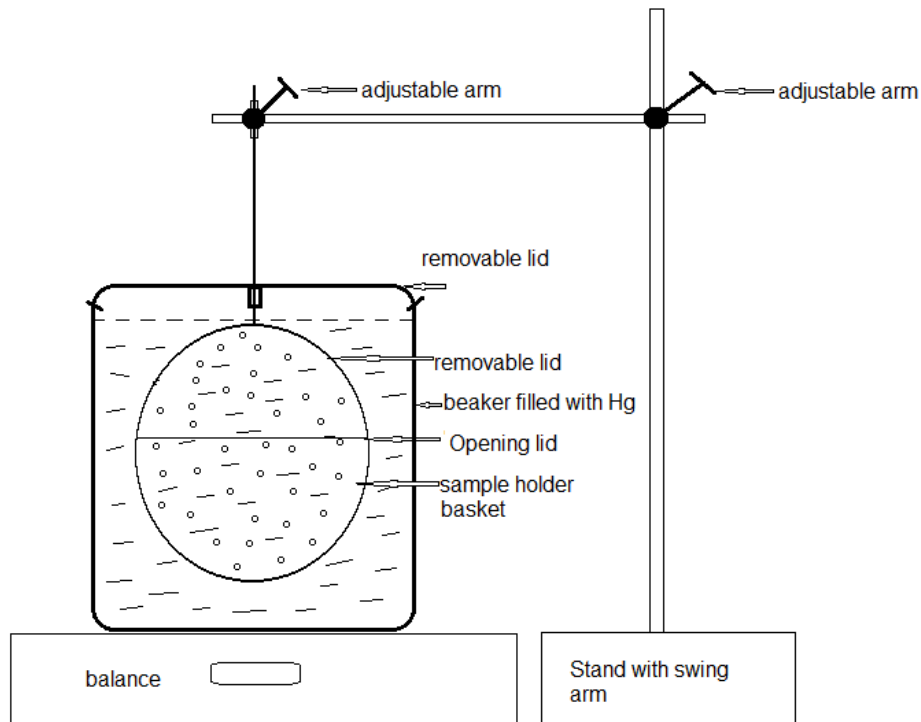

Figure 3.3 Setup for measuring bulk volume of cuttings samples by mercury immersion.

The following steps were followed to measure the dry bulk volume of the sample: (1) the weight of the empty basket was measured in air and in mercury. (2) The weight of the basket plus the sample was measured in air and in mercury. (3) Actual sample weight is equal to weight of the basket plus

the sample in air minus weight of empty basket in air. (4) Actual sample weight in Hg is equal to weight of the basket plus the sample in Hg minus weight of empty basket in Hg.

In order to get the dry bulk volume *(V$_{dry}$)* we divided actual sample weight in mercury by the density of mercury.

To get dry density (ρ$_{dry}$) we divide actual sample weight by dry bulk volume.

Porosity (*ϕ*) is then calculated as

$$\phi = (V_{dry} - V_g)/V_{dry} \tag{3.2}$$

For reference, measurement was done on five crushed chalk samples with known porosity and the excess bulk volume contribution (about 2%) is then corrected.

The MICP method is also used to measure porosity in cuttings samples and this is a standard method for characterizing pore throat radius distribution in porous media spanning from the micron-scale to the nano-scale (Coates et al. 1999; Nimmo 2004). The measurement was done using Micromeritics AutoPore IV 9500 and mercury pressure (*P$_c$*) from 27.51 MPa to 414 MPa and consequently mercury intruded pore throat radius (*r$_c$*) of down to 2.0 nm according to the Washburn (1921) equation given as

$$r_c = \frac{2\sigma_s cos\theta}{P_c} \tag{3.3}$$

where σ_s is the surface tension, for the air/mercury system 485 mN.m^{-1} (Adamson and Gast, 1997) is the standard universally used value. The contact angle *θ,* is assumed to be 0. The porosity is calculated as cumulative mercury volume in fraction of total volume (table 1)

For the NMR method, saturated shale plugs of 3.8 cm diameter were drilled from preserved core samples using synthetic brine with 189 g/l concentration equivalent to in situ concentration, in order to prevent desiccation of the samples. These were immediately immersed in the same brine using plastic containers and stored in the refrigerator at 15 0C. With this handling and the fact that they have been well preserved, we assumed that the sample is fully saturated. Low-field nuclear magnetic resonance (NMR) measurements were done on the shale samples at room temperature to examine the T2 relaxation time distribution of the fluids in the pore space. The instrument used is Oxford GeoSpec2 NMR Core Analyzer, operating at 2.0 MHz. The T2 relaxation spectra are generated using the WinDXP (Oxford Instruments, UK) software. The polarizing magnetic field (B0) is provided by a 49 mT permanent magnet oriented in the z-direction and the Carr–Purcell–

Meiboom–Gill (CPMG) pulse sequence with an echo spacing of 0.05 ms and length of 25 s per scan. We recorded 16 scans with 0.75 s dead time between scans. The initial amplitude of the raw decay curve is directly proportional to the number of polarized hydrogen nuclei in the pore fluid. Porosity is provided by the ratio of this amplitude to the tool response in water with the notion that the sample is fully saturated. The porosity results are summarized in table 1. For more details see Coates et al. (1999) and Josh et al. (2012).

3.3.2 Experimental setup for uniaxial consolidation test to obtain Permeability, Biot's coefficient and compressibility

Triaxial Hoek and oedometer cells were deployed in the Danish Geotechnical Institute (GEO) for the uniaxial compression tests on the preserved core samples. The Hoek cell is used for the velocity measurements and the oedometer cell for the determination of Biot's coefficient and permeability. The general layout of the experimental apparatus is shown in Figure 3.4 for Hoek cell and Figure 3.5 for the oedometer cell and all include the external high-accuracy linear variable differential transformers (LVDTs) mounted in a load frame positioning system to measure the axial deformation. The axial deformation measured by the load frame is corrected for the systems self-deflection (virtual infinite stiffness correction). The samples end surfaces were made flat to approximately within 0.01mm by grinding in order to maintain a perfect contact between test cell and the sample to minimize errors in strain measurements, which if not perfect, may induced radial strain, such that the true volumetric strain will not be measured from the LVDT reading. In addition the end surfaces of the sample must be exactly parallel and fit perfectly with the piston and the bottom porous plate. The core samples are plugged ($\pm$ 0.05 mm) to match the inside diameter of the cell. The dimensions of the samples are 38.2 mm (1.5 inch) in diameter to increase the drainage area and 24 mm (0.95 inch) in length to reduce the drainage distance. The experiments were conducted under room temperature of 25^0C on vertically oriented core plugs by applying vertical stress and strain corresponding to the in situ condition and the samples were loaded repeatedly initially to minimize the possible effects from bedding and microcracks. The axial stress and pore pressure for the test were designed to mimic the caprock stress condition in the relevant depth for the Fjerritslev Formation. In order to carry out ultrasonic velocity measurements, a sample for Oedometer testing is mounted in a cell with a system of pore pressure control, axial and radial displacement and ultrasonic transducers (Figure 3.4). The sample is allowed to drain at top and bottom in a servocontrolled load frame during the test. The axial stress is increased at 5 MPa/h up to a

maximum of 25 MPa at axial to radial stress ratio of 0.38 in a series of unloading and reloading stress cycles. This rate was chosen in order to reduce experimental time. The accuracy of the ultrasonic sensors was ±0.001 volts and prior to testing, each sensor was individually calibrated and the operation of the ultrasonic apparatus was verified using three aluminum specimens of 12 mm, 25mm and 50 mm length with the same elastic properties for reference. The lag time of the instrument is estimated by extrapolating a straight line in the plot of arrival time against the different length of the reference sample until it cuts the time axis.
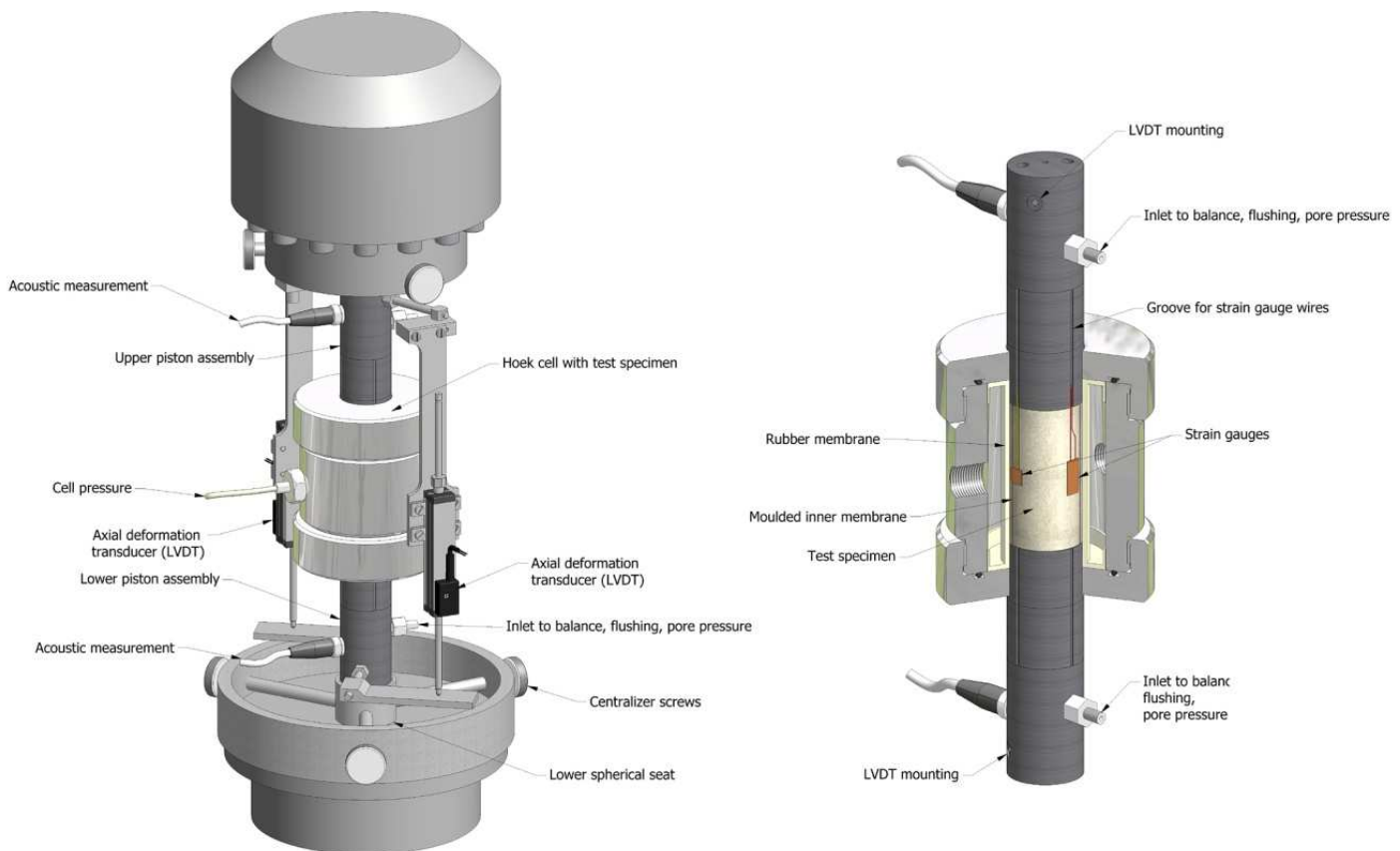
Figure 3.4 Illustration of and cross-section of the high stress uniaxial Hoek cell showing linear variable displacement transducer (LVDT), pore pressure sensor, P- and S-wave source and receiver crystals are shown, together with other components of the Hoek cell. The figure is supplied by the Danish Geotechnical Institute.

Ultrasonic velocities measured during the uniaxial compressional tests include V_p, shear V_{S1} and V_{S2} for vertical, horizontal and diagonal samples and the wave velocities were measured using the Birch (1960) pulse transmission technique with frequency of 200 KHz for the piezoelectric P and S wave signals and were recorded with a period of 5 minutes throughout the loading, unloading and

reloading stress paths of the experiment. To determine the absolute error in P- and S-wave measurements, the procedure similar to that of Hornby (1998) was used.
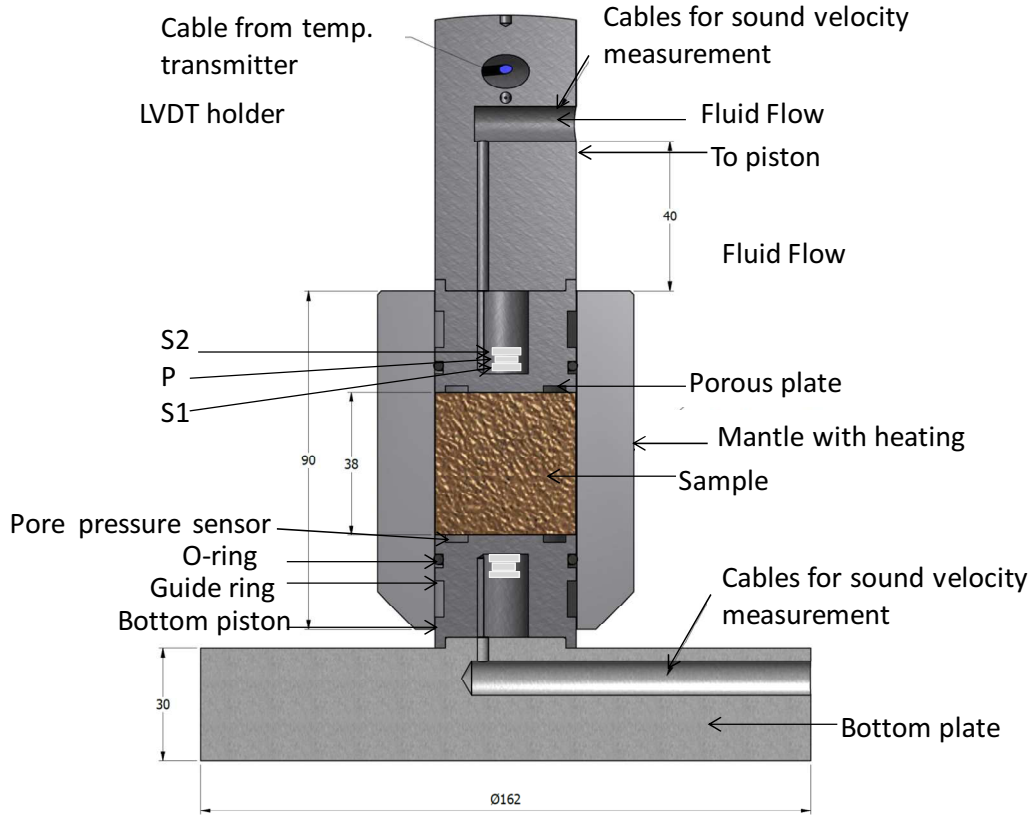
Figure 3.5 Cross-section of the high stress uniaxial Oedometer cell showing linear variable displacement transducer (LVDT) holder, pore pressure sensor, P- and S-wave source and receiver crystals together with other components of the Oedometer cell. The figure is made by the Danish Geotechnical Institute.

Considering that velocities are computed from the travel times of the transmitted ultrasonic pulse velocities can be calculated from the following expression,

$$V = \frac{H}{t_m - t_r} \tag{3.4}$$

where V is P-wave or S-wave velocity, H is sample height, t_m is the measured travel time needed for P- or S-wave to travel through the sample and t_r is a reference travel time from the head-to-head measurements. An example of waveforms for P and S- wave pulses recorded for the vertical and horizontal core samples from St. 2 Fjerritslev Formation shale at low (5 MPa), and high (20 MPa) stresses is shown in Fig. 6.
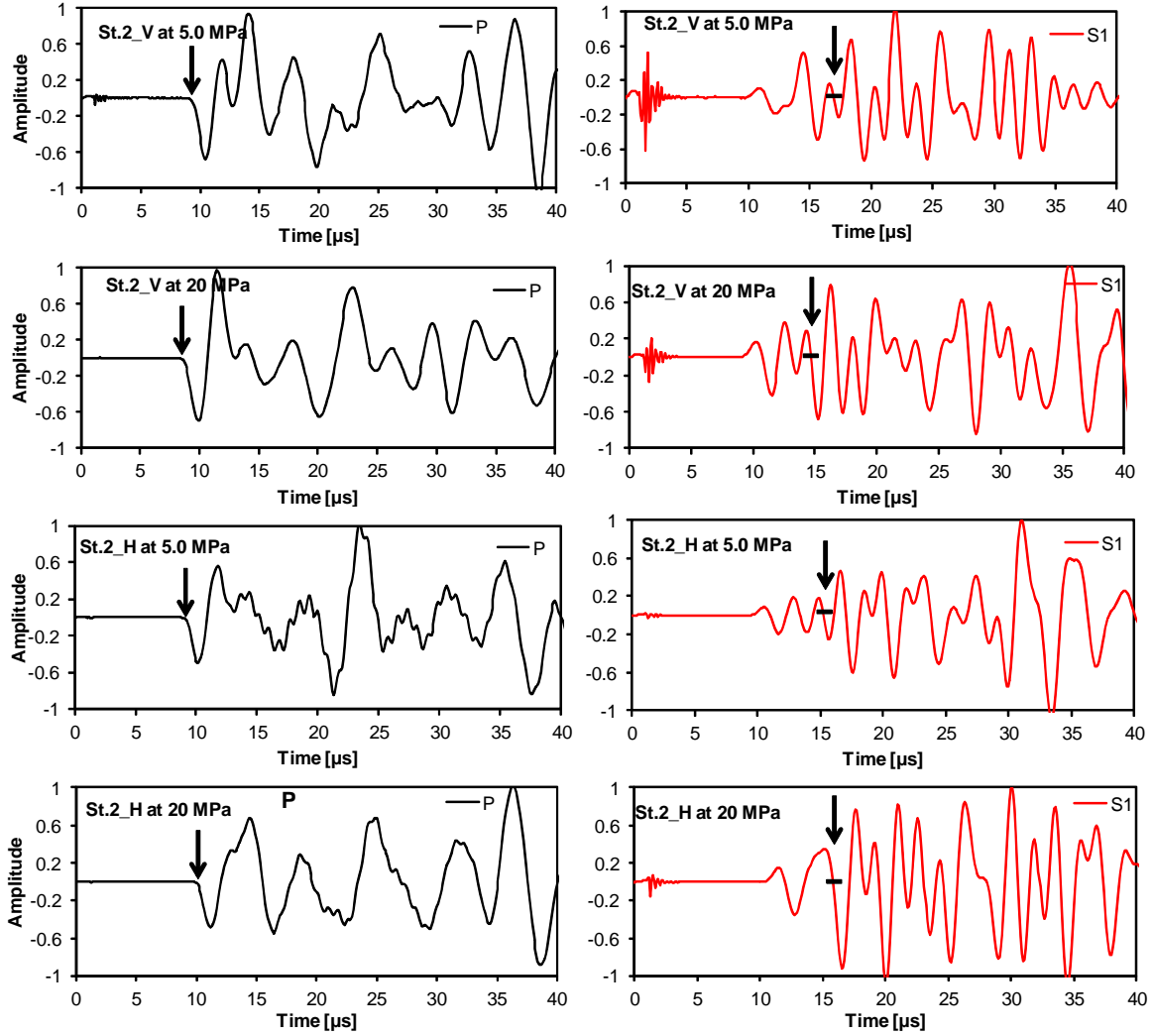
Fig. 3.6 Illustration of waveforms for P- (black) and S- wave (red) pulses recorded for the vertical and horizontal core samples from St. 2 Fjerritslev Formation shale at low (5 MPa), and high (20 MPa) stresses. The first arrival time picks of P- and S-waves are marked on the zero crossing waveforms by black arrow. The sample height range from 2.1 cm to 2.4 cm and the lag time for P-wave is 3.4 µs and for S_1 is 7.4 µs.

The resulting error ΔV in the wave velocity measurement can be estimated by partial differentiation

$$\Delta V = \frac{\partial V}{\partial H} \Delta H + \frac{\partial V}{\partial t_m} \Delta t_m + \frac{\partial V}{\partial t_r} \Delta t_r \tag{3.5}$$

where Δt_m and Δt_r are the errors in the travel time picks (human errors) for the measured and the reference travel times and ΔH is the magnitude of the error (error due the instrument) with respect to the sample height measurement. The absolute error in the velocity estimation is evaluated as

$$\Delta V = \frac{\Delta H}{t_m - t_r} + H \frac{\Delta t_m}{(t_m - t_r)^2} + H \frac{\Delta t_r}{(t_m - t_r)^2} \tag{3.6}$$

The maximum absolute error in the measurement is

$$\Delta V = \frac{\Delta H}{t_m - t_r} + 2H \frac{\Delta t}{(t_m - t_r)^2} \tag{3.7}$$

where $\Delta t = \Delta t_m = \Delta t_r$, To estimate errors, a precision of the LVDT sample length measurement of ± 0.04 mm or $\pm 0.2\%$. For 24 mm sample height, a typical value of $(t_m - t_r)$ for P-wave propagation is 3.4 µs and by setting a precision of the P-wave travel time picking of 0.02 µs, one can estimate the absolute error of the P-wave velocity measurement of ± 87 m s^{-1}. This corresponds to a relative error in the P-wave velocity estimation of approximately $\pm 2.5\%$ at a velocity of 3200 m s^{-1}. For same sample height, a typical value for S-wave propagation for $(t_m - t_r)$ is 7.4 µs and, setting a precision of the travel time picking of 0.03 µs, one can estimate the absolute error of the S-wave velocity measurement of ± 56 m s^{-1}. Therefore, the relative error in S-wave estimation is approximately $\pm 4\%$ for S-wave propagation at a velocity of 1200 ms^{-1}. From observations during the experimental work, it can be stated that the maximum absolute error for both V_p and V_s is less than ± 0.3 µs, including the picking error. It is important to note that the error picking is higher at low stresses compared to high stresses. At stresses between 15 and 20 MPa corresponding to the in situ conditions of our samples, the absolute error is much lower due to the improved accuracy of the travel time picking especially for S-wave velocity.

The velocity data measured from different orientations and bulk density data can be used to compute the elastic constants as

$$C_{33} = \rho V_{PV}^2 \tag{3.8}$$

$$C_{44} = \rho V_{SV}^2 \tag{3.9}$$

$$C_{11} = \rho V_{PH}^2 \tag{3.10}$$

$$C_{66} = \rho V_{SH}^2 \tag{3.11}$$

$$C_{13} = \left(-C_{44} + [4\rho^2 V_{PD}^4 - 2\rho V_{PD}^2 (C_{11} + C_{33} + 2C_{44}) + (C_{11} + C_{44})(C_{33} + C_{44})]^{1/2}\right) \tag{3.12}$$

where V_{PV} is the P-wave velocity normal to the bedding, V_{PH} is the P-wave velocity parallel to the bedding, V_{PD} is the P-wave velocity diagonal to the bedding, V_{SV} is the S-wave velocity normal to the bedding, ρ is the bulk density.

The anisotropic parameters ε, γ, and δ can be defined from eqs (8) – (12) according to Thomsen (1986) as

$$\varepsilon = (C_{11} - C_{33})/2C_{33} \tag{3.13}$$

$$\gamma = (C_{66} - C_{44})/2C_{44} \tag{3.14}$$

$$\delta = \frac{(C_{13} + C_{44})^2 - (C_{33} - C_{44})^2}{2C_{33}(C_{33} - C_{44})} \tag{3.15}$$

Constant rate of strain (CRS) tests were performed in the Oedometer on samples with the same dimension as those used in velocity measurements at different sample orientation to determine permeability perpendicular and parallel to the direction of geologic bedding. The stainless steel Oedometer cell has a highly polished diameter so effects of side friction were considered to be too small to affect the results. The samples were contained within a sample ring that fits the top cap and the base plate, both made of stainless steel; the top is equipped with a 2 mm thick porous disk connected to one drainage tube whereas the bottom is undrained to allow pore pressure build up. A backup pressure of about 0.5 MPa was applied. A pore pressure sensor was used to monitor the pore pressure at the bottom of the specimen. In order to setup a pressure gradient to meet the conditions for this kind of test, the sample was loaded initially at strain rate corresponding to 1.3 x 10^{-6}/s followed by a series of loading-unloading-reloading stress cycles. In these tests the strain rate is governed by the excess pore pressure. The excess pure pressure was controlled to maintain a fixed pore pressure ratio between 20% and 25% of the total axial stress while varying strain rate. The test was initiated with a fixed strain rate, but as the pore pressure ratio approaches the desired value, the strain rate is automatically adjusted to retain the pore pressure ratio such that permeability can be calculated from the slope of excess pore pressure and effective stress plot.

In order to determine Biot's coefficient the same procedure is repeated on another sample of the same material but in this case constant rate of strain is switch to constant rate of stress during the experiment.

The following steps were taken to complete the Biot's coefficient test which lasted for about four months; 1) Axial stress σ_a is increased to 0.5 MPa to keep the specimen firmly in the cell and the axial strain e_a, is reset in order to initialize. 2) Venting at the bottom of the sample before the filters

and tubes were then vacuum saturated with the formation brine to remove any air present and in this case the sample is allowed to drain at the bottom. 3) In order to set the backpressure, axial stress is increased at 1.0 MPa/hr to 1.0 MPa and pore pressure P_p is increased at 1 MPa/hr to 0.5 MPa. The sample is loaded at strain rate corresponding to 1.5 x $10^{-7}s^{-1}$ to 17.5 MPa and the pore pressure is increased at 1.0 MPa/hr through a series of loading-unloading-reloading cycles in order to minimize the bedding effect. The bottom and top valves are open between one and two hours to allow the pore pressure at both ends to equilibrate at 1.5 MPa as assessed by the pore pressure sensors. No confining stress is applied apart from the walls of the steel cell. The orthogonal component of the axial stress produces strain in radial direction such that any space between the test cell and the sample's peripheral surface is eliminated. 4) While maintaining at constant differential (confining minus pore pressure) pressure (σ_d) of 16 MPa, σ_a and P_p are increased simultaneously from 17.5 to 32.5 MPa and from 1.5 to 16.5 MPa, respectively at rate of 1 MPa/hr while allowing a creep phase at constant σ_a of 21 MPa and P_p of 1.5 MPa, as shown by the thick lines in enlarged part of the tests in Fig. 7a-c. 5) Axial stress is decreased during the unloading process to 17.5 MPa at rate of 1 MPa/hr while maintaining constant pore pressure at 16.5 MPa. 6) Axial and σ_d stress is increased and decreased during a reloading-unloading phase to 32.5 and 17.5 MPa for σ_a and 16 and 1.0 MPa for P_p as shown by the thick lines in the enlarged part of the tests in Fig. 7 (d-f). 7) Unloading of σ_a and P_p to atmospheric pressure.

Steps 4 and 6 are used for the calculation of Biots coefficient (α) by applying the equation used by Alam et al. (2011) and is given as

$$\alpha = 1 - \frac{\left(\frac{\partial e_a}{\partial P_p}\right)_{\sigma_d}}{\left(\frac{\partial e_a}{\partial \sigma_d}\right)_{P_p}} \tag{3.16}$$

Because the deformation is very small, in order to calculate $(\partial e_a/\partial P_p)_{\sigma_d}$, we assumed a linear chord from the stress-strain curve under loading at constant differential pressure as shown in Figure 3.7b and step 4.
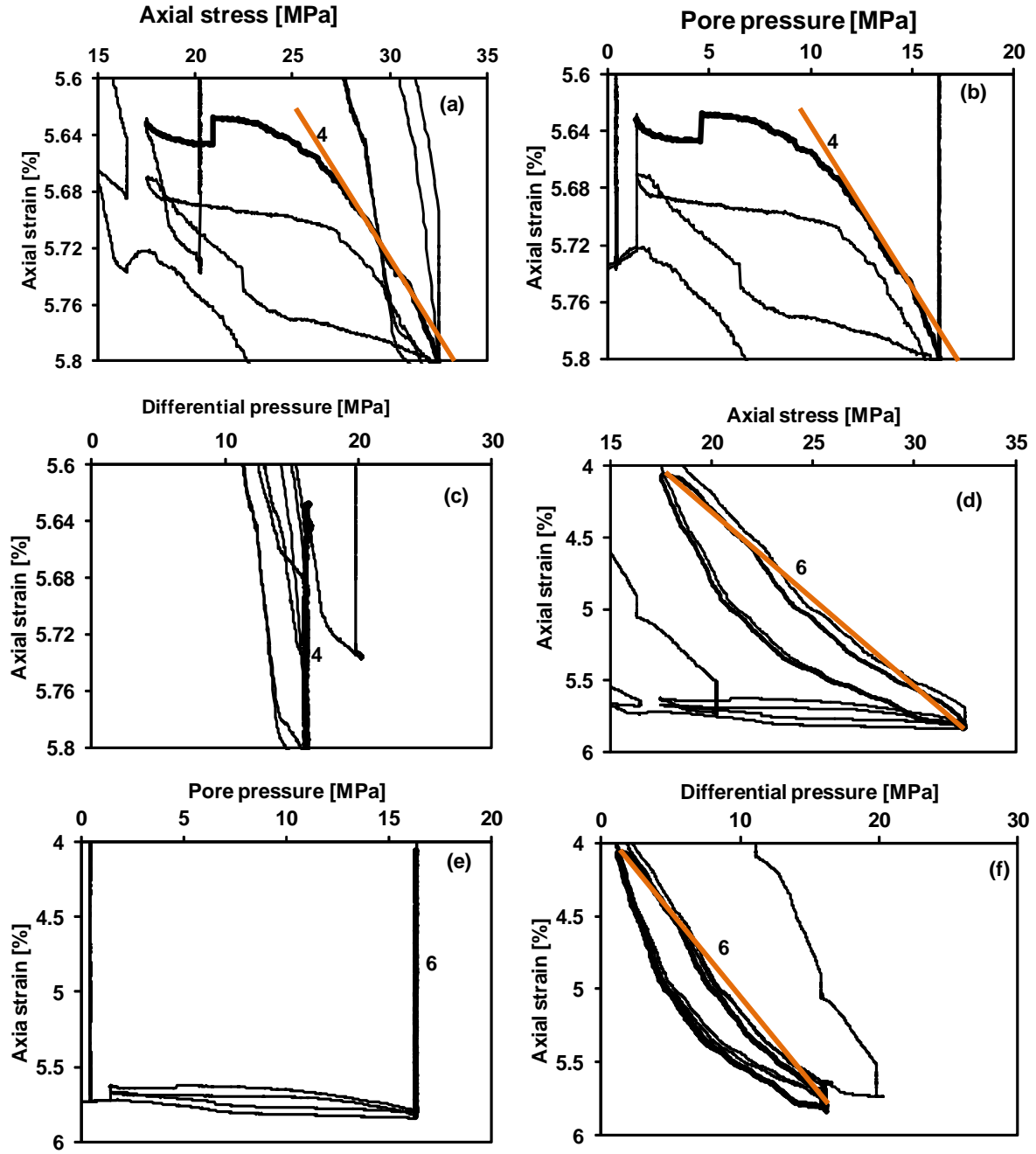
Fig. 3.7 *Stress-strain curves produced from the mechanical test as plotted in terms of axial stress, pore pressure, and differential pressure. a–c, sample with increasing axial stress and pore pressure at constant differential pressure. d–f, sample with increasing axial stress and differential pressure at constant pore pressure. The lines used to estimate the slopes are shown in Fig. (a), (b), (d) and (f).*

We also make the same assumption in calculating $(\partial e_a/\partial \sigma_a)_{P_p}$, from the stress-strain curve under loading at constant pore pressure as shown in Figure 3.7d and 3.7e, step 6. The resulting Biot's (*a*)

coefficient calculated is 0.84 ±0.04 and will be used for permeability calculation. The procedure for this kind of tests has been described in detail by Wissa et al. (1971) and Daigle and Dugan (2009).

3.3.2.1 Calculation of static and dynamic compressibility

Static uniaxial compressibility is computed from stress-strain data by using moving average to smoothen the data and graphically differentiating the strain stress slope as

$$M_{Stat}^{-1} = \frac{\Delta e}{\Delta \sigma} \tag{3.17}$$

where Δe is increment in uniaxial strain and $\Delta \sigma$ is increment in uniaxial stress.

Saturated dynamic compressibility (M_{sat}^{-1}) was computed from velocity and density (ρ_b) data as

$$M_{sat}^{-1} = (\rho_b V_P^2)^{-1} \tag{3.18}$$

Shear compressibility is given as

$$G_{sat}^{-1} = (\rho_b V_S^2)^{-1} \tag{3.19}$$

Although the measurements were done under drained condition, velocity data are undrained, so to obtain dry compressibility of the frame, we used Brown-Korringa (1975) fluid substitution formulation which is applicable to anisotropic material and then compared the results with Gassman's formulation applicable to isotropic material. Brown-Korringa formulation is given as

$$S_{ijkl}^{(dry)} - S_{ijkl}^{(sat)} = \frac{(S_{ij\alpha\alpha}^{(dry)} - S_{ij\alpha\alpha}^0)(S_{kl\alpha\alpha}^{(dry)} - S_{kl\alpha\alpha}^0)}{\left(S_{\alpha\alpha\beta\beta}^{(dry)} - S_{\alpha\alpha\beta\beta}^0\right) + (\beta_{fl} - \beta_0)\phi} \tag{3.20}$$

where

$S_{ijkl}^{(dry)}$ is effective elastic compliance tensor of dry rock, $S_{ijkl}^{(sat)}$ is effective elastic compliance tensor of rock saturated with pore fluid, $S_{kl\alpha\alpha}^0$ is effective elastic compliance tensor of mineral material making up rock, β_{fl} is compressibility of pore fluid, β_0 is compressibility of mineral material and is equal to $S_{\alpha\alpha\beta\beta}^0$, ϕ is porosity.

Gassmann's (1951) formulation for bulk compressibility is given as

$$K_{dry}^{-1} = \left(\frac{K_{sat}\left(\frac{\phi K_0}{K_{fl}} + 1 - \phi\right) - K_0}{\frac{\phi K_0}{K_{fl}} + \frac{K_{sat}}{K_0} - 1 - \phi} \right)^{-1} \tag{3.21}$$

Equation (3.21) can be written for uniaxial compressibility as

$$M_{dry}^{-1} = (K_{dry} + \frac{4}{3} G)^{-1}$$

(3.22)

where, K_{dry} is dry bulk modulus and G is shear modulus, K_0 is mineral modulus. In our calculation, we have used mineral modulus of 25 GPa (Han, 1986) obtained for Gulf of Mexico clay and for comparison we assumed K_0 of 10 GPa for the lower bound and 50 GPa for the upper bound.

3.3.2.2 Calculating permeability from measured data

Liquid permeability can be estimated from BET, specific surface and porosity based on laminar flow of fluid in a homogeneous porous medium (Kozeny 1927) as

$$k = c \frac{\phi^3}{S_g^2(1-\phi)^2}$$

(3.23)

where k, is liquid permeability (Klinkenberg, 1941); c is Kozeny's factor which can be estimated from porosity through a simple model of linear 3D interpenetrating tubes (Mortensen et al., 1998):

$$c = \left(4\cos\left(\frac{1}{3}\arccos\left(\phi\frac{8^2}{\pi^3} -1 \right) + \frac{4}{3}\pi \right) + 4 \right)^{-1}$$

(3.24)

ϕ, is porosity and S_g is grain surface per volume of grains. Knowing the grain density, ρ_g, of the minerals, the S_g is calculated

$$S_g = S_{BET} \times \rho_g$$

(3.25)

The specific surface with respect to the bulk, S, and specific surface with respect to pore, S_p, are calculated (Borre and Fabricius, 1998) as

$$S = S_g (1 - \phi)$$

(3.26)

$$S_p = S / \phi$$

(3.27)

The results are summarized in Table 3.1.

Permeability (k) can also be predicted from combined MICP and NMR T_2 data by using the equation presented by Hossain et al. (2011) as

$$k = c\phi\rho_e^2 \sum_{i-1}^{N} f_i(T_{2i})^2$$

(3.28)

where, f_i is a fraction of the total amplitude of each T_{2i}. The Kozeny's factor c was calculated using equation (8) and ρ_e is the effective surface relaxivity which can be calculated from MICP and NMR data as,

$$\rho_e = r_p/2T_2 \tag{3.29}$$

The same cumulative porosity data was used to tie corresponding T_2 and equivalent pore radius (r_p) data in order to calculate surface relaxivity.

Permeability can also be predicted from compressional, shear and bulk moduli because they are related to pore radius (Fabricius, 2011, Mbia et al., 2013) and these moduli can be calculated from velocity and bulk density data. Velocity and bulk density, ρ_b, can be obtained directly from logging data or from laboratory measurements, bulk density; ρ_b can be calculated from grain density ρ_g, porosity, ϕ and fluid density ρ_{fl},

$$\rho_b = \rho_g\,(1\text{-}\phi) + \rho_{fl}\phi \tag{3.30}$$

Elastic compressional modulus, M, was calculated as: $\quad M = \rho_b V_p^2 \tag{3.31}$

Elastic shear modulus, G, was calculated as: $\quad G = \rho_b V_s^2 \tag{3.32}$

Elastic bulk modulus, K, was as calculated as: $\quad K = M - 4G/3 \tag{3.33}$

The elastic moduli can be used to compute equivalent pore radius, r_p (Mbia et al. 2013; Fabricius, 2010) from empirical relationships given as:

$$r_{pM} = 8.3\ 10^{-9} + 5.7\ 10^{-7}\,M^{-2} \tag{3.34}$$
$$r_{pG} = 7.8\ 10^{-9} + 8.5\ 10^{-9}\,G^{-1} \tag{3.35}$$
$$r_{pK} = 6.6\ 10^{-9} + 5\ 10^{-7}\,K^{-2} \tag{3.36}$$

where r_{pM} is equivalent pore radius from compressional modulus, r_{pG}, from shear modulus and r_{pK} from bulk modulus. Radius is given in nm and moduli are given in GPa.

Permeabilities, k can be modelled by using eqn. (3.34) to (3.36) and Kozeny's relation so that we will have eqn. (3.37) to (3.39) as follows:

$$k_M = c(\phi r^2_{PM}/4) \tag{3.37}$$

$$k_G = c(\phi r^2_{PG}/4) \tag{3.38}$$

$$k_K = c(\phi r^2_{PK}/4)$$ (3.39)

where, c is Kozeny's constant and ϕ is porosity. The results are summarized in Table 3.1.

Permeability can be calculated from CRS test data of excess pore pressure build up (P_{Pe}) during a CRS test, strain rate, dynamic viscosity, sample height, and the measured Biot's coefficient value. The derivation from eqn. 3.40–3.49 relates Darcy's law to coefficient of consolidation and change in strain of the sample during compaction (Wissa et al. 1971). From Darcy's law in eqn. 3.1, we see that the volume fluid discharge, Q, is proportional to the pressure gradient. During compaction of the shale a net fluid flow is established due to the compaction of the pores. If we assume the fluid to be incompressible the compression of the pore-space in a given cross-section must be countered by a flow out of the cross-section. Deeply buried shale has some degree of cementation affecting the magnitude of pore compression which is expressed by Biot's coefficient, a (Biot 1941).

$$\frac{\partial V_p}{\partial z \partial t} = \frac{a \partial e}{\partial t} A = \frac{\partial Q}{\partial z}$$ (3.40)

Deformation is related to Biots effective stress (σ_{eff}), Alam et al. (2011) as

$$\sigma_{eff} = eM = \sigma_t - aP_P$$ (3.41)

where M is Oedometer modulus, σ_t is total uniaxial stress and P_P is pore pressure. By isolating P_P and differentiating with respect to z we arrive at:

$$\frac{\partial P_p}{\partial z} = \frac{\partial}{\partial z}\left(\frac{\sigma_t - eM}{a}\right) = -\frac{M}{\alpha}\frac{\partial e}{\partial z}$$ (3.42)

We substitute eqn. 3.42 into eqn.3.1 to have;

$$Q = \frac{kMA \partial e}{\mu a \partial z},$$ (3.43)

Differentiating eqn. 3.43 with respect z we can rewrite the right side of eqn. 3.40 as,

$$\frac{a \partial e}{\partial t} A = \frac{kMA \partial^2 e}{\mu a \partial z^2}$$ (3.44)

Then eqn. 3.44 becomes

$$\frac{\partial e}{\partial t} = C_v \frac{\partial^2 e}{\partial z^2} = \frac{kM \partial^2 e}{\mu a^2 \partial z^2}$$ (3.45)

The eqn. 3.45 is the basic equation of consolidation defined by Wissa et al. (1971) and C_v is the coefficient of consolidation and is given by $C_v = kM/\mu a^2$ for shale with some degree of cementation. Solving eqn. 3.45 with the boundary condition that the bottom of the sample remains fixed, after transients have dissipated, the solution of Wissa (1971) gives the difference between the strain (Δe) at the top and at the bottom of the sample as

$$\Delta e = 0.5 \frac{rH^2}{C_v} = 0.5 \frac{rH^2 \mu a^2}{kM} \tag{3.46}$$

where r is strain rate, H is sample height such that equation 38 expressed in terms of permeability becomes

$$k = 0.5 \frac{rH^2 \mu a^2}{M \Delta e} \tag{3.47}$$

Since the total stress σ_t does not depend on z, the difference in strain from top to bottom is caused by the difference in pore pressure.

$$\Delta e = e_{top} - e_{bot} = \frac{(\sigma_t - aP_{p,top}) - (\sigma_t - aP_{p,bot})}{M} = P_{pe} \frac{a}{M} \tag{3.48}$$

where P_{pe} is excess pore pressure and substituting equation 40 into 39, gives

$$k = 0.5 \frac{rH^2 \mu a}{P_{pe}} \tag{3.49}$$

Permeability can be estimate from Yang and Aplin (2007) with their empirical correlation as

$$k = 10^{-19.21} J_v^{1.118} \, \check{r}^{1.074} \tag{3.50}$$

where k_v is vertical permeability,

$J_v = 9/8 * \phi(sin(\alpha))^2 * J_1^3 / (1 + J_1 + J_1^2)$ and J_1 is the ratio of the largest radius of a pore to its throat radius, assumed to be the same for all pores for a given sample and α is the average pore alignment angle relative to bedding direction (degree), given as

$\alpha = 45^0 - 10.24^0 (n_{100} - n)$ and n_{100} is void ratio and is given as $n_{100} = 0.3024 + 1.687 clay + 1.951 clay^2$ and clay is the fractional clay content (mass of grains less than 2 x 10^{-6} m diameter).

Table 3.1 Cuttings and core data from well Vedsted-1, Stenlille-2 & 5 and Skjold Flank-1. ρ_g is grain density, BET is specific surface by N_2 adsorption, CEC is cation exchange capacity, ϕ_{HPMI} is Helium porosity -mercury immersion porosity, ϕ_{MICP} is mercury injection capillary pressure porosity, ϕ_{NMR} is nuclear magnetic resonance porosity, V_p and V_s are compressional and shear wave velocities, M^{-1} is the calculated uniaxial rock compressibility from consolidation and velocity data, k_{-BET} is modeled permeability by BET, $k_{-velocity}$ is the modeled permeability from elastic data, k_{NMR} is the modeled permeability from NMR, k_{CRS} is the measured permeability from constant rate of strain test. Experimental errors are: for $\rho_g < 0.03$ g/cm^3; for $\phi < 2$ %; for BET < 0.3 m^2/g; for CEC $< 5\%$; for $V_p < 0.1$ km/s and $V_s < 0.3$ km/s.

Well/Depth (m, msl)	Unit Age	Formation	ρ_g (g/cm³)	BET (m²/g)	CEC (mEq/100g)	ϕ_{HPMI} (%)	ϕ_{MICP} (%)	ϕ_{NMR} (%)	V_p (km/s)	V_s (km/s)	M^{-1}x10⁻⁴ (MPa⁻¹)	k_{-BET} (μD)	$k_{-velocity}$ (μD)	k_{-NMR} (μD)	k_{-CRS} (μD)
Vedsted-1															
1090		Børglum FM	2.68	24	26	35						5.3			
1115		Børglum FM	2.68	28	20	35						3.8			
1130		Flybjerg FM	2.67	31	32	31						2.1			
1140		Flybjerg FM	2.69	26	29	30						2.5			
1222		Haldager FM	2.64	14	21	27						5.9			
1255		Haldager FM	2.69	22	31	25						1.7			
1350			2.64	38	36	23						0.4			
1445			2.71	31	32	22						0.5			
1515			2.72	27	29	24						1.0			
1585		Fjerritslev FM	2.72	27	36	24						0.9			
1675			2.68	32	25	22						0.5			
1740			2.7	28	33	18						0.3			
1745			2.71	18	28	18						0.8			
2005			2.66	30	33	17						0.2			
2035		Gassum FM	2.67	27	34	16						0.2			
2040			2.66	30	33	15						0.1			
Stenlille 2															
1475			2.66	46	37	20	10					0.2			
1481			2.71	42	38	19	11					0.2			
Core 1484*			2.65	44	37	20	11	21	2.9 - 4.2	1.11- 2.2	0.3 - 0.6	0.2	0.8	0.8	0.2
1486			2.62	45	36	19	9					0.1			
Stenlille 5															
1419			2.67	43	29	18						0.1			
1420			2.61	32	28	26	12					1.0			
1421			2.64	39	31	25	9					0.6			
1422			2.67	44	34	19						0.2			
1423		Fjerritslev FM	2.64	42	37	26	10					0.6			
1428			2.68	43	39	21	11					0.2			
1429			2.64	47	39	20	14					0.2			
1522			2.64	36	33	18	12					0.2			
1527			2.66	43	32	21						0.2			
1530			2.64	42	33	19						0.2			
Core 1576*			2.59	32	31	17	9	18	3.0 - 4.1	1.7 - 2.1	0.3 - 0.6	0.2	0.5	0.6	
Skjold Flank-1															
3051			2.75	18	8.63	24			2.4	1.2		2.2	1.5		
3200			2.73	24	14.05	26			2.6	1.4		1.6	1.4		
3353			2.74	24	16.98	29			2.5	1.2		2.5	1.7		
3520			2.75	24	13.65	29			2.6	1.2		2.5	1.7		
3658		Fjerritslev FM	2.76	24	11.95	28			2.6	1.2		2.1	1.5		
3810			2.75	24	12.71	27			2.6	1.3		1.9	1.5		
3959			2.75	19	14.59	19			3.2	1.5		0.8	0.6		
4115			2.76	18	14.32	17			3.2	1.6		0.6	0.5		
4270			2.75	18	15.00	18			3.1	1.7		0.7	0.6		
4420			2.76	16	12.66	17			3.2	1.8		0.7	0.5		
4572			2.76	16	16.44	17			3.3	1.9		0.7	0.5		

Note: The "Jurassic" label appears vertically in the Unit Age column spanning the Stenlille 2 and Stenlille 5 sections.

3.4 Results

3.4.1 Petrography

Bulk mineralogical composition as derived from XRD of Fjerritslev Formation is presented in Fig. 3.8. The non-clay minerals identified include quartz, K-feldspar, plagioclase, calcite, dolomite and pyrite. Samples from Flyvbjerg and Haldager formations in Vedsted-1 are siltier than the Fjerritslev samples. Fjerritslev Formation samples from Vedsted-1 have comparable silt content to Stenille-2 and -5 well and are significantly siltier than the offshore well Skjold Flank-1. Pyrite is identified in all of the samples but is relatively abundant in Skjold Flank-1. The clay minerals identified include smectite, illite, kaolinite and chlorite. Illite and kaolinite dominate the clay fraction in all samples. Smecite is not identified in the offshore samples probably due to illitization of smectite as a result of increase in temperature with burial depth. There is thus only a minor difference in mineralogy in the Fjerritslev Formation between the onshore wells but significant difference in silt content compared to the offshore samples.

Backscatter electron micrographs images of selected samples of Fjerritslev Formation from the three locations (Fig. 3.9) support XRD analysis result. The images show significant amount of silt in the onshore samples compared with the offshore samples which are less silty with significant amount of clay minerals and visible pyrite. The pore networks are too small to be visible with BSEM but unloading fractures due to sample handling are clearly visible. Grain size distribution analysis (Fig. 3.10) was performed for two Stenlille samples and it shows that about 80% of the up to 63 µm grains have diameter < 2 µm fraction.

Grain density, BET specific surface, CEC, porosity, ultrasonic velocity compressibility and permeability results are summarized in table 1. Grain density varies from 2.61 g/cm^3 for onshore shale samples to 2.76 g/cm^3 for the offshore samples with higher content of pyrite. On the other hand BET specific surface and CEC tend to be higher for onshore samples of Vedsted-1 and Stenlille compared with the Skjold Flank-1 offshore samples probably due to the presence of smectite in the shallower onshore samples.
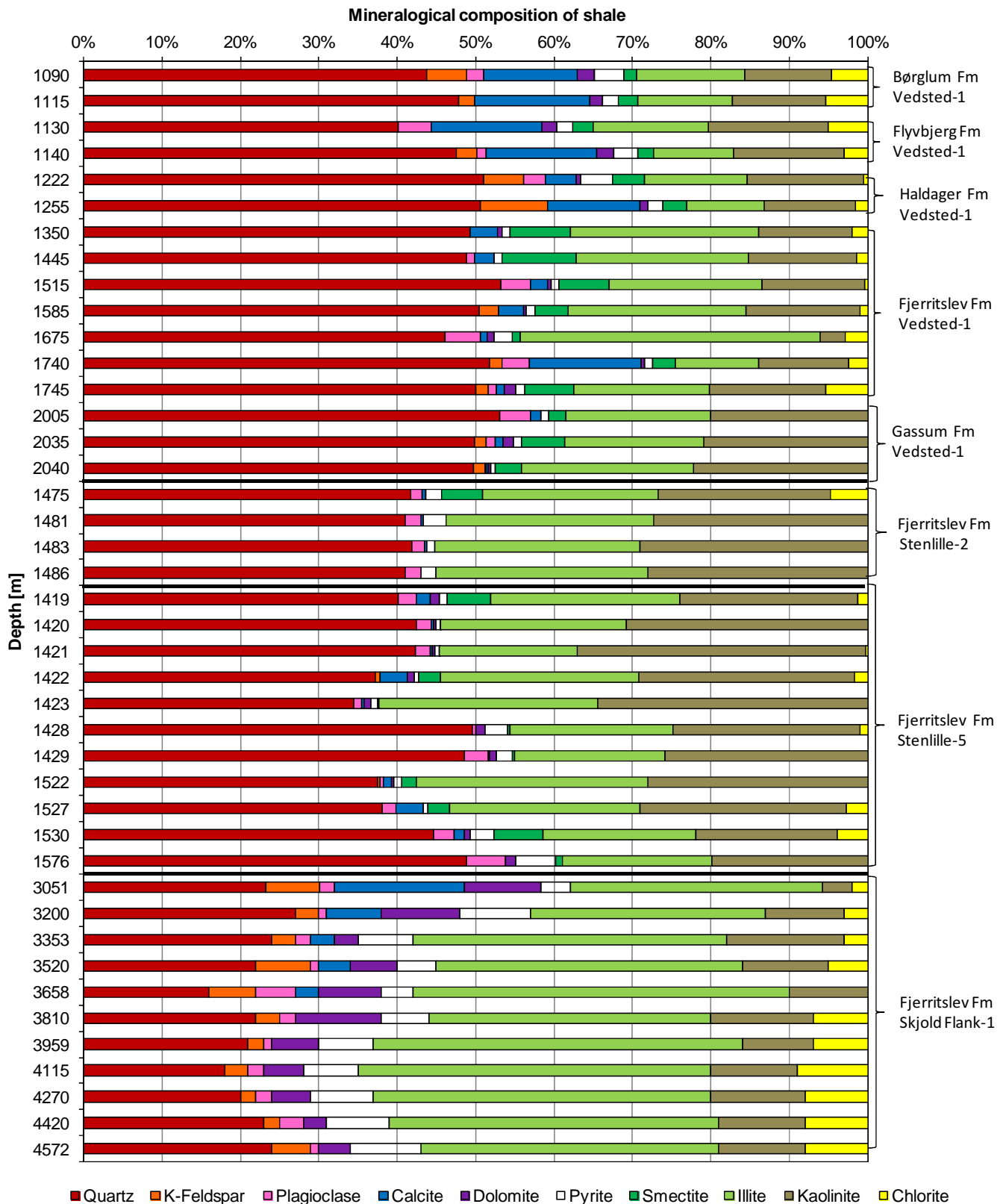
Figure 3.7 Mineralogical composition of cuttings samples based on X-ray diffractometry. Shale samples of Fjerritslev Formation from onshore wells (Vedsted-1 & Stenlille-2 & -5) are rich in silt (quartz and feldspar, about 50%) but as we move to offshore part of the formation (Skjold Flank-1) the amount of silt is lower relative to amount of pyrite and clay minerals.
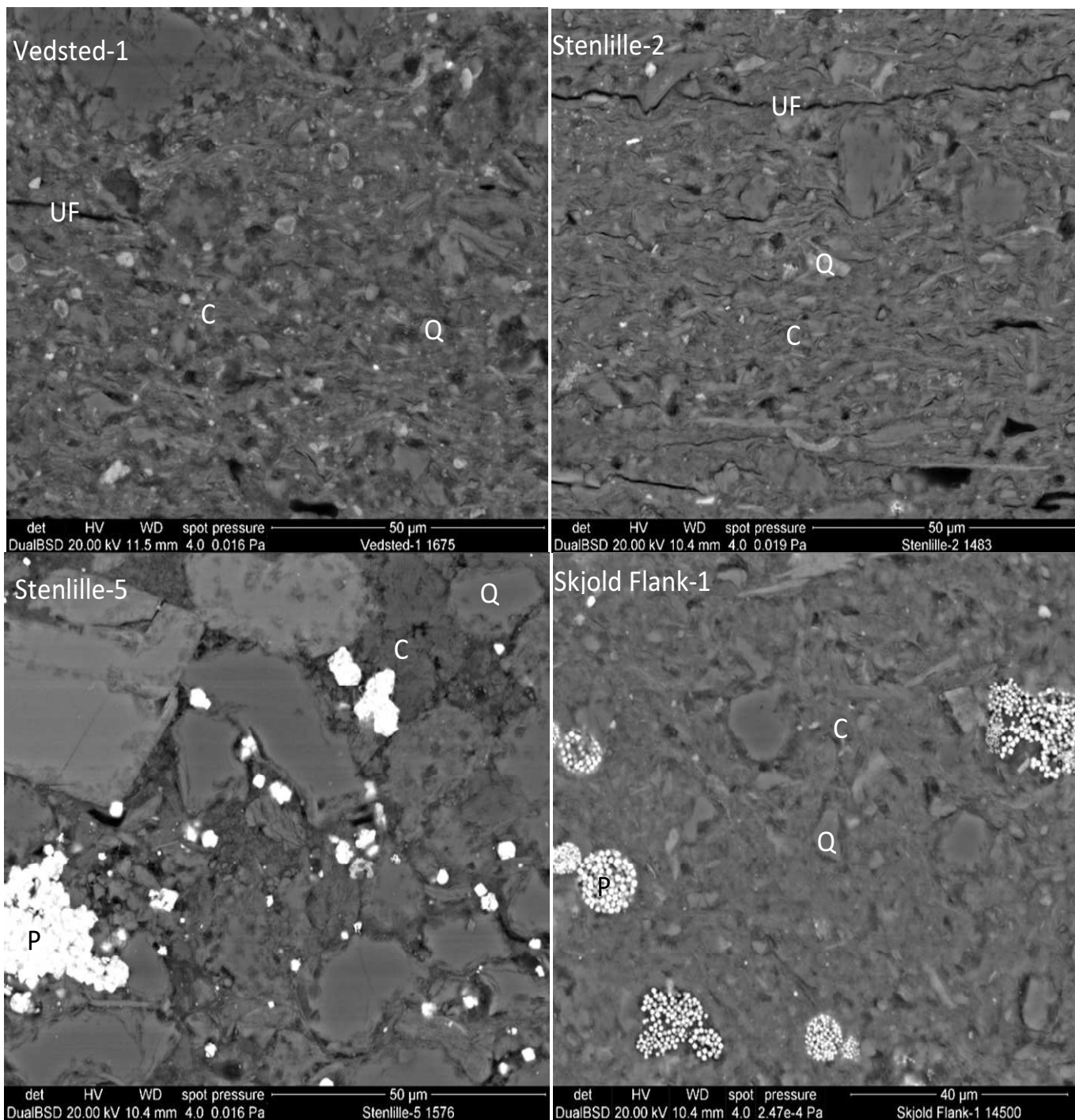
Figure 3.8 Backscatter electron micrographs of selected samples from Jurassic shale obtained from the three locations showing significant amount of silt (Q) to be present in the samples from the eastern wells while samples obtained from the Skjold Flank-1 offshore well are less silty to clay-rich (C) with significant amount of pyrite (P). The pore network is too small to be visible at this resolution, whereas unloading fractures (UF) due to sample retrieval are visible. Holes, where silt grains have fallen out of the sample are visible in the Vedsted 1675 m samples.
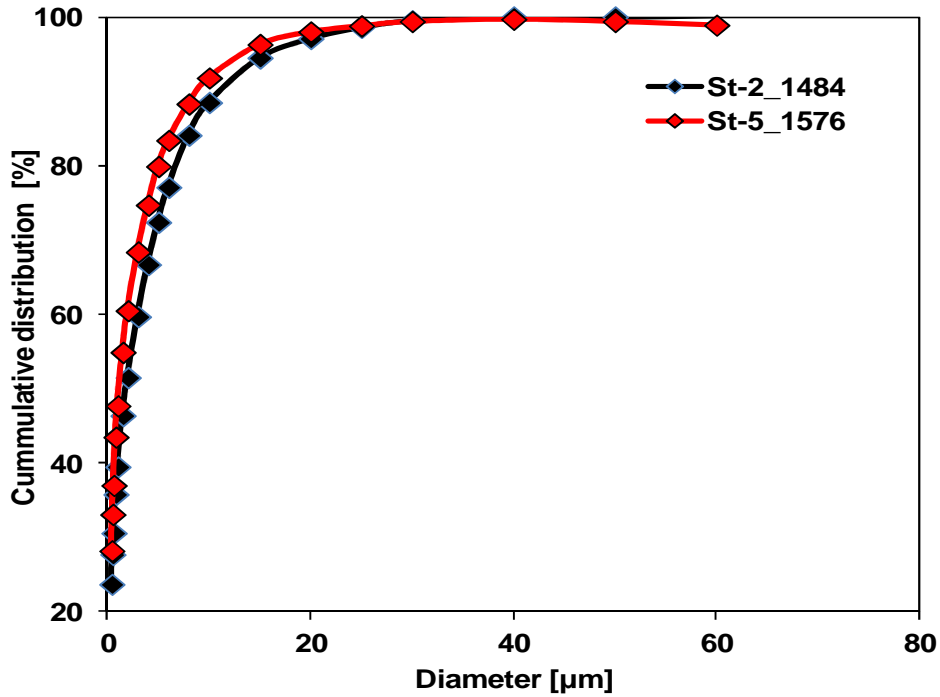
Figure 3.9 Cumulative grain size distribution for Fjerritslev Formation samples from Stenlille-2 and Stenlille-5 core samples. About 98% of the grains have diameter less than 20 μm.

3.4.2 Porosity

Porosity was obtained from cuttings and core samples using the three different methods and the results are summarized in table 3.1 and presented in Fig. 3.11a. The porosity vary from 32% in the shallower Børglum Formation at 1090 m to about 14 % in the deeper Fjerritslev Formation at 4700 m. MICP analysis on Fjerritslev Formation samples measured lower porosity ranging from 9 to 14%. The MICP measurements also give data for pore throat radius distribution as mercury intrude the sample with increasing pressure and the mean pore throat radius for the Fjerritslev Formation is estimated to be about 0.01 µm. Porosity measured by NMR analysis on Fjerritslev Formation ranges from 18 to 21%. Porosity results obtained from the three methods is compared in Fig. 3.11b. The results indicate that a higher porosity is measured by NMR method (21%) and HPMI method (20%) than MICP method (11%) for the same sample.
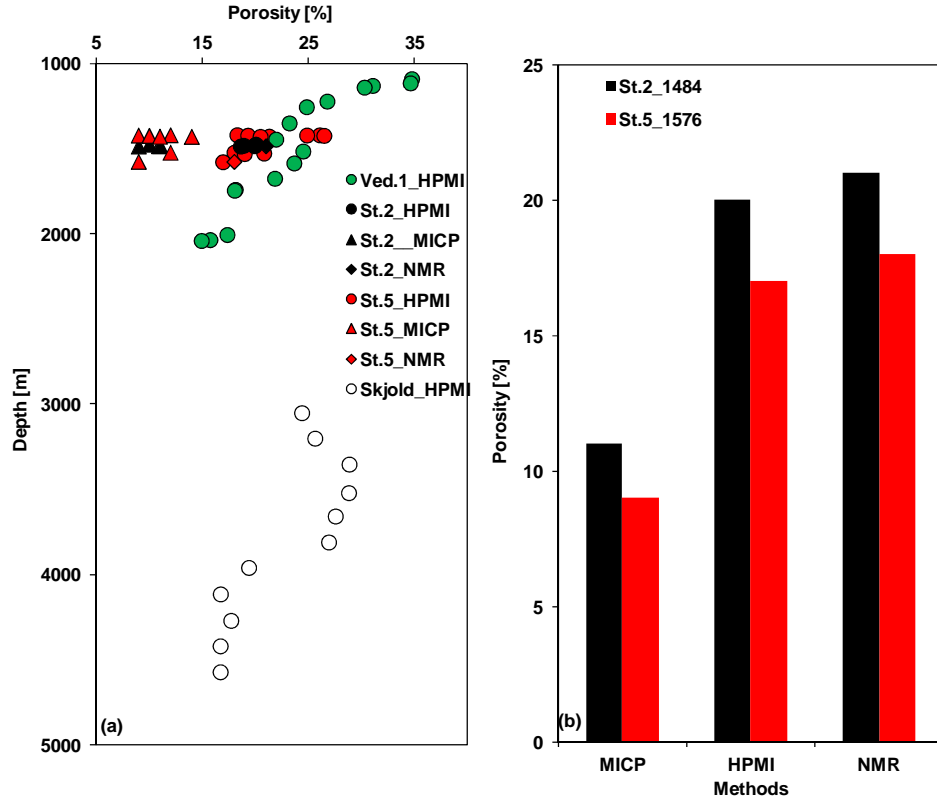
Figure 3.11 Porosity obtained from three independent methods for Fjerritslev Formation and also for comparison, six samples from shallower formations are included from Vedsted-1 well. a) Porosity versus depth for cuttings and selected core samples. b) Comparing porosity measurement on the same Fjerritslev Formation sample.

3.4.3 The static and dynamic compressibility

The results of velocity measured during consolidation experiments under uniaxial strain are presented in Fig. 12a for Stenlille-2 and Fig. 3.12b for Stenlille-5 samples. The samples were loaded from the surface condition to its in situ stress condition of up to 25 MPa. V_p of about 2.9 km/s and V_s of 0.8 km/s were measured at initial stress of about 0.5 MPa for the vertical sample of Stenlille-2 and increases sharply to about 3.3 km/s and 1.2 km/s at 5.0 MPa, but from this stress level to the maximum of 25 MPa, there is only a small increase in V_p and V_s to 3.4 km/s and 1.3 km/s. This trend is also seen for the other samples of Stenlille-2 and Stenlille-5. We also generally notice that V_p and V_s are higher in the direction parallel to geologic layering at all stress level (4.2 km/s and 2.2 km/s at 25 MPa) than in the diagonal (3.7 km/s and 1.7 km/s at 25 MPa) and vertical (3.4 km/s and 1.3 km/s at 25 MPa) directions. What is seen generally in all the measurements is how little velocity changes with stress above 5 MPa for these samples.

Fig. 3.13(a) shows that the elastic constants, c_{11}, c_{33}, c_{44}, c_{66} and $c_{13,}$ all increase as uniaxial stress increases for both Stenlille 2 and -5 Fjerritslev Formation shale. c_{11} increases from ~30 GPa to 40 GPa while c_{33} increases from ~20 GPa to 28 GPa as uniaxial stress increases from 0.5 to 25 MPa. c_{44}, and c_{66} increases from ~3 GPa to 6 GPa and 7 GPa to 11GPa respectively, over the same stress interval. c_{13} increase from 11 GPa to 20 GPa as uniaxial stress increases to 25 MPa. At initial stress c_{11} for St.2 shows higher response than c_{11} for St.5 while the opposite trend is seen at stress above 7 MPa for c_{33} for St.2 and St.5. At stress above 7 MPa c_{11} (26 GPa) for St.2 does not change significantly with increasing stress while c11 for St.5 increases steadily from 26 GPa to 31 GPa from 7 MPa to 25 MPa.
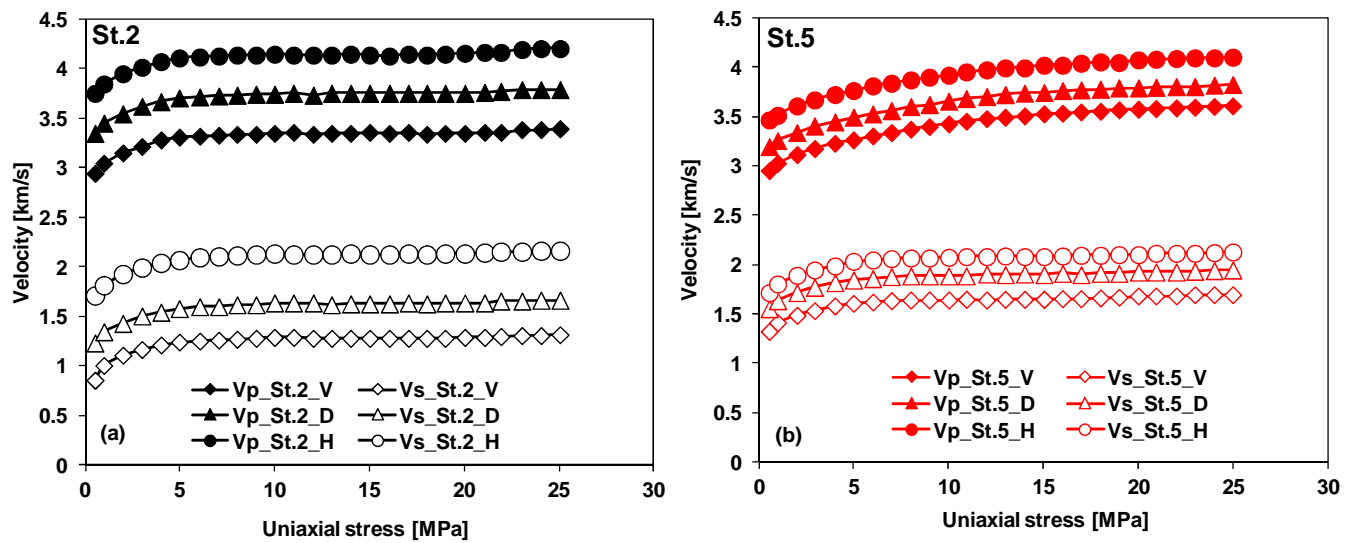

Fig. 3.12. Plots of ultrasonic compressional and shear wave velocity as a function of uniaxial stress for the uniaxial consolidation tests performed under drained conditions for vertical, diagonal and horizontal samples of Fjerritslev Formation from (a) Stenlille-2 and (b) Stenlille-5.

The elastic constants computed above are used to calculate the anisotropy parameters from eqs. 3.13 to 3.15 (Thomsen 1986). The influence of uniaxial stress on P-wave (ε) and S-wave (γ) anisotropic parameters and anellipticity parameter (δ) is shown in Fig. 13(b) for both St.2 and St.5 shale. The initial anisotropy at low stress is seen to be large for the two shale samples for P-wave and S-wave, but St.2 P-wave (0.31) and S-wave (0.68) anisotropy is larger than St.5 P-wave (0.19) and S-wave (0.39) anisotropy. The P-wave and S-wave anisotropic parameters generally decrease with increasing stress. ε decreases from 0.31 to 0.28 for St.2 and from 0.19 to 0.15 for St.5 as stress increases from 0.5 MPa to 25 MPa. γ decreases from 0.68 to 0.49 for St.2 and from 0.39 to 0.28 for St.5 as stress increases from 0.5 MPa to 25 MPa. On the other hand δ increases from -0.08 to 0.10

for St.2 and from -0.04 to 0.10 for St.5 as stress increases from 0.5 MPa to 25 MPa. Generally, δ does not show any significant difference between St.2 and St.5 with stress. The implication of these results is that Fjerritslev Formation shale is weakly to moderately anisotropic.

The experimental data of stress and strain is presented in Fig. 3.14 (a) and (c) for the vertical, diagonal and horizontal samples of the Fjerritslev Formation from Stenlille-2 and -5 wells. The compressibility computed from static and dynamic data are plotted against the expected range of in situ stresses (15 MPa – 19 MPa) and is illustrated in Fig. 3.14 (b) and (d). We find that static compressibility interpreted from the loading and reloading stress paths varies from 10 to 5 x 10^{-4} MPa^{-1} and is higher than that interpreted from the unloading stress path (0.2 to 6 x 10^{-4} MPa^{-1}). On the other hand, dynamic compressibility varies from 0.2 to 0.5 x 10^{-4} MPa^{-1}. Correlation of compressibility as shown in Fig. 3.14b and 3.14d indicate that static compressibility corresponds to dynamic compressibility at the beginning of the unloading stress path. The compressibility from loading stress path is elastoplastic due to the effect of strain induced by the closure of the unloading fractures during sample loading. This kind of compressibility is recommended for geotechnical purpose especially when constructing foundations. When the sample is loaded to its in situ stress condition, we expect all the unloading fractures to be closed. At the beginning of unloading stress path, the sample response elastically within a short time before reaching the transition zone where the effect of unloading fractures are activated and results in elastoplastic compressibility in the rest of the unloading stress path.
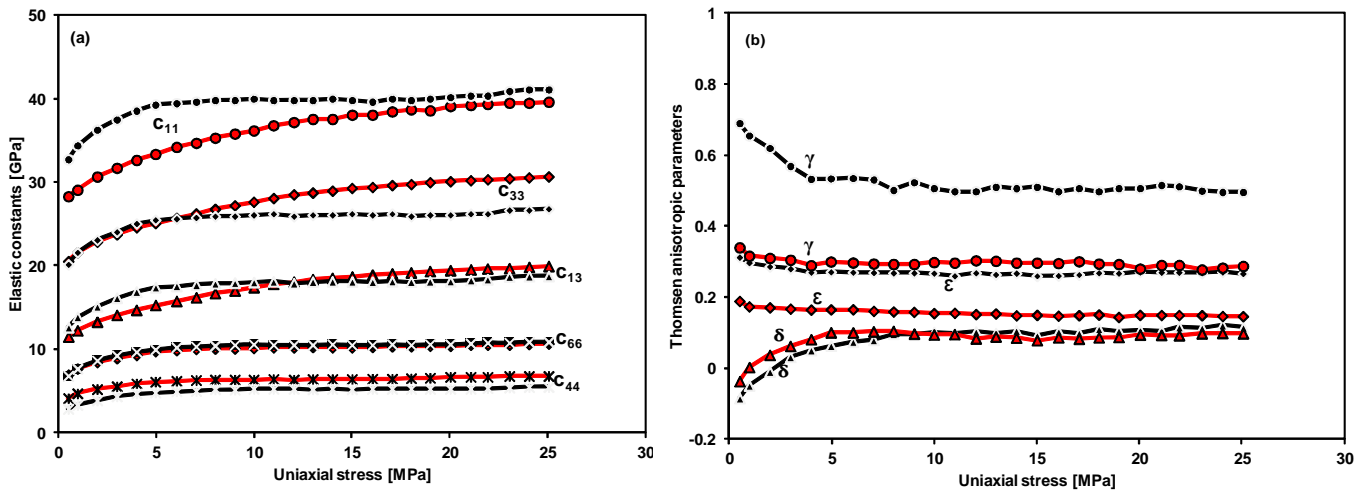

Fig. 3.13 *Uniaxial stress plotted against (a) Elastic constants and (b) P- (ε) and S-wave (γ) anisotropic parameters both show decrease with increasing uniaxial stress for St.2 and -5 samples. The wave front anellipticity parameter (δ) increases with increasing stress. St.2 is given black symbols and St.5 by red symbols.*
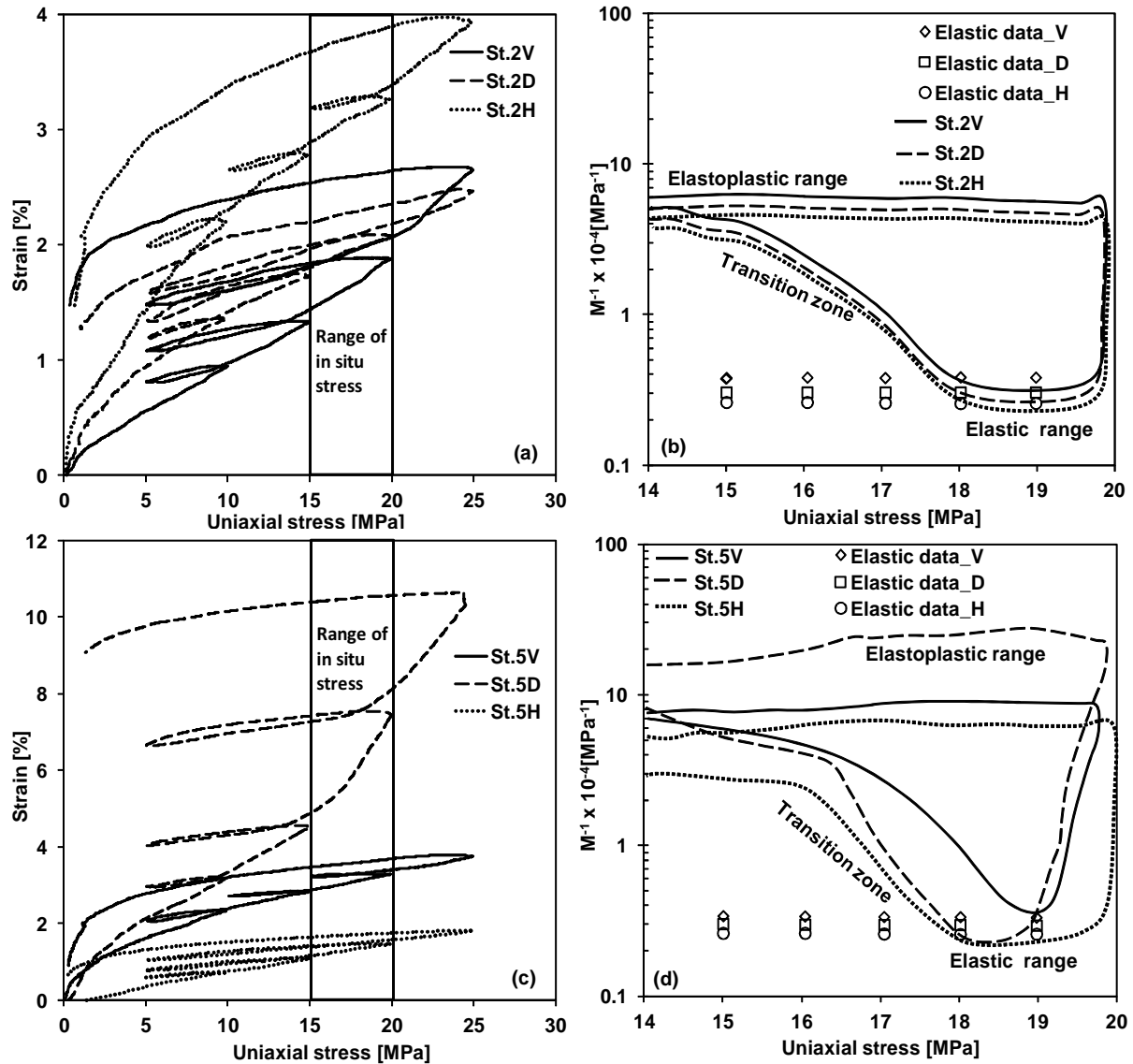
Fig. 3.14 *Plots of uniaxial strain as well as static and dynamic compressibilities against uniaxial stress for differently oriented samples of Fjerritslev Formation from Stenlille-2 and -5. Plots (a) and (d) show uniaxial strain against stress for the Vertical (V), diagonal (D) and horizontal (H) samples. Plots (b) and (e) show comparison of uniaxial static and dynamic compressibilities against stress.*

3.4.4 Permeability

Permeability predicted from BET specific surface and porosity data from thirty three cuttings samples vary from 0.1 to 1.6 µD. Figure 3.15 a) and b) present permeability results predicted from elastic moduli. They vary slightly with stress between 0.6 µD and 1.0 µD for Stenlille-2 and -5 samples. We find small difference in vertical, diagonal and horizontal permeability but in this case vertical permeability is seen from data on horizontal sample and vice versa.
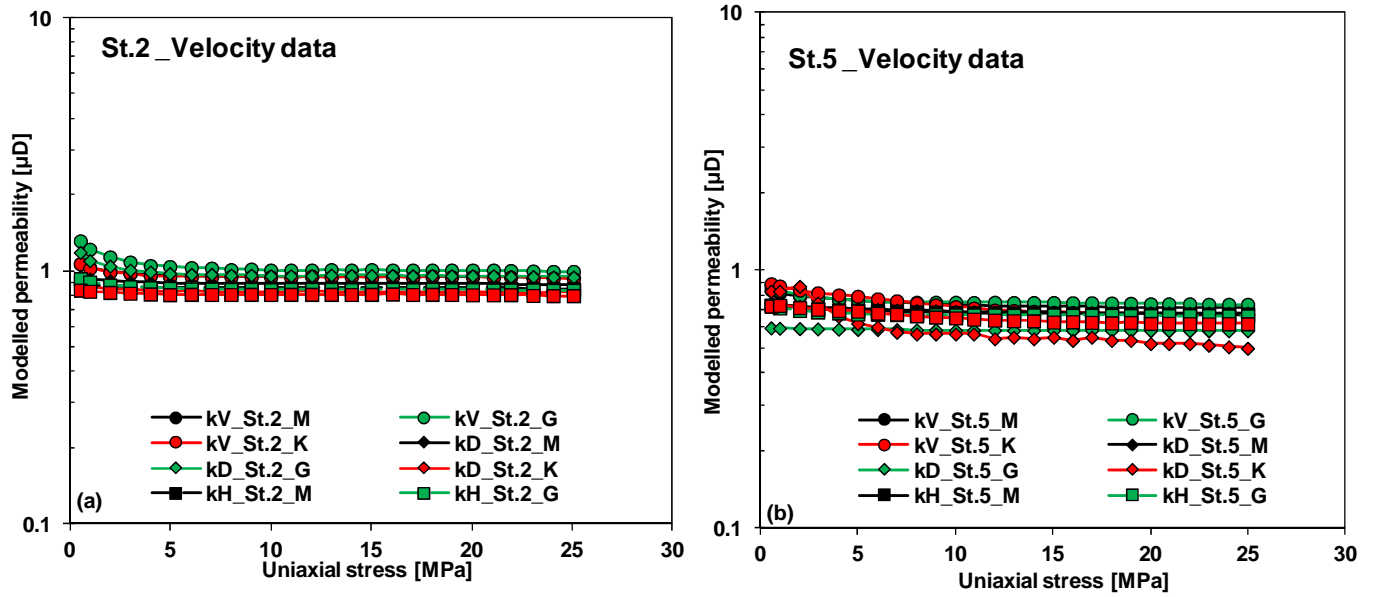
Figure 3.15 *Modelled permeability from compressional, shear and bulk moduli versus uniaxial stress for vertical, diagonal and horizontal samples. (a) for Stenlille-2 and (b) for Stenlille-5.*

Permeability predicted from MICP and NMR data vary between 0.5 and 0.8 µD for Stenlille-5 sample and Stenlille-2 samples. Figure 3.15 (a), (c) and (e) show stress-strain-excess pore pressure data from CRS tests and Figure 3.15 (b), (d) and (f) show the permeability results for vertical, diagonal and horizontal permeabilities. Permeability of the Fjerritslev Formation was interpreted at stress between 14 and 20 MPa corresponding to the depth from which the core samples were retrieved. We find that permeability is lower for the case where we have used the measured Biot's coefficient of 0.84 and is 0.2 µD for the vertical and diagonal samples and 3.0 µD for the horizontal sample. We also find that assuming a Biot's coefficient of 1.0 will give higher permeability corresponding to only plastic and no elastic deformation. Permeability measured by each method is correlated with porosity (Fig. 3.16a) and the result show that for a single porosity value the permeability can differ by one order of magnitude. The permeability of Fjerritslev Formation as modeled independently from the three different approaches has been compared with the measured permeability from CRS experiment for the same sample as shown in Figure 3.16 (b). The predicted permeabilities and the measured permeability are of same order of magnitude, but the modelled permeability from BET specific surface gave the lowest value compared with that from elastic and NMR data.
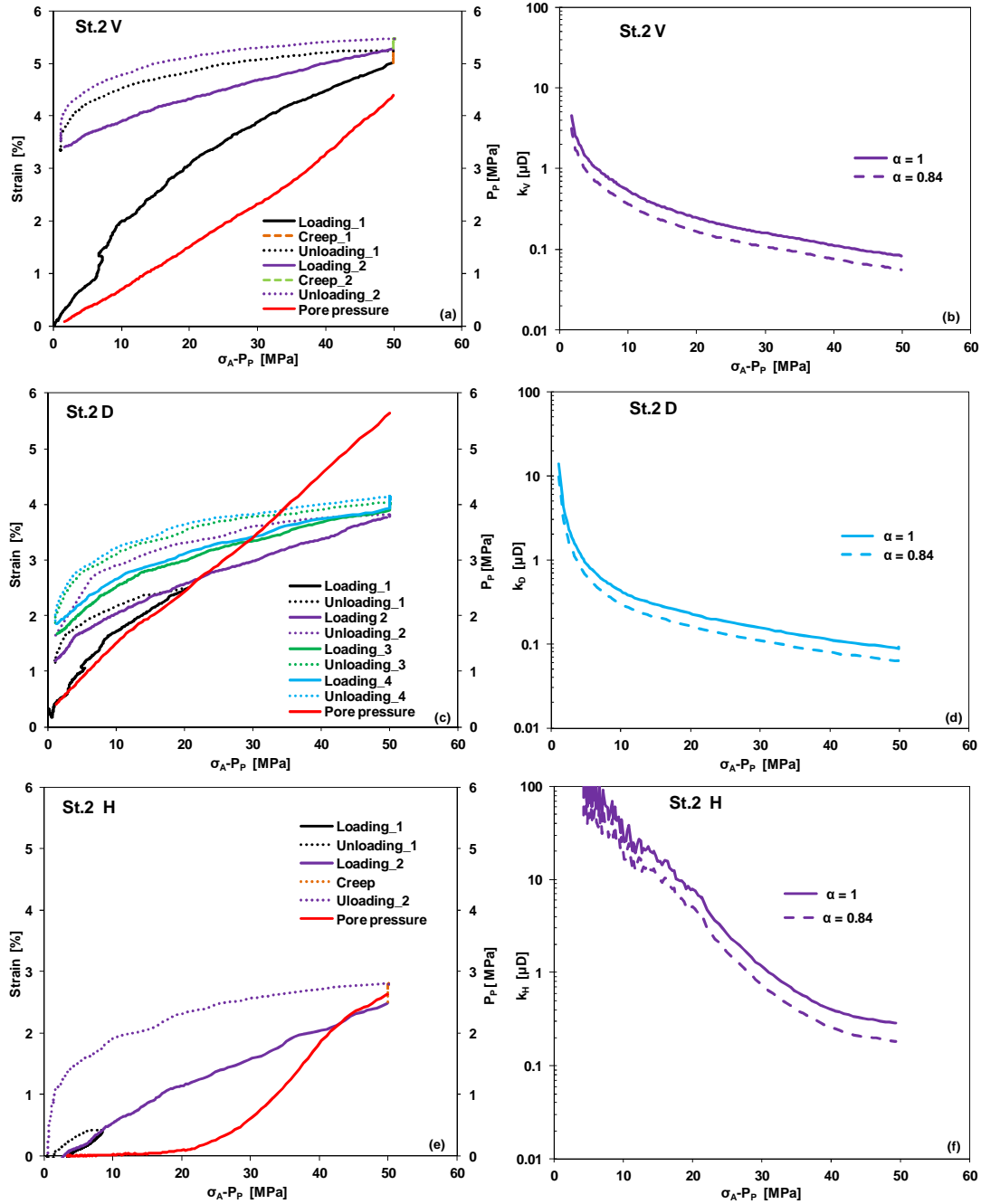
Figure 3.16 Plots of indirect permeability measurement from constant rate of strain (CRS) tests as a function of uniaxial stress minus pore pressure. (a) show consolidation test plots of uniaxial strain and excess pore pressure build up (P_{Pe}) used in permeability calculation against stress for the vertical, diagonal and horizontal samples. (b) show the calculated permeability assuming Biot's coefficient (α) of 1 as well as the measured α = 0.84.
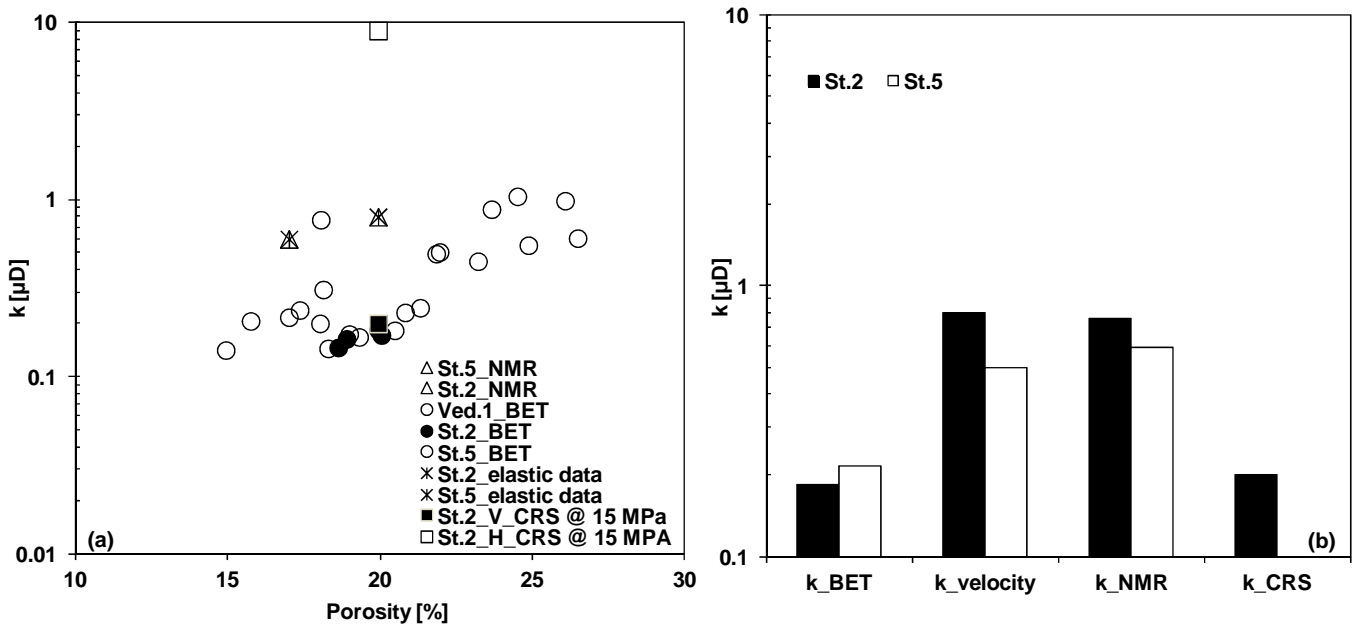
Figure 3.17 Plots of modeled and measured permeability. Permeability measured indirectly from CRS experiments are shown by the empty and black square corresponding to the vertical respectively the horizontal sample. (a) Plot of modeled and measured permeability versus porosity and (b) modeled and measured permeability for the same sample. Horizontal permeability point (9 μD) is not shown in Figure b.

3.5 Discussion

3.5.1 Porosity variation with methodology

Porosity measured from HPMI and NMR should in principle both represent total porosity and are expected to be higher than MICP porosity. The difference in porosity between MICP and NMR method is shown in Fig. 3.18. The MICP porosity measurement is a standard method used to characterize pore throat radius or diameter distribution in a porous medium. Fig. 3.18 shows that mercury is able to penetrate down to 1.7 nm pore throat radius at maximum pressure of 414 MPa, whereas pore throat radius less than 1.7 nm could not be intruded by non-wetting mercury phase and requires higher intrusion pressure. Since our shale samples were assumed to be fully saturated, we expected similar porosity from HPMI and NMR but NMR method gave higher porosity. Fig. 18b shows two families of T_2 distribution with mean of 0.6 ms and 30 ms contributing to the total NMR porosity. Since the samples are recovered from depth, stress relief coupled with sample handling prior to NMR tests often induces unwanted fractures or micro-cracks. The T_2 distribution with mean of 30 ms is due to the presence of micro-cracks and contributes with porosity of 1% for

the Stenlille-5 sample and Stenlille-2 sample. The 1–2% micro-cracks porosity corresponded with the deformation required to consolidate the samples to their in situ stress condition. The micro-crack porosity should be regarded as artifacts and are responsible for the too high NMR porosity and therefore should be disregarded from the total NMR porosity as this is not associated with in situ conditions
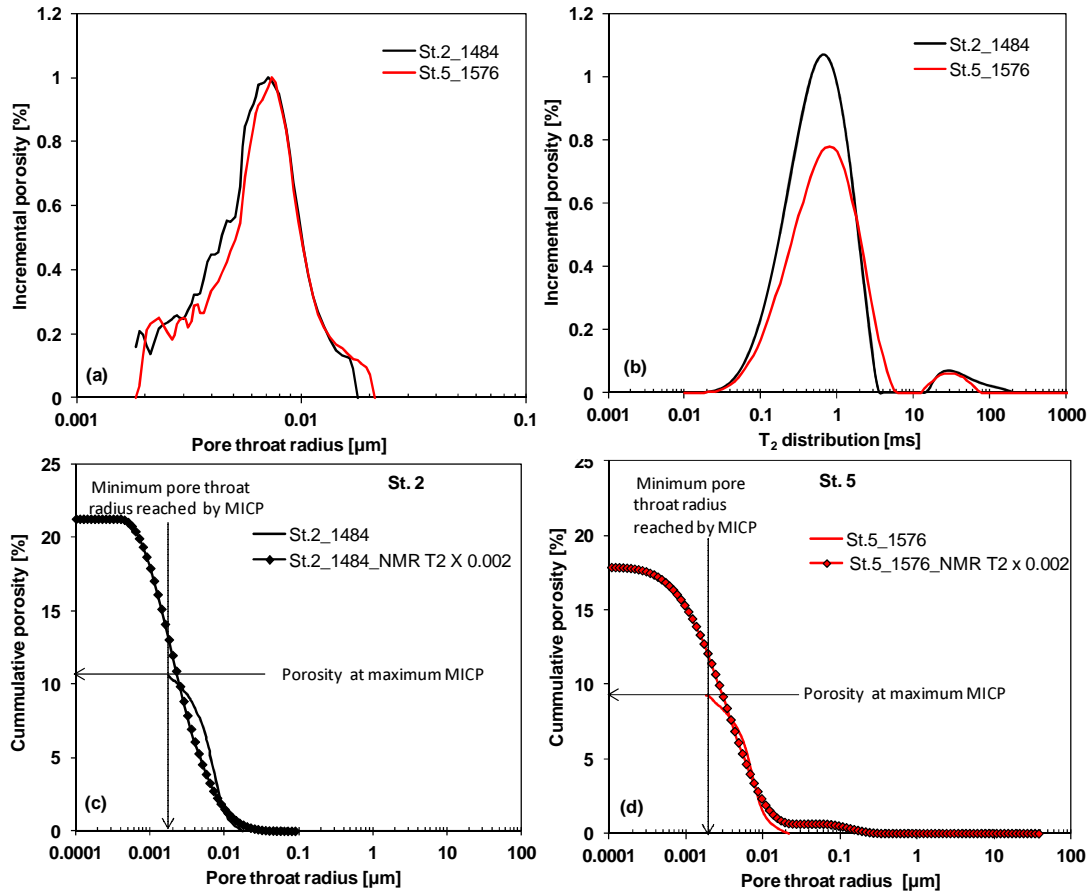
Fig. 3.18 *Incremental and cumulative porosity measured by NMR and MICP methods on samples from Stenlille (St.2, 1484 m and St.5, 1576 m). (a) Incremental porosity versus pore throat radius for Stenlille samples. (b) Incremental porosity versus T_2 distribution. (c) and (d) show transformation of NMR T_2 distribution to MICP pore throat radius and shows the fraction of pores that could not be intruded by mercury.*

3.5.2 Influence of elasticity and saturation on static and dynamic compressibility

The comparison of static and dynamic compressibility can be made base on the elasticity of the material. We have shown that static uniaxial compressibility can be compared with dynamic compressibility from compressional modulus at the beginning of the unloading stress path at in situ

stress conditions which display the elastic response of the shale material ($\sim 0.2 - 0.5$ x 10^{-4} MPa^{-1}). Our dynamic compressibility data are similar to previously published data on deep shales (Fjær 2009; Holt 2012). The interpretation of stress strain data from the loading stress path recorded higher static compressibility up to about ~ 10 x 10^{-4} MPa^{-1}. Published studies on shale indicate generally that compressibility estimated from stress strain data is higher than the one calculated from velocity of elastic waves (Walsh 1965; King 1970; Tutuncu et al. 1994; Yale et al. 1995; Fjær 2009; and Holt 2012). Justification of the difference between static and dynamic compressibility has primarily been due to drainage conditions (Simmons & Brace 1965; Cheng & Johnson 1981; Fjær et al. 2012), but also could be due to the procedure used to estimate elasticity from recorded testing data and the condition of the shale (Hendron et al., 1970). In addition lot of the early work done on shale was done on dried out samples which results in significant difference in strength, compressibility and other rock properties. Walsh and Brace (1966) explained that a difference may arise due to the presence of highly compliant cracks which affect static deformation differently than the dynamic. Accordingly Cheng and Johnson (1981) found that the ratio of static and dynamic moduli from shale core samples without measurable microcrack porosity is nearly 1.0 at stress of about 200 MPa. A difference between static and dynamic moduli has also been attributed to frequency and strain amplitude (Jizba and Nur 1990; Fjær et al. 2012). Dynamic measurements are done on a range of frequencies which are often associated with small strain amplitude while in the static measurements the rock is stressed at slower rate and is often associated with lower frequency and with larger strain (Johnson 1987).

The main factor that may be responsible for the difference between static and dynamic compressibility is the interpretation of the stress strain data. This is basically because determination of static compressibility from loading stress path includes the effect of fractures and the plastic processes taking place due to grain rearrangement resulting in elastoplastic compressibility which is higher. When the sample has been loaded to its in situ stress and the unloading fractures are now closed, as we begin the unloading process, it will take some time for the unloading fractures to be activated thereby resulting in elastic response of the material corresponding with the dynamic compressibility. In a related study Jizba and Nur (1990) performed hydrostatic experiments on 43 tight gas sandstone samples (dry) with clay content ranging from 0 to 66% and noticed a jump in bulk modulus of shale from 20 to 26 GPa at the beginning of unloading. Fjær et al. (2012) did drained uniaxial consolidation experiments on two outcrop samples (Mancos and Pierre) and also noticed an increase in static moduli that approached the dynamic modulus near the turning point of

stress path from loading to unloading. Elastic wave propagation in dry, clean (clay free) rock is a predominantly elastic process (Walsh, 1965) and any difference between static and dynamic compressibilities in such rocks would be caused by non-elastic processes which occur during loading and unloading and for a detailed quantitative discussion on these processes see David et al. (2012) and Fjær et al. (2012). At the very beginning of an unloading stress path, the rock can be assumed to behave purely elastically. During unloading under zero lateral strain, the measured static stiffness component is the same as the dynamic stiffness component obtained from the axial P-wave velocity, thus the anisotropy and stress history effect can be eliminated.

The ultrasonic measurements were carried out on saturated shale samples under draining condition during the uniaxial loading experiment. The velocity data measured under the draining condition are considered to be undrained since there is not enough time for the fluid to drain. In order to investigate the influence of pore fluid on the dynamic compressibility result reported earlier, we have used Brown-Korringa fluid substitution equation applicable for anisotropic media and Gassmann's fluid substitution equation commonly used for isotropic media for comparison purposes, to calculate dry dynamic compressibility by assuming mineral modulus of 25 GPa for Gulf clays (Han 1986). The results are shown in Fig. 3.19 (a) for Stenlille-2 and 3.19 (b) for Stenlille-5 samples. We find a small difference in dynamic compressibility between the saturated and the dry case for Brown-Korringa model which increases by 1.0 unit and that of Gassmann model which increases by 3 units.
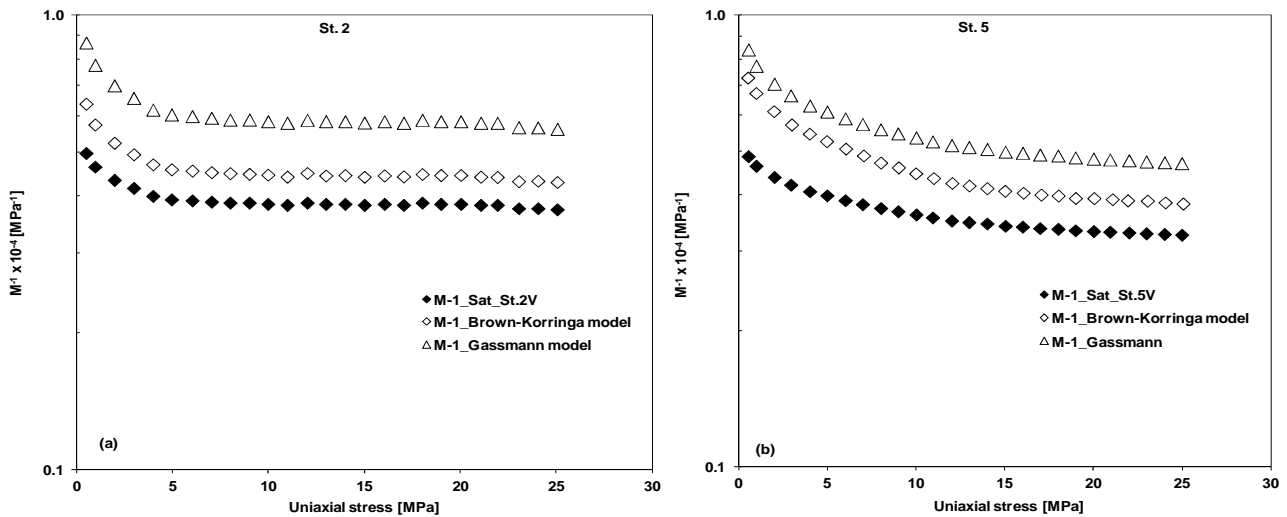

Fig. 3.19. Plots comparing dynamic compressibility for vertical, diagonal and horizontal samples in the saturated as well as the Brown-Korringa and Gassmann dry case versus uniaxial stress for (a), Stenlille-2 and (b) Stenlille-5 and by assuming mineral modulus of 25 GPa.

3.5.3 Influence of clay minerals on permeability

Permeability of Fjerritslev Formation shale was predicted from the specific surface of the solids measured by BET method and the equivalent pore radius modelled from elastic data by application of Kozeny's formulation. The MICP measurement at 414 MPa gives information on the cumulative porosity for only the pores with pore throat radius above 2.0 nm whereas the NMR measurement gives cumulative porosity information for all the pore sizes assuming that water fills all the pores in the shale. It is therefore possible to correlate the MICP and NMR data based on the corresponding cumulative porosity to determine the surface relaxivity and by applying eqn. 28 (Hossain et al. 2011), one can predict cumulative permeability from the contribution of pore fraction contributing to fluid flow. The predicted permeability from specific surface of the grains and pores by Kozeny's model and that from the MICP and NMR data compares with the measured permeability. Kozeny's predicted permeability is smaller than the measured permeability despite the fact that they fall in the same order of magnitude and this trend is shown clearly in Fig. 3.20 a, which corresponds with data from Dewhurst et al. (1999). Permeability is also predicted from MICP data based on the Yang and Aplin correlation and it gives a permeability result which is two to three orders of magnitude lower than both the Kozeny's model and the measured permeability. Considering that the MICP data gives average pore throat radius of 10 nm one could from Yang and Aplins model expect nanodarcy permeability generally instead of the predicted and the measured microdarcy permeability for this shale.
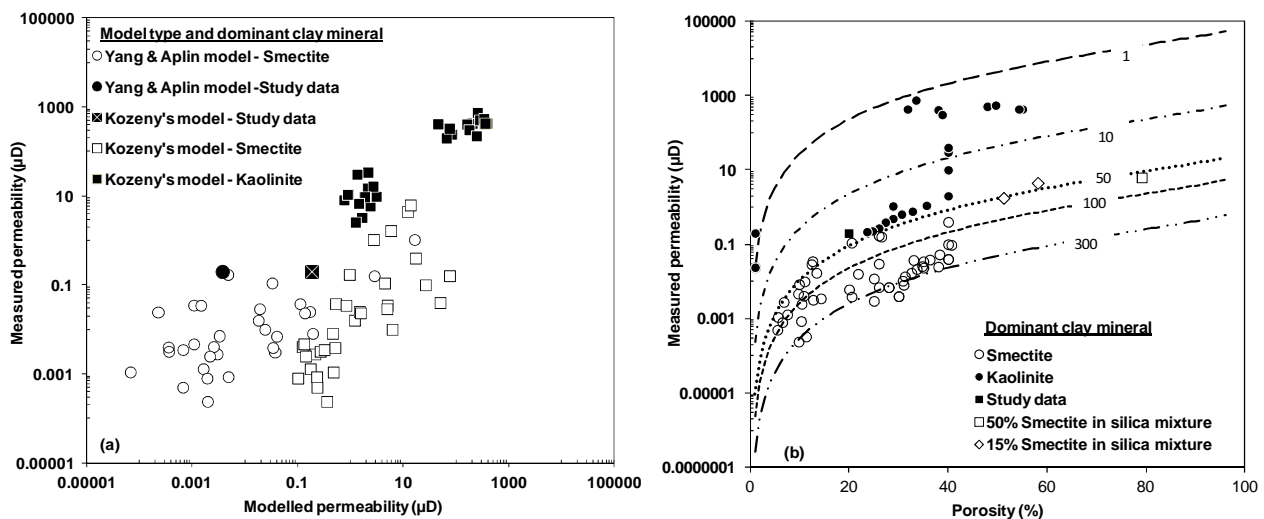
Fig. 20. *a) Relationship between predicted permeability from Kozeny's as well as Yang and Aplin's model as compared with measured permeability for both synthetic and natural shale material. b) Permeability porosity plot with lines of equal BET specific surface (m^2/g) modelled from Kozeny's equation. The literature data is from Daigle et al. 2011; Dewhurst et al. 1999; Horsrud et al. 1998; Mondol et al. 2008; and Yang and Aplin, 2007.*

Fig. 3.20 (a) compares modelled permeability to measured permeability for both synthetic and natural shale material obtained from the literature data as shown in Table 3.2. Fig. 3.20 (b) show permeability porosity plot with lines of equal BET specific surface modelled from Kozeny's equation. The results show that kaolinite rich shale tend to have higher permeability as estimated by both flow through and constant strain rate experiments, than shales rich in smectite. Kozeny's modelled permeability falls in the same order of magnitude as measured permeability for shale rich in kaolinite but overestimate permeability by two to three orders of magnitude for shale rich in smectite. Yang and Aplin modelled permeability fall within +/- 1 order of magnitude of the measured permeability for shale rich in smectite. Our shale permeability corresponds with literature data of shale rich in kaolinte but show higher permeability compared with shale rich in smectite. Fig. 3.20 (b) implies that shale rich in kaolinite together with higher silt content as it is for our case will give higher permeability. Accordingly data from Diamond (1970) on Macon kaolinite and clay rich with smectite shows that, at average pore size diameter of about 30 nm, cumulative mercury intrusion in Macon kaolinite at the pressure is three orders of magnitudes higher than in clay rich with smectite.

3.6 Conclusions

The objective of this study was to investigate porosity, compressibility and permeability of the Fjerritslev Formation (shale). Mineralogical analysis based on X-ray diffractometry (XRD) of forty two samples from onshore wells (Stenlille-2, -5 and Vedsted-1) and one offshore well (Skjold Flank-1) shows a clear trend in composition from the Northeast presently onshore of the Norwegian-Danish Basin where we encounter a gradient with more silty shale to less silty shale in the Southwest, offshore section of the Central Graben.

Porosity of Fjerritslev Formation was measured independently from three different methods (helium porosimetry-mercury immersion, mercury injection capillary pressure and nuclear magnetic resonance) gave different results indicating that the stated shale porosity is dependent on the method used. The results indicate that a higher porosity is measured by nuclear magnetic resonance method (21%) and helium porosimetry-mercury immersion method (20%) than mercury injection capillary pressure method (11%) for the same samples. The mercury injection capillary pressure method measured the lowest porosity for the formation because mercury which is the non-wetting phase

could not intrude smaller pore throats ≤ 1.7 nm at maximum intrusion pressure of 414 MPa which is the limit of the system. The nuclear magnetic resonance method which is expected to give similar results to the helium porosimetry-mercury immersion method, recorded higher porosity probably due to contribution from unloading micro-cracks introduced due to core unloading and sample handling. The additional porosity from micro-cracks should be neglected in the total porosity from nuclear magnetic resonance data.

The static and dynamic compressibility can be compared based on uniaxial geomechanical testing. We find that the elastic compressibility of Fjerritslev Formation as measured from uniaxial stress and strain data at the beginning of the unloading stress path correspond with dynamic compressibility data. The compressibility of this shale formation measured from core samples is one order of magnitude less than previously used for reservoir simulation studies for deep shales, but our result for the dynamic compressibility is comparable with previous literature data on deep shales. Our results show that it is possible to interpret useful shale compressibility data from geotechnical testing at the beginning of unloading stress path corresponding to the in situ stress condition. The geotechnical means of interpreting compressibility of shale from the loading stress path normally give higher compressibility limit which is safe for building foundations but may not be useful for reservoir simulation studies.

Permeability for the same shale material may range from micro to nanodarcy value depending on the methodology used for the evaluation. We found that Kozeny's modelled permeability from the specific surface of the grains and pores (as modelled from elastic data) and from MICP-NMR data fall in the same order of magnitude with measured permeability for shale rich in Kaolinite, but overestimates permeability by two to three orders of magnitudes for shale with high content of smectite. The empirical Yang and Aplin model gives good permeability estimate comparable to measured data for shales rich in smectite but underestimate permeability in kaolinite rich shale. This is probably because Yang and Aplin model was calibrated in London clay which is rich in smectite. It is therefore important that any model that is meant to estimate shale permeability should be calibrated on a large amount of data from both synthetic and natural shale samples. We also found that Biot's coefficient introduced in calculating shale permeability has a significant and systematic impact on shale permeability data.

4 Caprock Compressibility and Permeability and the Consequences for Pressure Development in CO_2 Storage Sites

4.1 Summary

Large scale CO_2 storage has previously been considered for the Vedsted structure located in the Northern part of Jylland in Denmark. Pressure buildup in the Gassum reservoir and transmission to the shallower Chalk Group where the brine-fresh water interface resides need to be investigated as part of site qualification, as overpressure can push brine into the fresh water zone and thereby affecting aquifer performance. Pressure transmission from the reservoir into the surrounding formations, when fractures and faults are ignored, will depend on the properties and thickness of the sealing rock. The most important property to be considered is caprock compressibility and permeability. Laboratory experiments on centimeter-scale plugs and dynamic sonic velocity data from relevant shale formations in Denmark indicate that shale compressibility is lower than often assumed for reservoir simulation studies. The measured compressibility for the Fjerritslev Formation is 0.5 x $10^{-5}\, bar^{-1}$, which is an order of magnitude lower than the standard compressibility ($4.5 \times 10^{-5}\, bar^{-1}$) normally used for reservoir simulation studies. The consequences of this lower compressibility are investigated in a simulation case study and the results indicate that higher overpressure is created in the reservoir and the caprock. Overestimating caprock compressibility can therefore underestimate overpressure within the storage and sealing formations and this can have significant implication in the presence of highly permeable fractures and faults. The caprock permeability is measured on core samples using a geotechnical method of constant rate of strain (CRS) experiments which seem to match the modeled permeability data for the Fjerritslev Formation. We found an average vertical permeability of 0.1 μD for the Fjerritslev Formation from the samples measured. The sensitivity of pressure development for the caprock permeability has been studied by varying from one to three orders of magnitude higher and one to two orders of magnitude lower than the measured permeability of 0.1 μD. Injecting 60 million tons (Mt) of CO_2 at a rate of 1.5 Mt/year into the Gassum Formation for 40 years indicates that, with permeability above 1.0 μD, overpressure can be transmitted through the 530 m thick Fjerritslev Formation caprock and further up into the overburden layers.

4.2 Introduction

4.2.1 Background

During the period 2007–2012 a Carbon Capture and Storage (CCS) demonstration project was considered in the North Jylland region of Denmark. The project would have involved the post-combustion capture of CO_2 from the Nordjyllandsværket coal power station at Aalborg followed by geological storage of the CO_2 in a nearby onshore saline aquifer (Gassum reservoir) within the Vedsted structure (Christensen et al., 2012). The project was temporarily stopped in 2011. The investigation license was active during 2011 and as a part of that, research activities were initiated related to key technical issues, one being to gain better understanding of formation pressure buildup and pressure transmission through the caprock Fjerritslev shale formation due to CO_2 injection. Various research studies have been evaluating pressure response as a result of injecting large volumes of CO_2 into saline aquifers for safe storage over long period of time. Most of these studies are conceptual due to the scarcity of site specific 2D or 3D seismic data and petrophysical data of the formations (Birkholzer et al., 2009; Buscheck et al., 2012; Zhou et al., 2008). One of the concerns raised in the licensing process is the environmental impact of large-scale pressure buildup in the storage formation (Gassum) and related brine displacement which may affect the quality of the fresh water resources in the overlying Chalk Group which may experience water table displacement and changes in discharge and recharge zones. This question can be addressed if overpressure maps are generated as input for hydrogeological modeling (not within the scope of this work) of brine displacement.

The Vedsted structure is an onshore saline aquifer targeted for CO_2 storage and without considering fluid production (i.e., extraction), which can increase CO_2 storage capacity and relieve pressure buildup, we are investigating this structure as an injection-only formation. In the absence of fluid production from injection-only-industrial scale saline formations, geological storage of CO_2 may result in a large pressure buildup and transmission, persisting both during and sometime after injection has ceased (Buscheck et al., 2012). Thus, pressure buildup is considered to be a limiting factor on CO_2 storage capacity and security, and storage-capacity estimates based on effective pore volume available for safe trapping of CO_2 may have to be substantially reduced (Birkholzer and Zhou, 2009). There is also the need to evaluate overpressure development

within the injection site in order to stay below the threshold pressure for fracturing of the caprock. Previous conceptual simulation studies (Birkholzer et al., 2009; Buscheck et al., 2012; Zhou et al., 2008) have shown that pressure development within the storage formation and lateral and vertical transmission to the surrounding and the overburden layers is largely determined by the hydraulic connectivity between the deep saline formations and the fresh water aquifers overlying them. The assumptions about hydraulic properties of the sealing layers are important in simulation studies for CO_2 sequestration. The main hydraulic properties to be investigated include compressibility, permeability and porosity of the caprock. In order to simulate CO_2 sequestration in the Gassum Formation reservoir (primary reservoir) and to investigate pressure buildup and transmission through the Fjerritslev Formation (primary caprock) to the overburden layers, our goal is to evaluate data for compressibility, permeability and porosity of the sealing formation, and then use this for building scenarios to illustrate the associated ranges of results and the consequences of uncertainty about input parameters.

4.2.2 Compressibility

In situ compressibility of shale can be determined from various sources: (a) sonic velocity and bulk density data of well logs, (b) measurements on centimeter to meter scale in the field or from, (c) ultrasonic velocity data measured in the laboratory on centimeter scale core samples (Mbia et al., 2013b). Compressibility determination from velocity and density data is often termed dynamic compressibility. Compressibility can also be determined from stress-strain data during geotechnical testing on centimeter scale core samples and this type is often referred as static compressibility. Urgent need for compressibility data for deeply buried caprocks has prompted these investigations. These data have been scarce and difficult to find in the available literature, probably because they were not that useful for reservoir simulation studies compared with reservoir rocks. Previous studies on reservoir rocks have shown that static compressibility from hydrostatic testing is often higher than dynamic by orders of magnitudes (Fjær, 2009; Holt, 2012; Tutuncu et al., 1994; King, 1970; Walsh, 1965; Yale et al., 1995). Acoustic wave propagation in dry, clean (clay free) rock is predominantly an elastic process (Walsh, 1965) and both dynamic and static compressibility determination in such rocks are supposed to be similar, but occurrences of non-elastic processes may cause them to differ according to Fjær et al. (2012). The differences between static and dynamic compressibility in rocks are suggested to be due to the departure from linear elasticity due to the influence of strain amplitude, length of stress path, stress history, rock volume involved, and

drainage conditions (Cheng and Johnston, 1981; Fjær et al., 2012; Simmons and Brace, 1965). Walsh and Brace (1966) explained that the difference may be due to the presence of highly compliant cracks which affect static deformation differently than the dynamic. The standard caprock compressibility used in many CO_2 reservoir simulation studies (Birkholzer et al., 2009; Buscheck et al., 2012; Jin et al., 2012; Pruess et al., 2002; Zhou et al., 2008) is 4.5×10^{-5} bar^{-1} which was measured for unconsolidated reservoir rocks by Newman (1973). Zhou et al. (2008) reported that up to 1.0×10^{-3} or 1.0×10^{-2} bar^{-1} order of magnitude can be achieved in plastic clays. Static compressibility under hydrostatic loading condition is different from uniaxial loading behavior (Khatchikian, 1995; Ong et al., 2001; Yi et al., 2005) and does not represent true reservoir conditions of stress (Anderson and Jones, 1985; Lachance and Anderson, 1983; Teevu, 1971). We will present experimental data on caprock compressibility determined from three different methods: (a) stress–strain, (b) ultrasonic velocity and (c) well log velocity data of Fjerritslev Formation (shale) from two analog wells Stenlille-2 and -5 (detailed laboratory procedure have been presented by Mbia et al. (2013b).

4.2.3 Permeability

Permeability of the shale matrix is an important parameter determining the extent to which pressure propagates in shale caprock. Unlike other sedimentary rocks, shales have very low permeability that often prevents vertical escape of pore fluids. This has resulted in abnormal pore pressure occurrences in some sedimentary basins (Berg and Habeck, 1982; Bigelow, 1994; Chapman, 1972, 1994; Dickey et al., 1968; Dickinson, 1953; Freed and Peacor, 1989; Magara, 1971; Schmidt, 1973). There are several factors that can naturally elevate the pore pressure in shale including compaction of fluid-saturated sediments (Dickinson, 1953; Magara, 1975a; Nazmul et al., 2007; Peltonen et al., 2009, 2008), transformation of smectite to illite (Freed and Peacor, 1989), and thermal expansion of fluids (Magara, 1975b). The abnormal pressures once generated can equilibrate to the hydrostatic gradient with time except when the vertical and horizontal escape of fluid is limited by a shale unit of high capillarity or very low permeability. This phenomenon of abnormal pressures is often associated with hydrocarbon generation where the shale prevents upward migration due to its low permeability and high capillarity to the non-wetting phase (Berg, 1975). In this study, we are dealing with case study of CO_2 sequestration in Gassum Formation, an onshore aquifer with normal hydrostatic pressure. The magnitude of overpressure development within the aquifer during the entire injection period will depend on the rate at which brine escapes

to the surrounding formations. In cases with sufficiently low caprock permeability this may also limit the flow of aqueous pore fluids (Bradley, 1975; Bredehoeft and Hanshaw, 1968; Deming, 1994; Hunt, 1990) and if this occurs we should expect more overpressure in the aquifer.

Shale permeability is shown in the literature to vary widely by orders of magnitude from as high as hundreds of microdarcies to as low as hundreds of nanodarcies (Armitage et al., 2011; Hou et al., 2012; Josh et al., 2012; Reece et al., 2012; Zhou et al., 2010) with values well above and below those required for pressure seals over characteristic geologic and reservoir production time scales (Bredehoeft et al., 1983; Dewhurst et al., 1999, 1998; Katsube et al., 1991; Kwon et al., 2001; Lin, 1978; Magara, 1971; Young et al., 1964). The variation depends on porosity, clay mineralogy and content, and texture (Dewhurst et al., 1998; Katsube et al., 1991; Kwon et al., 2004; Revil and Cathles, 1999), all of which may change with burial (Dzevanshir et al., 1986; Hower et al., 1976; Kim et al., 1999; Lee et al., 1985). Permeability may also depend on pore fluid composition if pore throats available for fluid flow are modified by local clay swelling and/or formation of hydrated complexes at clay-fluid interfaces (Norrish, 1972; Sparks, 1995; Scott and Smith, 1966; Sposito et al., 1999; Van Olphen, 1977). Clay aggregates made up of swelling clays exhibit extremely low permeability to the flow of water (Faulkner and Rutter, 2000; Moore et al., 1982), so permeability of clay aggregates depends on electrolytes in the pore fluid (Mesri and Olson, 1971; Olsen, 1972; Whitworth and Fritz, 1994). Permeability of deeply buried shales, with abundant illite and little or no smectites, are expected to show less chemical sensitivity than permeability of shallow mudstones with higher modal swelling clay contents. Yet, transport properties may continue to depend on fluid composition if cation exchange that occurs at inter granular clay-fluid interfaces and pores are affected by changed dimensions of the diffuse double layer (Kwon et al., 2004) and with all this in mind, it is still necessary to measure and model shale permeability of the caprock below which CO_2 is to be stored in order to make predictions about storage security.

4.3 Methodology

4.3.1 Petrophysical data collection

The ideal situation would be to use Fjerritslev Formation core samples from the Vedsted-1 well situated at the Vedsted structure for this study, but because of the lack of core material in this location, cuttings samples were used and for analogy combined with cuttings samples from two other wells penetrating the same formation although at another location (Stenlille-2 and Stenlille-5). The location of the wells and the distribution of the formation are shown in Figure 4.1. Preserved core samples were obtained from Stenlille-2 and Stenlille-5 as shown in the lithostratipraphy of the formations in Figure 4.2. Well logs and final well reports were used to develop a sampling strategy. Thirty-one cuttings samples and a number of plugs were drilled from the preserved core samples (Figure 4.3) and were studied. Retrieval of the core samples from their in situ stresses to surface condition causes the sample to expand, introducing unloading or artificial microscopic fractures as shown by Backscatter electron micrograph images of selected samples of Fjerritslev Formation in Figure 4.4. These fractures make laboratory testing susceptible to artifacts and interpretation errors unless special procedures are applied. Detailed experimental procedure, description, and results were presented by Mbia et al. (2014a).
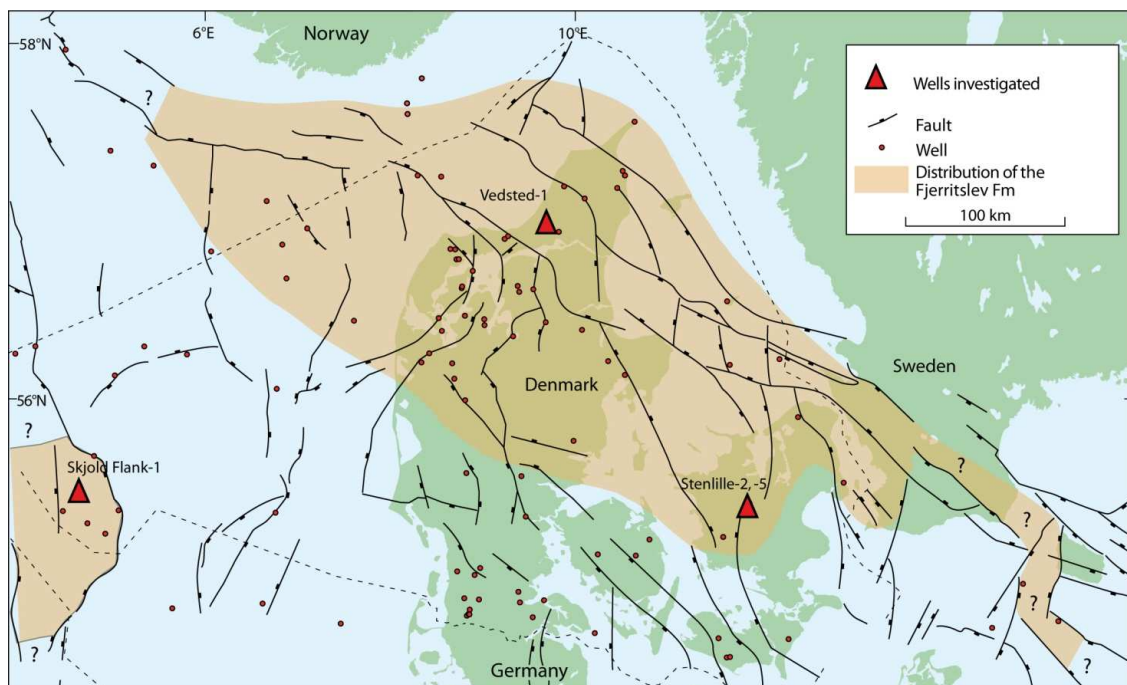

Figure 4.1 Map showing location of the three studied sites and the outline of the Fjerritslev Formation in the Norwegian-Danish Basin to the Northeast and North Sea Central Graben to the Southwest. Modified after Petersen et al. (2008).
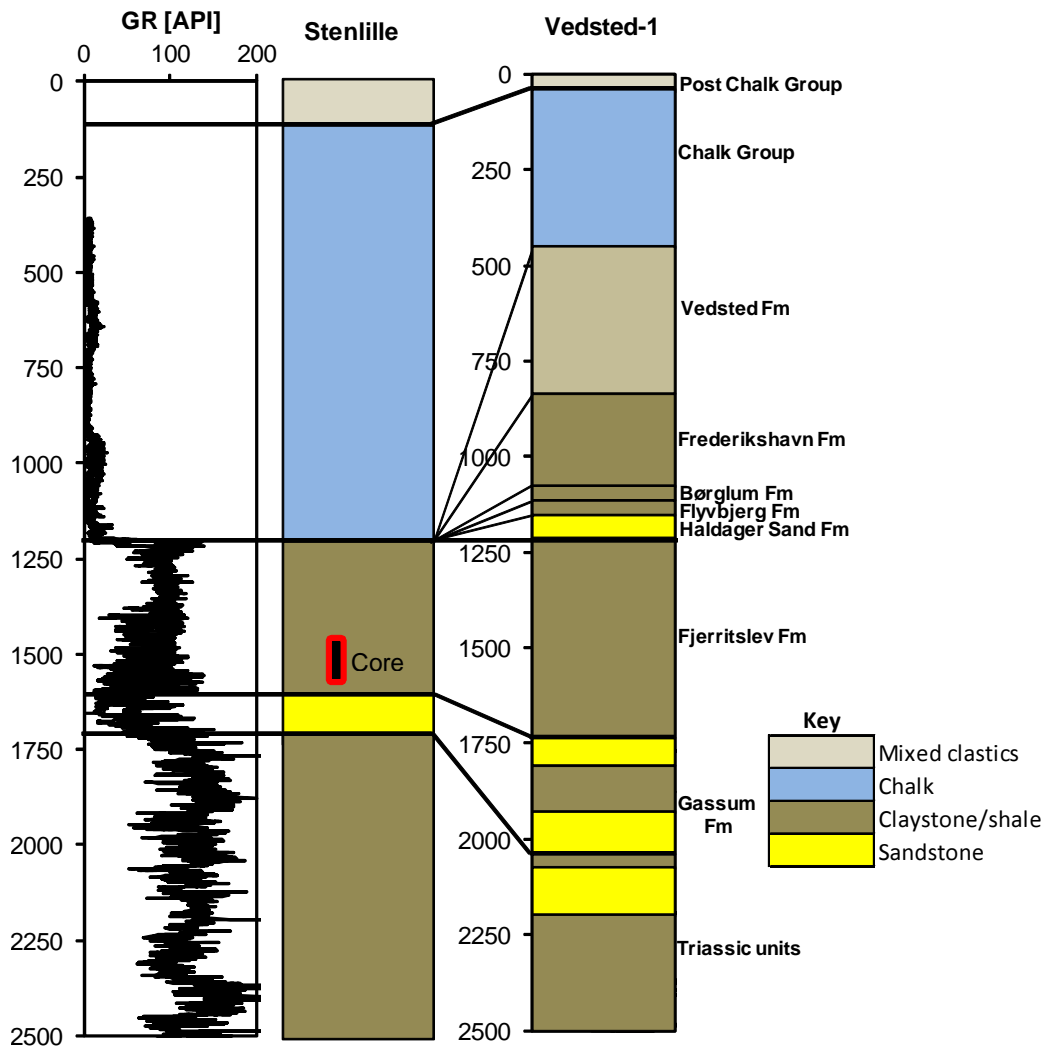
Figure 4.2 Lithostratigraphical correlation of Stenlille and Vedsted-1 wells from logging data. Core samples were taken from Fjerritslev Formation in Stenlille well as indicated by the plug shape with red border.

Figure 4.3 Core samples from which plugs were drilled for laboratory testing.
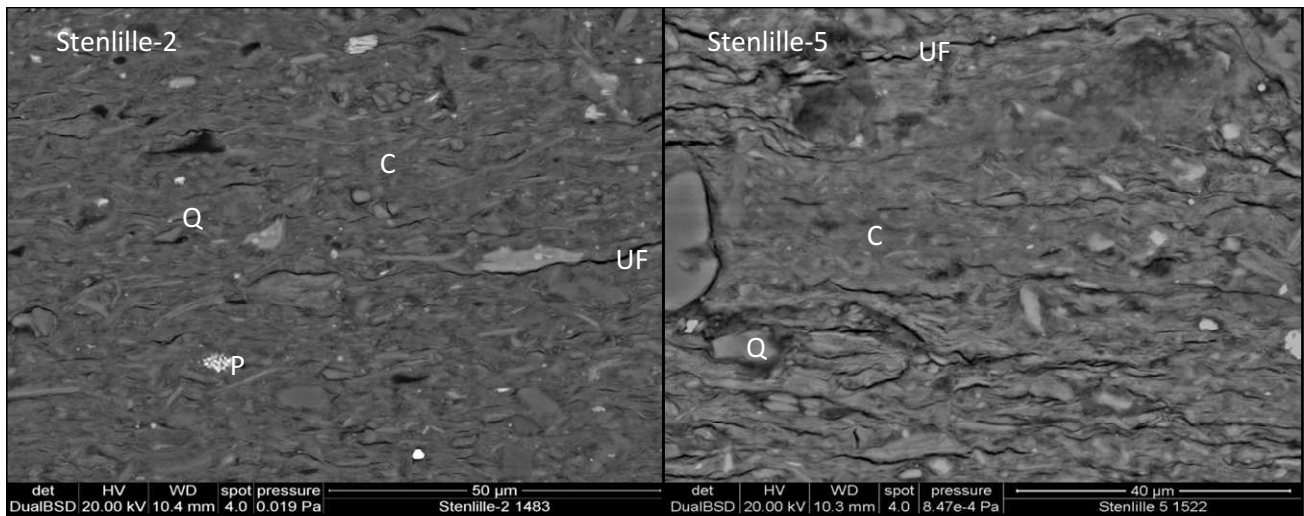
Figure 4.4 Backscatter electron micrographs images of selected samples from Jurassic shale obtained from the Stenlille wells showing significant amount of silt (Q) to be present in the clay-rich matrix (C) with framboidal pyrite (P). The pore network is too small to be visible at this resolution, whereas unloading fractures (UF) due to sample retrieval are visible. Holes, where silt grains have fallen out of the sample are also visible.

The bulk mineralogical composition as derived from X-ray diffraction (XRD) of samples from the Fjerritslev Formation shows on average 40% quartz, 1% K-feldspar, 1% plagioclase, 3% calcite, 2% dolomite and 2% pyrite as non-clay minerals. The clay fraction in all the samples is dominated by illite (23%) and kaolinite (27%) while chlorite occurs in small amount (about 1%). Porosity was measured by three different methods and includes: helium porosimetry-mercury immersion (HPMI), mercury injection capillary pressure (MICP) and nuclear magnetic resonance (NMR). Porosity analysis from HPMI method was carried out on cutting samples and the results range from 24% at 1390 m to about 11% in the deeper samples at 2100 m. MICP analysis was also performed on cuttings samples at depth interval between 1484 m and 1576 m and the porosity result range from 9% to 14%. NMR measurements were made on core samples and the porosity result ranges from 18% to 21%. Porosity results obtained from the three methods are shown in Figure 4.5. The results indicate that the porosity is dependent on the method used, and often the choice of caprock porosity data to use in simulation studies will depend on the individual modeler. In our case we have decided to use porosity data from MICP measurements which in essence is considered as a measure of the effective porosity which is available for fluid movement. HPMI and NMR in principle give a measure of total porosity and we expected similar porosity results from these two methods. Presence of unloading fractures in the core samples are regarded as artifacts and are

responsible for the too high NMR porosity and therefore the NMR porosity was disregarded as this is not associated with in situ conditions.
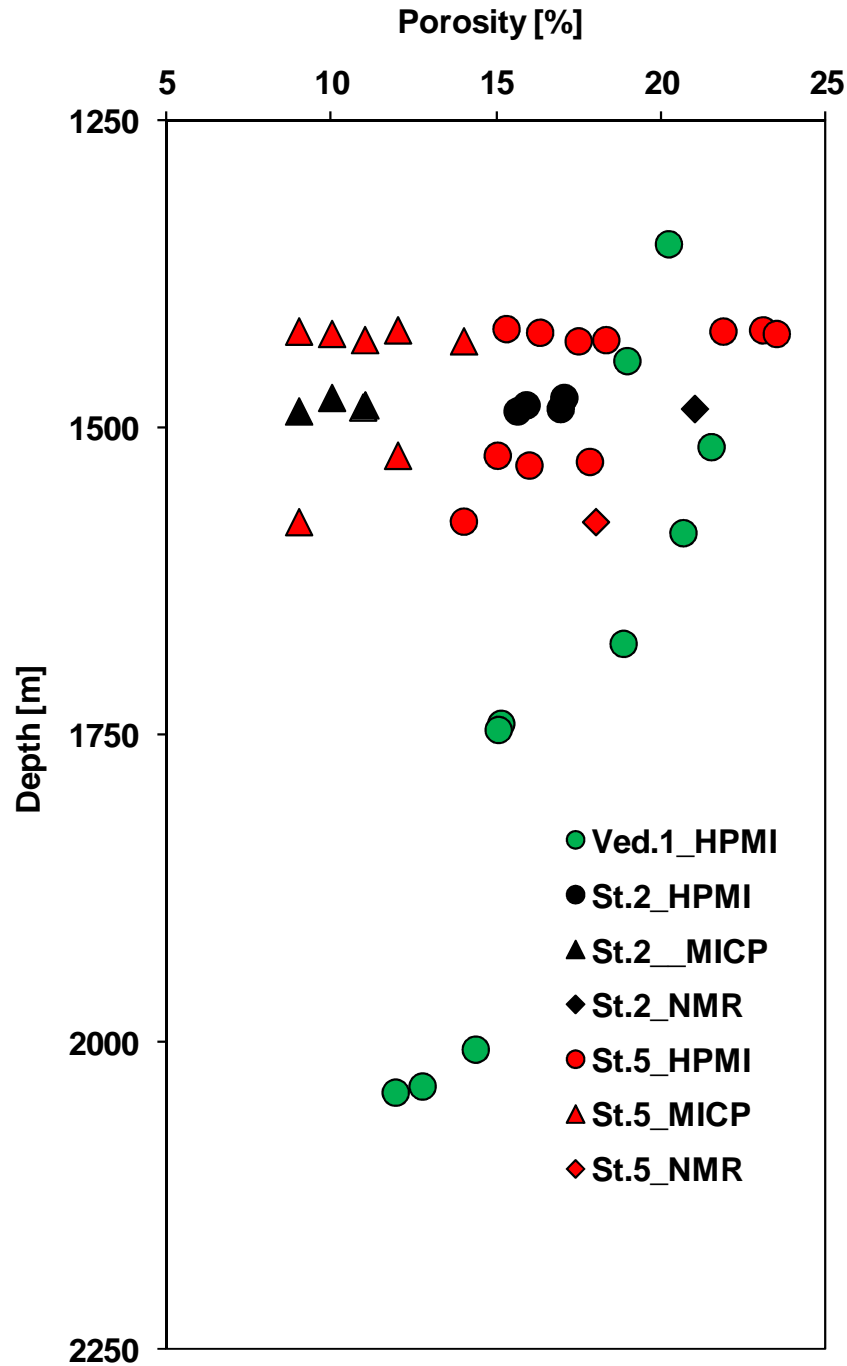

Figure 4.5 Porosity obtained from Helium porosimetry-mercury immersion (HPMI), mercury intrusion capillary pressure (MICP) and nuclear magnetic resonance (NMR) methods versus depth for cuttings and selected core samples from Vedsted-1 and Stenlille-2 and -5. Modified after Mbia et al. (2014a).

4.3.1.1 Permeability data

Permeability measurement was conducted on both vertical and horizontal core samples by constant rate of strain experiments as described by Wissa et al. (1971). The detailed laboratory procedure is described by Mbia et al. (2013b). The measured permeability gives 0.2 μD for vertical and 9.0 μD for the horizontal samples giving k_v/k_h ratio of approximately 0.02. The high value for horizontal permeability could be because the material is more isotropic in this direction due to their depositional history which might have enhanced pore connectivity. In addition the, Fjerritslev Formation permeability was obtained using three alternative methods: (a) modeled from Brunauer–Emmett–Teller (BET) specific surface and porosity using the Kozeny (1927) approach, (b) combined NMR and MICP data (Hossain et al., 2011), and (c) from elastic (velocity) data (Mbia et al., 2014a). The results are compared in the permeability-porosity plot shown in Figure 4.6. The modeled permeability ranges from 1.0 to 0.06 μD and the majority of the modeled permeability falls in the same order of magnitude as the measured vertical permeability.
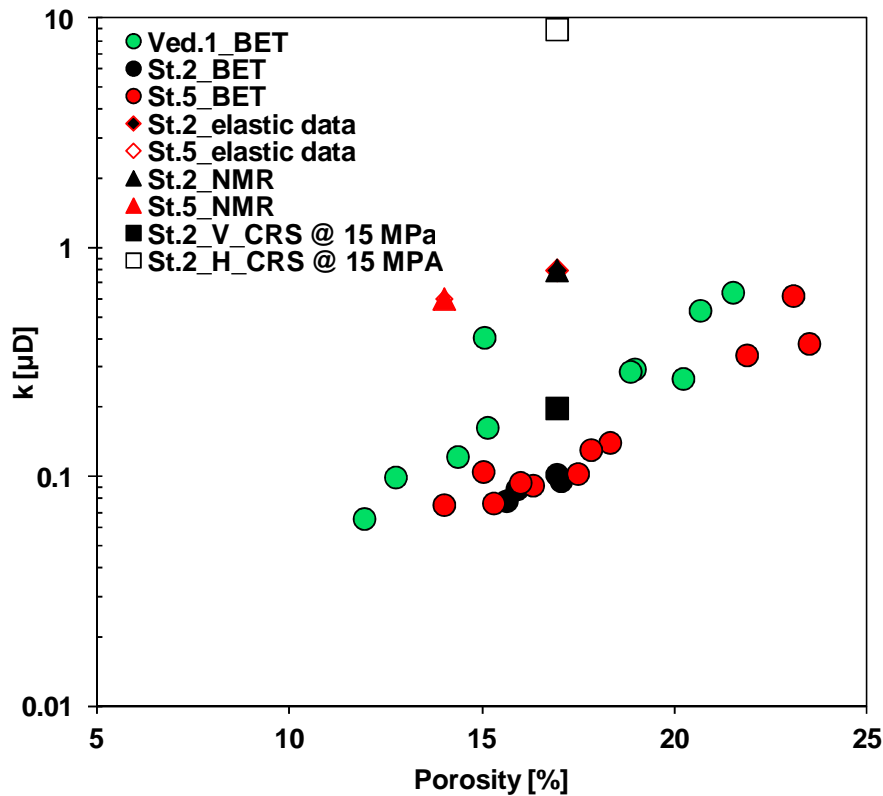
Figure 4.6 Plots of modeled and measured permeability versus HPMI porosity. Permeability measured indirectly from constant rate of strain (CRS) experiment is shown by the empty and black square corresponding to the vertical and the horizontal sample respectively. BET is permeability modeled from the specific surface of the grain and porosity by Kozeny's model. Elastic data is permeability modeled from equivalent pore radius (r_p) and r_p is modeled from compression, shear and bulk modulus. NMR is permeability modeled from combined NMR and MICP data.

4.3.1.2 Compressibility data

Laboratory measurements were carried out on 1½ inch diameter core plug samples from the Stenlille-2 and -5 wells and the detailed procedure is described by Mbia et al. (2013b). The experiments were performed under drained conditions. A series of uniaxially confined loading, unloading, and reloading stress paths were applied up to the in situ stress level to close all the unloading fractures shown in Figure 4.4. Static compressibility was determined from the loading and unloading stress paths. Compressibility determined from stress-strain loading-reloading data ranges from 4 to 10×10^{-5} bar^{-1} while that from the beginning of the unloading stress-strain data ranges from 0.2–0.6×10^{-5} bar^{-1}. The loading experiments were accompanied by continuous ultrasonic recording of compressional and shear wave velocities. The dynamic compressibility determined from ultrasonic compressional velocity data ranges from 0.3 to 0.5×10^{-5} bar^{-1} corresponding to static unloading compressibility at the beginning of the unloading stress path at reservoir conditions and these two compressibilities measure the elasticity of the material. Static compressibility from loading stress-strain tends to give higher values due to the influence of the unloading fractures. In reservoir simulation studies dynamic compressibility determined from compressional velocity data or from the early unloading stress-strain data in uniaxial consolidation experiments is preferable because it represents the elastic behavior of the material at reservoir conditions. Figure 4.7 shows the correlation of compressibility data assessed in the laboratory to field data of sonic velocity and bulk density of Stenlille-2 and -5 well logs.

4.3.2 Model set-up and parameters

4.3.2.1 Vedsted structure

The Vedsted structure located in the Northern part of Jylland in Denmark is situated in a small graben structure bounded by northwest–southeast trending faults. The graben is part of the Triassic rift system forming the deep Fjerritslev Trough (Michelsen et al., 2003). The site comprises the Gassum Formation and the Haldager Sand Formation forming primary and secondary reservoirs in the saline aquifer. The structure is mapped as a small elongate closure approximately 250 m high covering an area of about 31 km^2 and the depth to top Gassum reservoir is about 1900 m below mean sea level. The target reservoir layer is the 290 m thick Gassum Formation which is intercalated with low permeability shale sequences. The seal is the 530 m thick low permeable shale of the Fjerritslev Formation overlying the entire sequence constituting a flow barrier due to the high

capillary pressure and very low permeability. The reservoir is underlain by the Skagerrak Formation with uncertain properties. Overlying the primary caprock is the Haldager Sand Formation forming an upside storage potential with excellent reservoir properties. This formation has a net thickness of about 80 m with porosity of about 17% and permeability of 200–300 mD. The thickness of all overburden formations is presented in Table 4.1.

Figure 4.7 Plot showing correlation of mean value of compressibility obtained from ultrasonic velocity and that from unloading stress-strain data of laboratory measurements on core material to that from sonic velocity of well log data from Stenlille-2 and -5. M^{-1} is dynamic compressibility calculated from compressional modulus obtained from the sonic velocity log and St.2_dynamic is from laboratory data while St.2_static is obtained from the stress–strain unloading data during consolidation experiment.

4.3.2.2 Model parameters

In Table 1, we present the reservoir properties of the various formations in the Vedsted structure. The storage capacity for CO_2 in this case depends on the compressibility, permeability and porosity of the Gassum Formation but also on the properties of the Fjerritslev Formation. The sensitivity study is based on scenarios with varied compressibility and permeability of the Fjerritslev Formation as shown in Table 1. The low compressibility value of 0.5×10^{-5} bar^{-1}determined for the Fjerritslev Formation will be used in the simulation and compared with the higher compressibility value referred to as standard compressibility of 4.5×10^{-5} bar^{-1} normally used for caprocks in reservoir simulation studies. Similarly for the permeability sensitivity study, we have assigned the measured horizontal permeability value of 1.0 µD for the Fjerritslev Formation and then varied the permeability over one, two and three orders of magnitudes from the measured value to cover the wide range of permeability values for shales given in the literature. The other formations maintain their base case values for all the simulations. The ratio of vertical to horizontal permeability is chosen as 0.1 and is used for all the formations including caprock for simplification. This ratio corresponds with the literature data for reservoir rocks and it will still give us the average vertical permeability value for the Fjerritslev Formation. Other initial formation and fluid parameters are a hydrostatic pressure gradient of 100 bar/km, salinity of the formation water of 270 g/l, and a geothermal gradient of 30°/km. The relative permeability function used for the simulation was inspired by the data shown by Bennion and Bachu (2006) for the Viking Formation sandstone, and was for simplicity used for both the sandstone and the shale lithology (Figure 4.8a).

The capillary pressure curve was established as a type curve for the sandstone with 0.5 bar capillary entry pressure (Figure 4.8b). For the shale this curve was scaled to an entry pressure of 6.5 bar corresponding to a permeability level of around 0.3 µD according to correlation established by Thomas et al. (1968).

The compressibility of the fluids (CO_2 and water) is intrinsically taken into account in Schlumberger ECLIPSE 100 in terms of density variation with pressure.

We simulated a rate controlled injection of 1.5 tons of CO_2 per year through a single vertical well in the Vedsted structure (Figure 4.9a) which is completed in the eastern side of the dome shaped anticline in the Gassum reservoir (Figure 4.9b). 60 Mt of CO_2 is injection period is 40 years using the ECLIPSE 100 simulator tool. The aquifer is initially fully brine-saturated. The injection

pressure has been kept 30% below the measured fracture pressure to ensure that there is no reactivation of existing fractures or creation of new fractures during the injection process.

Table 4.1 Hydraulic properties of the formations in Vedsted site. The measured kv/kh ratio is 0.02 but for simplification we have used 0.1 ratio in EClIPSE 100 corresponding to other lithologies given in the literature. The measured values are only for caprock and for other lithologies, general estimates are given.

Formation	Thickness	Base & standard	Permeability k_h		k_v/k_h	Porosity
		Compressibility	Measured	Range		
	(m)	x 10^{-5} (bar^{-1})	(µD)	(µD)		(%)
Post Chalk	30	4.5	5×10^3		0.1	23
Chalk	420	4.5	2×10^3		0.1	25
Vedsted	390	4.5	15×10^3		0.1	21
Frederickshavn (shale)	230	0.5 & 4.5	1	$1 \times 10^3 - 1 \times 10^{-2}$	0.1	13
Børglum (shale)	50	0.5 & 4.5	1	$1 \times 10^3 - 1 \times 10^{-2}$	0.1	13
Flyvbjerg (shale)	20	0.5 & 4.5	1	$1 \times 10^3 - 1 \times 10^{-2}$	0.1	20
Haldager sand	80	4.5	267×10^3		0.1	17
Top Fjerritslev (shale)	174	0.5 & 4.5	1	$1 \times 10^3 - 1 \times 10^{-2}$	0.1	11
Middle Fjerritslev (shale)	174	0.5 & 4.5	1	$1 \times 10^3 - 1 \times 10^{-2}$	0.1	11
Base Fjerritslev (shale)	174	0.5 & 4.5	1	$1 \times 10^3 - 1 \times 10^{-2}$	0.1	10
Top Gassum (sandstone)	64	4.5	63×10^3		0.1	19
Middle Gassum (shale)	47	0.5 & 4.5	1	$1 \times 10^3 - 1 \times 10^{-2}$	0.1	9
Middle Gassum (shale)	47	0.5 & 4.5	1	$1 \times 10^3 - 1 \times 10^{-2}$	0.1	9
Middle Gassum (shale)	47	0.5 & 4.5	1	$1 \times 10^3 - 1 \times 10^{-2}$	0.1	9
Base Gassum (sandstone)	85	4.5	70×10^3		0.1	14
Skagerrak (sandstone)	331	4.5	20×10^3		0.1	14

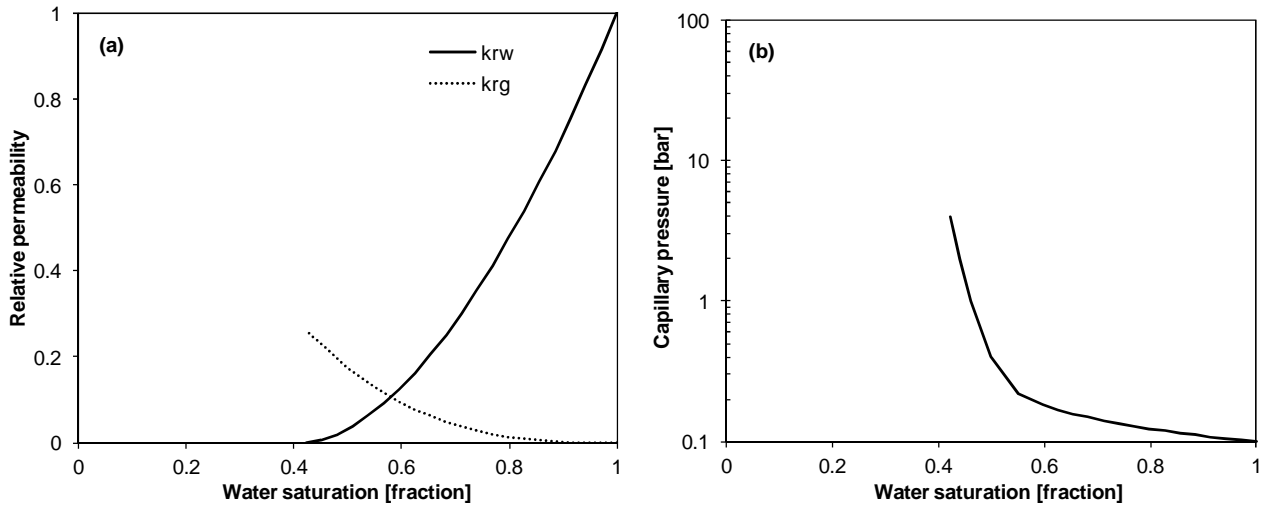1 µD = 1 x 10^{-18} m^2 1 bar = 1 x 10^5 Pa

Figure 4.8 Plots of relative permeability and capillary versus water saturation. a) and b) are sand stone data from Viking Formation (Bennion et al. 2006). a) Was also used for shale while (b) is scaled to an entry pressure of 6.5 bar corresponding to a permeability level of around 0.3 µD according to correlation established by Thomas et al. (1968).
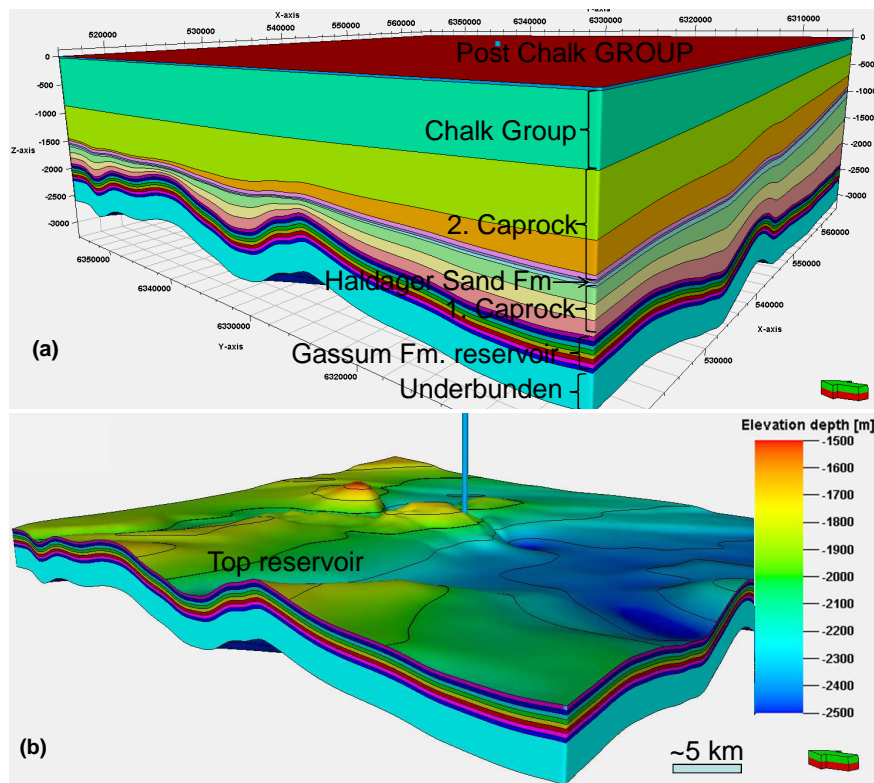
Figure 4. 9 Schematic representation of 3D cross-section of the model domain. (a) Entire 3D model from the sea bottom down to the Upper Triassic sandstone unit (underburden). (b) Top of the deep Gassum Formation (primary reservoir) sandwiched by thin layers of shale and the underburden. Overlying the Gasssum Formation is the Fjerritslev Formation comprising primary caprock, overlay by Haldager Sand Formation (secondary reservoir). Above the Haldager Formation is a succession of thick seconcary caprocks overlain by the Chalk Group within which the brine-fresh water interface resides.

4.4 Simulation results and discussion

4.4.1 CO_2 plume and migration

The injection of CO_2 in the Gassum Formation results in a CO_2 front which is driven upwards on the flank due to the buoyancy force and starts accumulating in the uppermost layer of the formation and immediately hits the less permeable caprock of Fjerritslev Formation. This process forms a CO_2 plume with the largest areal extent at the top of the storage formation. For simplicity we have chosen to show part of the reservoir around the injection well where the plume is limited. Figure 4.10 shows CO_2 saturation and distribution for the base case in the top reservoir around the injection well after 40 years of injection. The CO_2 saturation and distribution for the base case (Figure 4.10) is similar to that of the other cases. The plume is narrow in the injection layer and as the injected volume increases CO_2 rises due to the buoyancy force and then spreads out under the caprock (Fjerritslev Formation). For all cases the plume extends over an area of about 11–13 km^2 in the upper layer of the Gassum Formation filling the entire structure and spreading laterally after 40 years of injection. The shape of the plumes during the injection is determined by the morphology of the aquifer/caprock interface and in this case it is circular because the dome is fairly regular.
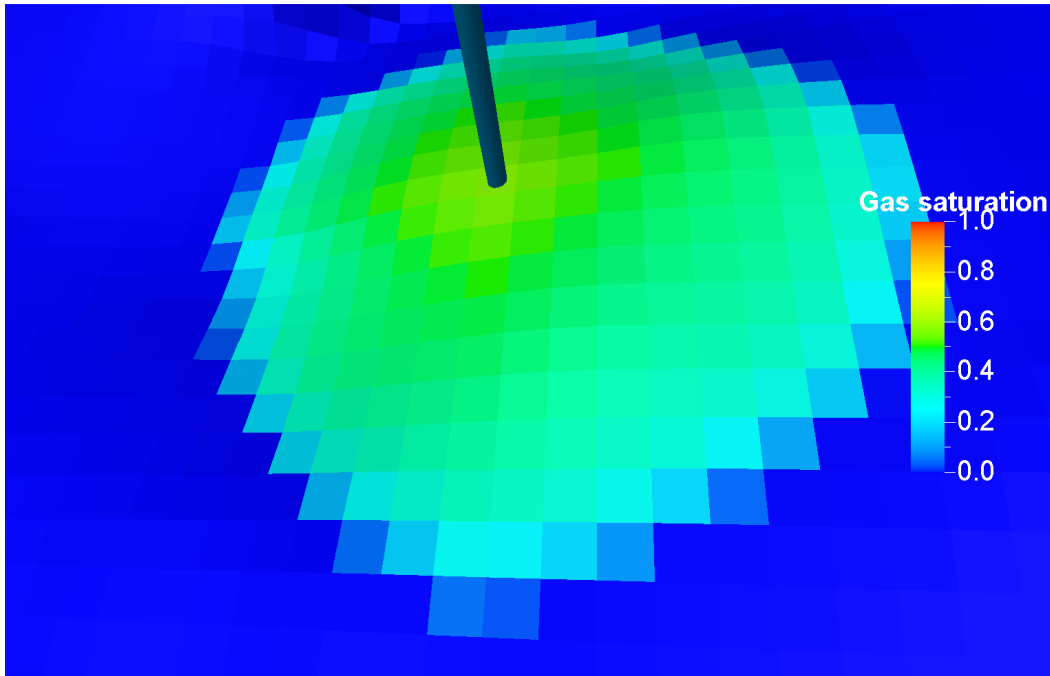

Figure 4.10 Saturation and distribution of CO_2 plume in the uppermost layer of Gassum reservoir after 40 years of 60 Mt CO_2 injection for the base case. Cell size is 0.2 × 0.2 km^2.

At the end of the injection period, the plume is restrained under the caprock layer. The low measured vertical permeability (0.1 µD) of the caprock layer and high capillary entry pressure causes the CO_2 plume to be fully trapped during the 40 years injection period.

4.4.2 Compressibility and pressure development in Vedsted structure

Figure 4.11 shows cross sections of the reservoir and the Fjerritslev Formation showing the areal extent of the pressure buildup and the transmission of pressure away from the injection well after 40 years of CO_2 injection for the measured or base case (Figure 4.11a) and the standard (Figure 4.11b) caprock compressibility. There is overpressure development throughout the entire lateral extension of the reservoir but the vertical transmission is limited to the lower layer of the 530 m thick Fjerritslev Formation sealing the reservoir. The difference in overpressure development between the base case and standard case compressibility can be seen in color contrast of the reservoir and the basal caprock in the two cross sections. However in order to compare the difference in vertical pressure development from the reservoir to the shallower aquifers we have extracted a vertical profile as shown on the cross sections. Figure 4.12 illustrates the resulting profile with red line for the base case and black line for the standard case compressibility.

The higher elastic modulus of the sealing layer, and thus reduction in effective compressibility increases the stiffness of the sealing layer which again increases pressure buildup in both the reservoir and the caprock compared to the standard case with higher compressibility. A higher compressibility causes more attenuation in the caprock and therefore reduces the resultant pressure buildup in both the reservoir and the caprock. The difference in overpressure between the base and the standard case is about 1-3 bar in the reservoir layer and about 5-6 bar in the lower section of the caprock. Despite the difference in pressure buildup in the caprock, the overpressure is contained within the Fjerritslev Formation for both compressibility cases but this could change in case the caprock is fractured or in the presence of vertically communicating faults.

Figure 4.13 presents maps of the top reservoir layer showing overpressure development from the injection well and lateral transmission after 40 years of CO_2 injection for the base (Figure 4.13a) and the standard (Figure 4.13b) case compressibility. By extracting the overpressure profiles across the 50 km lateral extent of the model, it is possible to compare the results for different layers. The overpressure profile, along the x-axis in Figure 4.13, is shown in Figure 4.14. Injecting 60 Mt of CO_2 into Gassum Formation for 40 years resulted in pressure buildup of about 40 and 35 bars for

the base and standard compressibility around the injection cell. At the end the of the injection period the pressure is transmitted to the boundary of the structure resulting in about 2.5 bar overpressure at the cells bordering the boundary cells. Pressure buildup at the boundary cells depends on the boundary condition applied. There are different boundary conditions applicable to reservoir simulation studies but in this case we have used a pore volume multiplier of 200 as estimated realistic value for boundary condition after having performed a sensitivity analysis of different values for pore volume multipliers. The overpressure difference shown in Figure 4.14 between the base and standard case is about 5 bar at the reservoir close to the injection cells and about 2 bar through the entire reservoir.
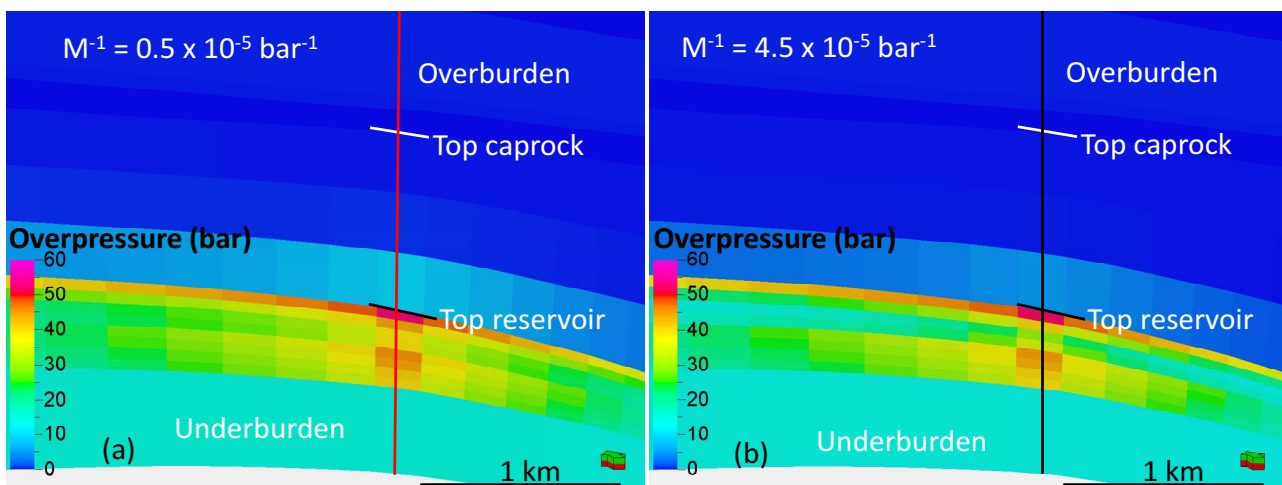

Figure 4.11 Cross section of the reservoir and the Fjerritslev Formation showing overpressure development (in bar) and transmission from the injection cells after 40 years of 60 Mt CO_2 injection. (a) The case with measured caprock compressibility; (b) the case with standard caprock compressibility.

Figure 4.12 Vertical profile from the injection cells (Figure 4.11) showing overpressure development and vertical transmission from the reservoir to mean sea level for both measured $(0.5 \times 10^{-5}$ $bar^{-1})$ and standard compressibility $(4.5 \times 10^{-5}$ $bar^{-1})$ case after 40 years of 60 Mt of CO_2 injection.

Figure 4.13 Map of the top reservoir showing overpressure development from the injection well and lateral transmission after 40 years of 60 Mt CO_2 injection. (a) The case with measured caprock compressibility; (b) the case with standard caprock compressibility. 50 km line indicates the profile across x-direction.
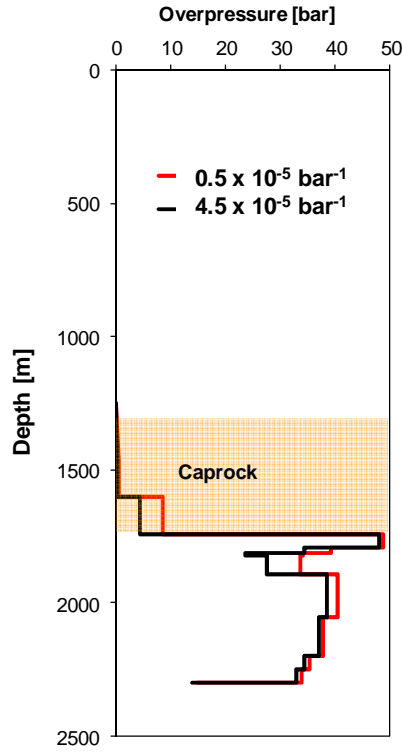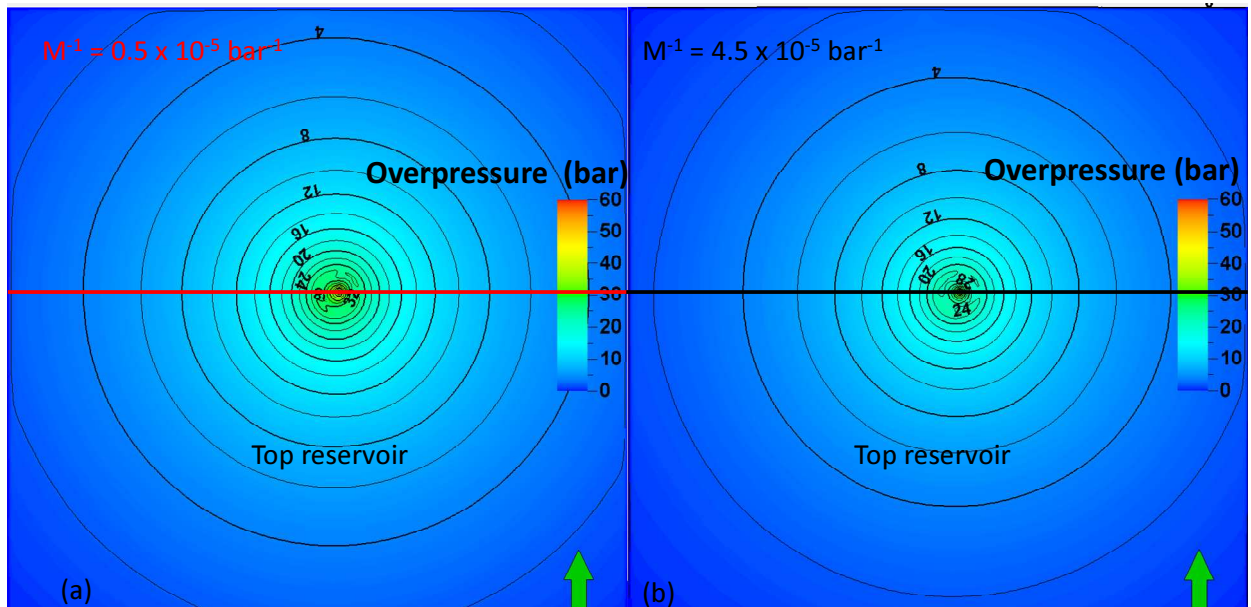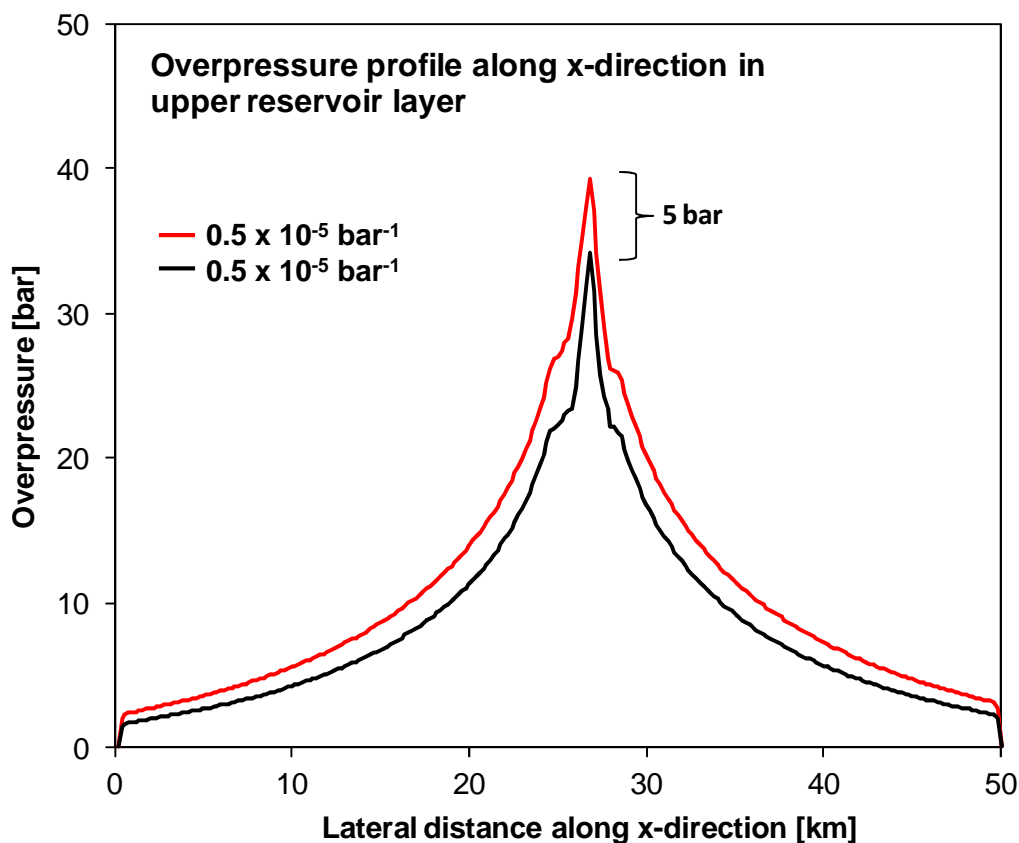
Figure 4.14 Pressure profile at top reservoir showing overpressure development and lateral transmission after 40 years of 60 Mt CO_2 injection for the case with measured and standard caprock compressibility.

4.4.3 Permeability and pressure development in Vedsted structure

The permeability of sealing layers plays an important role in lateral and vertical pressure development within the reservoir and the overlying aquifers. In order to evaluate the influence from caprock permeability and the consequences for pressure development in the Vedsted site, there is a need for considering a range of one to two orders of permeability below and above the experimental value. This will give an overview of possible scenarios of overpressure outcome with respect to varying caprock permeability. Figure 4.15 shows cross sections of the reservoir interbedded by shale layers and the overlying layers. The caprock permeability is varied by one and two order of magnitudes smaller than and greater than the base value of 0.1 μD and the resulting layers affected by overpressure is seen as light color while the blue color is where overpressure development is very minimal or is absent. Pressure buildup is greater in the reservoir layers but minimal or absent within the interbedded shale and shale layers. In order to compare vertical pressure development

within the Vedsted structure, a vertical overpressure profile at 0.2 km from the injection cell is shown for the top Triassic unit to the mean sea level in Figure 4.16. It is important to assess sensitivity of vertical overpressure development to caprock permeability within the structure and also to compare with the base case permeability. The results in Figure 4.16 indicate that the experimentally determined matrix permeability of 0.1 µD for the Fjerritslev Formation does not allow overpressure transmission beyond the lower 0.2 km of the 0.53 km thick caprock layer. Reducing the matrix permeability by one order of magnitude (0.01 µD) gives the same result of vertical overpressure as the experimental value. A further reduction by two orders of magnitude (0.001 µD) resulted in a perfect seal case where there is no overpressure effect in the caprock. On the other hand, increasing the Fjerritslev Formation permeability by one order of magnitude (1.0 µD) causes a 2.0 bar overpressure in the uppermost layer of the formation but still the pressure could not be transmitted to the Haldager Sand Formation which is overlying the caprock. Increasing the Fjerritslev Formation permeability by two orders of magnitude will allow pressure transmission from the Gassum reservoir to the Haldager Sand Formation and the effect is then confined by the Flyvbjerg Formation which forms a secondary seal.
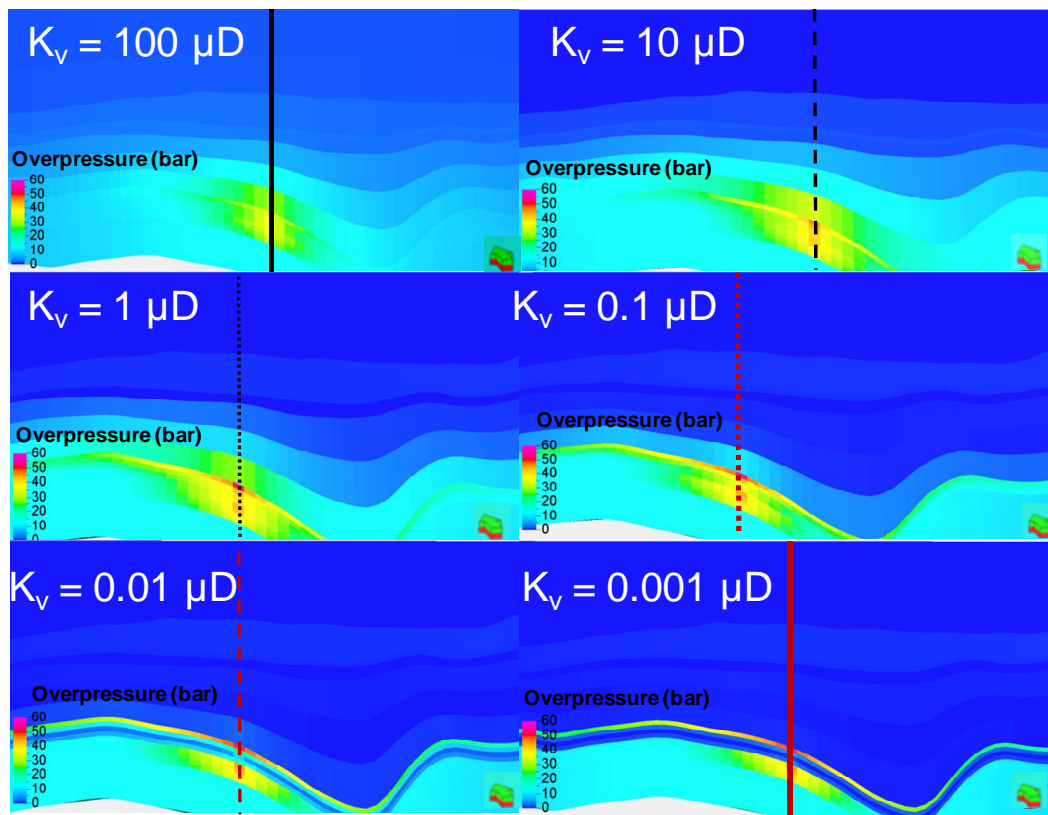

Figure 4.15 Cross section of the reservoir and the overlying layers showing overpressure development (in bar) and transmission after 40 years of 60 Mt CO_2 injection for cases with different caprock permeability varied by several order of magnitudes from the measured value of 0.1 µD.

In the worst case scenario, where Fjerritslev Formation permeability is increased by two (10 μD) and three (100 μD) orders of magnitude there is still no significant amount of pressure buildup in the shallow fresh water aquifer (Chalk Group). A relatively high permeability in the primary seal allows less pressure buildup in the Gassum Formation as some is transmitted vertically. The magnitude of vertical pressure buildup will also depend on the permeability of the layers above the primary caprock. This result suggests the importance of investigating hydrogeological layers and flow parameters, even at shallower depths.

However, the existence of faults connecting the reservoir and the overlying formations could strongly increase the magnitude of vertical pressure transmission, but this subject is not the scope of this work but will be addressed in subsequent work.

Figure 4.17 presents maps of the uppermost layer of Gassum Formation showing pressure buildup and lateral transmission after 40 years of CO_2 injection for different caprock permeabilities. The overpressure maps clearly show that as the Fjerritslev permeability is varied from 100 to 0.001 μD, pressure buildup in the reservoir formation increases and consequently enhances the lateral transmission reaching the boundary of the Vedsted structure for the cases with < 10 μD permeability. Figure 4.18 presents profiles showing the magnitude of overpressure along 50 km lateral distance through the injection cell. For the case with higher caprock permeability, the pressure buildup reaches 40 bar and reduces laterally to 0.5 bar, whereas for the lower permeability the pressure buildup reaches 53 bar at the injection point and reduces to 3 bar at the boundary. Figure 4.19 presents maps of the uppermost layer of Fjerritslev Formation showing pressure buildup and lateral transmission and Figure 4.20 presents profiles showing the magnitude of overpressure along 50 km lateral distance through the injection cell. The cases with higher caprock permeability (100, 10 and 1.0 μD) show pressure buildup of about 5 bar in the area close to the injection point and a reduction laterally to hydrostatic pressure before the project boundary is reached. There is no pressure buildup for the lower permeability cases including the base case. Figure 4.20 shows only the profile at the base Chalk Group for the case with caprock permeability of 100 μD where pressure builds up to 1.0 bar and is transmitted laterally over 15 km radius from the center of the base layer. The other case with less than 100 μD permeability shows no pressure builds up at the base of the Chalk Group (Figure 4.21).
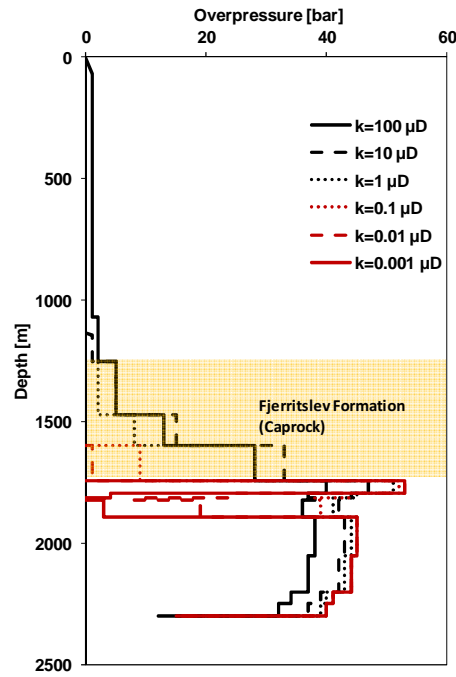
Figure 4.16 Vertical profile from the injection cells showing overpressure development and transmission from the reservoir to mean sea level after 40 years of 60 Mt CO_2 injection for different caprock permeabilities.
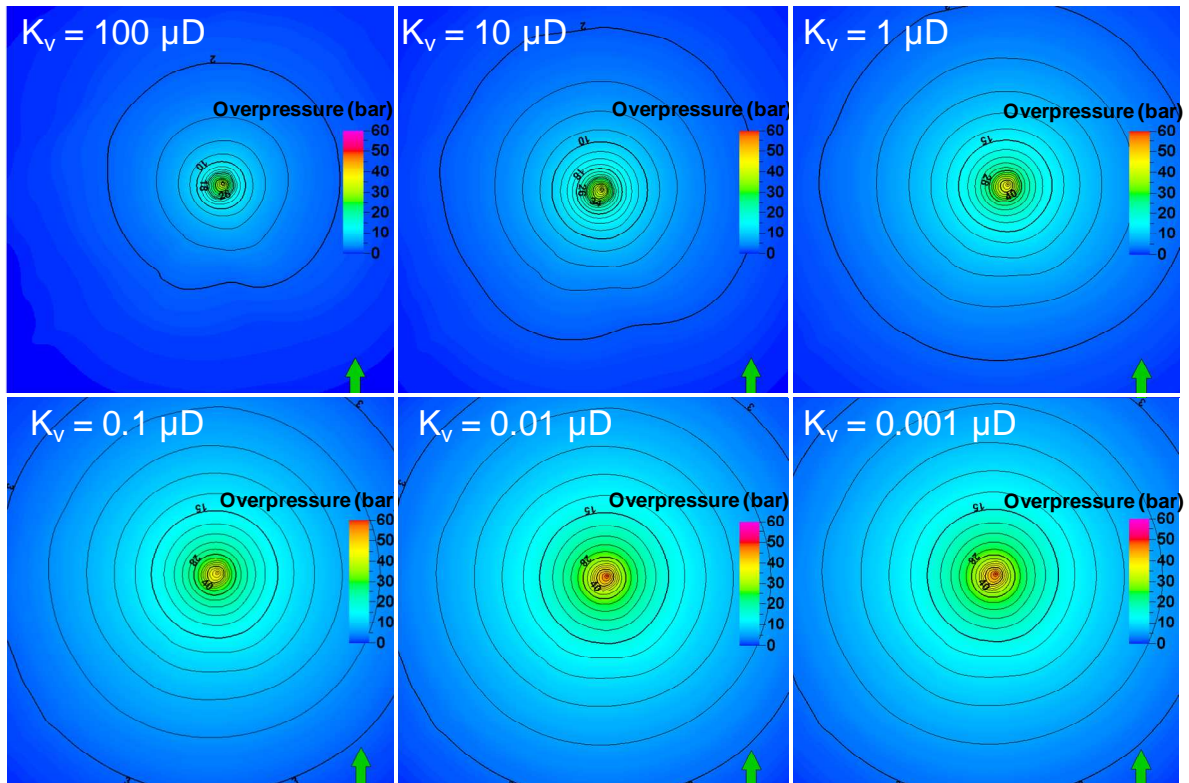
Figure 4.17 Map of the uppermost layer of the reservoir showing overpressure development (in bar) from injection well and the lateral transmission after 40 years of 60 Mt CO_2 injection for cases with different vertical caprock permeability varied in order of magnitudes from the measured value of 0.1 μD.
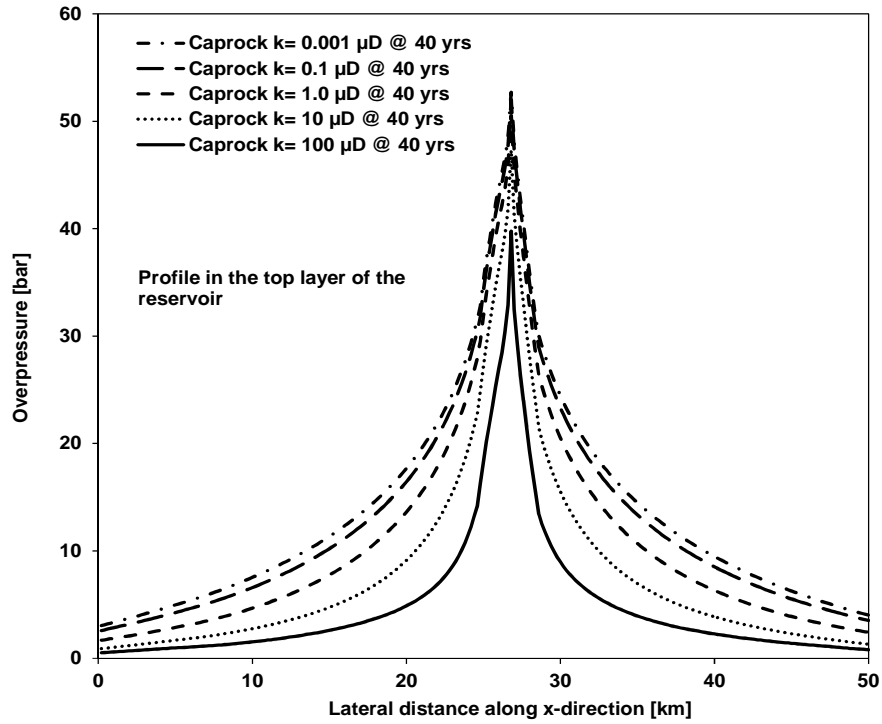
Figure 4.18 Pressure profile in the uppermost layer of the reservoir showing overpressure development and lateral transmission after 40 years of 60 Mt CO$_2$injection for the cases with different caprock permeability.
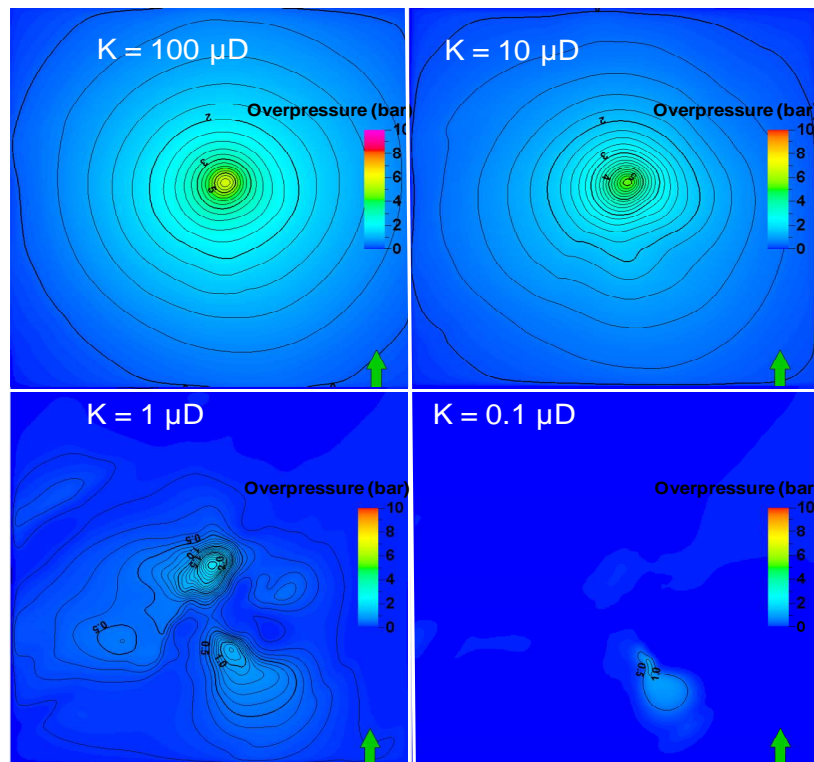
Figure 4.19 Map showing overpressure in the uppermost layer of the 530 m thick Fjerritslev caprock after 40 years of 60 Mt CO$_2$ injection. The irregularities in the maps for the 1 μD and 0.1 μD are interpreted as numerical artifacts.
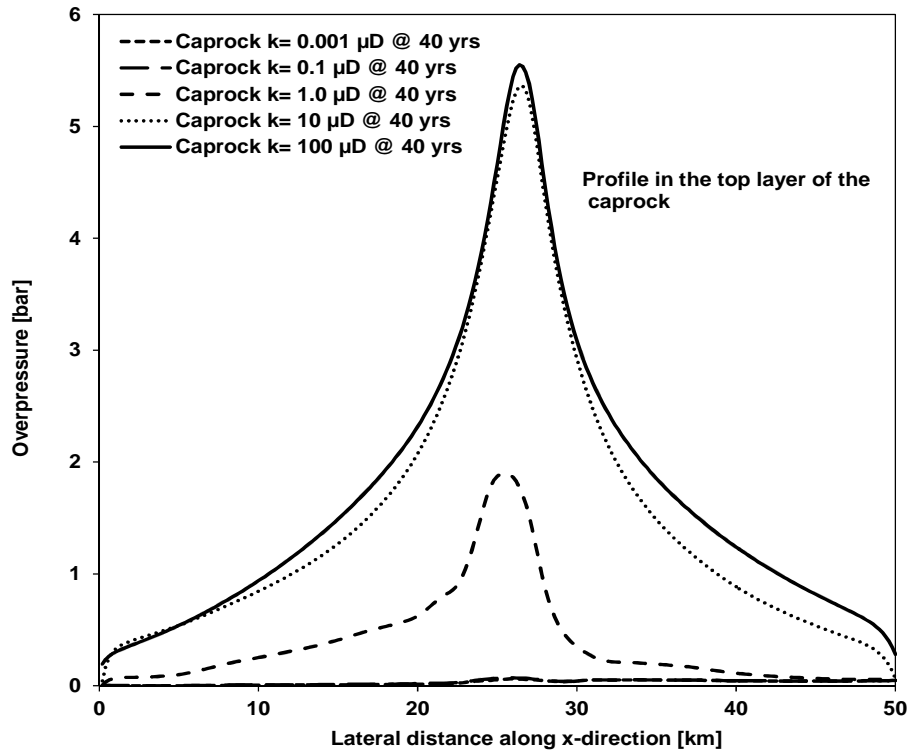
Figure 4.20 Pressure profile (Figure 4.18 for reference) in the uppermost layer of Fjerritslev Formation Caprock showing overpressure development and lateral transmission after 40 years of 60 Mt of CO_2 injection for the cases with different caprock permeability.

Figure 4. 21 Pressure profile (Figure 4.18 for reference) in the base Chalk Group showing overpressure development and lateral transmission after 40 years of 60 Mt CO_2 injection. The case with 100 μD caprock permeability shows slight overpressure while the other cases show no overpressure in the Base Chalk Group.
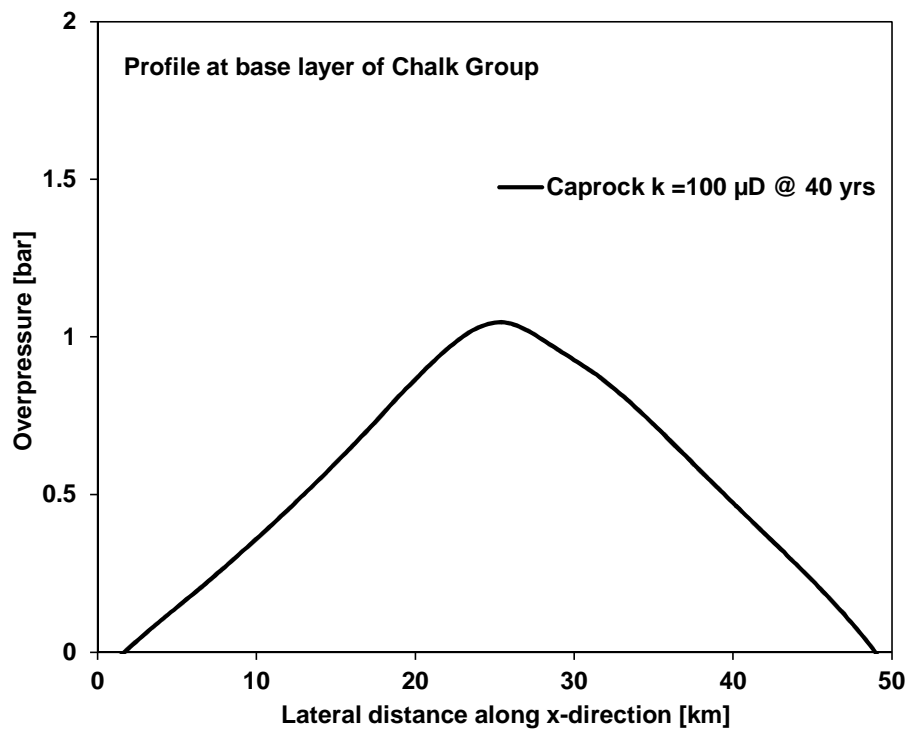
93
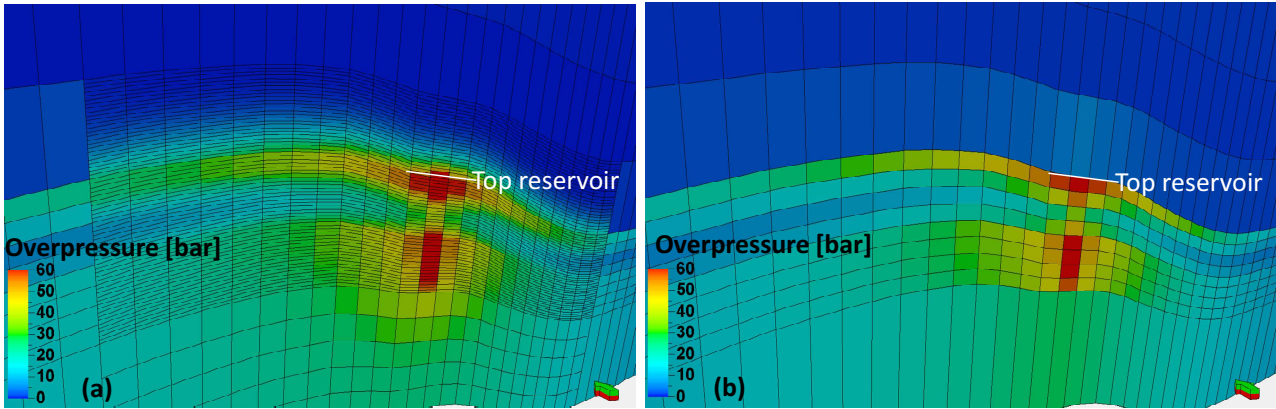
Figure 4.22 The overpressure development for both finer and coarser grids resolution. (a) Vertical grid refinement within the reservoir and the base caprock layers with each cell having vertical dimension of 20 m with the radius of 2.5 km from the injection well. (b) The coarse grid model used in this study and each cell has vertical dimension of 125 m.

4.4.4 Influence of grid effects, relaxation time, and the k_v/k_h ratio on pressure development in the Vedsted structure

4.4.4.1 Gridding

We are well aware that the rather coarse grid representing the Vedsted model might have some effect on the simulation results and the illustration of their magnitude. The decision about gridding was guided by practical computation time for the work on sensitivity analysis requiring multiple simulation runs. We therefore examined the effect of grid resolution on a single example of a simulation run of pressure propagation in order to illustrate the effects. In a grid-refined model, the grid cells within a radius of 2.5 km around the injection well in the reservoir and the base caprock layers were refined vertically to 20 m grid cell thickness as shown in Figure 4.22 (a). The result is compared with the coarse grid model used in this study (Figure 4.22b) with vertical dimension for the grid cells of 125 m and above. We accept that a large grid block size will tend to overestimate the amount of CO_2 dissolution and consequently might underestimate the pressure buildup compared with the fine grid model version We show the comparison of the results of the simulation by examining the amount of pressure buildup in the reservoir at the base of the caprock at the end of injection at 40 years in Figure 4.22 (a) and (b). It seems that grid resolution has very little effect on the average pressure buildup in the aquifer and the caprock. The difference between the fine and coarse grid is seen in the details of the extent of the overpressure propagation, but there is no major

difference in overpressure at the base of the caprock for the two cases. The effect of grid resolution on pressure was also investigated by Pickup et al. (2010) and their simulation results also showed that grid resolution had little effect on pressure buildup and concluded that coarse grids may be sufficient for initial assessment of storage potential.

4.4.4.2 Pressure relaxation after injection stop

Figure 4.23 shows the overpressure profile for the upper layer of the Gassum reservoir after 40 years of CO_2 injection (60 Mt) and 100 years after the end of the injection period. At the year 40, the overpressure in the upper layer of the reservoir reaches up to 55 bar. This overpressure declines rapidly in the first 5 years after the injection stops to about 20 bar and continues to decrease steadily 10 years after the end of the injection. After 100 years from the end of CO_2 injection in the Gassum reservoir the overpressure equilibrates close to the hydrostatic pressure in reservoir.
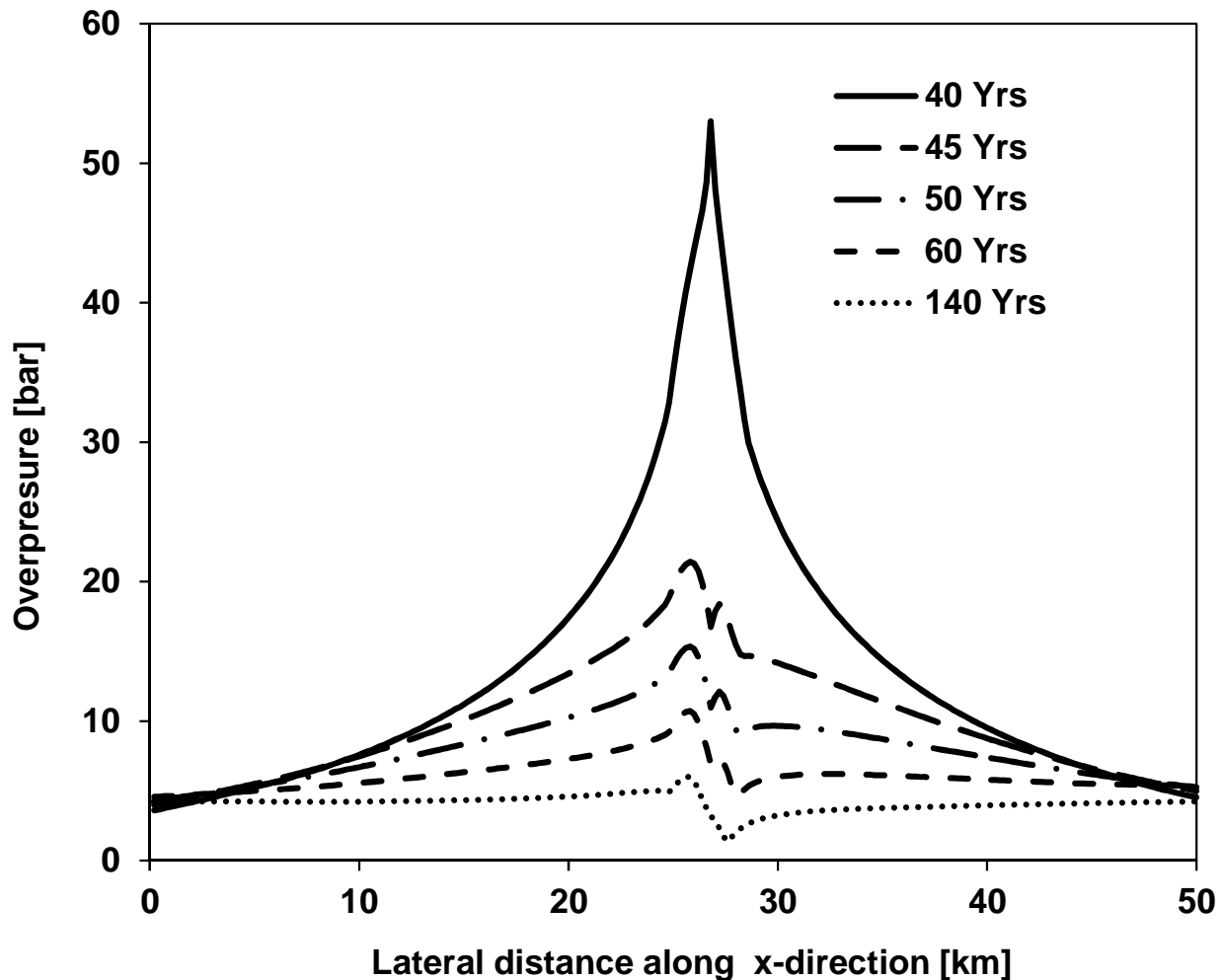
Figure 4.23 The overpressure development at after 40 years of 60 Mt of CO_2injection and 100 years after the stop of injection for the upper layer of Gassum reservoir. The irregularity in the profile peak is numerical artifacts due to the coarse grid used.

4.4.4.3 Permeability anisotropy

In our simulations have been used a permeability anisotropy of 0.1, which is a quite normal value for assumption about sub-grid cell layered heterogeneity. As our plug measurements for the shale gave a much smaller value of 0.02, we tested the effect of changing this anisotropy generally for the shale lithologies in the simulation. Figure 4.24 compares the result of overpressure development in the base of the caprock after 40 years of CO_2 injection for the measured vertical and horizontal permeability ratio of 0.02 and that of 0.1 used in these simulations. It is seen that using the k_v/k_h ratio of 0.1, the overpressure in the base of the Fjerritslev Formation is 10 bar higher than with a ratio of 0.02. It therefore has some importance to specify the k_v/k_h ratio of the lithology, or at least perform a sensitivity test when carrying out simulation studies for pressure development.
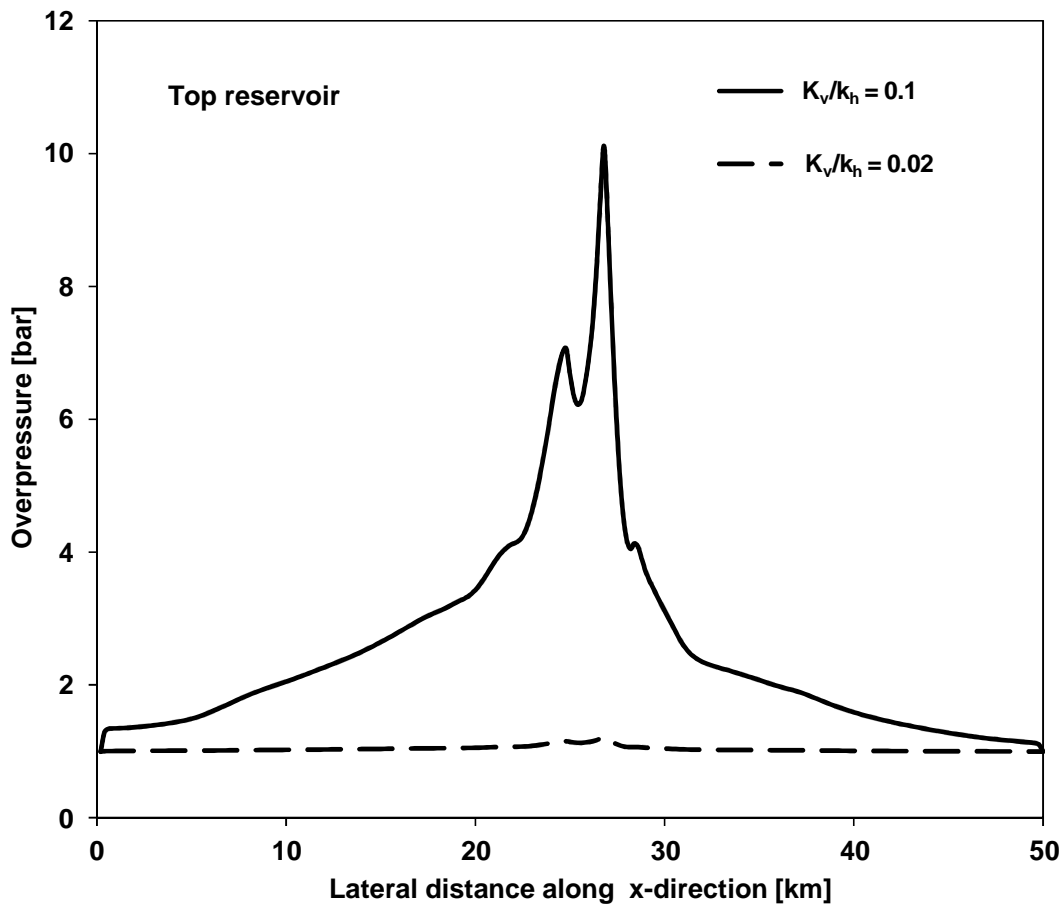
Figure 4.24 Comparison of the overpressure development in the base of the caprock after 40 years of 60 Mt of CO_2 injection for measured vertical and horizontal permeability ratio of 0.02 and the value of 0.1 used in these simulations. The irregularity in the profile peak is numerical artifacts due to the coarse grid used.

4.5 Conclusions

The influence of caprock compressibility and permeability and the consequences for pressure development have been studied for the Vedsted structure. These studies underscore the significance of obtaining valid experimental data for reservoir simulation studies. Laboratory experiments and dynamic sonic velocity data from relevant shale formations in Denmark show that shale compressibility is lower than often assumed for standard reservoir simulation studies and detailed laboratory work on this subjection is presented in the paper by Mbia et al. (2014a). The consequences of this low compressibility are investigated in a simulation case study. Laboratory measurements were carried out on centimeter-scale core plug samples from analog onshore wells. The experiments were performed under drained conditions. A series of uniaxially confined loading and unloading stress paths were applied to the in situ stress level to close up the induced unloading fractures. Static compressibility was determined from the loading and unloading stress paths. The loading experiments were undertaken with continuous ultrasonic recording of compressional and shear wave velocities. At reservoir conditions, dynamic compressibility is similar to the static compressibility at the beginning of the unloading stress path corresponding to elastic deformation. The analysis of both data sets indicates that Fjerritslev Formation compressibility is 0.5×10^{-5} bar^{-1} and is one order of magnitude lower than the standard value of 4.5×10^{-5} bar^{-1} normally used for shale compressibility in reservoir simulation studies.

The caprock permeability was measured by a geotechnical method of constant rate of strain (CRS) experiment and the result is compared with modeled permeability data for the same material. We found average vertical permeability of the Fjerritslev Formation (primary caprock) to be 0.1 μD.

The ECLIPSE 100 reservoir simulator has been used to investigate the effect of the measured caprock compressibility and permeability and the consequences for pressure buildup and transmission, vertically and laterally within the Vedsted structure. This has been evaluated when 60 Mt of CO_2 is injected into the Gassum Formation during 40 years.

The pressure buildup in the top of the storage formation is 5 bar higher for the measured caprock compressibility compared with the standard caprock compressibility normally used in reservoir simulation studies. This pressure difference can also play a significant role by increasing the magnitude of the overpressure in the shallower aquifers in the presence of permeable fractures and faults. Therefore well-designed investigations of formation properties are recommended when

carrying out reservoir simulation studies in order to minimize the risk of underestimating or overestimating pressure buildup in CO_2 storage sites.

The sensitivity of the pressure buildup and transmission for varying caprock permeability indicates that when increasing Fjerritslev Formation permeability from 0.1 µD to 1.0 µD, the overpressure could not be transmitted through the 530 m thick caprock, but by increasing further the permeability to 10 and 100 µD, overpressure is transmitted through the caprock and up to the Chalk Group. Reducing the caprock permeability by one or two orders of magnitude further reduces the vertical pressure buildup but increases lateral pressure buildup and the extent within the storage formation. It is also important to note that the ratio of vertical to horizontal permeability has some influence on the vertical pressure transmission.

5 Modelling of The Pressure Propagation due to CO_2 Injection and the Effect of Fault Permeability in a Case Study of the Vedsted Structure, Northern Denmark

5.1 Summary

Assessing the pressure buildup in CO_2 storage sites and especially the vertical propagation is vital for evaluation of site behavior and security. Vedsted structure in the Northern part of Jylland in Denmark consists of 290 m thick Gassum Formation at 2100 m depth forming the primary reservoir and is sealed by the 530 m thick Fjerritslev Formation which is mainly shale lithology with very low permeability. Overlying the caprock is a number of formations forming secondary reservoirs and seals including a 420 m thick Chalk Group which is overlain by 20 – 50 m Quaternary deposits. Seismic profiling of the structure shows the presence of northwest-southeast trending faults of which some originate in the upper layer of the Gassum reservoir and some reach the base Chalk Group layer. Two faults in the upper Gassum reservoir have been interpreted to be connected to the base Chalk Group. In order to evaluate potential risks associated with vertical pressure transmission via the faults through the caprock, a number of simulation cases have been run with various fault permeabilities spanning orders of magnitude to represent both the worst and best case scenarios. Fault rock permeability data were obtained from a literature study and range from 1000 mD (common in crystalline rock environment) for the worst case scenario down to 1.0 µD (common in sedimentary rock environment) for the best case scenario. The results show that after injecting 60 million tons (Mt) of CO_2 at a rate of 1.5 Mt/year for 40 years, overpressure is developed in the reservoir and about 5 bar is transmitted to the base Chalk Group for the 1000 mD fault permeability (worst) case, while for the 1.0 µD (best) case the pressure buildup is confined within the primary caprock. The results also show that, approximately 0.3 to 5.0 bar overpressure can be transmitted to the base Chalk Group when the fault permeability is above 1.0 mD.

5.2 Introduction

5.2.1 Background

Reservoir simulation was carried out as part of the subsurface characterization study of the prominent Carbon Capture and Storage (CCS) demonstration project in Vedsted site (Fig. 5.1) in the North Jylland region of Denmark. The study of the sensitivity of caprock (Fjerritslev Formation) permeability and compressibility on pressure development in the Gassum reservoir and both the vertical and lateral transmission was investigated by Mbia et al. (2014). The investigation using reservoir simulation shows that injection of 60 million tons (Mt) of supercritical CO_2 at rate of 1.5 Mt/yr for 40 years will cause overpressure buildup to about 55 bar in the storage formation. The overpressure was confined within the Gassum reservoir and the lower layer of the Fjerritslev caprock, and was not causing any overpressure in the overlying overburden layers during and after the end of injection period based on the measured caprock properties as input in the modelling. A possible route for vertical transmission of overpressure through the overburden layers via faults with high permeability is the subject of this study.

The tectonic history and evolution of the Danish Basin (Nielsen, 2003) involved the formation of some major fault zones (Børglum, Haldager and Fjerritslev faults) extending close to the Vedsted site from the Southeast to the Northwest of the Sorgenfrei–Tornquist Zone. The faults dip towards the Southwest except for the Fjerritslev fault that dips toward the Northeast of the Danish Basin as shown in Fig. 5.1. The Børglum and Fjerritslev faults are not of much concern because they appear to be outside the boundary of the Vedsted structure while the Haldager fault extends closer to the center of the structure and is of concern for the storage site evaluation. Although old 2D seismic data was available (acquired in the mid 90s), a new 2D seismic survey of the site was acquired in 2008. The 2D seismic database comprises 24 individual lines totaling about 220 line kilometers acquired and processed. The main objective of the structural interpretation and mapping based on the new seismic data is primarily to confirm the presence and size of the structural 4-way dip closure and the thickness variations of the primary reservoir of the Upper Triassic – Lower Jurassic Gassum Formation, and also the secondary reservoir in the Middle Jurassic Haldager Sand.

In addition the identification and mapping of faults, which potentially may crosscut seals, is an important issue. Four faults were mapped to reach from below and terminate at the base of the Chalk Group at 0.5 km depth below the surface. Five faults were mapped at the top of the Gassum

reservoir at about 2.0 km depth and two of these were interpreted to have a direct connection to the base Chalk Group faults as shown by the 2D seismic line in Fig. 1.
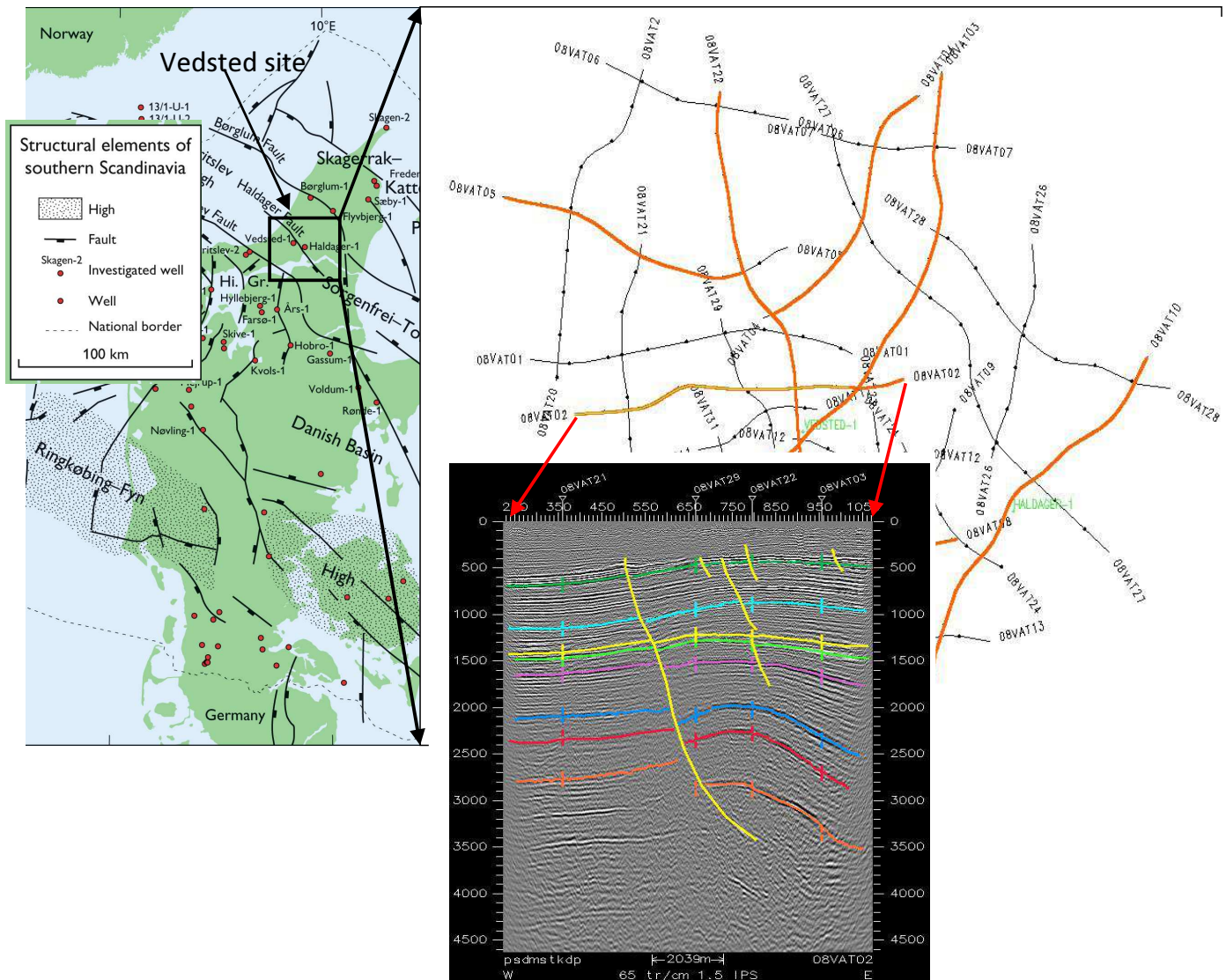
Fig. 5.1 Map showing the structural elements of the Norwegian-Danish basin modified from Nielsen (2003). The Vedsted site is zoomed to show location of key sections and line 08VAT02 is a 2D seismic line with interpretation that shows section across Northern part of Vedsted Structure. Colour code: Dark green is Base Chalk Group. Light blue is Top Frederikshavn Formation. Yellow is Top Haldager sand Formation. Light green is Base Haldager Sand Formation. Purple is Intra Fjerritslev Formation III member. Blue is near Top Gassum Formation. Red is near Top Skagerrak Formation. Orange is Intra Triassic marker. There exist minor extensional faults cutting the Base Chalk, but sole out in Lower Cretaceous.

The concern here is the environmental impact of large-scale pressure buildup in the storage formation (Gassum) and vertical transmission possibly causing brine displacement within the Chalk Group. This could ultimately lead to water table displacement and changes in the salt/fresh water

boundary residing in this layer. Our concern here is to investigate the possibility of vertical pressure transmission through these faults to the base Chalk Group which may cause ground water movement within the fresh water aquifer, although the latter subject is beyond the scope of this study.

5.2.2 CO_2 leakage and pressure transmission through caprocks

The long-term safety and viability of the commercial scale storage sites depend on the sealing capacity of and integrity of the caprock. The risks involving CO_2 storage have been associated with its leakage and pressure buildup and vertical transmission to the overburden layers. According to studies made by Song et al. (2013), there are a number of ways in which CO_2 can leak from the reservoir to the overburden. They include diffusive loss of dissolved gas through the caprock, leakage through the pore spaces after breakthrough pressure has been exceeded, leakage through faults or fractures, and well leakage. Leakage rates through faults or fracture networks are difficult to quantify whereas diffusive loss is usually considered to be low (Song et al., 2013). Leakage through faults in any site investigation should be addressed (IPCC, 2005) since this is one of the ways CO_2 can leak through the caprock.

5.2.3 Fault Modelling

Pre-existing or induced faults can act as both barriers and flow paths depending on the permeability of the fault zone. Fluid flow along faults can be inhibited by clay smears or shale gouges, cataclasis, and/or the cementation by authigenic minerals (Manzocchi et al., 1999). The fault is described as a zone with a particular thickness and shale content in a conceptual model. Fault transmissibility is decided by fault permeability and thickness, which depends on the geometry of the faults (fault surface and angle), fault deformation, fault pressure, and the mudstone packing of the faults. Estimation of the transmissibility is usually based on empirical data from the reservoir and outcrop samples and literature (Chang, 2007). When the fault is conductive and within the range of the CO_2 plume in the time considered, leakage may occur, leading to reduced sealing capacity. Chang and Bryant, (2007) set up a 2-D model with four different kinds of faults taken into consideration (declined-sealing, inclined-sealing, declined-conductive, and inclined-conductive) and found that there is a risk of leakage in both kinds of conductive faults and that this risk increases in inclined-conductive faults. Estublier and Lackner (2009) investigated the Snøhvit CO_2 storage in a multilayered reservoir model with faults and found that leakage would occur if a high permeability

fault were present. Similar results have been obtained in other recent modelling studies (Fornel et al., 2009; Oruganti et al., 2009).

Fracture density and faults are responsible for elevated permeability in naturally occurring rocks. Matrix permeability is found to be relatively low in shale rocks is 10^1 – 10^{-8} mD (Brace, 1980; Norton and Knapp, 1977) but much higher in fractured rocks. Fine-scale fracturing is closely related to faulting and the micro- and macro-fracture density increases significantly by at least an order of magnitude near faults (Anders and Wiltschko, 1994). It has been reported that over time spans of hundreds of years some hydrothermal mineral precipitation may occur in the fault zone thereby filling the fractures and void spaces and consequently decreasing the permeability (Anders and Wiltschko, 1994; Elders et al., 1979, 1984; Fournier, 1989; Rimstidt and Barnes, 1980; Sibson, 1987).

5.2.4 Fault permeability

The basic structural component in the faulting environment is the fracture (a surface across which the rock has broken and lost cohesion). Faulting may be composed of three architectural elements that include: the protolith (which is unfaulted, but may contain regional structures), the damage zone (which may contain small faults, fractures, fracture networks, and veins) and finally the core zone (which is composed of breccia and/ or fault gouge, in varying states of induration). The core zone is flanked by the damage zone and most of the displacement occurs in these zones. Various combinations and degrees of development of the damage and core zones yield a range of possible fault-zone architectures and permeability structures (Caine et al., 1996). Flow regimes in faulted sedimentary basins are strongly affected by differences in permeability of fault zones relative to their host rocks (Haneberg, 1995; Bredehoeft et al., 1992). Previous studies in hydrocarbon reservoirs have shown that individual fault zones may seal in some areas and leak in others, as a complex function of host-rock lithology, the deformation mechanisms operative during faulting, and fault zone diagenesis (e.g., Yielding et al., 1997; Smith, 1980). Fault zones are heterogeneous structures that cannot be simply defined as either barriers or conduits for fluid flow in either space or time (Caine et al., 1996; Knipe, 1993). The growing need for accurate simulation of subsurface fluid-flow regimes requires incorporating at least the bulk hydrologic properties of fault zones into numerical flow models (Rawling et al., 2001). Table 5.1 show permeability ranges (1 x 10^{-4} mD and 1600 mD) including values derived from different methods and materials, and from different scales

as described in the references for the clastic sedimentary systems. In this study we will vary the fault permeability in orders of magnitudes from 0.001 mD which is sealing to 1000 mD which is open. We will allow other bulk hydraulic and fluid properties of the fault zones to be the same as the host rock because we do not have additional information to guide possible variations.

Table 1 Fault permeability derived from different methods and materials, and from different scales as described in the references.

Fault permeability range (mD)	Locality/Fault rock type	Reference
9.0 – 1587	Crotone Basin, South Italy (Sandstone)	Balsamo and Storti 2011
8.0 – 145	Faulted siliciclastic aquifer in Central Texas	Nieto et al. 2012
$1.0 \times 10^{-2} – 1.0 \times 10^{2}$	Arbuckle reservoir in Kansas (Sandstone)	Franseen et al. 2003
$5 \times 10^{-2} – 1.0$	Restefond fault in Alpine foreland (Highly deformed sandstone lenses)	Leclère et al. 2012
$(0.1–200) \times 10^{-3}$	Middle Jurassic sandstone reservoirs in North Sea	Fisher and Knipe, 2001

5.3 Methodology

5.3.1 Model Setup and Parameters

5.3.1.1 Vedsted structure

The site model comprises the Gassum Formation as the primary reservoir and the full overburden including the Haldager Sand Formation forming a secondary reservoir in the saline aquifer. Figure 5.3 shows a map of the top reservoir layer with an x marked on the structure that can be described as a small elongate closure approximately 250 m high covering an area of about 31 km^2 and the depth to the top Gassum reservoir is about 1900 m below mean sea level.

The target reservoir layer is the 290 m thick Gassum Formation which is intercalated with low permeability shale sequences. The seal is the 530 m thick low permeability shale of the Fjerritslev Formation overlying the entire sequence constituting a flow barrier due to the high capillary entry pressure and very low permeability. The reservoir is underlain by the Skagerrak Formation with uncertain properties. Overlying the primary caprock is the Haldager Sand Formation forming an

overlying potential storage with excellent reservoir properties. This formation has a net thickness of about 80 m with porosity of about 17 % and permeability of 200–300 mD. The thickness of all overburden formations are presented in Table 5.2.

Table 2 Hydraulic properties of the formations in Vedsted site (Mbia et al. 2014). The measured k_v/k_h ratio is 0.02 but for simplification we have used ratio of 0.1 in ECLIPSE 100 corresponding to other lithologies given in the literature

Formation	Thickness	Compressibility	Permeability k_h	k_v/k_h	Porosity
	(m)	x 10^{-5} (bar^{-1})	(µD)		(%)
Post Chalk	30	4.5	5 x 10^3	0.1	23
Chalk	420	4.5	2 x 10^3	0.1	25
Vedsted	390	4.5	15 x 10^3	0.1	21
Frederickshavn (shale)	230	0.5	1	0.1	13
Børglum (shale)	50	0.5	1	0.1	13
Flyvbjerg (shale)	20	0.5	1	0.1	20
Haldager sand	80	4.5	267 x 10^3	0.1	17
Top Fjerritslev (shale)	174	0.5	1	0.1	11
Middle Fjerritslev (shale)	174	0.5	1	0.1	11
Base Fjerritslev (shale)	174	0.5	1	0.1	10
Top Gassum (sandstone)	64	4.5	63 x 10^3	0.1	19
Middle Gassum (shale)	47	0.5	1	0.1	9
Middle Gassum (shale)	47	0.5	1	0.1	9
Middle Gassum (shale)	47	0.5	1	0.1	9
Base Gassum (sandstone)	85	4.5	70 x 10^3	0.1	14
Skagerrak (sandstone)	331	4.5	20 x 10^3	0.1	14

1.0 D = 9.87 x 10^{-13} m^2 1 bar = 1 x 10^5 Pa

5.3.1.2 Grid geometry and block sizes

The model volume is 50 x 50 x 2.4 km^3 comprising the Gassum Formation which is the primary reservoir. The primary reservoir has been subdivided into 5 layers, including the upper sandstone layer which is about 64 m thick and the lower sandstone layer with a thickness of about 85 m. In

between the upper and the lower sandstone layers are three successive layers of shale with each having a thickness of about 47 m. The 530 m primary seal is subdivided into three equal layers. Overlying the primary caprock are series of secondary reservoirs and caprocks as shown in Table 5.2. The model consists of 250 grid blocks in the x-direction and 250 in the y-direction and a total of 19 layers with varying thicknesses in the z-direction, a total of about 1.2 million grid block cells are used in the simulation. In order to keep the fault model simple, we have digitized three connecting faults C1, C2 and C3 to represent the vertical connectivity. The simplified faults connect Gassum Formation (reservoir) vertically to the level of the Base Chalk Group at approximately 500 m depth, such that pressure can be transmitted to the Base Chalk Group during the injection period. Fig. 5.2 shows the schematic model with the three connecting faults as straight vertical corridors and these determine the direction of pressure propagation during the injection period. The three faults have the same width of about 0.2 km as the host grid block but with different lengths in the horizontal direction. Fault C1 is 5.2 km in length and extends Southward starting 2.4 km from the injection well. Faults C2 and C3 are 9.6 and 8.4 km in length, extending Northward starting 4.6 and 3.8 km from the injection well. In principle assigning different permeabilities to these fault block sizes will give the transmissivity of the faults in the simulator. The faults are thereby represented in the model as 200 m wide fault zones or damage zones with uniform permeability. This representation is of course severely simplified and results must be interpreted in this perspective.
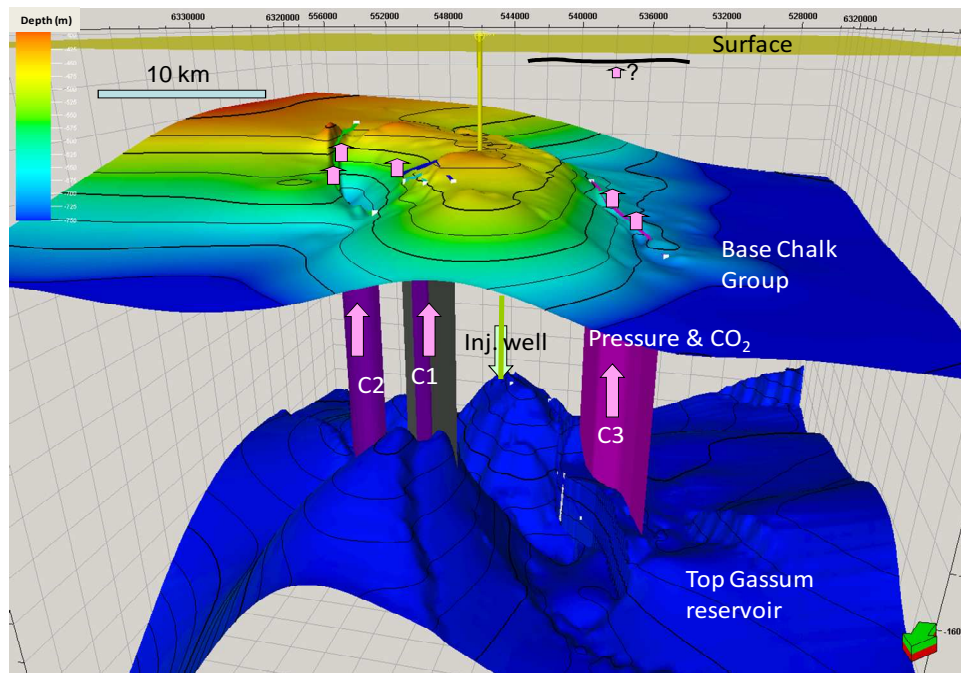

Fig. 2 *3D schematic model showing faults C1, C2 and C3 connecting top Gassum reservoir and Base Chalk Group. The purple arrows indicate the possible direction of pressure propagation along faults and the question mark indicate weather pressure will reach the surface or not.*

5.3.1.3 Model Parameters

In Table 5.2, we present the reservoir and the caprock properties of the various formations in the Vedsted structure. The storage capacity for CO_2 in this case depends not only on the compressibility, permeability and porosity of the Gassum Formation but also on the properties of the overlying Fjerritslev Formation. In this reservoir simulation, the boundary conditions for the site model have been modified to accommodate some of the lateral pressure transmission by using pore volume multipliers (factor 200) for the outmost cells in the model. The sensitivity study is based on varying the fault permeability from 1000 mD for the worst case scenario to about 1.0 µD for the best case scenario which covers the majority of the fault permeability data range available in the literature for sedimentary environments (Table 5.1). Fig. 5.3 shows a cross section of the Vedsted model with permeability distribution and only brine migration will occur through the faults. The porosity, permeability and compressibility of the caprock measured and the procedures and results are reported by Mbia et al. (2014a).
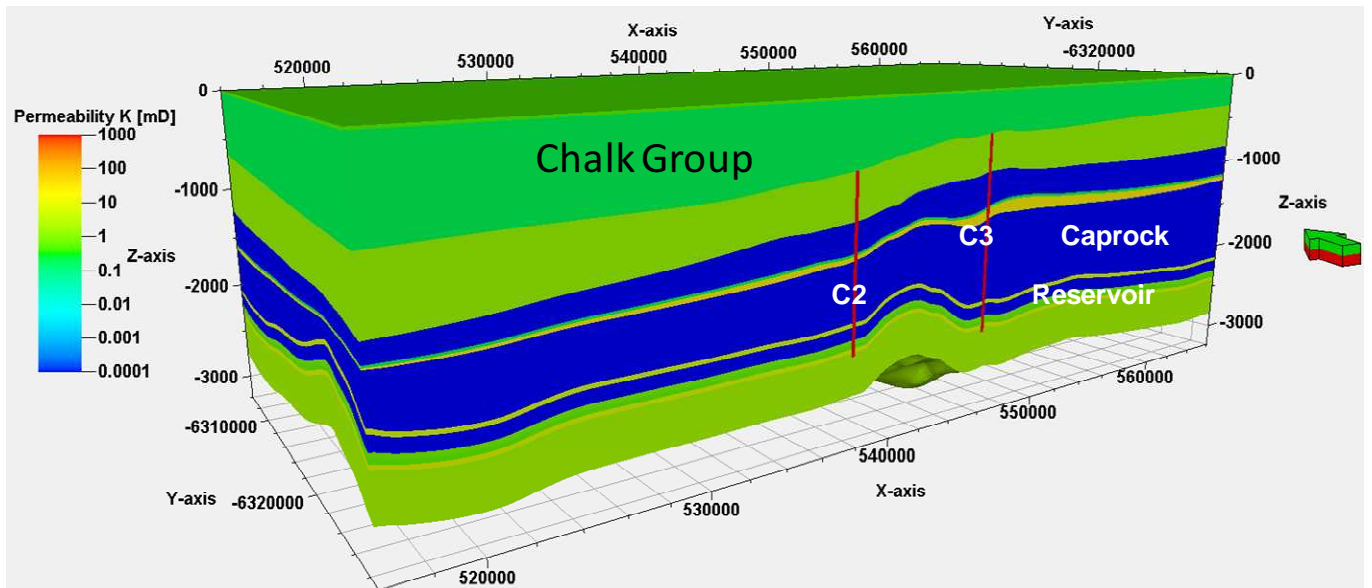
Figure 5.3 Cross section of Vedsted 3D model showing vertical permeability (k_h x 0.1) for each layer including that of the connecting faults.

The k_v/k_h ratio of vertical to horizontal permeability in the model used for all the formations including caprock for simplification is 0.1. The ratio for the fault rock is set to 1.0 reflecting uniform permeability. The ratio for the caprock formation has been measured for a single sample as 0.02 (Mbia et al. 2014a). Other initial formation and fluid parameters are assumed including a

hydrostatic pressure gradient of 100 bar/km, salinity of the formation water of 270 g/l, and a geothermal gradient of 30°/km. The PVT data including the formation volume factor, density and viscosity for the temperature of 66 ^{0}C for the Gassum reservoir are obtained from the commercial PVT software PVTsim (Calsep 2001). The brine density is calculated by the correlation of Rowe and Chow (1970). The brine viscosity is assumed to be independent of CO_2 content and pressure. It is calculated by the correlation of Batzle and Wang (1982). The value used is 0.8117 cp at T = 66 C (Gassum). The temperature at 1875 m (mid Gassum level) is estimated at 66 ^{0}C. The old data from the Vedsted-1 well, indicate that the brine is at 25% salinity which leads to a brine density of 1162.2 kg/m^3. Assuming hydrostatic pressure corresponding to this density leads to a Gassum datum pressure of 196 bar at the datum depth of 1724 m. As basis for the simulation the above reference pressure at reference reservoir (Gassum) depth is assumed for initialization. Based on that, the overpressure due to injection is extracted and illustrated.
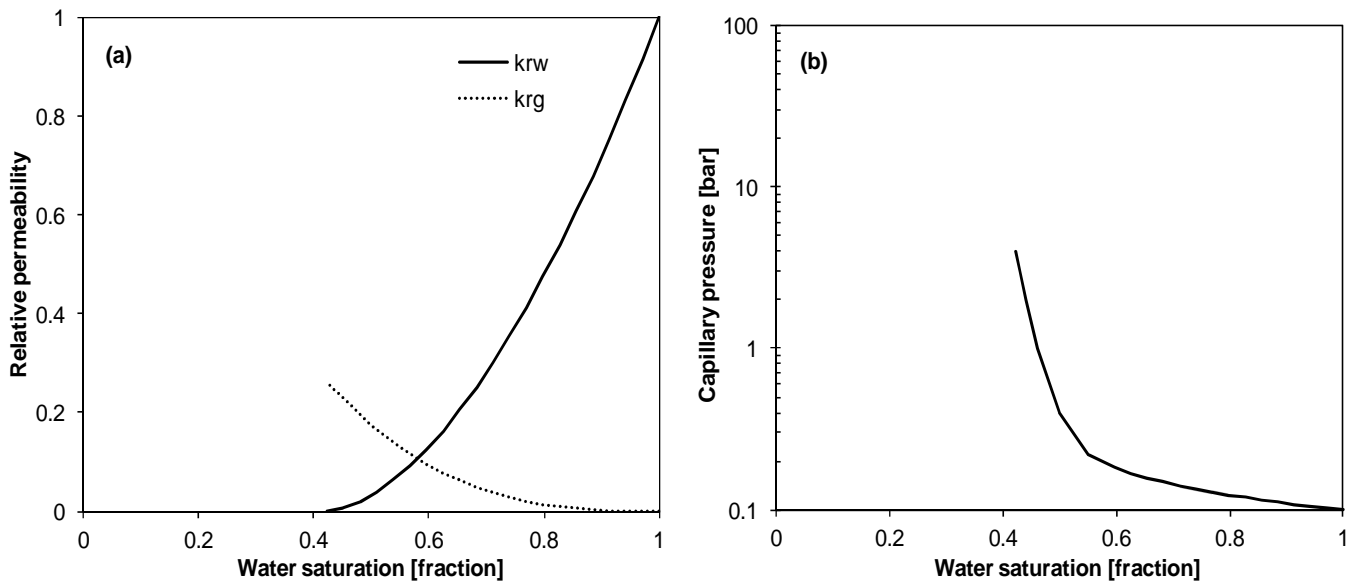
Figure 5.4 Plots of relative permeability and capillary pressure versus water saturation. a) and b) are based on sandstone data from Viking Formation (Bennion et al. 2006). a) was also used for shale while (b) for shale was scaled to an entry pressure of 6.5 bar corresponding to a permeability level of around 0.3 µD according to correlation established by Thomas et al. (1968).

The relative permeability function used for the simulation was inspired by the data shown by Bennion and Bachu (2006) for the Viking Formation sandstone, and was for simplicity used for both the sandstone and the shale lithology (Fig. 5.4a). The irreducible water saturation of 40% is used because using other values for irreducible water saturation and or saturation functions would only affect the CO_2 distribution, and probably not the more distant pressure propagation. The

application of Eclipse 100 for the CO_2-brine systems is obtained by using gas-oil phases to reflect the system, thereby using normal PVT descriptions for dissolution of CO_2 in the brine. Details on brine evaporation and halite precipitation are not included, as they are linked to only the near-well area under certain operating conditions.

The capillary pressure curve was established as a type curve for the sandstone with 0.1 bar capillary entry pressure (Fig. 5.4b). For the shale this curve was scaled to an entry pressure of 6.5 bar corresponding to a permeability level of around 0.3 µD according to correlation established by Thomas et al. (1968).

The compressibility of the fluids (CO_2 and water) is intrinsically taken into account in Schlumberger ECLIPSE 100 in terms of density variation with pressure. Eclipse 100 is Eclipse 100 is a black-oil simulator and a standard tool, well proven and used by the oil industry. It is based on finite differentiation of the relevant equations; that is it solves Darcy's law together with a generalised conservation equation (material balance). It is mainly applicable to three-phase and 3D fluid flow in porous media with cubic equation of state as shown by Holger et al. (2009).We simulated a rate controlled injection of 1.5 megatons (Mt) of CO_2 per year through a single vertical well in the Vedsted structure which is completed in the eastern side of the dome shaped anticline in the Gassum reservoir. The well is perforated through the whole reservoir section and the injection pressure is deemed sufficiently low not to supersede any fracturation limits. But since this is not the focus of our investigations, we have not supplied any details on fracturation pressure. 60 Mt of CO_2 was injected over a period of 40 years using the Eclipse 100 simulator tool. The aquifer was initially fully brine-saturated. The well is completed over full reservoir section, and CO_2 distributes in the layers according to permeability.

5.4 Simulation results and discussion

5.4.1 CO_2 plume and migration

Fig. 5.5 shows CO_2 saturation and distribution at the top layer of the Gassum reservoir for the 1000 mD fault permeability case, 40 years after injecting 60 Mt of supercritical CO_2. The CO_2 saturation and distribution for this case is similar to the other cases. For simplicity we have chosen to show only part of the reservoir section around the injection well where the plume is situated. The CO_2 front in the upper reservoir layer extends approximately 2.0 km from the injection well. The lateral

extension of the CO_2 plume for fault permeability of 1000 mD looks similar to the other cases. The plume spreads more in the upper layer of the reservoir compared to the bottom layer because of upward migration of the free CO_2 gas. The upward migration of the CO_2 is due to buoyancy and the lateral extension of the plume in the upper layer of the reservoir is due to the presence of the caprock with very low permeability confining all the CO_2 in the uppermost layer of the reservoir
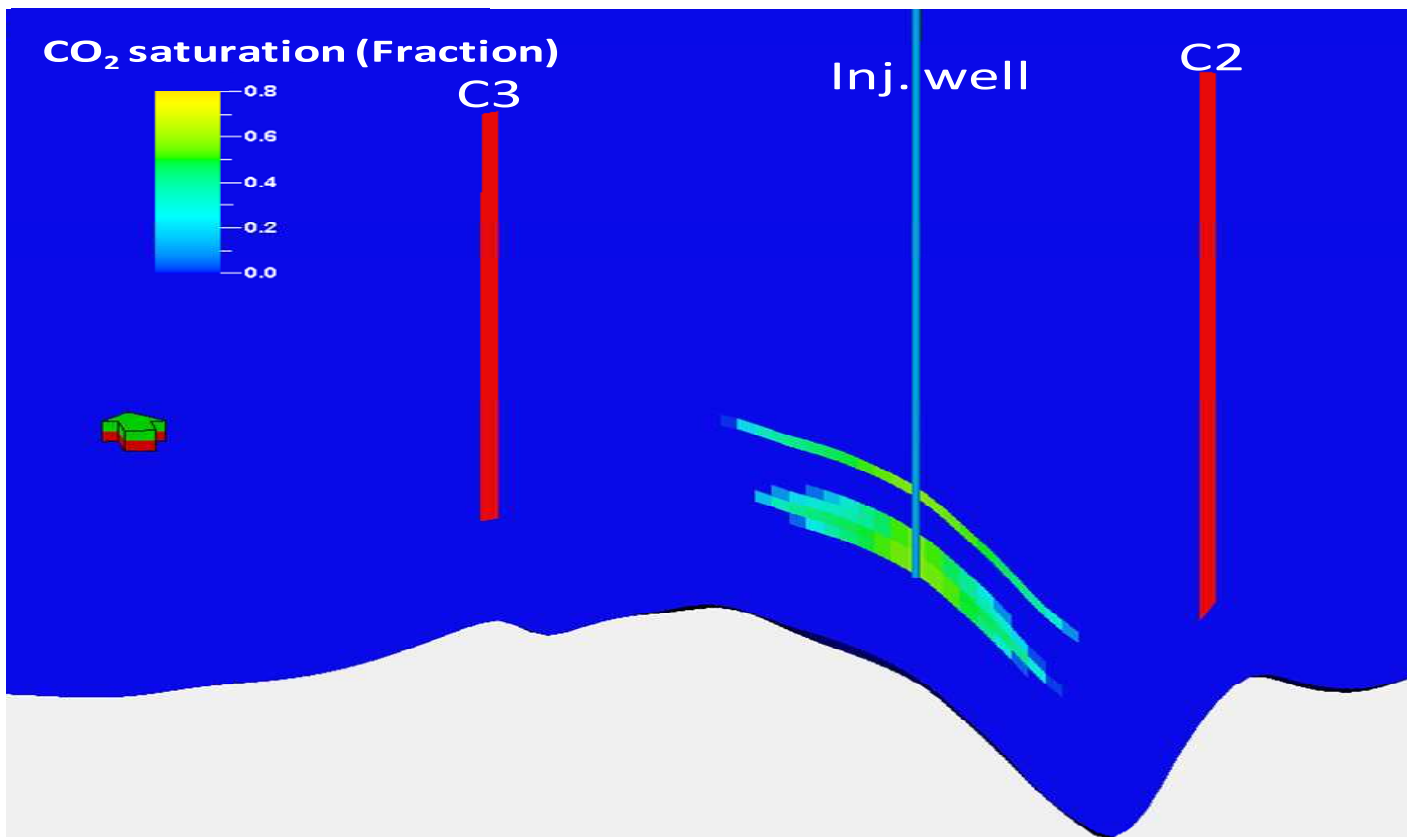
Fig. 5 *Cross section of the Vedsted structure showing gas saturation and migration of the CO_2 plume 40 years after injecting 60 Mt of CO_2 for the case of 1000 mD fault permeability. The CO_2 is injected in the full reservoir section and distributes according to permeability.*

5.4.2 Fault permeability and impact on vertical pressure development

Fig. 5.6 shows the cross section of the Vedsted structure and the resulting pressure development and propagation for the cases with different fault permeabilities 40 years after injecting 60 Mt of CO_2 into the Gassum Formation. Evaluating the effect of fault permeability on pressure buildup and vertical transmission as shown in the cross section, we can see that after the end of the injection period overpressure is transmitted beyond the Base Chalk Group to the surface. The overpressure transmission to the surface is seen for the case with fault permeability between 10 and1000 mD, as

we decrease fault permeability in orders of magnitude from 10 to 0.001 mD, vertical pressure propagation also reduces to the hydrostatic pressure above the primary caprock when fault permeability is smaller than 0.1 mD. It is important to note that cases with fault permeability above 10 mD in these simulations represent the worst case scenario because we are dealing with sedimentary rocks where the possibility of having faults with such high permeability may be small. Secondly the fact that the faults act as open conduits between the reservoir and the Base Chalk Group eases vertical pressure transmission without any obstacle as compared with the natural system where we have zones of different fault permeabilities which can limit vertical pressure transmission. Once overpressure is transmitted to the base of the Chalk Group at around 500 m depth, where the chalk matrix permeability is 2.0 mD, it is possible for the pressure to reach the surface through the low permeable matrix.
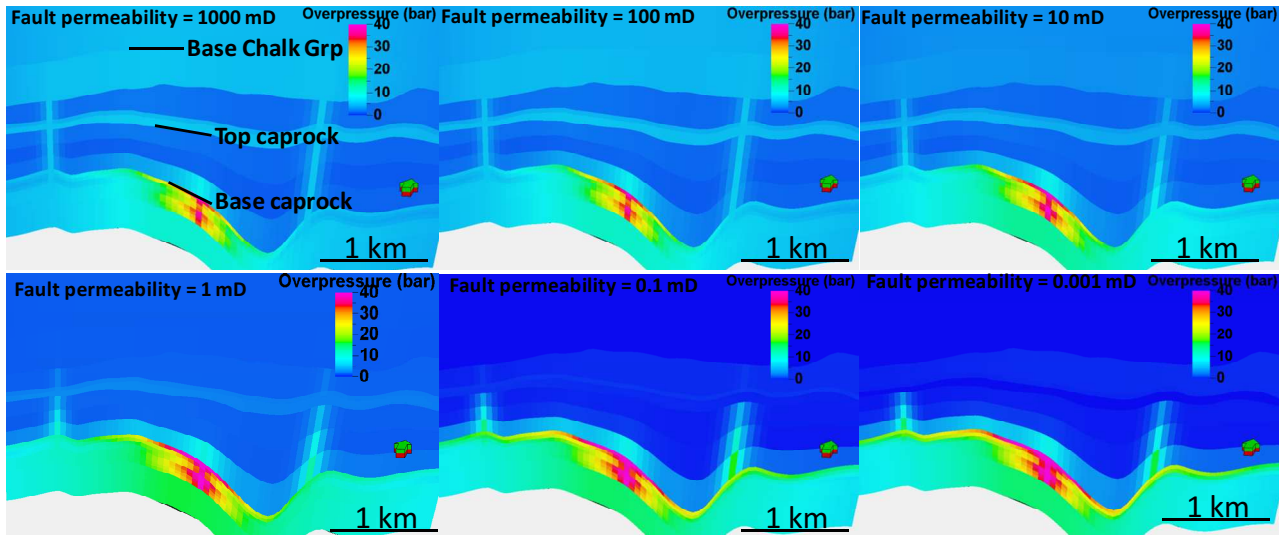
Figure 5.6 Cross sections of the Vedsted site within the injection well showing overpressure development (in bar) and transmission 40 years after injecting 60 Mt of CO_2 for cases with different fault permeability varied by several orders of magnitude covering the upper and lower range for possible fault permeabilities as reported in the literature data.

5.4.3 Fault permeability and impact lateral pressure development

Fig. 5.7 shows a map of the upper layer of the reservoir which is directly below the sealing layer. The result of the overpressure development and the extent of lateral transmission from the injection well 40 years after injecting 60 Mt of CO_2 is shown for cases with different fault permeabilities. Taking the worst case scenario with fault permeability 1000 mD, we can see that there is less pressure build-up around the injection well thereby resulting in less lateral extension. On the other hand the smaller fault permeability of 0.001mD resulted in a much higher pressure buildup around

the injection well and consequently leading to a larger lateral extension. This trend is seen as we decrease permeability by orders of magnitude from 1000 to 0.001 mD. Fig. 5.8 shows the overpressure profiles for the various fault permeability cases after the end of injection period. The overpressure in the top reservoir layers reaches 55 bar for the lowest 0.001 mD fault permeability case compared with 40 bar for the 1000 mD case.
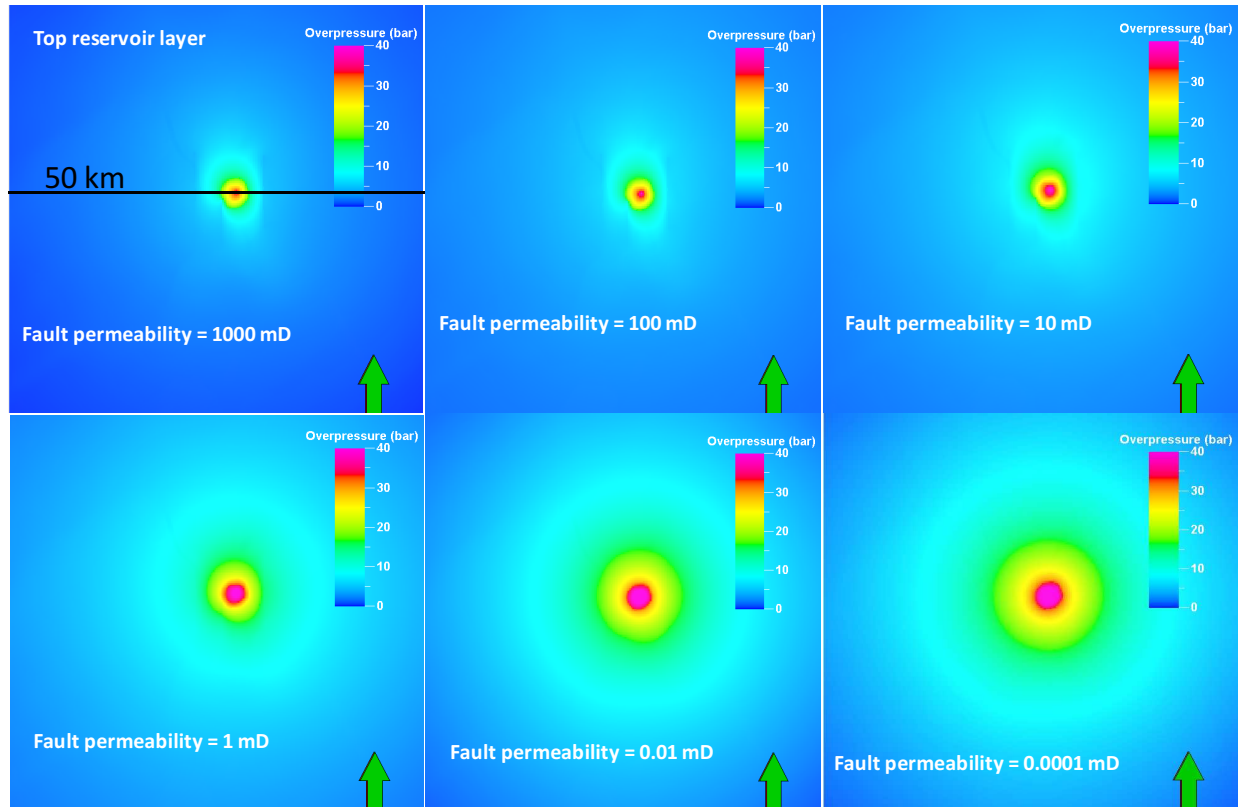
Figure 5.7 Map of the uppermost layer of the reservoir showing overpressure development (in bar) from injection well and the lateral transmission 40 years after injecting 60 Mt of CO_2 for cases with different fault permeability varied by orders of magnitude covering the upper and lower range for possible fault permeability as reported in the literature data.

This is explained with the CO_2 injection overpressure buildup in the reservoir being quickly transmitted into the overburden as it reaches the fault with higher permeability, but as we decrease fault permeability, the rate of vertical pressure transmission to the overburden is reduced, thereby causing overpressure around the injection well leading to larger lateral transmission in the reservoir layer. The choice of input for caprock compressibility can also affect the lateral pressure propagation in the reservoir slightly as has been shown (Mbia et al. 2014), but in this case this added effect has little influence on how pressure is transmitted via the faults.

Fig. 5.8 *Pressure profile in the uppermost layer of the reservoir showing overpressure development and lateral transmission r 40 years after injecting 60 Mt of CO_2 for the cases with different fault permeability.*

Analysis of the results based on the cross-sectional profiles (Fig. 9) indicates that overpressure buildup occurs in the top layer of the caprock in the cases with more than 1.0 mD fault permeability and up to 5 bar for the 1000 mD case. Overpressure is seen to develop in the Base Chalk Group at a depth of around 500 m for fault permeability above 1.0 mD. When permeability is lower than 1.0 mD no pressure buildup is observed. Analysis of the results based on the pressure profiles (Fig. 10) indicates that between 0.3 and 5.0 bar overpressure is observed in the Base Chalk Group for the 1.0 –1000 mD fault permeability cases.
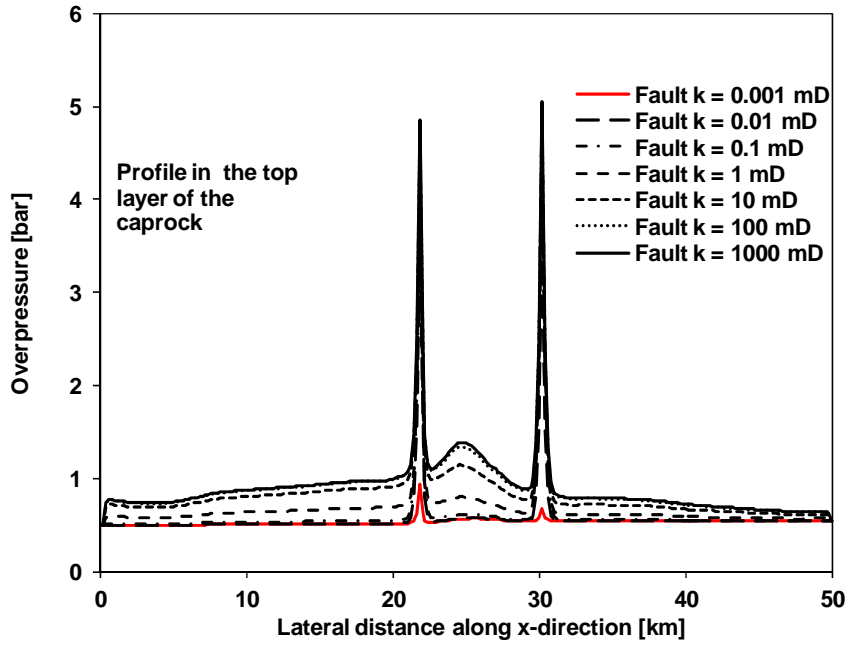
Fig. 5.9 *Pressure profile (Fig.8 for reference) in the upper layer of the caprock showing overpressure development and lateral transmission 40 years after injecting 60 Mt of CO_2 for the cases with different fault permeabilities.*

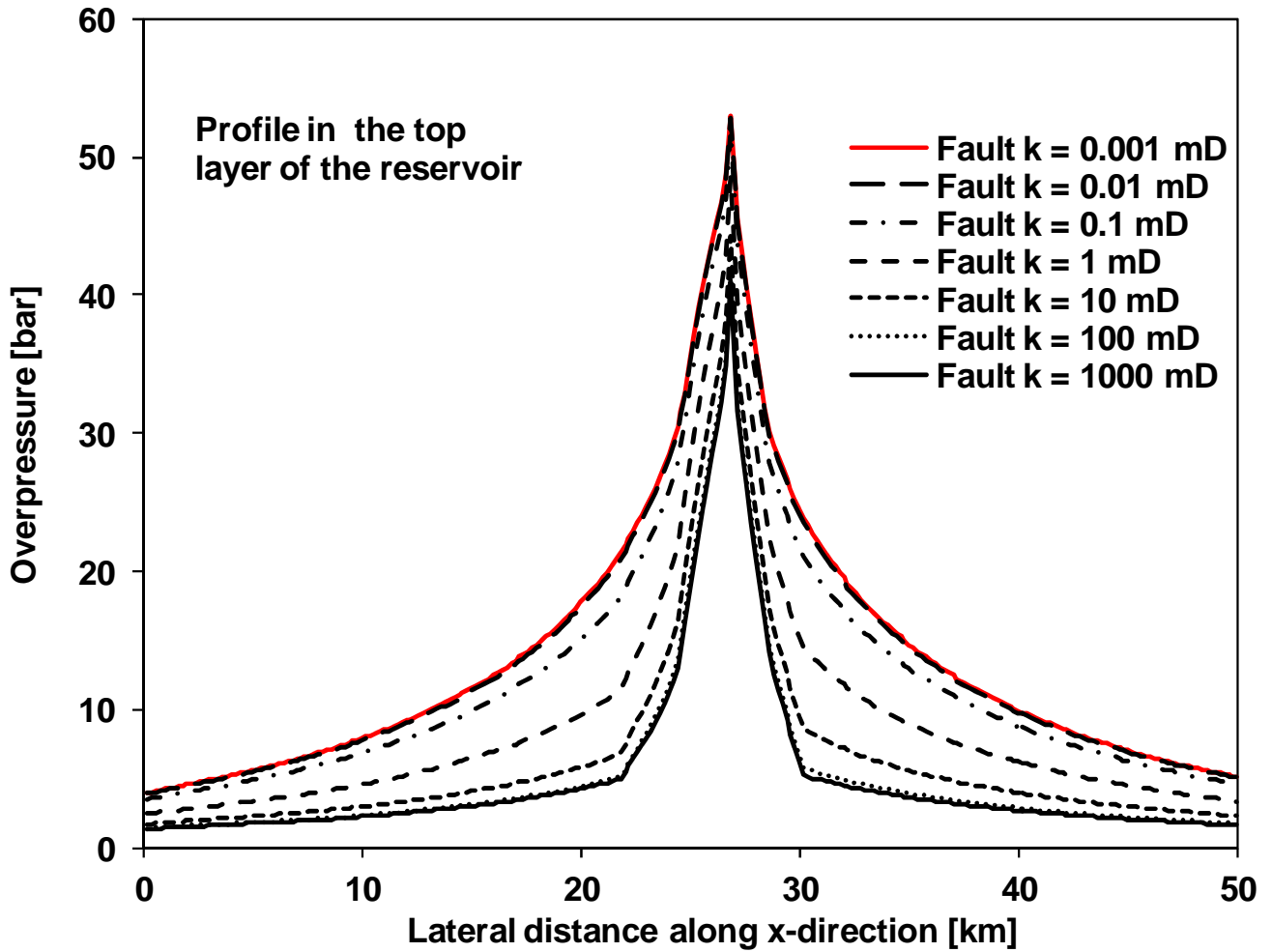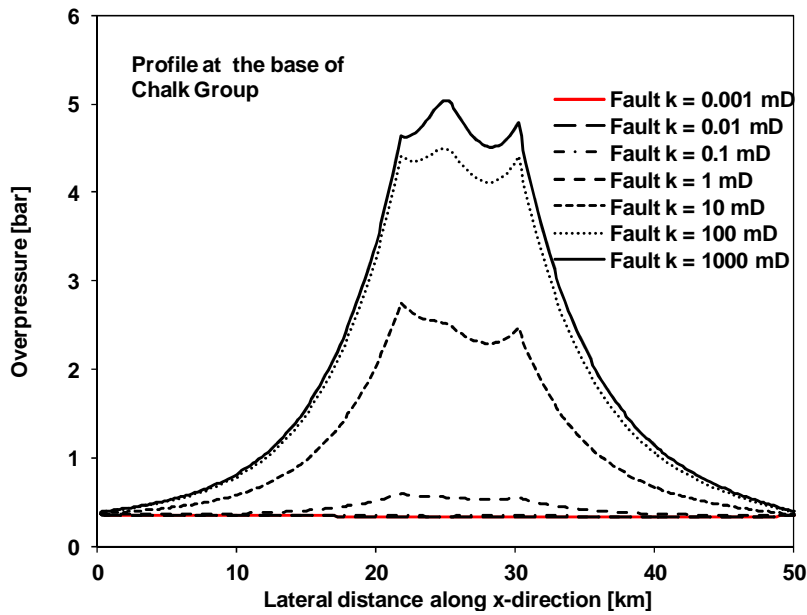***Fig. 5.10*** *Pressure profile in the base Chalk Group showing overpressure development and lateral transmission 40 years after injecting 60 Mt of CO_2 . Fault permeability above 1.0 mD will cause overpressure development in the Base Chalk Group.*

5.4.4 Permeability anisotropy

In the simulations permeability anisotropy of 0.1 is used for the reservoir and caprock system, which is a typical value to account for sub-grid cell layered heterogeneity. As our plug measurements for the shale gave a much smaller value of 0.02, we tested the effect of changing this anisotropy for the shale lithologies in the simulation as low as one order of magnitude (0.002) lower than the measured value (0.02).
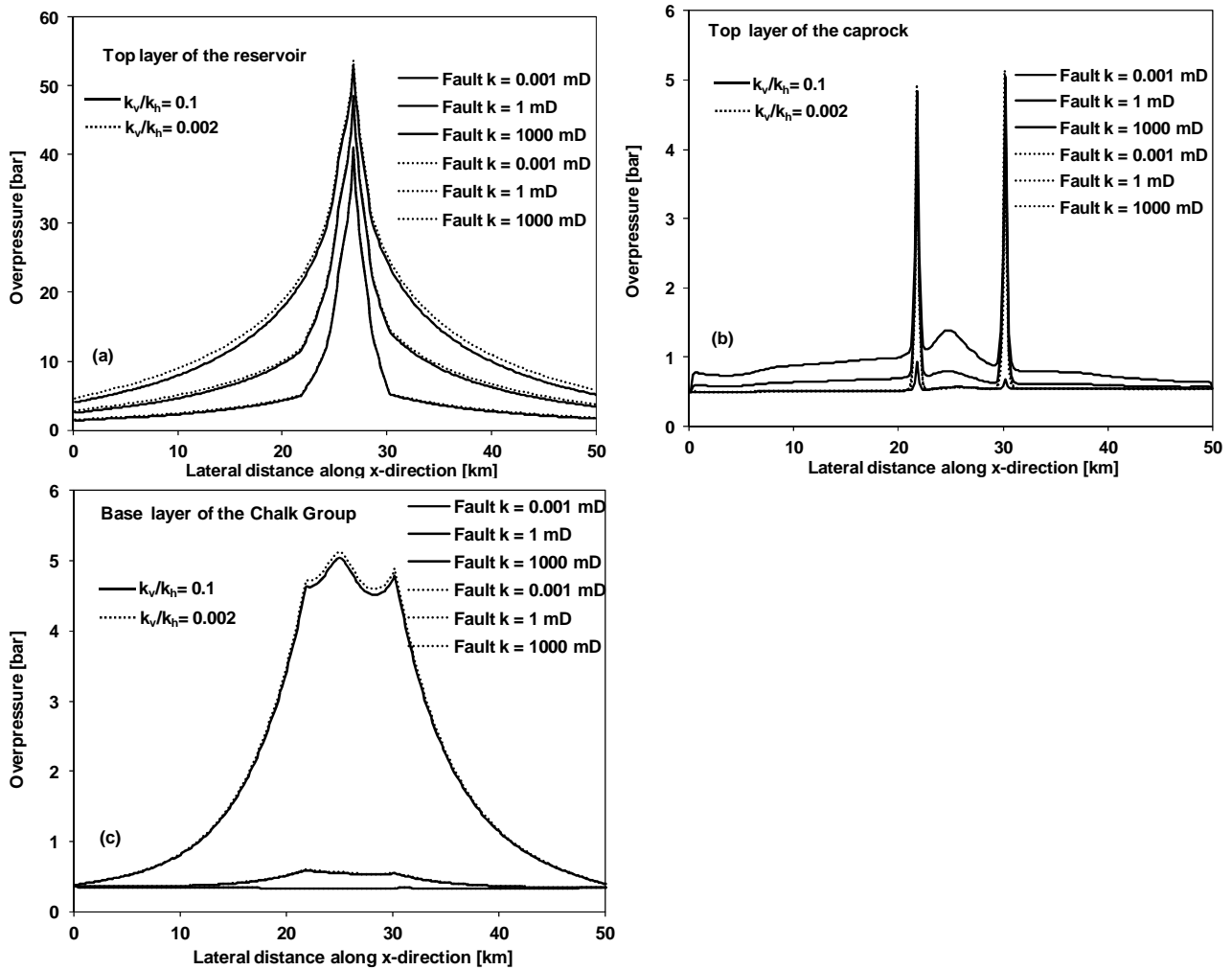
Figure 5.11 Overpressure development and lateral transmission 40 years after injecting 60 Mt of CO_2 for the case with k_v/k_h ratio of 0.002 and 0.1. a) is the pressure profile in the uppermost layer of the reservoir layer and b) and c) for the top caprock formation and base Chalk Group respectively.

Fig. 5.11 compares overpressure development in three layers of the reservoir model after 40 years of CO_2 injection for the vertical and horizontal permeability ratio for the shale layers of 0.002 and that of 0.1. It is seen that using the k_v/k_h ratio of 0.1, migration and distribution in the upper reservoir layer and the overpressure in the top Gassum and Fjerritslev formations and base Chalk

Group show no significant difference with a ratio of 0.002. It therefore implies that the k_v/k_h ratio used for the shale layers has very little effect on the pressure propagation which is in accordance with the results obtained by Mbia et al. (2014) in Fig. 5.11 where the difference in overpressure in the upper reservoir layer between 1.0 µD and 0.001 µD caprock permeability is less than 3 bar.

5.4.5 Pressure relaxation after shut -in

Fig. 5.12 shows the overpressure profile for the upper layer of the Gassum reservoir (5.12a), upper layer of the Fjerritslev Formation (5.12b) and base Chalk Group (12c) 40 years after CO2 injection (60 Mt) and for time-steps in the relaxation period up to100 years after the end of the injection period.

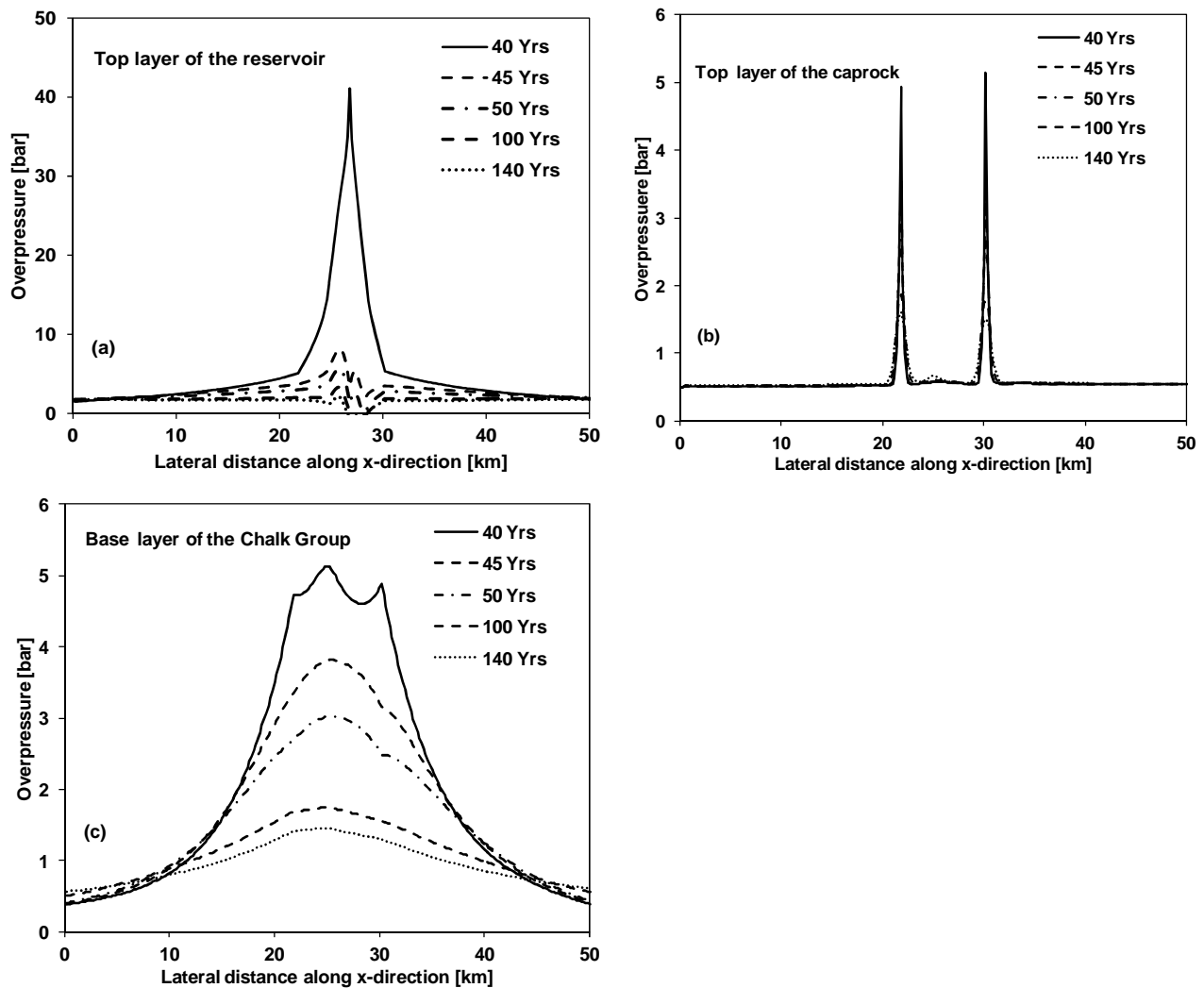*Figure 5.12 Overpressure development and lateral transmission 40 years after injecting 60 Mt of CO$_2$ and the corresponding relaxation times after the end of injection. a) is the pressure profile in the uppermost layer of the reservoir layer and b) and c) for the top caprock formation and base Chalk Group respectively.*

The case used fault permeability of 1000 mD in order to outline the maximum pressure change. At the year 40, the overpressure in the upper layer of the reservoir reaches up to 41 bar and 5 bar for the upper caprock layer and the base Chalk Group layer. This overpressure declines rapidly in the first 5 years after the end of injection to about 10 bar in the reservoir, and slowly in the upper caprock layer to about 2 bar and even more slowly in the base Chalk Group which shows only 1.0 bar reduction. 100 years after the end of the CO_2 injection in the Gassum reservoir the overpressure approaches hydrostatic pressure in the reservoir but is still at 1.5 and 1.0 bar in the upper caprock and base Chalk Group layer. As mentioned earlier the boundary conditions allow same degree of pressure relief at the model margins when the overpressure reaches the model boundary.

5.4.6 Gridding

The rather coarse grid representing the Vedsted model might have some effect on the simulation results and the illustration of various effects. The decision about gridding was guided by practical computation time for the work on sensitivity analysis requiring multiple simulation runs. We therefore examined the effect of grid resolution on a single example of a simulation run of pressure propagation and CO_2 plume migration in order to illustrate this effect. In a refined-grid model, the grid cells within a radius of 2.5 km around the injection well in the reservoir and the base caprock layers were vertically refined to 20 m grid cell thickness as shown in Fig. 5.13 (a). The result is compared with the coarse grid model used in this study (Fig. 5.13b) with vertical dimension for the grid cells of 125 m and above. We accept that a large grid block size will tend to overestimate the amount of CO_2 dissolution and consequently might underestimate the lateral extent of pressure buildup compared with the fine grid model version which can better capture a lateral pressure gradient which is much higher close to the well. We show the comparison of the results of the simulation by examining the amount of CO_2 migration in the reservoir at the base of the caprock at the end of injection at 40 years in Fig. 5.13 (a) and 5.13 (b). It is qualitatively illustrated that grid resolution has an effect on both the lateral and vertical extension of the CO_2 plume in the aquifer. The difference between the fine and coarse grid is seen in the extent of the plume. Fine grid resolution allows free CO_2 gas to migrate faster and further in the lateral direction than the coarse grid size model. In terms of overpressure propagation, there is no major difference in overpressure at the base of the caprock for the two cases. The effect of grid resolution on pressure was also reported by Pickup et al. (2010) and their simulation results also showed that grid resolution had

little effect on pressure buildup. In the near-well region in high salinity aquifers, the process of formation dry-out and possible clogging by salt precipitation can affect injectivity according to Pruess and Muller (2009), and they also concluded that coarse grids might be sufficient for initial assessment of storage potential.
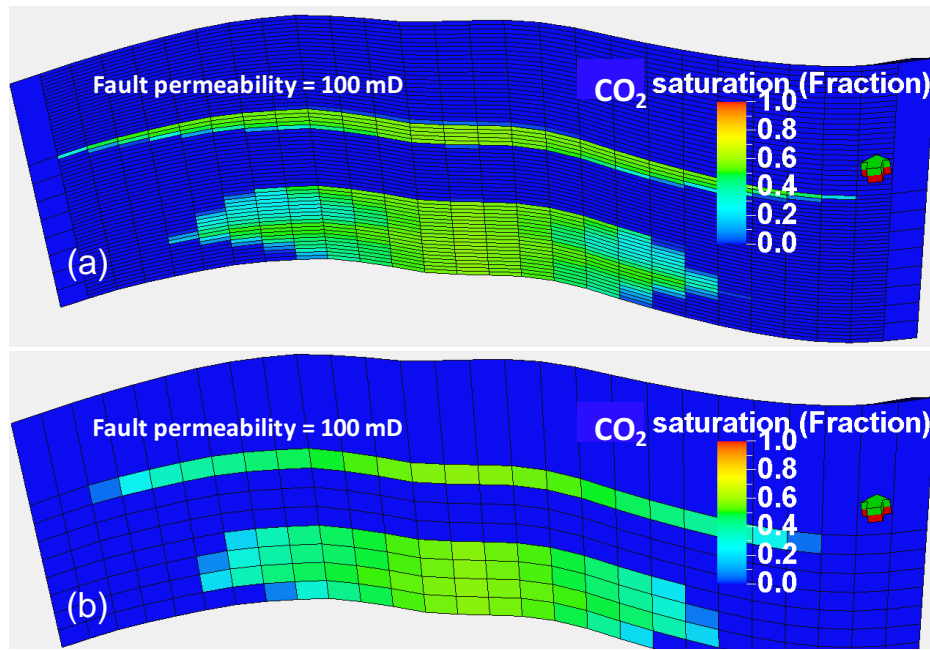
Figure 5.13 CO$_2$ saturation and migration for both finer and coarser grid resolution. a) is vertical grid refinement within the reservoir and the base caprock layers with each cell having vertical dimension of 20 m and the refinement extend within a radius of 2.5 km from the injection well. b) is the coarse grid model used in this study and each cell has vertical dimension of 125 m.

5.5 Conclusions

Based on a model case study we have investigated the dependence of pressure buildup in the reservoir and overburden on fault permeability. The study has simulated 40 years of injection of a total of 60 Mt of CO$_2$ and has assessed the possibility of pressure transmission to the overburden formations in the Vedsted structure. The investigation showed that, pressure buildup was confined within the base layer of the Fjerritslev caprock and there was no pressure buildup in the overburden formations based on the measured caprock compressibility and permeability in the absence of faults. These results are not presented in this paper but in the background section (Mbia et al. 2014)

Included in this model were three faults that connect the reservoir formation to the Base Chalk Group, the upper part of which hosts a fresh water aquifer. Literature data on fault permeability were gathered supplying an upper and a lower range of permeabilities. The simulation results showed that by changing fault permeability from 1000 mD, which represents the worst case scenario, pressure buildup is transmitted to the base Chalk Group (500 m depth) with about 5.0 bar overpressure. We used other fault permeability values (100, 10, 1, 0.1, and 0.001 mD) which span the range from the worst (open) to the best (sealing) case scenario and the results showed that between 0.5 and 5.0 bar overpressure is transmitted to the base Chalk Group.

We also briefly investigated the effect of permeability anisotropy, relaxation after the end of injection period and grid size on the CO_2 migration and the pressure propagation. We found that there is no significant difference in the results when we use k_v/k_h of 0.1or the value of 0.002. The maximum overpressure of 5.0 bar is seen in the base Chalk Group level and falls to about 1.2 bar 100 years after the end of the injection period. Fine and coarse grid resolution has not significant influence on pressure propagation in the model, but only affects allows the migration pattern of the free CO_2 gas in the injection area.

6.0 Concluding Remarks

The first aspect of this study has been to investigate and evaluate the petrophysical properties of Jurassic shales constituting the primary caprock lithology that seals deep Jurassic reservoirs. The evaluation is based on laboratory experiments and available logging data. The second aspect of this study is to use the measured shale data as input parameters to Jurassic caprocks for reservoir simulation study in order to investigate pressure development and propagation in Vedsted site due to industrial scale CO_2 storage. Pressure buildup and CO_2 leakage due to CO_2 storage are the imminent risks associated with storage sites which need to be evaluated because if these risks occur depending on the magnitude may lead to potential ground water movement and contamination within the affected site. The petrophysical properties of shale that have been studied to have significant influence on pressure transmission include permeability and compressibility. Shale permeability and compressibility depend on solid (mineralogy, grain density, cation exchange capacity etc) and reservoir properties (porosity, pore radius, etc, at in situ conditions.

The laboratory data of cuttings material obtained from shale sections in Skjold Flank-1 well of the Danish North Sea, supplemented with data from artificially consolidated samples of kaolinite and smectite. Equivalent pore radius can be calculated from porosity and specific surface of all samples. This forms a basis for predicting equivalent pore radius from logging data. Cuttings were used to establish empirical relationships between equivalent pore radius and elastic moduli. The relationships are independent of mineralogical composition and give a correlation coefficient (R^2) of 0.97 for bulk modulus and compressional modulus and a correlation coefficient of 0.85 for shear modulus based on 41 data points.

These empirical equations were used to predict equivalent pore radius from the elastic moduli calculated from sonic velocity and bulk density logs from the Skjold Flank-1. The predicted equivalent pore radius show an overall depth-wise decrease, but is highest in the lower part of the Cenozoic shale sections (20 nm) and decreases to 8 nm in the deeper Jurassic shale section. A relatively modest equivalent pore radius of around 15 nm in the youngest sediments is related to the relatively low porosity of these silty shales. The overall reduction in the equivalent pore radius with depth can be correlated with the changing mineralogical composition of the shale from smectite rich Cenozoic shale to illite rich Jurassic shale causing a decrease in specific surface.

The quantification of shale porosity, compressibility and permeability from independent methods has been made on core and cuttings material obtained from the Fjerritslev Formation (shale). Mineralogical analysis based on X-ray diffractometry (XRD) of forty two samples from onshore wells (Stenlille-2, -5 and Vedsted-1) and one offshore well (Skjold Flank-1) shows a clear trend in composition from the Northeast presently onshore of the Norwegian-Danish Basin where we encounter a gradient with more silty shale to less silty shale in the Southwest, offshore section of the Central Graben.

Porosity of Fjerritslev Formation was measured independently from three different methods (Helium porosimetry-mercury immersion, mercury injection capillary pressure and nuclear magnetic resonance) gave different results indicating that the stated shale porosity is dependent on the method used. The results indicate that a higher porosity is measured by nuclear magnetic resonance method (21%) and helium porosimetry-mercury immersion method (20%) than mercury injection capillary pressure method (11%) for the same samples. The mercury injection capillary pressure method measured the lowest porosity for the formation because mercury could not assess all the pores in shale due to their high specific surface area. The nuclear magnetic resonance method which is expected to give similar results to the helium porosimetry-mercury immersion method, recorded higher porosity probably due to contribution from unloading micro-cracks introduced due to core unloading and sample handling. The additional porosity from micro-cracks should be neglected in the total porosity from nuclear magnetic resonance data.

Laboratory measurements were carried out on centimeter-scale core plug samples from analog onshore wells. The experiments were performed under drained conditions. A series of uniaxially confined loading and unloading stress paths were applied to the in situ stress level to close up the induced unloading fractures. Static compressibility was determined from the loading and unloading stress paths. The loading experiments were undertaken with continuous ultrasonic recording of compressional and shear wave velocities. At reservoir conditions, dynamic compressibility is similar to the static compressibility at the beginning of the unloading stress path corresponding to elastic deformation. The analysis of both data sets indicates that Fjerritslev Formation compressibility is 0.5×10^{-5} bar^{-1}. The compressibility of this shale formation measured from core samples is smaller by a factor of 10 or more than previously published data on shale. The reason is probably that a too conservative procedure has been used for estimating shale compressibility in earlier studies.

Permeability for the same shale material may range from micro to nanodarcy value depending on the methodology used for the evaluation. We found that Kozeny's modelled permeability from the specific surface of the grains and equivalent pore radius (as modelled from elastic data) and from MICP-NMR data to fall in the same order of magnitude with measured permeability for shale rich in Kaolinite, but overestimates permeability by two to three orders of magnitudes for shale with high content of smectite. The empirical Yang and Aplin model gives good permeability estimate comparable to measured data for shales rich in smectite. This is probably because Yang and Aplin model was calibrated in London clay which is rich in smectite. It is therefore important that any model that is meant to estimate shale permeability should be calibrated on a large amount of data from both synthetic and natural shale samples. We also found that Biot's coefficient introduced in calculating shale permeability has a significant and systematic impact on shale permeability data.

The sensitivity of caprock compressibility and permeability and the consequences for pressure development in Vedsted site were investigated through reservoir simulation studies using Schlumberger ECLIPSE 100 reservoir simulator. The results are based on 40 years after injection of 60 Mt of supercritical CO_2 into the Gassum Formation at a rate of 1.5 Mt/year. The sensitivity of the caprock compressibility was evaluated and comparison made between the measured average value 0.5×10^{-5} bar^{-1} and the normally used standard value of 4.5×10^{-5} bar^{-1}. The overpressure difference in the top of the storage formation is 5 bar higher for the measured caprock compressibility compared with the standard caprock compressibility. This overpressure difference can also play a significant role by increasing the magnitude of the overpressure in the shallower aquifers in the presence of permeable fractures and faults. Therefore well-designed investigations of formation properties are recommended when carrying out reservoir simulation studies in order to minimize the risk of underestimating or overestimating pressure buildup in CO_2 storage sites. The sensitivity of the pressure buildup and transmission for varying caprock permeability indicates that when increasing Fjerritslev Formation permeability from 0.1 μD to 1.0 μD, the overpressure could not be transmitted through the 530 m thick caprock, but by increasing further the permeability to 10 and 100 μD, overpressure is transmitted through the caprock and up to the Chalk Group. Reducing the caprock permeability by one or two orders of magnitude further reduces the vertical pressure buildup but increases lateral pressure buildup and the extent within the storage formation. It is also important to note that the ratio of vertical to horizontal permeability has some influence on the vertical pressure transmission.

The evaluation of the sensitivity of the measured caprock compressibility and permeability data on pressure buildup and transmission results showed that overpressure in the reservoir could not be transmitted beyond the lower layer of the Fjerritslev Formation. These findings allowed us to investigate another potential risk that is associated with the Vedsted site, namely the identification and mapping of faults, which potentially may crosscut seals. Four faults were mapped to reach from below and terminate at the base of the Chalk Group at 0.5 km depth below the surface. Five faults were mapped at the top of the Gassum reservoir at about 2.0 km depth and two of these were interpreted to have a direct connection to the base Chalk Group faults as shown in 2D seismic line. In this study we used base simulation case and introduced the fault model. Included in the model were three faults that connect the reservoir formation to the Base Chalk Group, the upper part hosting a fresh water aquifer. Literature data on fault permeability were gathered supplying an upper and a lower range of permeabilities. The simulation results showed that by changing fault permeability from 1000 mD, which represents the worst case scenario, pressure buildup is transmitted to the base Chalk Group with about 5.0 bar overpressure. We used other fault permeability values (100, 10, 1, 0.1, and 0.001 mD) which span the range from the worst to the best case scenario and the results showed that between 0.5 and 5.0 bar overpressure is transmitted to the base Chalk Group.

We also briefly investigated the effect of permeability anisotropy, relaxation after the end of injection period and grid size on the CO_2 migration and the pressure propagation. We found that there is no significant difference in the results when we use k_v/k_h of 0.1 or the value of 0.02. The maximum overpressure of 5.0 bar is seen in the base Chalk Group level and falls to about 1.2 bar 100 years after the end of the injection period. Fine grid resolution allows free CO_2 gas to migrate slightly further in the lateral direction than in the coarse grid model.

7 Recommendations for Future Work

The following recommendation are made for future work

- ➢ Simulation study of the Vedsted site in order to investigate the sensitivity of the overpressure to the ground water movement in the base Chalk Group layer.
- ➢ Investigation of the possibility of CO_2 leakage through the wells and faults is also important for Vedsted site qualification.
- ➢ Additional laboratory measurements from independent methods to quantify the compressibility and permeability of the secondary caprocks in the Vedsted structure can be interesting in future simulation study of the site.
- ➢ Experimental study on samples from the Haldager fault zone in order to have site specific data for the fault permeability can also be of interest in the site evaluation.
- ➢ Couple fluid flow, geomechanical simulations in 3-D reservoir modelling of CO_2 storage in Vedsted structure can also be very informative and interesting.
- ➢ Fracture tests of the Fjerritslev Formation at reservoir conditions can be give information on the fracture pressure which is also of interest to site.

8 List of references

Alam, M. M., Fabricius, I. L. & Christensen, H. F. 2012. Static and dynamic effective stress coefficient of chalk. Geophysics, 77, 1–11.

Alam, M., 2011. Rock physical aspects of CO_2 injection in chalk. PhD thesis submitted to the Department of Environment and Resources, Technical University of Denmark.

Anders, M.H., Wiltschko, D.V., 1994. Microfracturing, pale-ostress and the growth of faults. J. Struct. Geol. 16, 795–815.

Anderson, M. A. & Jones, F. O. 1985. A comparison of hydrostatic stress and uniaxial strain pore volume compressibilities using nonlinear elastic theory. Proceedings of the 26th US Symposium on Rock Mechanics, 403–410.

Andsbjerg, J., Nielsen, L.H., Johannessen, P. & Dybkjær, K. 2001. Divergent development of depositional environments in the Danish Central Graben and the Norwegian–Danish Basin following the Jurassic North Sea Doming event. In: Martinsen, O.J. & Dreyer, T. (eds): Sedimentary environments offshore Norway – Palaeozoic to Recent. Norwegian Petroleum Society (NPF) Special Publication 10, 175–197.

Armitage, P.J., Faulkner, D.R., Worden, R.H., Aplin, A.C., Butcher, A.R., Iliffe, J., 2011. Experimental measurement of, and controls on, permeability and permeability anisotropy of caprocks from the CO_2 storage project at the Krechba Field, Algeria. Journal of Geophysical Research 116, p 18.

Balsamo, F. and Storti, F., 2011. Size-dependent comminution, tectonic mixing, and sealing behavior of a "structurally oversimplified" fault zone in poorly lithified sands: Evidence for a coseismic rupture? Geological Society of America Bulletin; 123, no. 3-4; 601-619.

Bennion, D.B., Bachu, S., 2006. Supercritical CO2and H2S – brine drainage and imbibition relative permeability relationships for inter-granular sandstone and carbonate formations. In: SPE Europec/EAGE Annual Conference and Exhibition, Vienna, Austria, 12–15 June.

Berg, R. R. & Habeck, M. F.1982. Abnormal pressures in the lower Vicksburg, McAllen ranch fields, south Texas, Trans. Gulf Coast Association of Geological Society, 32, 247– 253.

Berg, R.R., 1975. Capillary pressures in stratigraphic traps. AAPG Bulletin 59,939–956.

Bergman, M., Winter, E.M., 1995. Disposal of carbon dioxide in aquifers in the U.S. Energy Convers. Manage. 36, 523–526.

Best, M. E. and Katsube, T. J. 1995. Shale permeability and its significance in hydrocarbon exploration. The Leading Edge, March, 1995, 65–170.

Bigelow, E. L. 1994. Global occurrences of abnormal pressures, in Studies in Abnormal Pressures, edited by Fertl, W. H., Chapman, R. E. and Hotz, R. E. Elsevier Science, New York , pp. 1 – 17,.

Biot, M. A. 1941. General theory of three-dimensional consolidation. Journal of Applied Physics, 12, 155–164

Biot, M. A. 1956a. Theory of propagation of elastic waves in a fluid-saturated porous solid: I. Low-frequency range: The Journal of the Acoustical Society of America, 28, 168–178.

Birkholzer, J. T., Zhou, Q., Tsang C. F. 2009. Large-scale impact of CO_2 storage in deep saline aquifers: A sensitivity study on pressure response in stratified systems. International Journal of Greenhouse Gas control, 3, 181–194.

Birkholzer, J.T., Zhou, Q., 2009. Basin-scale hydrogeologic impacts of CO_2 storage capacity and regulatory implications. International Journal of Greenhouse Gas Control 3 (6), 745–756.

Bjørlykke, K., 1998. Clay mineral diagenesis in sedimentary basins; a key to the prediction of rock properties; examples from the North Sea Basin. Clay minerals. 33, 15-34.

Borre, M. & I. L. Fabricius, 1998. Chemical and mechanical processes during burial diagenesis of chalk: An interpretation based on specific surface data of deep-sea sediments, Sedimentology, 45, 755–769

Brace, W.F., 1980. Permeability of crystalline and argillaceous rocks, Int. J. Rock Mech. Mining Sci., in press, 1980.

Bradley, J.S., 1975. Abnormal formation pressure. AAPG Bulletin 59, 957–973.

Bredehoeft, J. D., Neuzil, C. E. and Milly, P. C. D. 1983. Regional flow in the Dakota aquifer - A study of the role of confining layers. U.S. Geological Survey Water0 Supply Pap. 2237, 45 pp.

Bredehoeft, J.D., Belitz, K., and Sharp-Hansen, S., 1992. The hydrodynamics of the Bighorn Basin: A study of the role of faults: American Association of Petroleum Geologists Bulletin, 76, 530–546.

Bredehoeft, J.D., Hanshaw, B.B., 1968. On the maintenance of anomalous fluid pressures: I. Thick sedimentary sequences. Geological Society of America Bulletin 79, 1097–1106.

Bredehoeft, J.D., Neuzil, C.E., Milly, P.C.D., U.S. Geological Survey Water Supply Paper 2237 1983. Regional flow in the Dakota aquifer – a study of the role of confining layers. P, 45.

Brunauer, S., Emmett, P. H. & Teller, E., 1938. Adsorption of gases in multimolecular layers. Journal of the American Chemical Society. 60, 309–319.

Buscheck, T.A., Chen, M., Sun, Y., Hao, Y., Elliot, T.R., 2012. Two-stage, integrated, geothermal-CO_2storage reservoirs: an approach for sustainable energy production, CO_2-sequestration security, and reduced environmental risk. Lawrence Livermore National Laboratory, Contract DE-AC52-07NA27344.

Caine, J.S., Evans, J.P., and Forster, C.B., 1996. Fault zone architecture and permeability structure: Geology, 24, 1025–1028.

Chalbaud, C., Robin, M., Lombard, J.-M., Bertin, H., and Egermann, P. 2010. Brine/CO_2 Interfacial Properties and Effects on CO_2 Storage in Deep Saline Aquifers. Oil & Gas Science and Technology – Rev. IFP, 65, 541–555.

Chang, K. W., 2007. A simulation study of injected CO_2 migration in the faulted reservoir. Ph.D Dissertation, the University of Texas at Austin, 2007.

Chang, K. W., Bryant, S. L., 2007. Dynamics of CO_2 plumes encountering a fault in a reservoir. In Procedings of the National Energy Technology Laboratory 6th Annual Conference on Carbon Capture and Sequestration, Pittsburgh, PA, 2007.

Chapman, R. E. 1972. Clays with abnormal interstitial fluid pressures. American Association Petroleum Geology Bulletin, 56, 790–795.

Chapman, R. E. 1994. The geology of abnormal pore pressures, in Studies in Abnormal Pressures, edited by Fertl, W. H., Chapman, R. E. and Hotz, R. E. Elsevier Science., New York pp. 19–49.

Chenevert, M. E. and Sharma, A. K. 1991. Permeability and effective pore pressure of shale. Proc. SPE/IADC Drill. Conf., SPE/IADC 21918. Amsterdam, the Netherlands, 11–14 March, 1991.

Cheng, C.H. & Johnston, D .H. 1981. Dynamic and static moduli. Geophysical Research Letters, 8, 39–42.

Chester, F.M., Evans, J.P., and Biegel, R.L., 1993. Internal structure and weakening mechanisms of the San Andreas Fault: Journal of Geophysical Research, 98, 771–786.

Christensen, N. P., Dirschauer, W., Gortz, S., 2012. Carbon capture and storage – a pragmatic way to reduce CO_2 emissions. Energy and Environment 23 (2 & 3).

Chu, C.L., Wang, C.Y., Lin, W., 1981. Permeability and frictional properties of San Andreas fault gouges. Geophysicla Research Letters, 8, 565–568.

Coates, G. R., Xiao, L., & Prammer, M.G. 1999. NMR Logging: Principles and Applications. Halliburton Energy Services, Houston. P, 234.

Colten-Bradley, V. A., 1987. Role of pressure in smectite dehydration-Effects on geopressure and smectite-illite transformation. American Association of Petroleum Geology. 71, 1414–1427.

Cui, X., Bustin, M. M. A. and Bustin, M. R. 2009. Measurements of gas permeability and diffusivity of tight reservoir rocks: different approaches and their applications. Geofluids, 9, no. 3, 208–223.

Daigle, H., and Dugan, B. 2009. Extending NMR data for permeability estimation in fine-grained sediments. Marine and Petroleum Geology, 26, 1419–1427.

Daigle, H., and Dugan, B. 2011. An improved technique for computing permeability from NMR measurements in mudstones. Journal of Geophysical Research, 116, p, 14.

Darcy, H. 1856. Les fontaines publiques de la ville de Dijon: Paris, Dalmont, p, 647.

Darvish, G. R., Lindeberg, E., Holt, T., and Utne, S. A., 2006. Laboratory Experiments of Tertiary CO_2 injection into a fractured core Paper SPE 99649 presented at the 2006 SPE/DOE Symposium on Improved Oil Recovery in Tulsa, Oklahoma, U.S.A., 22–26 April (2006)

David, E. C., Brantut, N., Schubnel, A., and Zimmerman R. W. 2012. Sliding crack model for nonlinearity and hysteresis in the uniaxial stress-strain curve of rock". International Journal of Rock Mechanics, 52, p, 9–17.

Deming, D., 1994. Factors necessary to define a pressure seal. AAPG Bulletin 78, 1005–1009.

Dewhurst, D. N., and Siggins, F. A. 2006. Impact of fabric, microcracks and stress field on shale anisotropy. Geophys. J. Int., 165, 135 –148.

Dewhurst, D.N., Aplin, A.C., Sarda, J.P., 1999. Influence of clay fraction on pore-scale properties and hydraulic conductivity of experimentally compacted mudstones. Journal of Geophysical Research 104 (29), 261–329.

Dewhurst, D.N., Aplin, A.C., Sarda, J.P., Yang, Y., 1998. Compaction driven evolution of porosity and permeability in natural mudstones: an experimental study. Journal of Geophysical Research 103, 651–661.

Diamond, S. 1970. Pore size distribution in clays. Clays and Clay Mineralogy, 18, 7–23.

Dickey, P.A., Shriram, C.R., Paine, W.R., 1968. Abnormal pressures in deep wells of southwestern Louisiana. Science 160, 609–615.

Dickinson, G., 1953. Geological aspects of abnormal reservoir pressures in Gulf Coast Louisiana. American Association Petroleum Geology Bulletin 37, 410–432.

Dypvik, H., 1983. Clay mineral transformations in Tertiary and Mesozoic sediments from the North Sea. American Association of Petroleum Geosciences. 67, 160-165

Dzevanshir, R.D., Buryakovskiy, L.A., Chilingarian, G.V., 1986. Simple quantitative evaluation of porosity of argillaceous sediments at various depths of burial. Sedimentary Geology 46, 169–175.

Elders, W.A., Bird, D.K., Williams, A.E., Schiffman, P., 1984. Hydrothermal flow regime and magmatic heat source of the Cerro Prieto geothermal system, Baja California, Mexico. Geothermics 13, 27–47.

Elders, W.A., Hoagland, J.R., McDowell, S.D., Cobo, J. M. 1979. Hydrothermal mineral zones in the geothermal reservoir of Cerro Prieto. Geothermics 8, 201–209.

Estublier, A., Lackner, A. S., 2009. Long-term of the Snøhvit CO_2 storage. Energy Procedia, 1, 3221–3228.

Evans, J.P., Forster, C.B., and Goddard, J.V., 1997. Permeability of fault related rocks, and implications for hydraulic structure of fault zones: Journal of Structural Geology, 19, 1393–1404.

Fabricius, I. L, Røgen, B. & Gommesen, L., 2007. How depositional texture and diagenesis control petrophysical and elastic properties of samples from five North Sea chalk fields. Petroleum Geoscience, 13, 81–95.

Fabricius, I. L. 2011. Relationship between Elastic Moduli and Pore Radius in Clay Aggregates. 73rd EAGE Conference & Exhibition incorporating SPE EUROPEC 2011 Vienna, Austria, 23–26 May 2011.

Faulkner, D. R., and Rutter, E. H. 2000. Comparisons of water and argon permeability in natural clay-bearing fault gouge under high pressure at 20C. Journal of Geophysical Research, 105, 16,415– 16,426.

Faulkner, D.R., Rutter, E.H., 1998. The gas-permeability of clay-bearing fault gouge at 20 ^{0}C. In: Knipe, R.J., Jones, G., Fischer, Q. (Eds.), Faulting, Fault Sealing and Fluid-flow in Hydrocarbon Reservoirs. Geological Society of Special Publication, 147, 147–156.

Ferguson, R. C., Nichols, C., Leeuwen, T. V., and Kuuskraa, V. A., 2009, Storing CO_2 with enhanced oil recovery. Proceedings of the 9th International Conference on Greenhouse Gas Control Technologies (GHGT-9), 16–20 November 2008, Washington DC, USA.

Fisher, Q.J., Knipe, R.J., 2001. The permeability of faults within siliciclastic petroleum reservoirs of the North Sea and Norwegian Continental Shelf. Marine and Petroleum Geology 18, 1063–1081.

Fjær, E., 2009. Static and dynamic moduli of weak sandstone. Geophysics 74,103–112.

Fjær, E., Stroisz, A. M., & Holt, R. M. 2012. Combining static and dynamic measurements for evaluation of elastic dispersion. American Rock Mechanics Association proceedings of the 46th US Rock Mechanics / Geomechanics Symposium held in Chicago, IL, USA, 24-27 June 2012.

Fornel, A., Vallaure, T., 2009. Modeling of CO_2 storage and long term behavior in the Casablanca field. Energy Procedia, 1, 2919–2927.

Forsans, T. M. & Schmitt, L. 1994. Capillary forces: The neglected factor in shale stability studies? Proceedings of European Rock Mechanics Symposium 94. A. A. Balkema, Rotterdam, 1994, 71–84.

Fournier, R.O., 1989. Geochemistry and dynamics of the Yellowstone National Park hydrothermal system. Annu. Rev. Earth Planet. Sci. 17, 13–53.

Franseen, E.K. et. al., 2003. Geologic Characteristics of Arbuckle Reservoirs in Kansas, TORP Fifteenth Oil Recovery Conference Proceedings, March 2003, Wichita, Kansas. US.

Freed, R. L., & Peacor, D. R. 1989. Geopressured shale and sealing effect of smectite to illite transition, American Association Petroleum Geology Bulletin, 73, 1223–1232.

Gale, J., 2004. Geological storage of CO2: what do we know, where are the gaps, and what more needs to be done? Energy 29 (9–10), 1329–1338.

Garcia-Bengochea, I., Lovell, C. W. and Altchaeffl A. G. 1979. Pore distribution and permeability of silty clays. Journal of Gotechnical and Geoenvironmental Engineering, 105, 839– 856.

Gassmann, F. 1951. Elastic waves through a packing of sphere. Geophysics, 16, 673–685.

Gozalpour, F., Ren, S. R., and Tohidi, B., 2005, CO_2 EOR and storage in oil reservoir. Oil & Gas Science and Technology 60, 537–546.

Gunter, W.D., Bachu, S., Law, D.H.-S., Marwaha, V., Drysdale, D.L., McDonald, D.E., McCann, T.J., 1996. Technical and economic feasibility of CO2 disposal in aquifers within the Alberta sedimentary basin, Canada. Energy Convers. Manage. 37 (6–8), 1135–1142

Hall, P. L., Astill, D. M. & McConnell, J. D. C., 1986. Thermodynamic and structural aspects of the dehydration of smectites in sedimentary rocks. Clay Minerals. 21, 633–648

Han, D. 1986, Effects of Porosity and Clay Content on Acoustic Properties of Sandstones and Unconsolidated Sediments, Ph. D. dissertation, Stanford University.

Han, W. S., McPherson, B. J., Lichtner, P. C., Wang, F. P. 2010. Evaluation of trapping mechanisms in geologic CO_2 sequestration: Case study of SACROC northern platform, a 35-year CO_2 injection site. American Journal of Science, 310, 282–324.

Haneberg, W.C., 1995. Steady-state groundwater flow across idealized faults: Water Resources Research, 31, 1815–1820.

Hendron, Jr., Mesri, G., Gambe, J. C., and Way, G. 1970. '' Compressibility Characteristics of Shales Measured by Laboratory and In Situ Tests,'' Determination of the in Situ Modulus of Deformation of Rock, ASTM STP 477, American Society for Testing and Material, pp. 137–153.

Hepple, R.P., Benson, S.M., 2005. Geologic storage of carbondioxide as a climate change mitigation strategy: performance requirements and the implications of surface seepage. Environ. Geol. 47, 576–585.

Hildenbrand, A., Schlomer, S., Krooss, B. M. and Littke, R. 2004. Gas breakthrough experiments on pelitic rocks: Comparative study with N_2, CO_2, and CH_4. Geofluids, 4, 61– 80.

Holloway, S., 1996. An overview of the Joule II Project: the underground disposal of carbon dioxide. Energy Convers. Manage. 37 (6–8), 1149–1154.

Holloway, S., 2005. Underground sequestration of carbondioxide-a viable greenhouse gas mitigation option. Energy 30, 2318–2333.

Holt, R. M. 2012. Static vs. Dynamic Behavior of Shale. American Rock Mechanics Association proceedings of the 46th US Rock Mechanics / Geomechanics Symposium held in Chicago, IL, USA, 24–27 June 2012.

Hornby, B.E. 1998. Experimental laboratory determination of the dynamic elastic properties of wet, drained shales. Journal of Geophysical Research, B, Solid Earth and Planets, 103, 29945–29964.

Horsrud, P., Sønstebø, E. F., and Bøe, R. 1998. Mechanical and Petrophysical Properties of North Sea Shales. International Journal of Rock Mechanic and Mining Science, 35, 1009–1020.

Hossain, Z., Fabricius, I.L., Grattoni, C.A., Solymar, M., 2011. Petrophysical properties of greensand as predicted from NMR measurements. Petroleum Geoscience 17, 111–125.

Hou, Z., Rockhold, M.L., Murray, C.J., 2012. Evaluating the impact of caprock and reservoir properties on potential risk of CO2leakage after injection. Environmental Earth Sciences 66, 2403–2415.

Howard, J. J. & Roy, D. M., 1985. Development of layer charge and kinetics of experimental smectite alteration. Clays minerals. 33, 81-88.

Howard, J. J. 1991. Porosimetry Measurement of Shale Fabric and its Relationship to Illite/Smectite Diagenesis. Clays and Clay Minerals, 39, 355–361.

Hower, J. E., Eslinger, E. V., Hower, M. E. & Perry, E. A., 1976. Mechanism of burial metamorphism, 1; mineralogical and chemical evidence. Geological Society of America. 87, 725–737.

Hower, J., Eslinger, E.V., However, M.E., Perry, E.D., 1976. Mechanism of burial metamorphism of argillaceous sediment. I. Mineralogical and chemical evidence. Geological Society of America Bulletin 87, 725–737.

Hunt, J.M., 1990. Generation and migration of petroleum from abnormally pressured fluid compartments. AAPG Bulletin 74, 1–12.

IPCC., 2005. Special report on carbon dioxide capture and storage. In Prepared by Working Group III of the Intergovernmental Panel on Climate Change; Metz, B., Davidson, O., de Coninck, H. C., Loos, M., Meyer.

Jaffe, A., 2010. Shale gas will rock the world: Retrieved January 26.2011, from the Wall Street Journal:http://online.wsj.com/article/SB10001424052702303491304575187880596301668.html.

Jin, M., Mackay, E., Quinn, M., Hitchen, K., Akhurst, M., 2012. Evaluation of the CO_2 storage capacity of the captain sandstone formation. In: The EAGE Annual Conference and Exhibition Incorporating SPE Europe, Copenhagen, Denmark, 4–7June 2012.

Jizba, D. and Nur, A.1990. Static and dynamic moduli of tight gas sandstones and their relation to formation properties. SPWLA 31st Annual Logging Symposium. June 24–27. 1990

Johnson, D. H. 1987. Physical properties of shale at temperature and pressure. Journal of Geophysical Research, 52, 1391–1401.

Josh, M., Esteban, L., Delle, P., Sarout, C., Dewhurst, J., Clennell, D.N.M.B., 2012. Laboratory characterisation of shale properties. Journal of Petroleum Science and Engineering 88–89, 107–124.

Katsube, T. J., Mudford, B.S., Best, M. E., 1991. Petrophysical characteristics of shale from the Scotian shelf. Geophysics 56, 1681–1689.

Khatchikian, A., 1995. Deriving reservoir pore-volume compressibility from well logs. Society of Petroleum Engineering Advanced Technology Series 4.

Kim, J.W., Bryant, W.R., Watkins, J.S., Tieh, T.T., 1999. Electron microscopic observations of shale diagenesis, offshore Louisiana USA, Gulf of Mexico. Geo-Marine Letter 18, 234–240.

King, M.S., 1970. Static and dynamic moduli of rocks under pressure. Proceedings of the 11th US Symposium on Rock Mechanics, 329–351.

Klinkenberg, L. J., 1941. The permeability of porous media to liquids and gases. Drilling and Production Practice, 2, 200–213.

Knipe, R.J., 1993. The influence of fault zone processes and diagenesis on fluid flow, in Horbury, A.D., and Robinson, A.G., eds., Diagenesis and basin development: American Association of Petroleum Geologists Studies in Geology, 36, 135–151.

Kozeny, J., 1927. Ueber kapillare Leitung des Wassers im Boden. Sitzungsberichteder Kaiserlichen Akademie der Wissenschaften. Wien 136, 271–306.

Kuila, U., Prasad, M. & Batzle, M., 2010. Pore size distribution and Ultrasonic Velocities of compacted Na-montmorillonite clays. 8th Biennial International Conference and Exposition on Petroleum Geophysics, Hyderabad 2010.

Kwon, O., Kroneberg, A.K., Gangi, A.F., Johnson, B., Herbert, B., 2004. Permeability of illite-bearing shale: 1-anisotropy and effects of clay content and loading. Journal of Geophysical Research 109 (B10), B10205.

Kwon, O., Kronenberg, A.K., Gangi, A.F., Johnson, B., 2001. Permeability of Wilcox Shale and its effective pressure law. Journal of Geophysical Research B: Solid Earth and Planets 106, 19339–19353.

Lachance, D. P, Anderson, M. A. 1983. Comparison of uniaxial strain and hydrostatic stress pore-volume compressibilities in the nugget sandstone. Paper SPE 11971 presented at the 58th SPE Annual Technical Conference and Exhibition, 1983.

Leclère, H., Buatier, M., Charpentier, D., Sizun, J-P., Labaume, P., Cavailhes, T., 2012. Formation of phyllosilicates in a fault zone affecting deeply buried arkosic sandstones: their influence on petrophysic properties (Annot sandstones, French external Alps). Swiss Geological Society, 105, 299–312.

Lee, J. H., Ahn, J. H. & D. Peaco. 1985. Textures in layered silicates progressive changes through diagenesis and low temperature metamorphism. Journal of Sedimentary Petrology, 55, 532–540.

Lee, J.H., Ahn, J.H., Peaco, D., 1985. Textures in layered silicates progressive changes through diagenesis and low temperature metamorphism. Journal of Sedimentary Petrology 55, 532–540.

Leonards, G. A. 1962. Engineering Properties of Soils. McGraw-Hill, New York.

Lin, W. 1978. Measuring the permeability of Eleana argillite from area 17, Nevada test site, using the transient method. Lawrence Livermore National Laboratory Livermore, California Rep.UCRL-52604, pp 11.

Lindgreen, H. & Hansen, P. L., 1991. Ordering of illite smectite in Upper Jurassic claystones from North Sea. Clay Minerals. 26, 105-125.

Macey, H. H. 1942. Clay–water relationship and the internal mechanisms of drying. Transactions of the British Ceramic Society, 41, 73–121.

Magara, K., 1971. Permeability considerations in generation of abnormal pressures. Society of Petroleum Engineering Journal 11, 236–242.

Magara, K., 1975a. Reevaluation of montmorillonite dehydration as cause of abnormal pressure and hydrocarbon migration. AAPG Bulletin 59, 292–302.

Magara, K., 1975b. Importance of aquathermal pressuring effect in Gulf Coast. AAPG Bulletin 59, 2037–2045.

Mallon, A. J., Swarbrick, R. E. and Katsube, T. J. 2005. Permeability of fine-grained rocks: New evidence from chalks. Geology, 33, 21–24.

Manzocchi, T., 1999. Towards an Improved Fault Representation in Two phase Reservoir Simulation. Extended abstracts 61st EAGE Conference and Technical Exhibition, Helsinki, 1, 1999, C-05.

Marcussen, Ø., Thyberg, B. I., Peltonen, C., Jahren, J., Bjørlykke, K. & Faleide, J. I., 2009. Physical properties of Cenozoic mudstones from the northern North Sea: Impact of clay mineralogy on compaction trends. AAPG Bulletin. 93, 127-150.

Mbia, E. N. & Fabricius, I. L. 2012. Pore Radius and Permeability Prediction from Sonic Velocity. Third EAGE Shale Workshop Shale Physics and Shale Chemistry, 23-25 January 2012, Barcelona, Spain.

Mbia, E. N., Fabricius, I. L & Oji, C. O. 2013. Equivalent Pore Radius and velocity of elastic waves in shale Skjold Flank-1 Well, Danish North Sea. Journal of Petroleum Science and Engineering, 109, 280 – 290..

Mbia, E.N., Fabricius, I.L., Krogsbøll, A., Frykman, P., Dalhoff, F., 2014a. Permeability, compressibility and porosity of Jurassic shale from the Norwegian–Danish Basin. Journal of Petroleum Geosciences.

Mbia, E.N., Frykman, P., Nielsen, M.C., Fabricius, I.L. Pickup, G. E., Bernstone, C., 2014. Caprock compressibility and permeability and the consequences for pressure development in CO_2 storage sites. International Journal of Greenhouse Gas Control, 22, 139 – 153.

Mesri, G., and Olson, R. E. 1971. Mechanisms controlling the permeability of clays. Clays Clay Miner, 19, 151– 158.

Michaels, A. S. & Lin, C. S. 1954. Permeability of Kaolinite. Industrial and Engineering Chemistry, 46, 1239–1246.

Michelsen, O., Nielsen, L.H., Johannessen, P.N., Andsbjerg, J. and Surlyk, F. 2003. Jurassic lithostratigraphy and stratigraphic development onshore and offshore Denmark. In: Ineson, J.R. & Surlyk, F. (eds): The Jurassic of Denmark and Greenland. Geological Survey of Denmark and Greenland Bulletin 1, 147–216. Danish Triassic succession. Marine and Petroleum Geology 19, 563–587.

Mizoguchi, K., Hirose, T., Shimamoto, T., 2000. Permeability structure of the Nojima fault at Funaki, Hokudan-cho, Japan. Gekkanchikyu-gougai (Earth Monthly) 31, 58–65 (in Japanese).

Mondol, N. H., Bjørlykke, K., Jahren, J. & Høeg, K. 2007. Experimental mechanical compaction of clay mineral aggregates – changes in physical properties of mudstones during burial. Marine and Petroleum Geology, 24, 289–311.

Mondol, N. H., Jehren, J., Bjørlykke, K. & Brevik, I., 2008. Elastic properties of clay minerals. The leading Edge. 27, 758-770.

Mondol, N.H., Bjørlykke, K., Jahren, J., and Høeg, K. 2008. Experimental compaction of clays: relationship between permeability and petrophysical properties in mudstones. Petroleum Geoscience, 14, 319–337

Moore, D. E., Morrow, C. A. and Byerlee, J. D. 1982. Use of swelling clays to reduce permeability and its potential application to nuclear waste repository sealing. Geophysical Research. Letter, 9, 1009–1012.

Morrow, C.A., Shi, L.Q., and Byerlee, J.D., 1981. Permeability and strength of San Andreas fault gouge under high pressure: Geophysical Research Letters, 8, 325–328.

Morrow, C.A., Shi, L.Q., and Byerlee, J.D., 1984. Permeability of fault gouge under confining pressure and shear stress: Journal of Geophysical Research, 89, 3193–3200.

Mortensen, J., Engstrøm, F. & Lind, I. 1998. The relation among porosity, permeability, and specific surface of chalk from the Gorm field, Danish North Sea. SPE Reservoir Evaluation and Engineering, 1, 245–251.

Neuzil, C. E. 1994. How permeable are clays and shales? Water Resource Research, 30, 145– 150.

Newman G.H. 1973. Pore-Volume Compressibility of Consolidated, Friable, and Unconsolidated Reservoir Rocks Under Hydrostatic Loading. Society of Petroleum Engineers paper 3835, Journal of Petroleum Technolgy, 25, 129-134.

Newman, G.H., 1973. Pore-volume compressibility of consolidated, friable, and unconsolidated reservoir rocks under hydrostatic loading. Journal of PetroleumTechnology, 25, 129–134.

Nielsen, L. H. 2003. Late Triassic – Jurassic development of the Danish Basin and the Fennoscandian Border Zone, southern Scandinavia. Geological Survey of Denmark and Greenland Bulletin 1, 459–526.

Nieto Camargo, J.E., Jensen, J. L., 2012. Analysis of Fault Permeability Using Mapping and Flow Modeling, Hickory Sandstone Aquifer, Central Texas. Natural Resources Research, 21, No. 3.

Nimmo, J. R. 2004. Porosity and Pore Size Distribution, in Hillel, D., ed. Encyclopedia of Soils in the Environment: London, Elsevier, 3, 295–303.

Norrish, K. 1972. Factors in the weathering of mica to vermiculite. Paper presented at the Proceedings on International Clay Conference, Madrid, 1972, J. M. Serratosa, ed., Div. Ciencias C.S.I.C., Madrid, 417-432.

Norton, D., Knapp, R., 1977. Transport phenomena in hydrothermal systems: The nature of porosity. Am. J. Sci. 22, 913–936.

Olsen, H.W., 1972. Liquid movement through kaolinite under hydraulic, electric, and osmotic gradients. American Association Petroleum Geology Bulletin 56, 2022–2028.

Ong, S., Zheng, Z., Chajlani, R., 2001. Pressure-dependent pore volume compressibility a cost effective log based approach. In: Paper SPE 72116 Presented at the SPE Asia Pacific Improved Oil Recovery Conference, Kuala Lumpur, Malaysia.

Oruganti, Y. D., Bryant, S. L., 2009. Pressure build-up during CO_2 storage in partially confined aquifers. Energy Procedia, 2, 3315−3322.

Pearson, M. J., 1990. Clay mineral distribution and provenance in Mesozoic and Tertiary mudrocks of the Moray Firth and Northern North Sea. Clay Minerals. 25, 519–542.

Peltonen, C. B., Marcussen, Ø., Bjørlykke, K. & Jahren, J., 2008. Mineralogical control on mudstone compaction: a study of the Late Cretaceous to Early Tertiary mudstones of the Vøring and Møre Basins, Norwegian Sea. Petroleum Geoscience. 14, 127–138.

Peltonen, C., Marcussen, Ø., Bjørlykke, K. & Jahren, J., 2009. Clay mineral diagenesis and quartz cementation in mudstones: The effects of smectite to illite reaction on rock properties. Marine and Petroleum Geology. 26, 887–898.

Petersen, I.H., Nielsen, H.L., Bojesen-Koefoed, A.J., Mathiesen, A., Kristensen, L., Dalhoff, F., 2008. Evaluation of the quality, thermal maturity and distribution of potential source rocks in the Danish part of the Norwegian–Danish Basin. Geological Survey of Denmark and Greenland Bulletin, 16.

Pickup, G.E., Kiatsakulphan, M., Mills, J.R., 2010. Analysis of grid resolution for simulations of CO_2 storage in deep saline aquifers. In: 12th European Conference on the Mathematics of Oil Recovery, Oxford, UK, 6–9 September.

Pittman, E. D. 1992. Relationship of porosity and permeability to various parameters derived from mercury injection-capillary pressure curves for sandstone. Association Petroleum Geology Bulletin, 76, 191–198.

Pollastro, R. M., 1985. Mineralogical and morphological evidence for the formation of illite at the expense of illite/smectite. Clays Clay minerals. 33, 265–274.

Pruess, K., Garcia, J., Kovscek, T., Oldenburg, C., Rutqvist, J., Steefel, C., Xu, T., 2002. Inter comparison of numerical simulation codes for geologic disposal of CO_2. Lawrence Berkeley National Laboratory, Berkeley, CA, LBNL-51813.

Rawling, C.G., Goodwin, B.L., Wilson, L.J., 2001. Internal architecture, permeability structure, and hydrologic significance of contrasting fault-zone types. Geological Society of America, 29, 43–46.

recovery: Energy Procedia, 1(1), 1989-1996.

Reece, J.S., Flemings, P.B., Dugan, B., Long, H., Germaine, J.T., 2012. Permeability-porosity relationships of shallow mudstones in the Ursa Basin, northern deepwater Gulf of Mexico. Journal of Geophysical Research 117, B12102,http://dx.doi.org/10.1029/2012JB009438.

Revil, A., Cathles III, L.M., 1999. Permeability of shaly sands. Water Resources Research 35, 651–662.

Rhett, DW, Teufel, LW.1992. Effect of reservoir stress path on compressibility and permeability of sandstones. Paper SPE 24756 presented at the 67th SPE Annual Technical Conference and Exhibition, Washington D. C 3, 965–972.

Rimstidt, J.D., Barnes, H.L., 1980. The kinetics of silica–water reactions. Geochim. Cosmochim. Acta 44, 1683–1699.

Scheidegger, A. E. 1974. The Physics of Flow through Porous Media, 3rd ed., University of Toronto Press, Toronto.

Schmidt, G. W. 1973. Interstitial water composition and geochemistry of deep Gulf Coast shales and sandstones. American Association Petroleum Geology Bulletin, 57,321– 337.

Scott, A.D., Smith, S.J., 1966. Susceptibility of interlayer potassium in micas to exchange with sodium. Clays Clay Minerals 14, 69–81.

Sibson, R.H., 1987. Earthquake rupturing as a mineralizing agent in hydrothermal systems. Geology 15, 701–704.

Sigda, J.M., Goodwin, L.B., Mozley, P.S., and Wilson, J.L., 1999. Permeability alteration in small-displacement faults in poorly lithified sediments: Rio Grande rift, central New Mexico, in Haneberg, W.C., et al., eds., Faults and subsurface fluid flow in the shallow crust: American Geophysical Union Monograph 113, 51–68.

Simmons, G., Brace, W.F., 1965. Comparison of static and dynamic measurements of compressibility of rocks. Journal of Geophysical Research 70, 5649–5656.

Smith, D.A., 1980. Sealing and non-sealing faults in the Louisiana Gulf Coast salt basin: American Association of Petroleum Geologists Bulletin, 64, 145–172.

Song, J., Zhang, D., 2013. Comprehensive Review of Caprock-Sealing Mechanisms for Geologic Carbon Sequestration. Environmental Science and Technology, 47, 9–22.

Sparks, D. L. 1995. Environmental Soil Chemistry. Academic Press, San Diego California, 267 pp.

Sposito, G., Skipper, N.T., Sutton, R., Park, S.-H., Soper, A.K., Greathouse, J.A., 1999.Surface geochemistry of the clay minerals. Proceedings of National Academy of Science 96, 3358–3364.

Teevu, D., 1971. Prediction of formation compaction from laboratory compressibility data. Society of Petroleum Engineers Journal 21, 263–271.

Thomas, L.K., Katz, D.L., Tek, M.R., 1968. Threshold pressure phenomena in porous media. SPE Journal 8 (2), 174–184.

Thomsen, L. 1986. Weak elastic anisotropy, Geophysics, 51, 1954–1966.

Tutuncu, A.N., A.L. Podio, and M.M. Sharma. 1994. Strain amplitude and stress dependence of static moduli in sandstones and limestones. In: Proceedings from the 34th US Symposium on Rock Mechanics. 489–496.

Van der Meer, L.G.H., 1992. Investigations regarding the storage of carbon dioxide in aquifers in the Netherlands. Energy Convers. Manage. 33 (5–8), 611–618

Van Olphen, H., 1977. An Introduction to Clay Colloid Chemistry, 2nd ed. John Wiley, Hoboken, NJ, pp. 318.

Walsh, J., Brace, W., 1966. Elasticity of rock: a review of some recent theoretical studies. Rock Mechanics and Engineering Geology 4, 283–297.

Walsh, J.B., 1965. The effect of cracks on the uniaxial compression of rocks. Journal of Geophysics Research 70, 399–411.

Whitworth, T.M., Fritz, S.J., 1994. Electrolyte-induced solute permeability effects in compacted smectite membranes. Applied Geochemistry 9, 533–546.

Wissa, A.E.Z., Christian, J.T., Davis, E.H., Heiberg, S., 1971. Consolidation at constant rate of strain. Journal of the Soil Mechanics and Foundation Engineering Division, American Society of Civil Engineers 97, 1393–1413.

Yale, D.P., Nieto, J.A., Austin, S.P., 1995. The effect of cementation on the static and dynamic mechanical properties of the Rotliegendes sandstone. In: Proceedings of the 35th US Symposium on Rock Mechanics, pp. 169–175.

Yang, Y. L. & Aplin, A. C. 1998. Influence of lithology and effective stress on the pore size distribution and modelled permeability of some mudstones from the Norwegian margin. Marine and Petroleum Geology, 15, 163–175

Yang, Y., & Aplin, A. C. 2007. Permeability and petrophysical properties of 30 natural mudstones. Journal of Geophysical Research, 112, pp 14.

Yi, X., Ong, S.H., Russell, J.E., 2005. Characterizing pore compressibility, reservoir compaction and stress path under uniaxial strain condition for non linear elastic rock. In: Presentation at

Alaska Rocks 2005. The 40th U.S. Symposium on Rock Mechanics (USRMS): Rock Mechanics for Energy, Mineral and Infrastructure Development in the Northern Regions, Anchorage, Alaska, 25–29 June.

Yielding, G., Freeman, B., and Needham, D.T., 1997. Quantitative fault seal prediction: American Association of Petroleum Geologists Bulletin, 81, 897–917.

Young, A., Low, P.F., McLatchie, A.S., 1964. Permeability studies of argillaceous rocks. Journal of Geophysical Research 69, 4237–4245.

Zhang, S., Klimentidis, E. R. & Barthelemy, P. 2011. Porosity and Permeability Analysis on Nanoscale FIB-SEM 3D Imaging of Shale Rock. International Symposium of the Society of Core Analysts held in Austin, Texas, USA, September 18th - 21st, 2011

Zhou, Q., Birkholzer, J.T., Tsang, C.F., Rutqvist, J., 2008. A method for quick assessment of CO_2 storage capacity in closed and semi-closed saline formations. International Journal of Greenhouse Gas Control 2, 626–639.

Zhou, X., Zeng, Z., Liu, H., 2010. Laboratory testing on pierre shale for CO_2 sequestration under clayey. In: 44th U.S. Rock Mechanics Symposium and 5th U.S.–Canada Rock Mechanics Symposium, Salt Lake City, UT, 27–30 June.

9 Appendix

The appendix contains published journal papers and peer read extended abstracts

a) Mbia E. N., Fabricius I.L., Collins, O., 2013. Equivalent pore radius and velocity of elastic waves in shale. Skjold Flank-1 Well, Danish North Sea. Journal of Petroleum Science and Engineering, 109 (2013) 280–290.

c) Mbia E. N., Fabricius I.L., Frykman P., Bernstone C., Pickup G., Nielsen, C. M., 2014. Caprock Compressibility and Permeability and the Consequences for Pressure Development in CO_2 Storage sites. International Journal of Greenhouse Gas Control 22, 139–153.

I) Mbia, E. N., Fabricius, I.L., Frykman, F., Krogsbøll, A., Dalhoff, F., 2014. Quantifying Porosity, Compressibility and Permeability in Shale. Extended abstract and presentation at the Fourth EAGE Shale Workshop 6–9 April 2014, Porto, Portugal.

II) Mbia, E. N., Fabricius, I.L., Frykman, F., Nielsen, C.M, Bernstone, C., Pickup, G., 2013. Caprock compressibility and the consequences for pressure development in CO_2 storage sites. Extended abstract and presentation at the 7th Trondheim CCS Conference (TCCS-7), 04–06 of June 2013 in Trondheim, Norway.

III) Mbia, E.N., Fabricius, I.L. & Krogsbøll, A. Different Methods of Predicting Permeability in Shale. Extended abstract and presentation at the third EAGE Shale Workshop Shale Physics and Shale Chemistry, 4–7 June 2012, Copenhagen, Denmark.

IV) Mbia, E. N. & Fabricius, I. L, 2012. Pore Radius and Permeability Prediction from Sonic Velocity. Extended abstract and presentation at the 3rd EAGE Shale Workshop, 23–25 January 2012 in Barcelona, Spain.

V) Mbia, E.N & Fabricius, I.L., 2011. Petrophysics of Shale Intervals in the Skjold Field, Danish North Sea. Extended abstract and presentation at the 73rd EAGE Conference & Exhibition incorporating SPE EUROPEC, 23–26 May 2011 in Vienna Austria.

a

Equivalent pore radius and velocity of elastic waves in shale. Skjold Flank-1 Well, Danish North Sea

Mbia, E.N., Fabricius, I.L., and Oji, C.O.

Equivalent pore radius and velocity of elastic waves in shale. Skjold Flank-1 Well, Danish North Sea

Ernest N. Mbia *, Ida L. Fabricius, Collins O. Oji

Department of Civil Engineering, Technical University of Denmark, Brovej Bygning 118, 2800 Kgs. Lyngby, Denmark

ABSTRACT

Equivalent pore radius links permeability and porosity of a porous medium. This property can be calculated from specific surface and porosity data measured in the laboratory. We can obtain porosity information from logging data but specific surface information can only be obtained from laboratory experiments on cuttings or core samples. In this study we demonstrate that elastic moduli as calculated from bulk density and velocity of elastic waves relate to equivalent pore radius of the studied shale intervals. This relationship establishes the possibility of calculating equivalent pore radius from logging data.

We used cuttings samples and available well logs to characterize Cenozoic, Cretaceous and Jurassic shale sections in the Skjold Flank-1 well of Danish North Sea. Logging data and well reports were used to select 31 shale cuttings samples and experimental data for porosity, grain density and BET specific surface were obtained from these samples using kaolinite and smectite as reference. The cuttings samples were also characterized with respect to mineralogical composition, content of organic carbon and cation exchange capacity.

Equivalent pore radius was calculated from porosity and BET data. It varies from 5 nm for some Cretacous and Jurassic shale samples to about 25 nm in some Cenozoic samples. Pore radius is controlled by shale mineralogy and the degree of compaction.

We found exponential relationships between equivalent pore radius and elastic moduli, and these empirical relationships were used to calculate equivalent pore radius for the Cenozoic, Cretaceous and Jurassic shale sections in Skjold Flank-1 well from elastic moduli. Elastic moduli were calculated from sonic velocity and density logs. The calculated equivalent pore radius logs vary from 27 nm at 500 m to 13 nm at 2000 m within Cenozoic shale and from 12 nm to about 6 nm in the deeper Cretaceous and Jurassic shale intervals. Cross plots of the equivalent pore radius with neutron porosity and gamma ray data separate the Cenozoic shale section with high equivalent pore radius from Cretaceous and Jurassic sections.

1. Introduction

Equivalent pore radius links permeability and porosity when modeling flow through porous media, but it is not straight forward to predict this property for shale. In gas shale plays, gas flow occurs mainly through interconnected fracture network systems which is constantly recharged by gas flowing through the shale matrix which is dominated by micropores (≤ 2 nm) and mesopores ranging from 2 nm to 50 nm (Kuila et al., 2010). Gas flow in nanometer pores may be a combination of Knudsen diffusion and slip flow while larger pores are dominated by Darcy-like flow. Modeling this flow requires knowledge of pore radius and pore-size distribution (Kuila et al., 2010).

Shale is known to forms source rocks for hydrocarbon generation and seals to hydrocarbon reservoirs and aquifers. Shale can be rich in organic matter ($\geq 2\%$ weight fraction total organic carbon (TOC)) and contain huge estimated gas reserves of about 1000 trillion cubic feet (TCF) in North America and 200 TCF in Europe (Jaffe, 2010). Recently the term "reservoir" is being used for shales with huge gas potentials. In shale clay minerals typically constitute the load bearing framework containing sub-micrometer pore size resulting in low permeability (Pearson, 1990). Several authors have discussed the inter-relationship between clay mineralogical composition and petrophysical properties of shale and have shown that change in temperature and effective stress causes diagenetic transformation of clay minerals as reflected in other petrophysical properties (Hower et al., 1976; Dypvik, 1983; Howard and Roy, 1985; Pollastro, 1985; Hall et al., 1986; Colten-Bradley, 1987; Bjørlykke, 1998; Peltonen et al., 2008, 2009; Marcussen et al., 2009).

Prasad (2003) used a collection of velocity, porosity, and permeability data from limestone and sandstone and showed that, by grouping the data in different hydraulic units based on pore space properties, a positive correlation between velocity and

* Corresponding author. Tel.: +45 45 25 14 16.
  E-mail addresses: ernm@byg.dtu.dk, nchambia@yahoo.com (E.N. Mbia),
ilfa@byg.dtu.dk (I.L. Fabricius), eugene_oji@yahoo.com (C.O. Oji).

permeability can be established. For synthetic clay samples an exponential relationship was found between equivalent pore radius and elastic moduli (Fabricius, 2011, partly based on data from Mondol et al., 2008). So, although in many cases empirical relations between elastic wave velocity and porosity are found (Raymer et al., 1980; Nur et al., 1995), information on equivalent pore radius gives a more general correlation. Elastic modulus is a bulk property which is related to the compliance of the material and carries information of the bulk density or porosity as well as specific surface or pore geometry. According to Prasad (2003) there exist relationships between velocity and permeability

because both are governed by volumetric and geometric considerations, whereas porosity is only a volumetric description.

The objective of this work is to predict equivalent pore radius from elastic moduli as calculated from laboratory data such that it is possible to predict this parameter from field data of density and sonic logs. Shape factor determination in shale is beyond the scope of this study. We base the work on cuttings data for porosity, specific surface and density. Secondly, we will then assess relationships between the predicted equivalent pore radius and other logging data. We have used logging data and available reports to select cuttings samples from Cenozoic, Cretaceous and Jurassic shale sections in the Skjold Flank-1 well. Skjold Flank-1 is located in the Central Graben of the North Sea Basin (Fig. 1). The well penetrated five litho-stratigraphical units including shale-dominated Cenozoic Post Chalk group (73–2128 m), the chalk-dominated primarily Cretaceous Chalk Group (2128–2773 m), the Cretaceous shale rich Cromer Knoll Group (2773–2857 m), the shale-dominated Jurassic (2857–4411 m) and Triassic units (4411–4599 m). The Chalk Group and the Triassic units are not included in this work, so we will group the data into "Cenozoic shale", "Cretaceous shale" and "Jurassic shale".

2. Methodology

2.1. Logging data

The logs used for this study include mud log, caliper, resistivity, gamma ray, density, neutron, as well as P-wave and S-wave velocity logs (Fig. 2). The mud log was compiled during drilling operation and records the lithology. The caliper log tool measures the hole-diameter. Resistivity logs measure the formation's resistivity to the passage of an electric current. The following resistivity tools were used.

Micro-spherically-focused resistivity (MSFL), laterolog deep resistivity (LLD) and laterolog shallow resistivity (LLS). The natural gamma ray log records the gamma radioactivity of the formation. The radiation originates from the radioactive decay of naturally occurring uranium, thorium and potassium. The radioactivity is measured in API units. The density log records bulk density (ρ_b). Porosity is calculated from the bulk density log data by considering

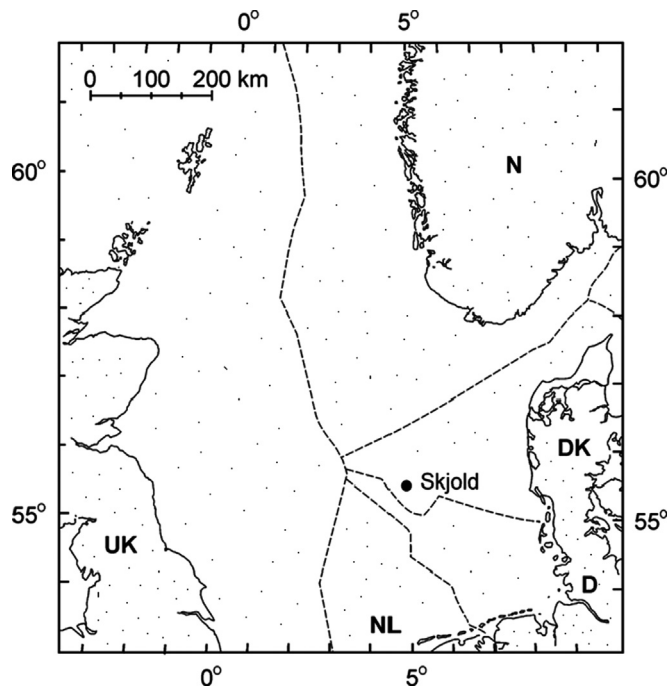**Fig. 1.** Skjold Flank-1 well is located near the Skjold field, Danish North Sea (modified after Fabricius et al., 2007).
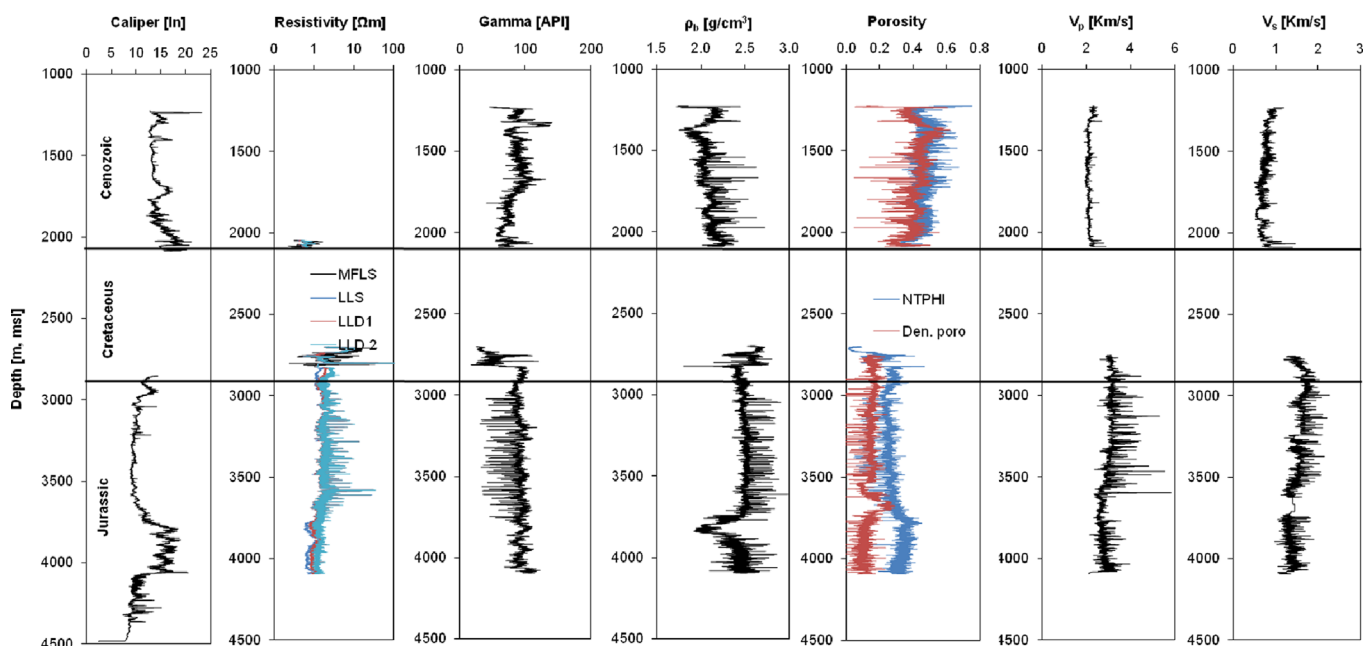

Fig. 2. Petrophysical well logs showing Cenozoic, Cretaceous and Jurassic shale sections in Skjold Flank-1 well. Cretaceous chalk section is shown as blank. The NTPHI is limestone calibrated porosity from neutron log and Den. Poro is porosity from density log assuming 100% water saturated limestone.

Table 1

Cuttings data. Semi-quantitative mineralogy based on X-ray diffractometry (XRD) of bulk and $< 2\,\mu m$ fractions. In Cenozoic and two youngest Cretaceous shale samples, smectite and illite are semiquantified as separate phases, although they may occur as interlayered phases.

Period	Depth (m, msl)	Non-clay minerals (%)						Clay minerals (%)			
		Quartz	K-feldspar	Plagioclase	Calcite	Dolomite	Pyrite	Smectite	Illite	Kaolinite	Chlorite
Cenozoic	552	37	6	10	2			9	16	14	6
	707	38	2	7	1		2	8	31	6	5
	863	41	4	3	4		2	10	23	9	4
	872	34	3	3	2		14	11	19	9	5
	1009	31	11	9	2		10	9	13	11	4
	1164	34	4	5	1		12	10	14	16	4
	1338	28	1	1			9	9	32	17	3
	1484	24	1	1			10	10	33	19	2
	1622	22	2	1	2		7	11	35	15	5
	1768	23	2				10	8	36	11	10
	1923	21	2	2			4	11	39	12	9
	2070	20	1	1			4	10	38	20	6
Cretaceous	2691	20	1		19		9	12	27	10	2
	2719	22			28		5	11	25	6	3
	2746	13		3	34		6		30	9	5
	2774	25			35		7		23	6	4
	2807	26			33		5		27	4	5
	2829	13			33		4		35	7	8
	2850	29	2	3	10		8		31	14	3
	2871	28	2	3	10	3	5		33	13	3
Jurassic	3051	24	2	7	17	10	4		33	4	2
	3200	27	1	3	7	10	9		30	10	3
	3353	24	2	3	3	3	7		40	15	3
	3520	22	1	7	4	6	5		39	11	5
	3658	16	5	6	3	8	4		48	10	
	3810	22	2	3		11	6		36	13	7
	3959	21	1	2		6	7		47	9	7
	4115	18	2	3		5	7		45	11	9
	4270	20	2	2		5	8		43	12	8
	4420	23	3	2		3	8		42	11	8
	4572	24	1	5		4	9		38	11	8

the average grain density of the solids from laboratory data as shown in Table 1. All sections were assumed to be saturated with brine with average density of 1.18 g/cm^3. The neutron porosity log is used as an indicator of porosity and lithology in combination with the density log. The neutron density log is given in porosity units as calibrated in 100% water saturated limestone.

The sonic data were obtained by the SDT log. It does not have a separate shear source, so we are dependent on shear waves that were refracted back only when larger than the mud velocity. The recorded shear is thus sometimes uncertain when recorded with this log. The sonic log records velocity of elastic waves in the formation as expressed in travel time, quoted as Δt, which is the inverse velocity. We recalculated travel times to P-wave and S-wave velocities (V_p and V_s). Cross plots of gamma ray with bulk density, neutron porosity, compressional and shear wave velocities (Fig. 3a–d) split Cretaceous and Jurassic shale sections from the Cenozoic shale section, which show higher gamma ray response in some intervals, higher neutron porosity, lower bulk density, as well as lower compressional and shear wave velocity.

2.2. Cuttings-data

The sample material consisted of unwashed cuttings. Well logs and final well reports were used to develop a sampling strategy for the well, and cuttings samples were taken at approximately 50–100 m spacing in shale intervals, so as to represent changes in the petrophysical logs. The well is vertical with only minor deviation and all depths are given as vertical depth, in meters from sea level. Thirty-one shale cuttings samples were collected for this study, 12 samples from the Cenozoic section, 8 samples from Cretaceous shale, and 11 samples from the Jurassic. The samples were carefully washed with deionized water several times to

remove all the drilling mud and left in methanol for two weeks to dissolve salts. Silver nitrate was used to check for the presence of salts. It is worth noting the difficulty involved in cleaning shale samples with very low permeability which may prevent methanol from getting into the micropores to dissolve all the salts. The cleaned samples were then dried in an oven at about 60 °C for three days. Upon completion of this cleaning process, each sample was handpicked for cavings. The final samples weigh from 55 to 95 g, and the following parameters were determined and the results are presented in Tables 1 and 2.

2.2.1. Mineralogy from X-ray diffractometry

Bulk samples were ground in an agate mortar and pressed into a sample holder for X-ray diffraction (XRD) analysis. For analysis of the clay fraction, approximately 0.5 g samples were shaken with distilled water for 15 min, mixed with 10 ml of 1 M NaCl, and then repeatedly dispersed and centrifuged to recover the $< 2\,\mu m$ fraction. This suspension was treated with acetic acid to remove carbonate minerals. The $< 2\,\mu m$ clay fraction (using the Navier–Stoke's equation) was extracted with a pipette to a frosted glass slide. Then the water was allowed to evaporate overnight to achieve basal orientation of the clay minerals for XRD analysis. For identification of clay minerals four X-ray diffractograms were taken: air-dried, ethylene glycol-solvated at 60 °C for 2 days, subsequently heated to 350 °C/2 h and 550 °C/2 h. The XRD pattern was obtained by Cu-Kα X-ray radiation by using Ni filter with variable divergence slit through 2–65° 2θ. The XRD data and intensities versus angle of diffraction were used to calculate lattice distances (d-values) by using Bragg's law, and minerals were identified. The bulk mineral composition was assessed semi-quantitatively according to method used at University of Aarhus
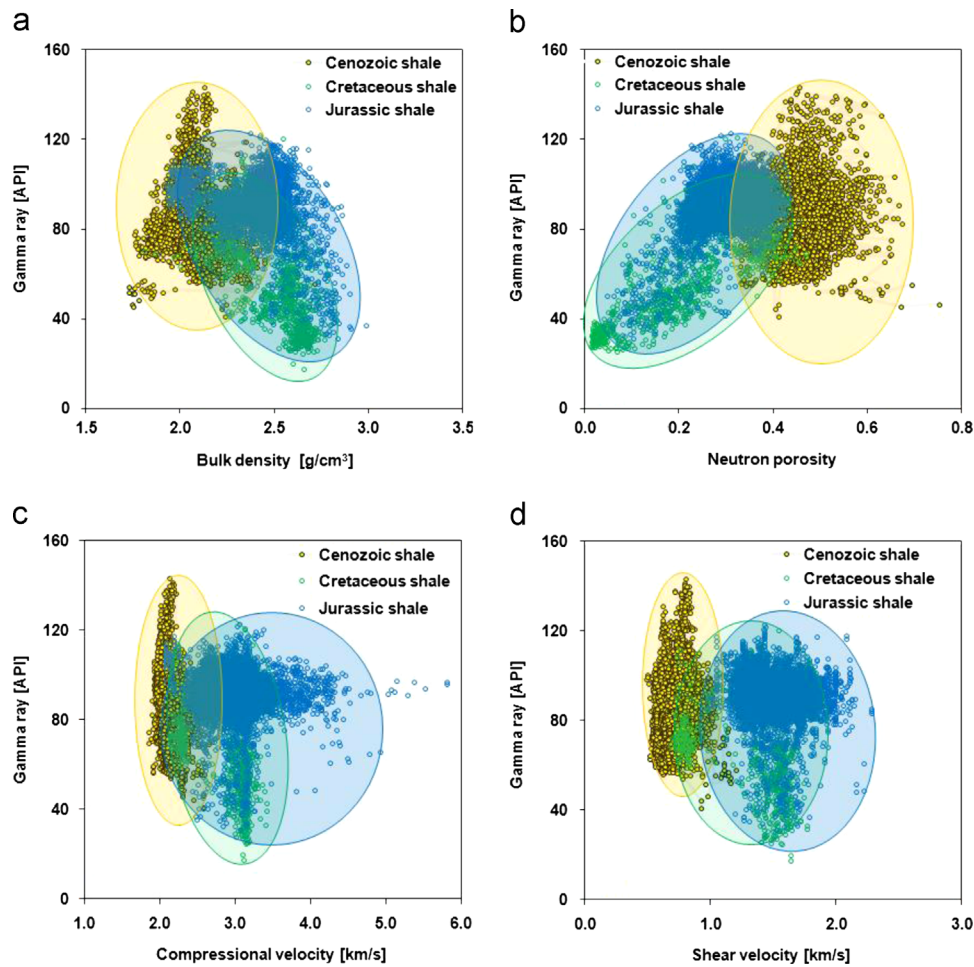
Fig. 3. Cross plots of gamma ray log versus other logging data from Skjold Flank-1. The data are split according to geological age: Cenozoic, Cretaceous and Jurassic. (a) Gamma ray versus bulk density. (b) Gamma ray versus neutron porosity. (c) Gamma ray versus P-wave velocity. (d) Gamma ray versus S-wave velocity.

by O. Bjørslev. On bulk samples net peak height, h, was measured on the following peaks where a correction factor was applied: Quartz: 0.25 h(100); K-feldspar 0.10 h(220); Plagioclase: 0.10 h (002); Calcite: 0.076 h(104); Dolomite: 0.076 h(104); Pyrite: 0.085 h(200); Clay minerals 1 h(020). Semi-quantification was then done from the relative corrected peak height. Clay mineral groups were then semiquantified from the glycolated oriented samples. The peak areas of the 17 Å, 10 Å, and 7 Å peaks were measured and corrected by factors 1, 3 and 1.15 respectively. This allows an estimate of contents of Smectite, Illite, and combined Chlorite and Kaolinite. Chlorite and Kaolinite were then semiquantified from the ratio of the height of the 14 Å peak after heating to 550 °C to the height of the 7 Å peak corrected by a factor 1.5 on the untreated oriented sample.

2.2.2. Determination of porosity by He-porosimetry and mercury immersion

We first measured the grain volume, V_g, of each sample by helium porosimetry. To get grain density, ρ_{grain}, we divided sample weight with sample volume. Since we could not measure the bulk volume of the cuttings samples by caliper, we had to employ a mercury immersion method. In order to carry out this measurement a special set-up was designed which includes weighing balance with a swing arm and perforated steel basket. The basket has a lid and is attached to the swing arm. A beaker glass was filled with mercury to an expected level.

The following steps were taken to obtain the volume of the sample: (1) The weight of the empty basket was measured in air and in mercury. (2) The weight of the basket plus the sample is measured in air and in mercury. (3) Actual sample weight is equal to weight of the basket plus the sample in air minus weight of empty basket in air. (4) Actual sample weight in Hg is equal to weight of the basket plus the sample in Hg minus weight of empty basket in Hg. To get the dry bulk volume (V_{dry}) we divided actual sample weight in mercury by the density of mercury. To get dry density (ρ_{dry}) we divide actual sample weight by dry bulk volume. Porosity (ϕ) is then derived as

$$\phi = (V_{dry} - V_g)/V_{dry} \qquad (1)$$

For calibration, similar cuttings were obtained by crushing a plug with known porosity, and we found a relative error of $\pm 2\%$.

2.2.3. BET specific surface

The specific surface of the samples (BET) was determined by nitrogen adsorption according to the method developed by Brunauer et al. (1938). A Gemini III 2375 surface area analyzer apparatus (Micrometrics Instruments Corp.) was used. To preserve the sample mineralogy, we degassed samples for 4 h at 70 °C on a FlowPrep060 degasser (Micrometrics Instruments Corp.) using nitrogen as a carrier gas. The determination of specific surface area was achieved in two steps: (1) evaluation of the adsorbed monolayer volume, and (2) conversion of this quantity to specific surface area by means of the molecular area (a_m). The test was

Table 2

Cuttings data from well Skjold Flank-1. ρ_g is the grain density, ϕ is the mercury porosity, R_p is the equivalent pore radius, BET is the specific surface by N_2 adsorption, CEC is the cation exchange capacity, $CaCO_3$ is the carbonate presented as equivalent calcium carbonate; TOC is the total organic carbon, Th is thorium, U is uranium and K is potassium identified by spectral gamma radiometry, V_p and V_s are compressional and shear velocities obtained by averaging ten data points from corresponding depths in the logging data. Experimental errors are: for ρ_g <0.03 g/cm³; for CEC $<5\%$; for BET <0.3 m²/g; for $\phi < 2\%$; for $CaCO_3 < 0.2\%$; for TOC $<0.2\%$; for Th <0.5 ppm; for U <0.2 ppm; for K $<0.02\%$. Data for kaolinite and smectite are given for reference.

Sample	Depth (m)	ρ_g (g/cm³)	CEC (mEq/100 g)	BET (m²/g)	ϕ	$CaCO_3$ (%)	TOC (%)	Th (ppm)	U (ppm)	K (%)	V_p (km/s)	V_s (km/s)
Kaolinite		2.61		11	0.55						1.25	0.28
Kaolinite		2.61		11	0.45						1.36	0.34
Kaolinite		2.61		11	0.30						1.50	0.45
Kaolinite		2.61		11	0.32						1.56	0.47
Kaolinite		2.61		11	0.17						1.98	0.77
Kaolinite		2.61		11	0.11						2.18	0.90
Smectite		2.62		25	0.55						1.54	0.32
Smectite		2.62		25	0.49						1.62	0.37
Smectite		2.62		25	0.45						1.67	0.40
Smectite		2.62		25	0.39						1.88	0.51
Smectite		2.62		25	0.36						1.98	0.59
Cenozoic	552	2.65	38	30	0.35	6	0.6	14.40	4.98	1.87	2.32	0.81
Cenozoic	707	2.65	26	30	0.39	6	0.9	12.90	4.38	1.74	2.25	0.77
Cenozoic	863	2.65	22	30	0.35	4	1.1	11.60	4.58	1.63	2.29	0.93
Cenozoic	872	2.74	27	31	0.35	5	1.1	12.90	5.38	1.68	2.35	0.97
Cenozoic	1009	2.65	36	30	0.34	4	0.9	13.90	4.38	1.66	2.50	0.97
Cenozoic	1164	2.68	48	28	0.45	4	0.9	12.80	5.88	1.81	1.97	0.72
Cenozoic	1338	2.68	55	28	0.45	2	0.8	9.40	5.98	1.77	2.01	0.61
Cenozoic	1484	2.68	46	28	0.49	3	2.6	8.10	3.58	1.90	1.99	0.57
Cenozoic	1622	2.65	43	30	0.46	2	3.5	7.40	6.48	1.85	2.10	0.73
Cenozoic	1768	2.65	48	30	0.52	4	1.4	7.30	5.68	2.22	1.95	0.71
Cenozoic	1923	2.65	29	30	0.47	2	1.0				1.85	0.71
Cenozoic	2070	2.67	39	23	0.30	5	0.7				2.65	1.15
Cretaceous	2691	2.75	9	23	0.27	56					2.50	1.12
Cretaceous	2719	2.71	22	18	0.16	27					3.20	1.55
Cretaceous	2746	2.71	7	18	0.20	72					3.13	1.33
Cretaceous	2774	2.69	8	18	0.15	44					2.90	1.68
Cretaceous	2807	2.72	15	18	0.15	52		2.30	4.68	0.69	3.30	1.43
Cretaceous	2829	2.74	10	18	0.15	66					4.06	1.60
Cretaceous	2850	2.73	22	18	0.17	10					3.24	1.52
Cretaceous	2871	2.74	20	24	0.20	11					2.93	1.38
Jurassic	3051	2.75	9	18	0.21	28	2.0	7.70	4.68	1.86	2.44	1.20
Jurassic	3200	2.73	14	24	0.23	15	2.4	4.70	3.48	1.42	2.61	1.41
Jurassic	3353	2.74	17	24	0.26	13	2.5	7.10	2.38	1.34	2.53	1.22
Jurassic	3520	2.75	14	24	0.26	13	2.3				2.55	1.22
Jurassic	3658	2.76	12	24	0.25	11	2.4	7.80	2.88	1.68	2.64	1.20
Jurassic	3810	2.75	13	24	0.24	7	2.6				2.55	1.27
Jurassic	3959	2.75	15	19	0.16	5	1.4	9.60	3.68	1.78	3.20	1.55
Jurassic	4115	2.76	14	18	0.14	7	1.4	9.00	4.98	2.17	3.21	1.57
Jurassic	4270	2.75	15	18	0.15	6	1.7	8.20	5.18	2.15	3.06	1.71
Jurassic	4420	2.76	13	16	0.14	6	2.2				3.16	1.75
Jurassic	4572	2.76	16	16	0.14	5	1.2	10.30	4.38	1.94	3.26	1.85

carried out in duplicate. The specific surface, S, with respect to bulk volume was calculated as

$$S = BET * \rho_{dry} \tag{2}$$

2.2.4. Cation exchange capacity (CEC)

The CEC was measured by Ba-ion exchange. First 0.1 M $BaCl_2$ (pH=5.8) solution was added to each sample so that Ba^{2+} ions replace the bases such as Ca^{2+}, K^+, Mg^{2+} and Na^+. Afterwards the concentration of the bases was measured with inductively coupled plasma-optical emission spectrophotometry (ICP-OES). To analyze the cation-exchange capacity which is known as the effective CEC, the samples were next immersed in a dilute $BaCl_2$ solution with an ionic strength of about 0.01 M. Then the Ba^{2+} which replaced the bases was removed with an excess of $MgSO_4$. The Mg^{2+} lost for the exchange with Ba^{2+} is measured with the ICP-OES to determine the effective CEC.

Measurement of CEC on shale samples with carbonate gave significantly higher CEC exchangeable bases than expected. Analysis showed that calcium carbonate in shale samples increases the CEC exchangeable bases which gave exaggerated values of effective CEC. We normally expect that the effective CEC is higher than the CEC exchangeable bases but that was not the case. We measured the carbonate content of each sample and realized that the higher the percentage of carbonate in shale sample, the higher the contribution of calcium cations. In a sample with 72% carbonate content, the contribution of calcium cations from carbonate is about 78% of the CEC exchangeable bases. While shale samples with low carbonate content of about 8% contributes only 1% of calcium cations to the CEC exchangeable bases. In order to correct for this error we treated selected carbonate bearing shale samples with CH_3COOH acid at pH=2, to remove the carbonate before carrying out renewed CEC measurements. From these CEC results it was possible to apply a correction factor to obtain the effective CEC for the remaining carbonate containing shale samples by plotting the ratio of CEC and CEC carbonate free against carbonate content. During the removal of carbonate, also cations from shale supposed to contribute to the CEC exchangeable base were leached out and replaced by the acid cations (H_3O^+).

2.2.5. Carbonate content and total organic carbon (TOC)

The carbonate content was obtained by means of dissolution with 1 M HCl followed by titration with 1 M NaOH. The error is $\pm 0.2\%$. Data are presented as equivalent $CaCO_3$. The total organic carbon content (TOC) was measured by combustion in a LECO (CS-200) Carbon/Sulfur Analyzer-oven with an error of $\pm 5\%$.

2.2.6. Gamma spectrometry

The concentrations of U, Th and K were measured on powdered samples by a NaI-crystal gamma spectrometer with an error for U: < 0.2 ppm, for Th: < 0.5 ppm, and for K: $< 0.02\%$.

2.2.7. Equivalent pore radius prediction

Experimental data obtained in this work together with data from Fabricius (2011) on pure kaolinite and smectite were used to model the relationship between elastic moduli and equivalent pore radius. The experimental data used includes porosity (ϕ), BET specific surface, grain density (ρ_g), compressional and shear wave velocities in the water saturated state. For the Skjold Flank-1 shale, velocity data was collected by averaging sonic velocity log data in 5 m intervals from the same cuttings depths which gives approximately the same resolution. For the pure kaolinite and smectite laboratory velocity data from Mondol et al. (2008) were used. The frequency of elastic waves from logging differs from frequency of laboratory measurements, but we expect only insignificant dispersion of wave velocity due to small pore size and consequent high critical frequency. The bulk density, ρ_b, is calculated as

$$\rho_b = \rho_g(1-\phi) + \rho_{fl}\phi \tag{3}$$

where ρ_{fl} is the fluid density

Elastic compressional modulus, M, is given as

$$M = \rho_b V_p^2 \tag{4}$$

Elastic shear modulus, G, is given as

$$G = \rho_b V_s^2 \tag{5}$$

Elastic bulk modulus, K, is calculated as

$$K = M - (4/3)G \tag{6}$$

For modeling pore radius, we need information on ϕ, and the specific surface of the bulk sample S.

The equivalent pore radius, R_p, is defined as:

$$R_p = 2\phi S = 2/S_p \tag{7}$$

where S_p is the specific surface relative to pore space.

3. Results

3.1. Mineralogical composition

Results from XRD analysis is shown in Fig. 4 and Table 1. The non-clay fraction consists mainly of quartz. Quartz content decreases from about 40% in the younger Cenozoic sediments to about 20% in the deeper Cenozoic. In Cretaceous and Jurassic shales the quartz content varies stratigraphically between 15% and 30%. Feldspar (K-feldspar and plagioclase) is most prevalent in younger Cenozoic sediments and in the Jurassic (5–15%), whereas it is sparser in older Cenozoic and Cretaceous shale. Calcite content is below 5% in the Cenozoic and Jurassic shale samples, whereas in Cretaceous samples up to about 35% calcite was found. Dolomite was not detected in Cenozoic and Cretaceous samples (save the oldest), whereas 5–10% dolomite was identified in the Jurassic shale samples. Pyrite is also identified in these geologic intervals and varies stratigraphysically in Cenozoic shale from 2% to about 14% and from 4% to about 9% in Cretaceous and Jurassic shales.

The main clay minerals identified include smectite, illite, kaolinite and chlorite. Smectite (10–15%) is present in the Cenozoic and in the youngest Cretaceous samples (deepest smectite bearing sample is from 2719 m, msl). Below this depth no smectite was identified. Although Smectite and Illite are partly interlayered, they are semiquantified as separate phases (Fig. 4). Illite is the dominating clay mineral throughout, and most prevalent in older Cenozoic (30–40%) as well as oldest Cretaceous and Jurassic (30–
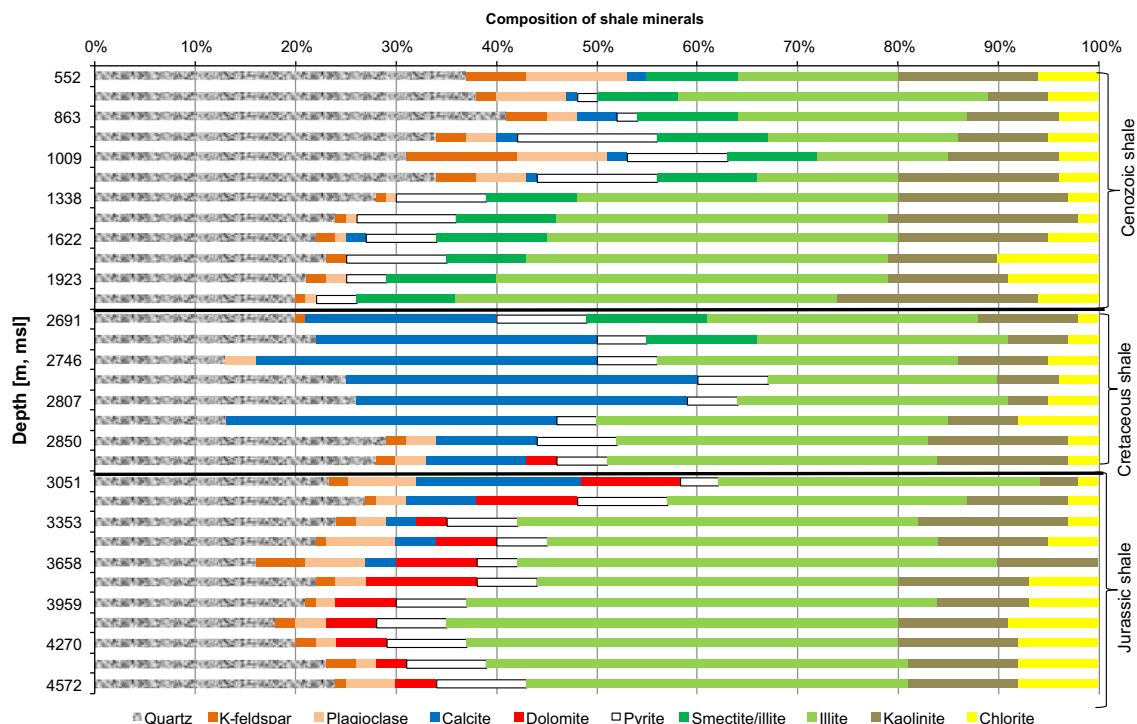

Fig. 4. Mineralogical composition of cuttings samples based on X-ray diffractometry.

50%) samples. The content of kaolinite and chlorite does not vary much with depth and constitutes 5–10% for chlorite and 6–20% for kaolinite.

3.2. Petrophysical properties

The results of grain density, porosity, equivalent pore radius, BET specific surface, CEC, equivalent carbonate content, TOC, spectral gamma data, and elastic wave velocities are summarized in Table 2. Plots of these petrophysical properties as a function of burial depth are shown in Fig. 5a–l. Grain density (Fig. 5a) shows no significant depth trend for Cenozoic shale samples but varies between 2.65 and 2.75 g/cm³. There is significant increase in grain density with depth from 2.69 g/cm³ in Cretaceous shales samples to about 2.76 g/cm³ in Jurassic samples. Porosity (0.3–0.5) and equivalent pore radius (10–27 nm) show higher values in Cenozoic shale samples (Fig. 5b and c) which reduces with depth to about 0.15 for porosity and 7 nm for equivalent pore radius in the deeper Jurassic sediments. Porosity and pore radius show opposite depth trend to that seen in grain density.

BET specific surface and cation exchange capacity show higher values for the Cenozoic shale samples in comparison with the low values obtained for the Cretaceous and Jurassic samples. The BET specific surface decreases with depth from 30 m²/g in Cenozoic samples to < 20 m²/g in deeper Jurassic samples (Fig. 5d). Cation exchange capacity varies from 25 to 55 mEq/100 g in Cenozoic shale, while it is significantly lower (10–20 mEq/100 g) in Cretaceous and Jurassic shale (Fig. 5e). Carbonate content is low in Cenozoic and older Jurassic shales as compared to Cretaceous and younger Jurassic shale. This reflects the content of carbonate minerals by XRD (Figs. 4 and 5f). The total organic carbon content (TOC) is generally lower in Cenozoic samples (0.6–1.4%) than in Jurassic samples (1.2–2.6%), but Cenozoic samples at 1484 m and 1622 m, msl, have relatively high TOC of 2.6% and 3.5% (Fig. 5g). The variation in TOC is not reflected in the radioactivity of these shale samples (Fig. 5h–j). The most conspicuous trends are the decreasing depth trend of Th in Cenozoic shale (from 15 to 5 ppm), and the more modest increasing depth trend in Jurassic shale from 5 to 10 ppm (Fig. 5h).
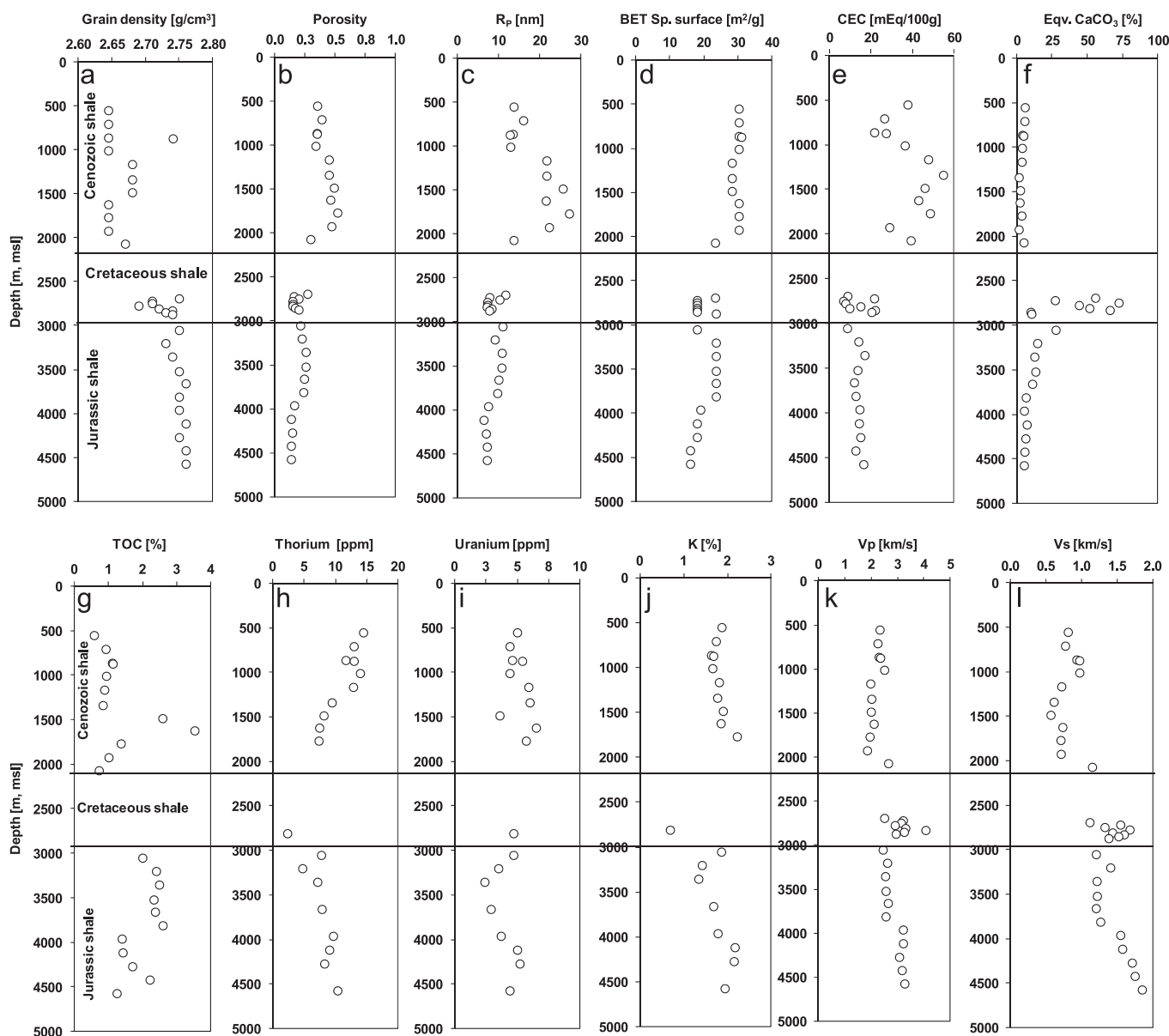

Fig. 5. Depth plots of cuttings data: (a) grain density, (b) porosity, (c) calculated equivalent pore radius, (d) BET specific surface, (e) cation exchange capacity (CEC), (f) carbonate content, (g) total organic carbon (TOC), (h) thorium content, (i) uranium content, (J) potassium content, (k) compressional wave velocity and (l) shear wave velocity.
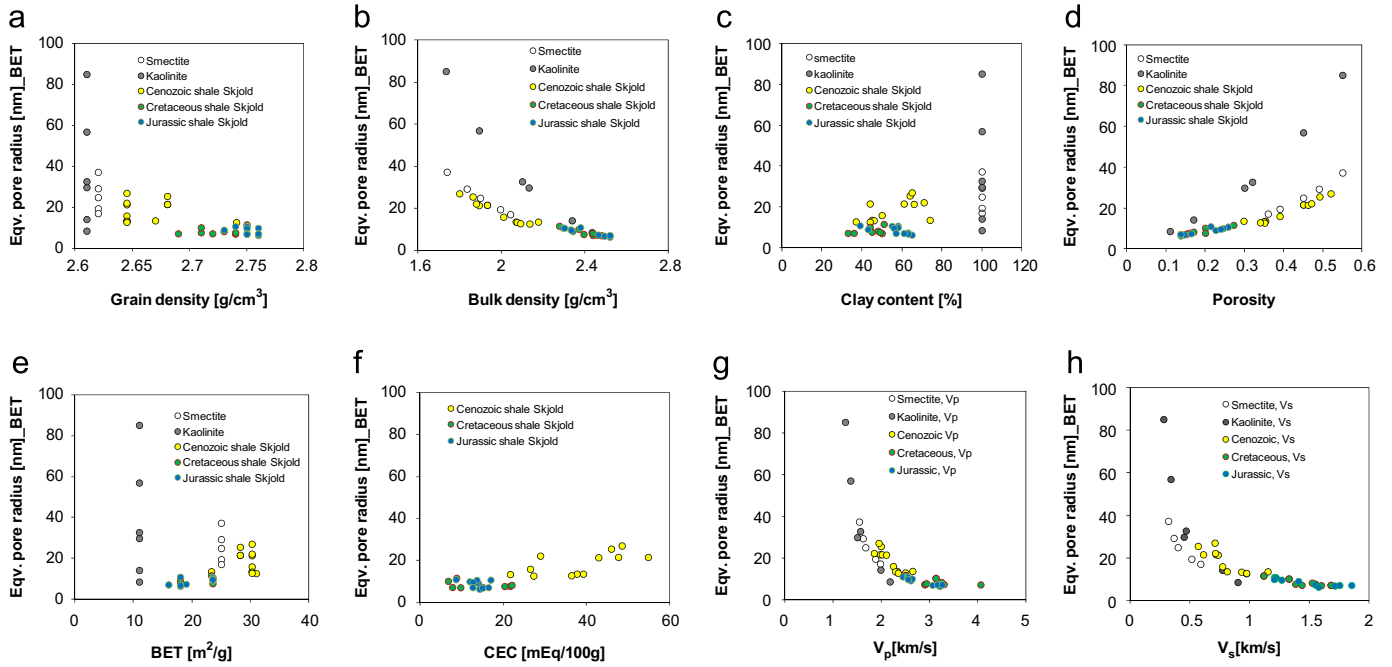
Fig. 6. Cross plots of cuttings data: pore radius calculated from BET and porosity versus: (a) grain density, (b) bulk density, (c) clay content, (d) porosity, (e) specific surface from BET, (f) cation exchange capacity, (g) compressional wave velocity, (h) shear wave velocity. Data for pure smectite and kaolinite are shown for reference.

P-wave and S-wave velocities (Figs. 5k and l) show similar depth trend behavior as grain density but opposite to that of porosity and equivalent pore radius from Cenozoic to Jurassic shale samples which increases from 0.8 to 1.6 km for S-wave and from 2.3 to 3.3 km/s for P-wave velocity.

3.3. Equivalent pore radius

We investigated the relationships between the equivalent pore radius and the other petrophysical parameters as shown in Fig. 6a–h and found clear relationships between pore radius and acoustic velocity as well as pore radius and bulk density. Despite clear trends between bulk density and equivalent pore radius, kaolinite and smectite show separate trends (Fig. 6b) while there exists a single trend for both minerals for the correlation of elastic moduli and equivalent pore radius (Fig. 7a–c). This implies that we can possibly predict pore radius from elastic properties.

Elastic moduli were calculated from experimental data from Cenozoic, Cretaceous and Jurassic shales of Skjold Flank-1 well and from artificially compacted kaolinite and smectite (Mondol et al., 2008) (Fig. 7a–c). Compressional modulus vary from 4 to about 30 GPa, shear modulus from 0.1 to 9 GPa and bulk modulus from 4 to 24 GPa. For pure kaolinite, the equivalent pore radius from BET specific surface and porosity varies from 86 nm to 9 nm with increasing compaction. For pure smectite equivalent pore radius varies from 37 nm to 17 nm with increasing compaction. The cross plots of the calculated pore radius with elastic moduli (Fig. 7a–c) combine the data set into an exponential relationship independent of the mineralogy. These relationships were used to compute empirical equations from which the equivalent pore radius, R_p, was calculated:

$$R_{pM} = 8.3 \times 10^{-9} + 5.7 \times 10^{-7} M^{-2} \qquad (8)$$

$$R_{pG} = 7.8 \times 10^{-9} + 8.5 \times 10^{-9} G^{-1} \qquad (9)$$

$$R_{pK} = 6.6 \times 10^{-9} + 5 \times 10^{-7} K^{-2} \qquad (10)$$

where R_{pM} is equivalent pore radius from compressional modulus, R_{pG}, from shear modulus and R_{pK} from bulk modulus. Radius is given in nm and moduli are given in GPa.

The plot of the equivalent pore radius versus the equivalent pore radius modeled from the compressional modulus gives a correlation coefficient of 0.97, whereas modeling from shear and bulk modulus gave a correlation coefficient of respectively 0.85 and 0.97 with total of 41 data points (Fig. 7d–f). The computed empirical equations were applied to the density and sonic velocity logs and the equivalent pore radius log for the Cenozoic, Cretaceous and Jurassic shale sections in Skjold Flank-1 well was compared with other logs as shown in Fig. 8a–e. In Cenozoic shale the equivalent pore radius vary between 12 nm and 20 nm. In the deeper Cretaceous and Jurassic shale pore radius varies between 12 nm and about 6 nm.

4. Discussion

4.1. Cenozoic shale

The younger Cenozoic sediments, above 1200 m, msl are silty shales with high quartz and relatively high feldspar content. A low content of calcite is reflected in low carbonate content and also relatively high pyrite content is noticed. The clay minerals in order of abundance are illite, kaolinite, smectite and chlorite. These younger Cenozoic shales have a relatively low porosity of 0.35–0.40 probably reflecting poor sorting caused by the high silt content. A relatively high detrital content is indeed reflected in a relatively high content of Thorium. A relatively high specific surface (BET) and low grain density probably reflect interlayered clays dominated by smectite and stratigraphical variation in pyrite content. Poor sorting and smectite dominated clay thus result in low porosity and high BET and consequent modest equivalent pore radius of c. 15 nm.

The older Cenozoic shales are poorer in quartz and tend to have higher porosity (up to 0.5) than the younger Cenozoic sediments. The older Cenozoic shales are dominated by illite-dominated
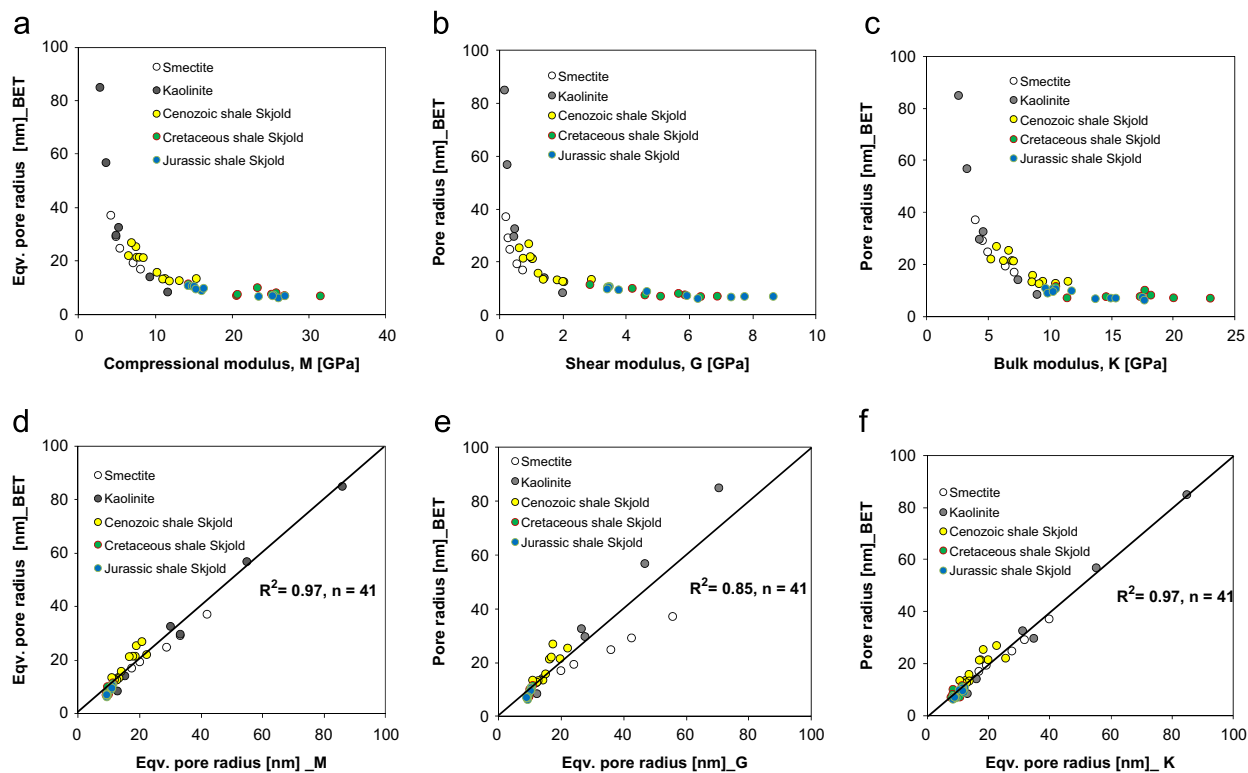
Fig. 7. Cross plots of cuttings data: pore radius calculated from BET and porosity versus: (a) compressional modulus, M, (b) shear modulus, G, (c) bulk modulus, K, (d) pore radius estimated from M, (e) pore radius estimated from G, (f) pore radius estimated from K. Data for pure smectite and kaolinite are used as reference.
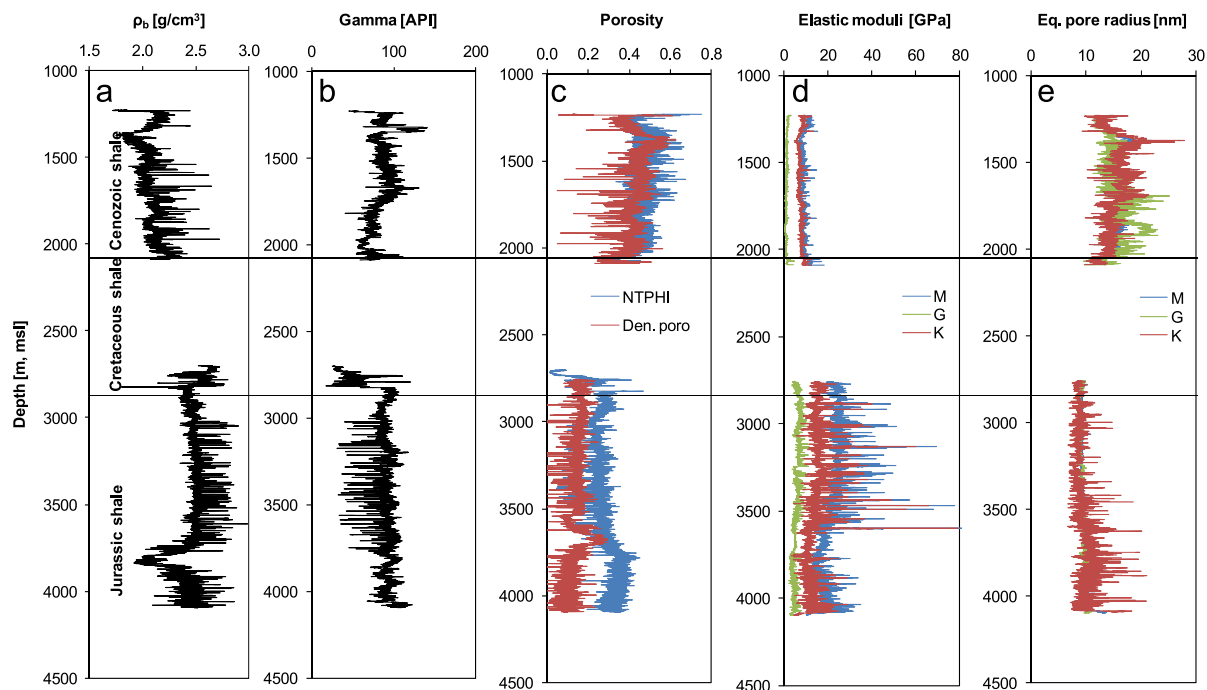

Fig. 8. Depth plots of logging data: (a)–(c) bulk density, gamma ray and porosity, (d) elastic moduli (M, G and K), (e) pore radius estimated from M, G and K.

mixed layered clays, so in spite of the higher clay content, specific surface is similar to that of the younger section. The resulting equivalent pore radius is consequently high: 20–25 nm. The equivalent pore radius is well predicted from bulk modulus and compressional modulus, and less well predicted from the shear modulus (Fig. 7d–f). Nevertheless it is the shear modulus-based

prediction of equivalent pore radius in combination with the neutron log which gives the most effective separation of Cenozoic data points from older data points (Fig. 9d–e). In spite of a high content of feldspar and Thorium the younger Cenozoic sediments with moderate pore radius only cause a small bias towards higher radioactivity for Cenozoic sediments (Fig. 9a–c).
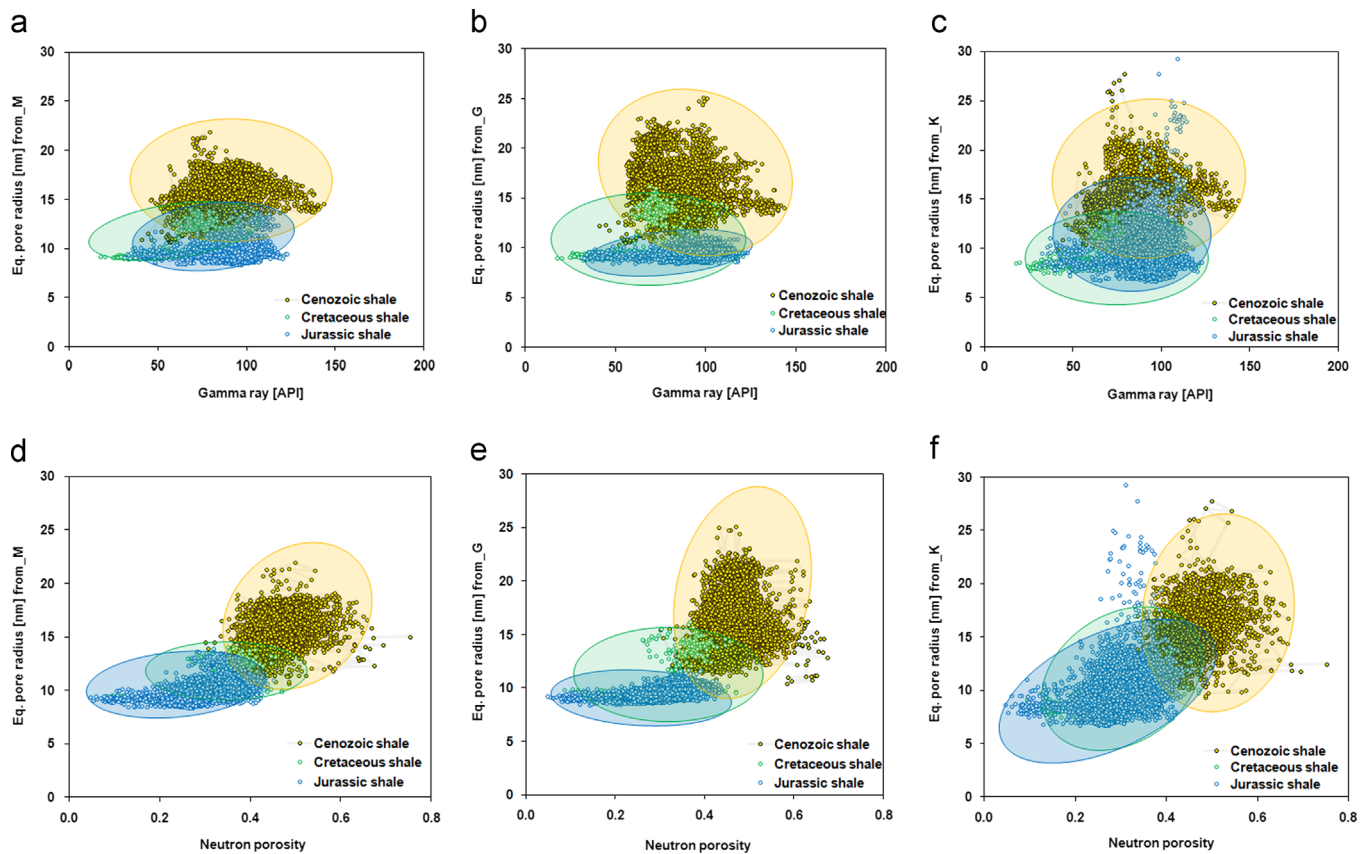
Fig. 9. Cross plots of logging data: pore radius estimated from elastic moduli versus: (a)–(c) gamma ray and (d)–(f) neutron porosity. The data are split according to geological age: Cenozoic, Cretaceous and Jurassic. (a) and (d) Pore radius estimated from compressional modulus M, (b) and (e) pore radius estimated from shear modulus, G, (c) and (f) pore radius estimated from bulk modulus, K.

4.2. Cretaceous shales

Cretaceous shales form a relatively thin section below the thick Chalk Group. Calcite, quartz and pyrite constitute a total of 40–50% of each sample, with the abundance of calcite declining with depth. The clay minerals identified comprise mixed layered smectite respectively illite dominated clays, as well as kaolinite and chlorite. Below 2719 m, msl (corresponding to around 85 °C) no smectite was found. Depositional smectite may have transformed to illite by diagenesis. A diagenetic transformation of mixed layered illite-smectite is known as illitization and described in the North Sea shales by several authors (Hower et al., 1976; Dypvik, 1983; Howard and Roy, 1985; Pollastro, 1985; Hall et al., 1986; Colten-Bradley, 1987, Bjørlykke, 1998; Peltonen et al., 2008; Marcussen et al., 2009). The transition to smectite free clay is reflected in the increased grain density and lower specific surface and cation exchange capacity.

In spite of the lower specific surface, the predicted equivalent pore radius in Cretaceous shale is small: around 10 nm. This is caused by a low porosity (0.15–0.20). Relatively high velocities of elastic waves and relatively low specific surface relative to the overall depth trends indicate a relatively high degree of diagenetic cementation (Fig. 5d, k and l). On cross plots of equivalent pore radius versus gamma ray and neutron porosity log Cretaceous shale tends to overlap Jurassic shale (Fig. 9).

4.3. Jurassic shales

The Jurassic shale section is inter-bedded with thin layers of sandstone or dolomite stringers as indicated by low GR and high density log peaks (Fig. 2). XRD analysis indicates that quartz occurs as the main non-clay mineral, that plagioclase and dolomite are present in all samples, while calcite significantly reduces as we get to lower Jurassic shale. This is also reflected in a depth-wise decreasing content of carbonate (Figs. 4 and 5f). Clay minerals generally constitute 60% of the solids. The clay minerals identified comprise primarily illite, but also kaolinite and minor amounts of chlorite (Fig. 4). An increasing maturation of illite is indicated by a depth-wise increasing K-content (Fig. 5j) which is consistent with other Jurassic samples from the Central Trough studied by Lindgreen and Hansen (1991).

The predicted equivalent pore radius in the Jurassic shale tends to decrease with depth from 10 to 7 nm. This is a reflection of decreasing porosity which counteracts a decreasing specific surface (Fig. 5b and d). Cretaceous and Jurassic shale intervals tend to overlap in the cross plots of equivalent pore radius versus gamma ray and neutron porosity log data (Fig. 9). The best separation is obtained from equivalent pore radius predicted from compressional modulus, where a relatively well defined trend of equivalent pore radius versus neutron porosity is found for Jurassic shale (Fig. 9d).

5. Conclusions

Petrophysical well logs and well cuttings were used to characterize Cenozoic, Cretaceous and Jurassic shale sections in Skjold Flank-1 well of the Danish North Sea. The data were supplemented with data from artificially consolidated samples of kaolinite and smectite. Equivalent pore radius can be calculated from porosity and specific surface of all samples. This forms a basis for predicting equivalent pore radius from logging data.

Cuttings were used to establish empirical relationships between equivalent pore radius and elastic moduli. The relationships are independent of mineralogical composition and give a correlation coefficient (R^2) of 0.97 for bulk modulus and compressional modulus and a correlation coefficient of 0.85 for shear modulus based on 41 data points.

These empirical equations were used to predict equivalent pore radius from the elastic moduli calculated from sonic velocity and bulk density logs from the Skjold Flank-1. The predicted equivalent pore radius shows an overall depth-wise decrease, but is highest in the lower part of the Cenozoic shale sections (20 nm) and decreases to 8 nm in the deeper Jurassic shale section. A relatively modest equivalent pore radius of around 15 nm in the youngest sediments is related to the relatively low porosity of these silty shales. The overall reduction in the equivalent pore radius with depth can be correlated with the changing mineralogical composition of the shale from smectite rich Cenozoic shale to illite rich Jurassic shale causing a decrease in specific surface.

Acknowledgments

References

Bjørlykke, K., 1998. Clay mineral diagenesis in sedimentary basins; a key to the prediction of rock properties; examples from the North Sea Basin. Clay Miner. 33, 15–34.

Brunauer, S., Emmett, P.H., Teller, E., 1938. Adsorption of gases in multimolecular layers. J. Am. Chem. Soc. 60, 309–319.

Colten-Bradley, V.A., 1987. Role of pressure in smectite dehydration-Effects on geopressure and smectite-illite transformation. Am. Assoc. Pet. Geol. 71, 1414–1427.

Dypvik, H., 1983. Clay mineral transformations in Tertiary and Mesozoic sediments from the North Sea. Am. Assoc. Pet. Geol. Bull. 67, 160–165.

Fabricius, I.L., 2011. Relationship between elastic moduli and pore radius in clay aggregates. In: 73rd EAGE Conference & Exhibition incorporating SPE EUROPEC 2011 Vienna, Austria, 23–26 May 2011.

Fabricius, I.L, Birte, R., Lars, G., 2007. How depositional texture and diagenesis control petrophysical and elastic properties of samples from five North Sea chalk fields. Petroleum Geoscience 13, 81–95.

Hall, P.L., Astill, D.M., McConnell, J.D.C., 1986. Thermodynamic and structural aspects of the dehydration of smectites in sedimentary rocks. Clay Miner. 21, 633–648.

Howard, J.J., Roy, D.M., 1985. Development of layer charge and kinetics of experimental smectite alteration. Clay Miner. 33, 81–88.

Hower, J.E., Eslinger, E.V., Hower, M.E., Perry, E.A., 1976. Mechanism of burial metamorphism: 1. Mineralogical and chemical evidence. Geol. Soc. Am. Bull. 87, 725–737.

Jaffe, A., 2010. Shale gas will rock the world: Retrieved January 26, 2011. Wall Street J. ⟨http://online.wsj.com/article/SB10001424052702303491304575187880596301-668.html⟩.

Kuila, U., Prasad, M., Batzle, M., 2010. Pore size distribution and ultrasonic velocities of compacted Na-montmorillonite clays. In: 8th Biennial International Conference and Exposition on Petroleum Geophysics, Hyderabad 2010.

Lindgreen, H., Hansen, P.L., 1991. Ordering of illite smectite in Upper Jurassic claystones from North Sea. Clay Miner. 26, 105–125.

Marcussen, Ø., Thyberg, B.I., Peltonen, C., Jahren, J., Bjørlykke, K., Faleide, J.I., 2009. Physical properties of Cenozoic mudstones from the northern North Sea: impact of clay mineralogy on compaction trends. Am. Assoc. Pet. Geol. Bull. 93, 127–150.

Mondol, N.H., Jehren, J., Bjørlykke, K., Brevik, I., 2008. Elastic properties of clay minerals. Leading Edge 27, 758–770.

Nur, A., Mavko, G., Dvorkin, J., and Gal, D., 1995. Critical porosity:the key to relating physical properties to porosity in rocks. In: 65th Annual International Meeting, Society of Exploration Geophysicists, Expanded Abstracts, pp. 878–881.

Pearson, M.J., 1990. Clay mineral distribution and provenance in Mesozoic and Tertiary mudrocks of the Moray Firth and Northern North Sea. Clay Miner. 25, 519–542.

Peltonen, C.B., Marcussen, Ø., Bjørlykke, K., Jahren, J., 2008. Mineralogical control on mudstone compaction: a study of the Late Cretaceous to Early Tertiary mudstones of the Vøring and Møre Basins, Norwegian Sea. Pet. Geosci. 14, 127–138.

Peltonen, C., Marcussen, Ø., Bjørlykke, K., Jahren, J., 2009. Clay mineral diagenesis and quartz cementation in mudstones: the effects of smectite to illite reaction on rock properties. Mar. Pet.Geol. 26, 887–898.

Pollastro, R.M., 1985. Mineralogical and morphological evidence for the formation of illite at the expense of illite/smectite. Clays Clay Miner. 33, 265–274.

Prasad, M., 2003. Velocity-permeability relations within hydraulic units. Geophysics 68, 108–117.

Raymer, D.S., Hunt, E.R., Gardner, J.S., 1980. An improved sonic transit time-to-porosity transform. Presented at 21st Annual Logging Symposium Transactions., Society of Professional Well Log Analysts, pp. 1–13.

C

Caprock compressibility and permeability and the consequences for pressure development in CO₂ storage sites

Mbia, E.N., Frykman, P., Nielsen, M.C., Fabricius, I.L. Pickup, G. E., Bernstone, C.,
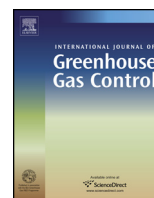
Caprock compressibility and permeability and the consequences for pressure development in CO$_2$ storage sites

Ernest N. Mbia [a,1], Peter Frykman [b,*], Carsten M. Nielsen [b], Ida L. Fabricius [c], Gillian E. Pickup [d], Christian Bernstone [a,e]

[a] Vattenfall, Støberigade 14, DK-2450 Copenhagen NV, Denmark
[b] Geologic Survey of Denmark and Greenland, Øster Voldgate 10, DK-1350 Copenhagen K, Denmark
[c] Department of Civil Engineering, Technical University of Denmark, Brovej Building 118, DK-2800 Kongens Lyngby, Denmark
[d] Institute of Petroleum Engineering Heriot-Watt University, Riccarton, Edinburgh, EH14 4AS Scotland, UK
[e] Vattenfall AB, SE-169 56 Solna, Sweden

ABSTRACT

Large scale CO$_2$ storage has previously been considered for the Vedsted structure located in the Northern part of Jylland in Denmark. Pressure buildup in the Gassum reservoir and transmission to the shallower Chalk Group where the brine–fresh water interface resides need to be investigated as part of site qualification, as overpressure can push brine into the fresh water zone and thereby affecting aquifer performance. Pressure transmission from the reservoir into the surrounding formations, when fractures and faults are ignored, will depend on the properties and thickness of the sealing rock. The most important property to be considered is caprock compressibility and permeability. Laboratory experiments on centimeter-scale plugs and dynamic sonic velocity data from relevant shale formations in Denmark indicate that shale compressibility is lower than often assumed for reservoir simulation studies. The measured compressibility for the Fjerritslev Formation is 0.5×10^{-5} bar^{-1}, which is an order of magnitude lower than the standard compressibility (4.5×10^{-5} bar^{-1}) normally used for reservoir simulation studies. The consequences of this lower compressibility are investigated in a simulation case study and the results indicate that higher overpressure is created in the reservoir and the caprock. Overestimating caprock compressibility can therefore underestimate overpressure within the storage and sealing formations and this can have significant implication in the presence of highly permeable fractures and faults. The caprock permeability is measured on core samples using a geotechnical method of constant rate of strain (CRS) experiments which seem to match the modeled permeability data for the Fjerritslev Formation. We found an average vertical permeability of 0.1 μD for the Fjerritslev Formation from the samples measured. The sensitivity of pressure development for the caprock permeability has been studied by varying from one to three orders of magnitude higher and one to two orders of magnitude lower than the measured permeability of 0.1 μD. Injecting 60 million tons (Mt) of CO$_2$ at a rate of 1.5 Mt/year into the Gassum Formation for 40 years indicates that, with permeability above 1.0 μD, overpressure can be transmitted through the 530 m thick Fjerritslev Formation caprock and further up into the overburden layers.

© 2014 Elsevier Ltd. All rights reserved.

1. Introduction

1.1. Background

During the period 2007–2012 a Carbon Capture and Storage (CCS) demonstration project was considered in the North Jylland region of Denmark. The project would have involved the post-combustion capture of CO$_2$ from the Nordjyllandsværket coal power station at Aalborg followed by geological storage of the CO$_2$ in a nearby onshore saline aquifer (Gassum reservoir) within the Vedsted structure (Christensen et al., 2012). The project was temporarily stopped in 2011. The investigation license was active during 2011 and as a part of that, research activities were initiated related to key technical issues, one being to gain better understanding of formation pressure buildup and pressure transmission through the caprock Fjerritslev shale formation due to CO$_2$ injection. Various research studies have been evaluating pressure response as a result of injecting large volumes of CO$_2$ into saline aquifers for safe storage over long period of time. Most of these studies are conceptual due to the scarcity of site specific 2D or 3D seismic data and petrophysical data of the formations (Birkholzer

et al., 2009; Buscheck et al., 2012; Zhou et al., 2008). One of the concerns raised in the licensing process is the environmental impact of large-scale pressure buildup in the storage formation (Gassum) and related brine displacement which may affect the quality of the fresh water resources in the overlying Chalk Group which may experience water table displacement and changes in discharge and recharge zones. This question can be addressed if overpressure maps are generated as input for hydrogeological modeling (not within the scope of this work) of brine displacement.

The Vedsted structure is an onshore saline aquifer targeted for CO_2 storage and without considering fluid production (i.e., extraction), which can increase CO_2 storage capacity and relieve pressure buildup, we are investigating this structure as an injection-only formation. In the absence of fluid production from injection-only-industrial scale saline formations, geological storage of CO_2 may result in a large pressure buildup and transmission, persisting both during and sometime after injection has ceased (Buscheck et al., 2012). Thus, pressure buildup is considered to be a limiting factor on CO_2 storage capacity and security, and storage-capacity estimates based on effective pore volume available for safe trapping of CO_2 may have to be substantially reduced (Birkholzer and Zhou, 2009). There is also the need to evaluate overpressure development within the injection site in order to stay below the threshold pressure for fracturing of the caprock. Previous conceptual simulation studies (Birkholzer et al., 2009; Buscheck et al., 2012; Zhou et al., 2008) have shown that pressure development within the storage formation and lateral and vertical transmission to the surrounding and the overburden layers is largely determined by the hydraulic connectivity between the deep saline formations and the fresh water aquifers overlying them. The assumptions about hydraulic properties of the sealing layers are important in simulation studies for CO_2 sequestration. The main hydraulic properties to be investigated include compressibility, permeability and porosity of the caprock. In order to simulate CO_2 sequestration in the Gassum Formation reservoir (primary reservoir) and to investigate pressure buildup and transmission through the Fjerritslev Formation (primary caprock) to the overburden layers, our goal is to evaluate data for compressibility, permeability and porosity of the sealing formation, and then use this for building scenarios to illustrate the associated ranges of results and the consequences of uncertainty about input parameters.

1.2. Compressibility

In situ compressibility of shale can be determined from various sources: (a) sonic velocity and bulk density data of well logs, (b) measurements on centimeter to meter scale in the field or from, (c) ultrasonic velocity data measured in the laboratory on centimeter scale core samples (Mbia et al., 2013a,b). Compressibility determination from velocity and density data is often termed dynamic compressibility. Compressibility can also be determined from stress–strain data during geotechnical testing on centimeter scale core samples and this type is often referred as static compressibility. Urgent need for compressibility data for deeply buried caprocks has prompted these investigations. These data have been scarce and difficult to find in the available literature, probably because they were not that useful for reservoir simulation studies compared with reservoir rocks. Previous studies on reservoir rocks have shown that static compressibility from hydrostatic testing is often higher than dynamic by orders of magnitudes (Fjær, 2009; Holt, 2012; Tutuncu et al., 1994; King, 1970; Walsh, 1965; Yale et al., 1995). Acoustic wave propagation in dry, clean (clay free) rock is predominantly an elastic process (Walsh, 1965) and both dynamic and static compressibility determination in such rocks are supposed to be similar, but occurrences of non-elastic processes may cause them to differ according to Fjær et al. (2012). The differences

between static and dynamic compressibility in rocks are suggested to be due to the departure from linear elasticity due to the influence of strain amplitude, length of stress path, stress history, rock volume involved, and drainage conditions (Cheng and Johnston, 1981; Fjær et al., 2012; Simmons and Brace, 1965). Walsh and Brace (1966) explained that the difference may be due to the presence of highly compliant cracks which affect static deformation differently than the dynamic. The standard caprock compressibility used in many CO_2 reservoir simulation studies (Birkholzer et al., 2009; Buscheck et al., 2012; Jin et al., 2012; Pruess et al., 2002; Zhou et al., 2008) is 4.5×10^{-5} bar^{-1} which was measured for unconsolidated reservoir rocks by Newman (1973). Zhou et al. (2008) reported that up to 1.0×10^{-3} or 1.0×10^{-2} bar^{-1} order of magnitude can be achieved in plastic clays. Static compressibility under hydrostatic loading condition is different from uniaxial loading behavior (Khatchikian, 1995; Ong et al., 2001; Yi et al., 2005) and does not represent true reservoir conditions of stress (Anderson and Jones, 1985; Lachance and Anderson, 1983; Teevu, 1971). We will present experimental data on caprock compressibility determined from three different methods: (a) stress–strain, (b) ultrasonic velocity and (c) well log velocity data of Fjerritslev Formation (shale) from two analog wells Stenlille-2 and -5 (detailed laboratory procedure have been presented by Mbia et al. (2013a,b)).

1.3. Permeability

Permeability of the shale matrix is an important parameter determining the extent to which pressure propagates in shale caprock. Unlike other sedimentary rocks, shales have very low permeability that often prevents vertical escape of pore fluids. This has resulted in abnormal pore pressure occurrences in some sedimentary basins (Berg and Habeck, 1982; Bigelow, 1994; Chapman, 1972, 1994; Dickey et al., 1968; Dickinson, 1953; Freed and Peacor, 1989; Magara, 1971; Schmidt, 1973). There are several factors that can naturally elevate the pore pressure in shale including compaction of fluid-saturated sediments (Dickinson, 1953; Magara, 1975a; Nazmul et al., 2007; Peltonen et al., 2009, 2008), transformation of smectite to illite (Freed and Peacor, 1989), and thermal expansion of fluids (Magara, 1975b). The abnormal pressures once generated can equilibrate to the hydrostatic gradient with time except when the vertical and horizontal escape of fluid is limited by a shale unit of high capillarity or very low permeability. This phenomenon of abnormal pressures is often associated with hydrocarbon generation where the shale prevents upward migration due to its low permeability and high capillarity to the non-wetting phase (Berg, 1975). In this study, we are dealing with case study of CO_2 sequestration in Gassum Formation, an onshore aquifer with normal hydrostatic pressure. The magnitude of overpressure development within the aquifer during the entire injection period will depend on the rate at which brine escapes to the surrounding formations. In cases with sufficiently low caprock permeability this may also limit the flow of aqueous pore fluids (Bradley, 1975; Bredehoeft and Hanshaw, 1968; Deming, 1994; Hunt, 1990) and if this occurs we should expect more overpressure in the aquifer.

Shale permeability is shown in the literature to vary widely by orders of magnitude from as high as hundreds of microdarcies to as low as hundreds of nanodarcies (Armitage et al., 2011; Hou et al., 2012; Josh et al., 2012; Reece et al., 2012; Zhou et al., 2010) with values well above and below those required for pressure seals over characteristic geologic and reservoir production time scales (Bredehoeft et al., 1983; Dewhurst et al., 1999, 1998; Katsube et al., 1991; Kwon et al., 2001; Lin, 1978; Magara, 1971; Young et al., 1964). The variation depends on porosity, clay mineralogy and content, and texture (Dewhurst et al., 1998; Katsube et al., 1991; Kwon et al., 2004; Revil and Cathles, 1999), all of which may change with burial (Dzevanshir et al., 1986; Hower et al., 1976;
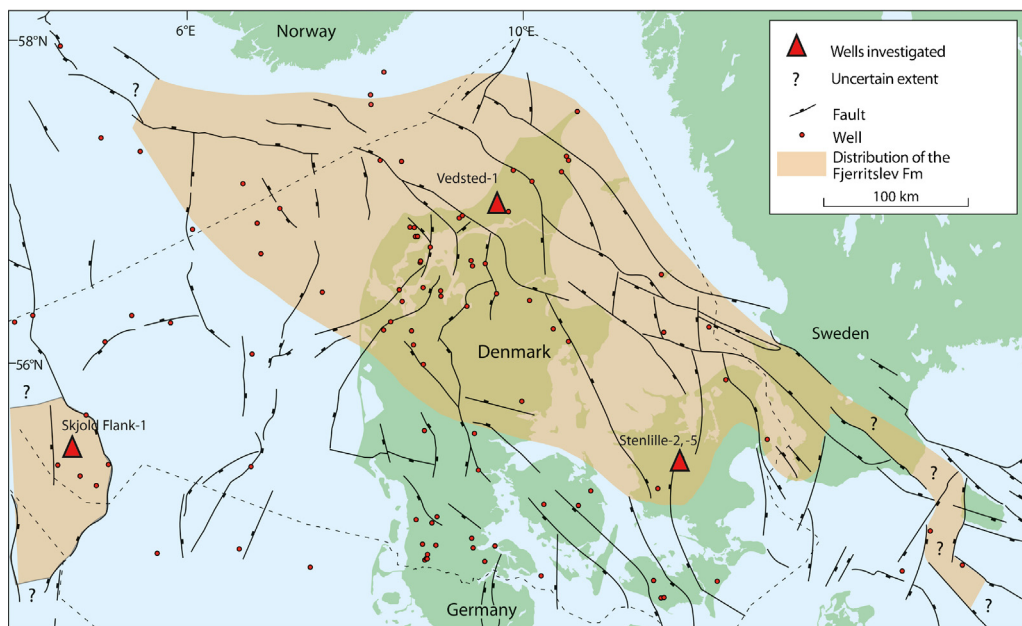
Fig. 1. Map showing location of Stenlille and Vedsted-1 wells and the outline of the extent of the Fjerritslev Formation in the Norwegian–Danish Basin to the Northeast and North Sea Central Graben to the Southwest.
Modified after Petersen et al. (2008).

Kim et al., 1999; Lee et al., 1985). Permeability may also depend on pore fluid composition if pore throats available for fluid flow are modified by local clay swelling and/or formation of hydrated complexes at clay-fluid interfaces (Norrish, 1972; Sparks, 1995; Scott and Smith, 1966; Sposito et al., 1999; Van Olphen, 1977). Clay aggregates made up of swelling clays exhibit extremely low permeability to the flow of water (Faulkner and Rutter, 2000; Moore et al., 1982), so permeability of clay aggregates depends on electrolytes in the pore fluid (Mesri and Olson, 1971; Olsen, 1972; Whitworth and Fritz, 1994). Permeability of deeply buried shales, with abundant illite and little or no smectites, are expected to show less chemical sensitivity than permeability of shallow mudstones with higher modal swelling clay contents. Yet, transport properties may continue to depend on fluid composition if cation exchange that occurs at inter granular clay–fluid interfaces and pores are affected by changed dimensions of the diffuse double layer (Kwon et al., 2004) and with all this in mind, it is still necessary to measure and model shale permeability of the caprock below which CO_2 is to be stored in order to make predictions about storage security.

2. Methodology

2.1. Petrophysical data collection

The ideal situation would be to use Fjerritslev Formation core samples from the Vedsted-1 well situated at the Vedsted structure for this study, but because of the lack of core material in this location, cuttings samples were used and for analogy combined with cuttings samples from two other wells penetrating the same formation although at another location (Stenlille-2 and Stenlille-5). The location of the wells and the distribution of the formation are shown in Fig. 1. Preserved core samples were obtained from Stenlille-2 and Stenlille-5 as shown in the lithostratipraphy of the formations in Fig. 2. Well logs and final well reports were used to develop a sampling strategy. Thirty-one cuttings samples and a number of plugs were drilled from the preserved core samples (Fig. 3) and were studied. Retrieval of the core samples from their in situ stresses to surface condition causes the sample to expand,

introducing unloading or artificial microscopic fractures as shown by Backscatter electron micrograph images of selected samples of Fjerritslev Formation in Fig. 4. These fractures make laboratory testing susceptible to artifacts and interpretation errors unless special procedures are applied. Detailed experimental procedure, description, and results were presented by Mbia et al. (2013a,b).

The bulk mineralogical composition as derived from X-ray diffraction (XRD) of samples from the Fjerritslev Formation shows on average 40% quartz, 1% K-feldspar, 1% plagioclase, 3% calcite, 2% dolomite and 2% pyrite as non-clay minerals. The clay fraction in all the samples is dominated by illite (23%) and kaolinite
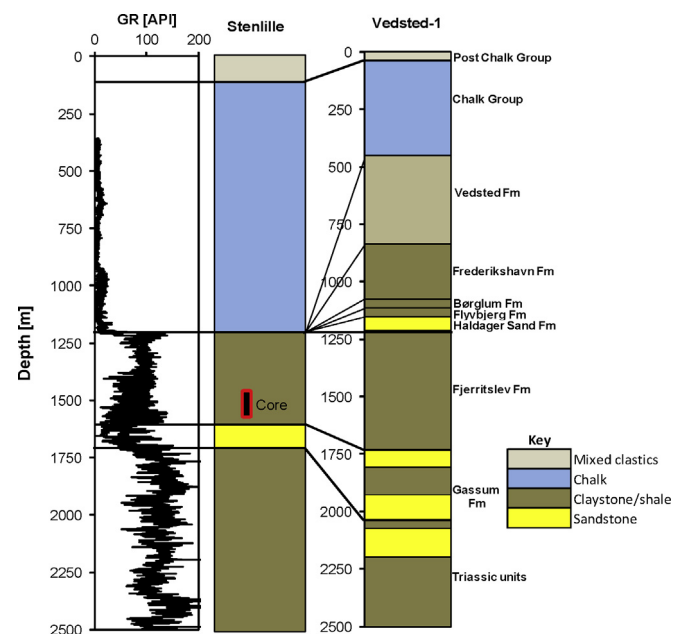

Fig. 2. Lithostratigraphical correlation of Stenlille and Vedsted-1 wells from logging data. The gamma-ray log (GR) from a Stenlille well is shown. Core samples were taken from Fjerritslev Formation in Stenlille well as indicated by the plug shape with red border.
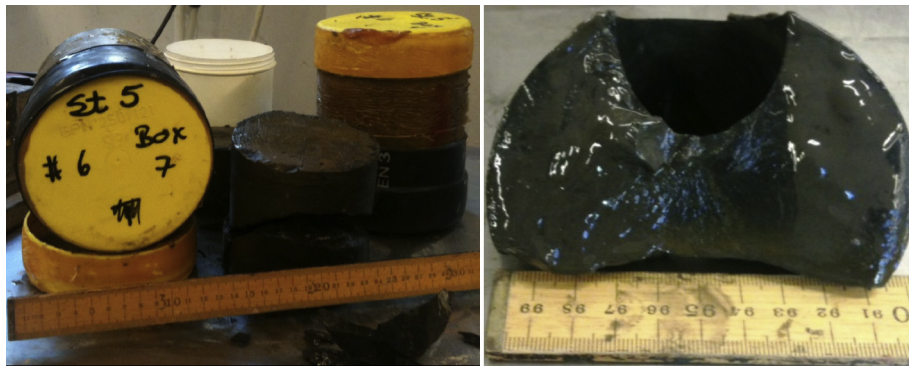
Fig. 3. Core samples from which plugs were drilled for laboratory testing.

(27%) while chlorite occurs in small amount (about 1%). Porosity was measured by three different methods and includes: helium porosimetry-mercury immersion (HPMI), mercury injection capillary pressure (MICP) and nuclear magnetic resonance (NMR). Porosity analysis from HPMI method was carried out on cutting samples and the results range from 24% at 1390 m to about 11% in the deeper samples at 2100 m. MICP analysis was also performed on cuttings samples at depth interval between 1484 m and 1576 m and the porosity result range from 9% to 14%. NMR measurements were made on core samples and the porosity result ranges from 18% to 21%. Porosity results obtained from the three methods are shown in Fig. 5. The results indicate that the porosity is dependent on the method used, and often the choice of caprock porosity data to use in simulation studies will depend on the individual modeler. In our case we have decided to use porosity data from MICP measurements which in essence is considered as a measure of the effective porosity which is available for fluid movement. HPMI and NMR in principle give a measure of total porosity and we expected similar porosity results from these two methods. Presence of unloading fractures in the core samples are regarded as artifacts and are responsible for the too high NMR porosity and therefore the NMR porosity was disregarded as this is not associated with in situ conditions.

2.1.1. Permeability data

Permeability measurement was conducted on both vertical and horizontal core samples by constant rate of strain experiments as described by Wissa et al. (1971). The detailed laboratory procedure is described by Mbia et al. (2013a,b). The measured permeability gives 0.2 µD for vertical and 9.0 µD for the horizontal samples giving k_v/k_h ratio of approximately 0.02. The high value for horizontal permeability could be because the material is more isotropic in

this direction due to their depositional history which might have enhanced pore connectivity. In addition the, Fjerritslev Formation permeability was obtained using three alternative methods: (a) modeled from Brunauer–Emmett–Teller (BET) specific surface and porosity using the Kozeny (1927) approach, (b) combined NMR and MICP data (Hossain et al., 2011), and (c) from elastic (velocity) data (Mbia et al., 2013a,b). The results are compared in the permeability-porosity plot shown in Fig. 6. The modeled permeability ranges from 1.0 to 0.06 µD and the majority of the modeled permeability falls in the same order of magnitude as the measured vertical permeability.

2.1.2. Compressibility data

Laboratory measurements were carried out on 1½ inch diameter core plug samples from the Stenlille-2 and -5 wells and the detailed procedure is described by Mbia et al. (2013a,b). The experiments were performed under drained conditions. A series of uniaxially confined loading, unloading, and reloading stress paths were applied up to the in situ stress level to close all the unloading fractures shown in Fig. 4. Static compressibility was determined from the loading and unloading stress paths. Compressibility determined from stress-strain loading-reloading data ranges from 4 to 10×10^{-5} bar^{-1} while that from the beginning of the unloading stress–strain data ranges from 0.2–0.6×10^{-5} bar^{-1}. The loading experiments were accompanied by continuous ultrasonic recording of compressional and shear wave velocities. The dynamic compressibility determined from ultrasonic compressional velocity data ranges from 0.3 to 0.5×10^{-5} bar^{-1} corresponding to static unloading compressibility at the beginning of the unloading stress path at reservoir conditions and these two compressibilities measure the elasticity of the material. Static compressibility from loading stress-strain tends to give higher values due to the influence
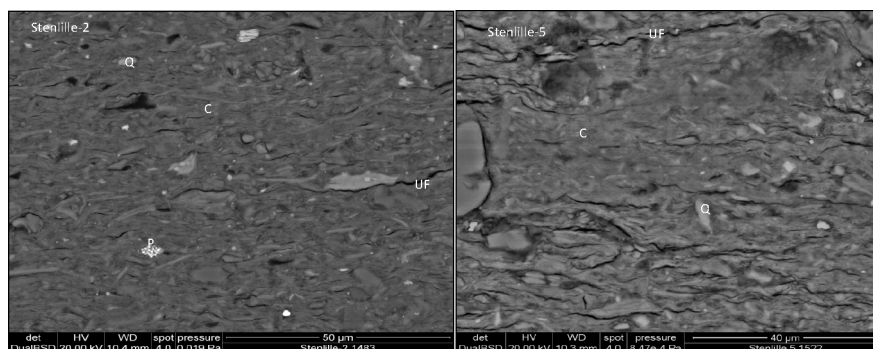

Fig. 4. Backscatter electron micrographs images of selected samples from Jurassic shale obtained from the Stenlille wells showing significant amount of silt (Q) to be present in the clay-rich matrix (C) with framboidal pyrite (P). The pore network is too small to be visible at this resolution, whereas unloading fractures (UF) due to sample retrieval are visible. Holes, where silt grains have fallen out of the sample are also visible.
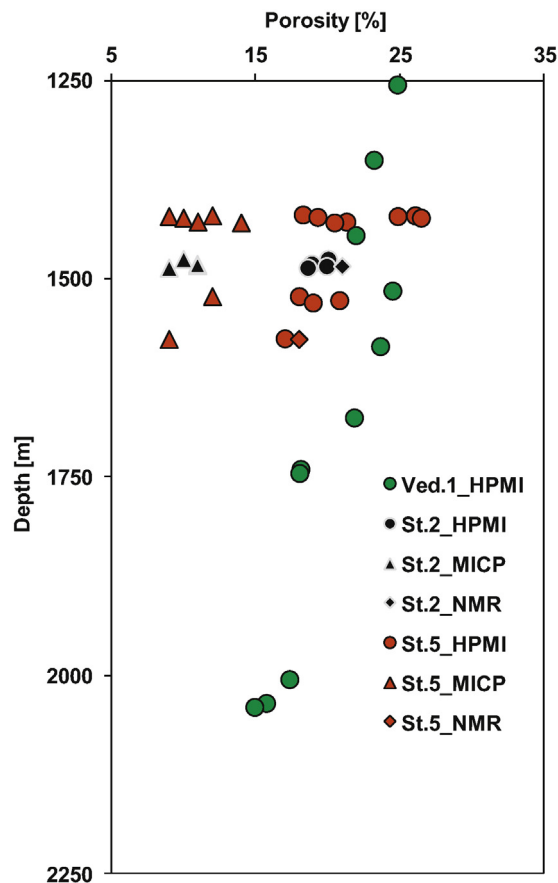
Fig. 5. Porosity obtained from Helium porosimetry-mercury immersion (HPMI), mercury intrusion capillary pressure (MICP) and nuclear magnetic resonance (NMR) methods versus depth for cuttings and selected core samples from Vedsted-1 and Stenlille-2 and -5.

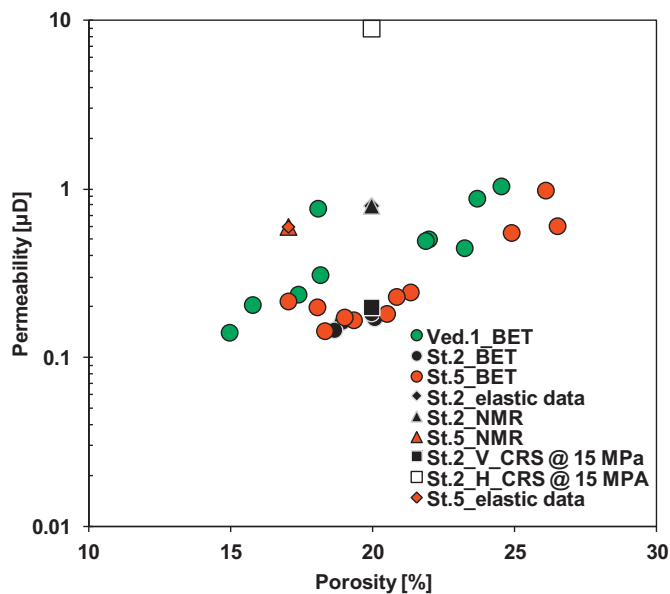Modified after Mbia et al. (2013a,b).

Fig. 6. Plots of modeled and measured permeability versus HPMI porosity. Permeability measured indirectly from constant rate of strain (CRS) experiment is shown by the empty and black square corresponding to the vertical and the horizontal sample respectively. BET is permeability modeled from the specific surface of the grain and porosity by Kozeny's model. Elastic data is permeability modeled from equivalent pore radius (r_p) and r_p is modeled from compression, shear and bulk modulus. NMR is permeability modeled from combined NMR and MICP data.
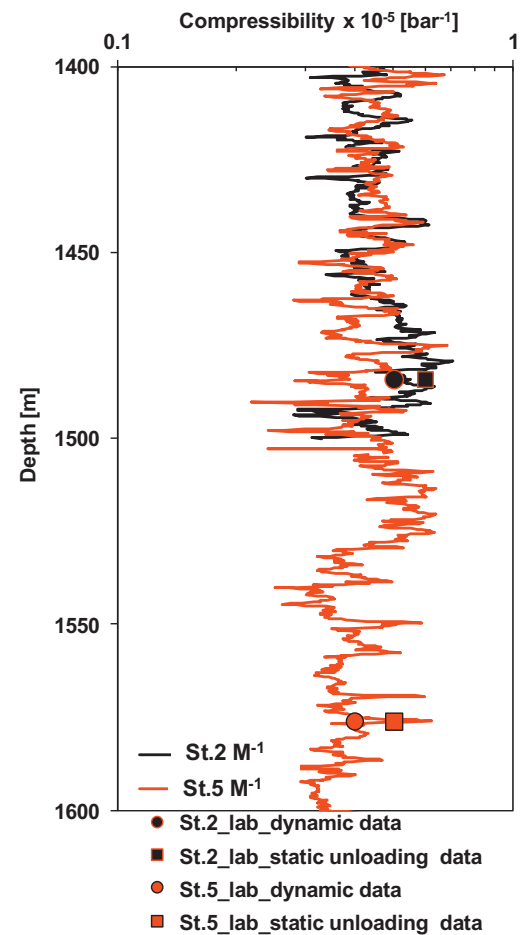

Fig. 7. Plot showing correlation of mean value of compressibility obtained from ultrasonic velocity and that from unloading stress–strain data of laboratory measurements on core material to that from sonic velocity of well log data from Stenlille-2 and -5. M^{-1} is dynamic compressibility calculated from compressional modulus obtained from the sonic velocity log and St.2 dynamic is from laboratory data while St.2 static is obtained from the stress–strain unloading data during consolidation experiment.

of the unloading fractures. In reservoir simulation studies dynamic compressibility determined from compressional velocity data or from the early unloading stress–strain data in uniaxial consolidation experiments is preferable because it represents the elastic behavior of the material at reservoir conditions. Fig. 7 shows the correlation of compressibility data assessed in the laboratory to field data of sonic velocity and bulk density of Stenlille-2 and -5 well logs.

2.2. Model set-up and parameters

2.2.1. Vedsted structure

The Vedsted structure located in the Northern part of Jylland in Denmark is situated in a small graben structure bounded by northwest–southeast trending faults. The graben is part of the Triassic rift system forming the deep Fjerritslev Trough (Michelsen et al., 2003). The site comprises the Gassum Formation and the Haldager Sand Formation forming primary and secondary reservoirs in the saline aquifer. The structure is mapped as a small elongate closure approximately 250 m high covering an area of about 31 km^2 and the depth to top Gassum reservoir is about 1900 m below mean sea level. The target reservoir layer is the 290 m thick Gassum Formation which is intercalated with low permeability shale sequences. The seal is the 530 m thick low permeable shale

Table 1
Hydraulic properties of the formations in Vedsted site. The measured k_v/k_h ratio is 0.02 but for simplification we have used 0.1 ratio in EClIPSE 100 corresponding to other lithologies given in the literature. The measured values are only for caprock and for other lithologies, general estimates are given.

Formation	Thickness (m)	Base & standard Compressibility $\times 10^{-5}$ (bar^{-1})	Permeability k_h Measured (μD)	Range (μD)	k_v/k_h	Porosity (%)
Post Chalk	30	4.5	5×10^3		0.1	23
Chalk	420	4.5	2×10^3		0.1	25
Vedsted	390	4.5	15×10^3		0.1	21
Frederickshavn (shale)	230	0.5 & 4.5	1	$1 \times 10^3 - 1 \times 10^{-2}$	0.1	13
Børglum (shale)	50	0.5 & 4.5	1	$1 \times 10^3 - 1 \times 10^{-2}$	0.1	13
Flyvbjerg (shale)	20	0.5 & 4.5	1	$1 \times 10^3 - 1 \times 10^{-2}$	0.1	20
Haldager sand	80	4.5	267×10^3		0.1	17
Top Fjerritslev (shale)	174	0.5 & 4.5	1	$1 \times 10^3 - 1 \times 10^{-2}$	0.1	11
Middle Fjerritslev (shale)	174	0.5 & 4.5	1	$1 \times 10^3 - 1 \times 10^{-2}$	0.1	11
Base Fjerritslev (shale)	174	0.5 & 4.5	1	$1 \times 10^3 - 1 \times 10^{-2}$	0.1	10
Top Gassum (sandstone)	64	4.5	63×10^3		0.1	19
Middle Gassum (shale)	47	0.5 & 4.5	1	$1 \times 10^3 - 1 \times 10^{-2}$	0.1	9
Middle Gassum (shale)	47	0.5 & 4.5	1	$1 \times 10^3 - 1 \times 10^{-2}$	0.1	9
Middle Gassum (shale)	47	0.5 & 4.5	1	$1 \times 10^3 - 1 \times 10^{-2}$	0.1	9
Base Gassum (sandstone)	85	4.5	70×10^3		0.1	14
Skagerrak (sandstone)	331	4.5	20×10^3		0.1	14

1μD $= 1 \times 10^{-18}$ m^2; 1 bar $= 1 \times 10^5$ Pa.

of the Fjerritslev Formation overlying the entire sequence constituting a flow barrier due to the high capillary pressure and very low permeability. The reservoir is underlain by the Skagerrak Formation with uncertain properties. Overlying the primary caprock is the Haldager Sand Formation forming an upside storage potential with excellent reservoir properties. This formation has a net thickness of about 80 m with porosity of about 17% and permeability of 200–300 mD. The thickness of all overburden formations is presented in Table 1.

2.2.2. Model parameters

In Table 1, we present the reservoir properties of the various formations in the Vedsted structure. The storage capacity for CO_2 in this case depends on the compressibility, permeability and porosity of the Gassum Formation but also on the properties of the Fjerritslev Formation. The sensitivity study is based on scenarios with varied compressibility and permeability of the Fjerritslev Formation as shown in Table 1. The low compressibility value of 0.5×10^{-5} bar^{-1} determined for the Fjerritslev Formation will be used in the simulation and compared with the higher compressibility value referred to as standard compressibility of 4.5×10^{-5} bar^{-1} normally used for caprocks in reservoir simulation studies. Similarly for the permeability sensitivity study, we have assigned the measured horizontal permeability value of 1.0μD for the

Fjerritslev Formation and then varied the permeability over one, two and three orders of magnitudes from the measured value to cover the wide range of permeability values for shales given in the literature. The other formations maintain their base case values for all the simulations. The ratio of vertical to horizontal permeability is chosen as 0.1 and is used for all the formations including caprock for simplification. This ratio corresponds with the literature data for reservoir rocks and it will still give us the average vertical permeability value for the Fjerritslev Formation. Other initial formation and fluid parameters are a hydrostatic pressure gradient of 100 bar/km, salinity of the formation water of 270 g/l, and a geothermal gradient of 30°/km.

The relative permeability function used for the simulation was inspired by the data shown by Bennion and Bachu (2006) for the Viking Formation sandstone, and was for simplicity used for both the sandstone and the shale lithology (Fig. 8a).

The capillary pressure curve was established as a type curve for the sandstone with 0.5 bar capillary entry pressure (Fig. 8b). For the shale this curve was scaled to an entry pressure of 6.5 bar corresponding to a permeability level of around 0.3 μD according to correlation established by Thomas et al. (1968).

The compressibility of the fluids (CO_2 and water) is intrinsically taken into account in Schlumberger ECLIPSE 100 in terms of density variation with pressure.
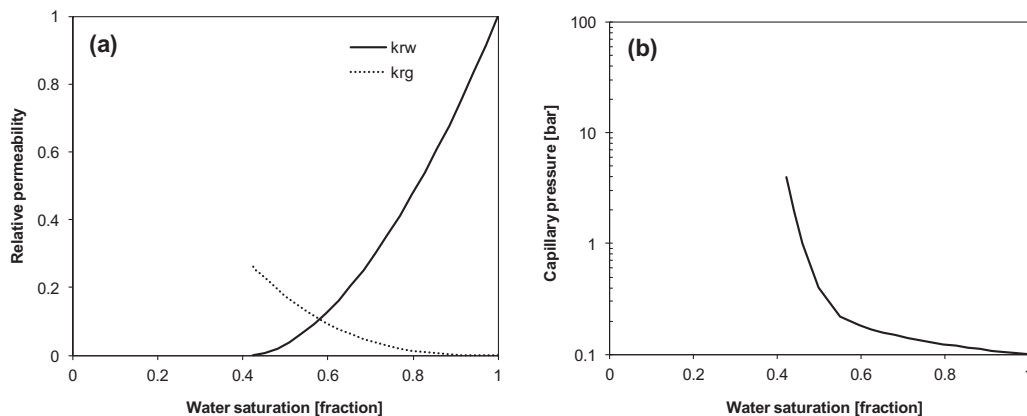

Fig. 8. Plots of relative permeability and capillary versus water saturation. a) and b) are sand stone data from Viking Formation (Bennion and Bachu, 2006). a) Was also used for shale while (b) is scaled to an entry pressure of 6.5 bar corresponding to a permeability level of around 0.3 μD according to correlation established by Thomas et al. (1968).
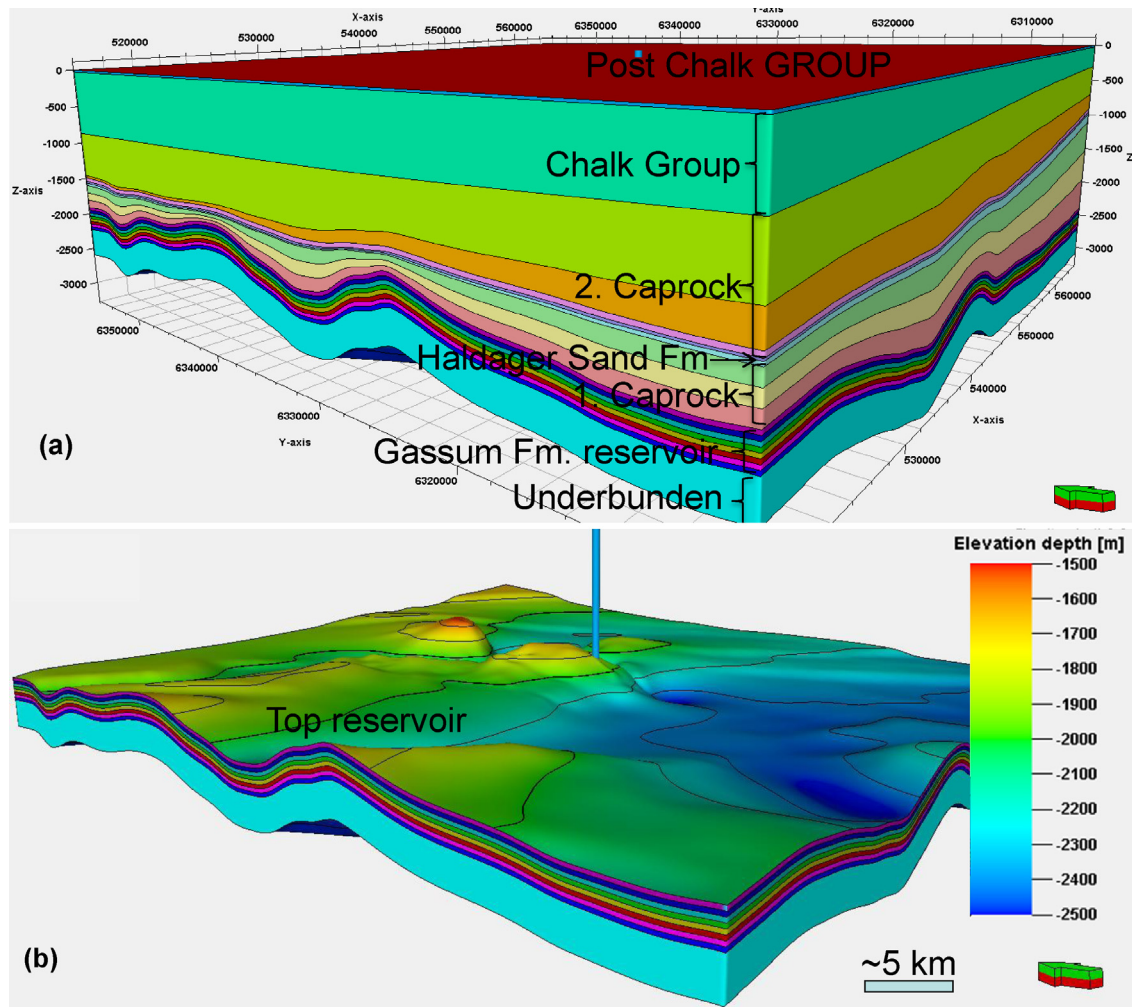
Fig. 9. Schematic representation of 3D cross-section of the model domain. (a) Entire 3D model from the sea bottom down to the Upper Triassic sandstone unit (underburden). (b) Top of the deep Gassum Formation (primary reservoir) sandwiched by thin layers of shale and the underburden. Overlying the Gasssum Formation is the Fjerritslev Formation comprising primary caprock, overlay by Haldager Sand Formation (secondary reservoir). Above the Haldager Formation is a succession of thick seconcary caprocks overlain by the Chalk Group within which the brine–fresh water interface resides.

We simulated a rate controlled injection of 1.5 tons of CO_2 per year through a single vertical well in the Vedsted structure (Fig. 9a) which is completed in the eastern side of the dome shaped anticline in the Gassum reservoir (Fig. 9b). 60 Mt of CO_2 is injection period is 40 years using the ECLIPSE 100 simulator tool. The aquifer is initially fully brine-saturated. The injection pressure has been kept 30% below the measured fracture pressure to ensure that there is no reactivation of existing fractures or creation of new fractures during the injection process.

3. Simulation results and discussion

3.1. CO₂ plume and migration

The injection of CO_2 in the Gassum Formation results in a CO_2 front which is driven upwards on the flank due to the buoyancy force and starts accumulating in the uppermost layer of the formation and immediately hits the less permeable caprock of Fjerritslev Formation. This process forms a CO_2 plume with the largest areal extent at the top of the storage formation. For simplicity we have chosen to show part of the reservoir around the injection well where the plume is limited. Fig. 10 shows CO_2 saturation and distribution for the base case in the top reservoir around the injection well after 40 years of injection. The CO_2 saturation and distribution

for the base case (Fig. 10) is similar to that of the other cases. The plume is narrow in the injection layer and as the injected volume increases CO_2 rises due to the buoyancy force and then spreads out under the caprock (Fjerritslev Formation). For all cases the plume extends over an area of about 11–13 km² in the upper layer of the
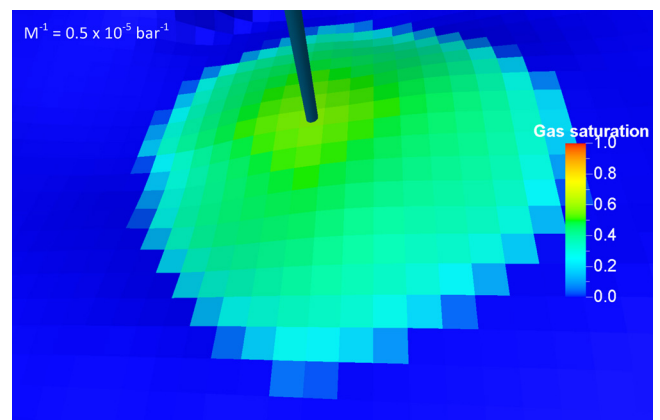

Fig. 10. Saturation and distribution of CO_2 plume in the uppermost layer of Gassum reservoir after 40 years of 60 Mt CO_2 injection for the base case. Cell size is 0.2 × 0.2 km².
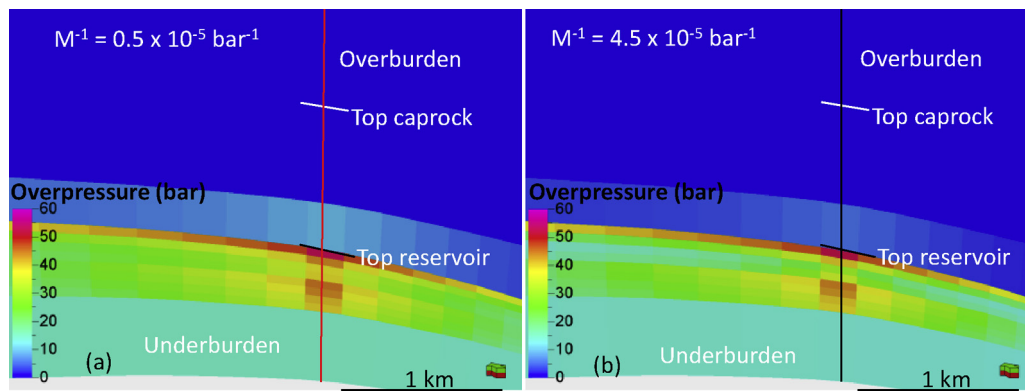
Fig. 11. Cross section of the reservoir and the Fjerritslev Formation showing overpressure development (in bar) and transmission from the injection cells after 40 years of 60 Mt CO_2 injection. (a) The case with measured caprock compressibility; (b) the case with standard caprock compressibility.

Gassum Formation filling the entire structure and spreading laterally after 40 years of injection. The shape of the plumes during the injection is determined by the morphology of the aquifer/caprock interface and in this case it is circular because the dome is fairly regular.

At the end of the injection period, the plume is restrained under the caprock layer. The low measured vertical permeability (0.1 μD) of the caprock layer and high capillary entry pressure causes the CO_2 plume to be fully trapped during the 40 years injection period.

3.2. Compressibility and pressure development in Vedsted structure

Fig. 11 shows cross sections of the reservoir and the Fjerritslev Formation showing the areal extent of the pressure buildup and the transmission of pressure away from the injection well after 40 years of CO_2 injection for the measured or base case (Fig. 11a) and the standard (Fig. 11b) caprock compressibility. There is overpressure development throughout the entire lateral extension of the reservoir but the vertical transmission is limited to the lower layer of the 530 m thick Fjerritslev Formation sealing the reservoir. The difference in overpressure development between the base case and standard case compressibility can be seen in color contrast of the reservoir and the basal caprock in the two cross sections. However in order to compare the difference in vertical pressure development from the reservoir to the shallower aquifers we have extracted a vertical profile as shown on the cross sections. Fig. 12 illustrates the resulting profile with red line for the base case and black line for the standard case compressibility.

The higher elastic modulus of the sealing layer, and thus reduction in effective compressibility increases the stiffness of the sealing layer which again increases pressure buildup in both the reservoir and the caprock compared to the standard case with higher compressibility. A higher compressibility causes more attenuation in the caprock and therefore reduces the resultant pressure buildup in both the reservoir and the caprock. The difference in overpressure between the base and the standard case is about 1–3 bar in the reservoir layer and about 5–6 bar in the lower section of the caprock. Despite the difference in pressure buildup in the caprock, the overpressure is contained within the Fjerritslev Formation for both compressibility cases but this could change in case the caprock is fractured or in the presence of vertically communicating faults.

Fig. 13 presents maps of the top reservoir layer showing overpressure development from the injection well and lateral transmission after 40 years of CO_2 injection for the base (Fig. 13a) and the standard (Fig. 13b) case compressibility. By extracting the overpressure profiles across the 50 km lateral extent of the model, it is possible to compare the results for different layers. The

overpressure profile, along the x-axis in Fig. 13, is shown in Fig. 14. Injecting 60 Mt of CO_2 into Gassum Formation for 40 years resulted in pressure buildup of about 40 and 35 bars for the base and standard compressibility around the injection cell. At the end of the injection period the pressure is transmitted to the boundary of the structure resulting in about 2.5 bar overpressure at the cells bordering the boundary cells. Pressure buildup at the boundary cells depends on the boundary condition applied. There are different boundary conditions applicable to reservoir simulation studies but in this case we have used a pore volume multiplier of 200 as estimated realistic value for boundary condition after having performed a sensitivity analysis of different values for pore volume
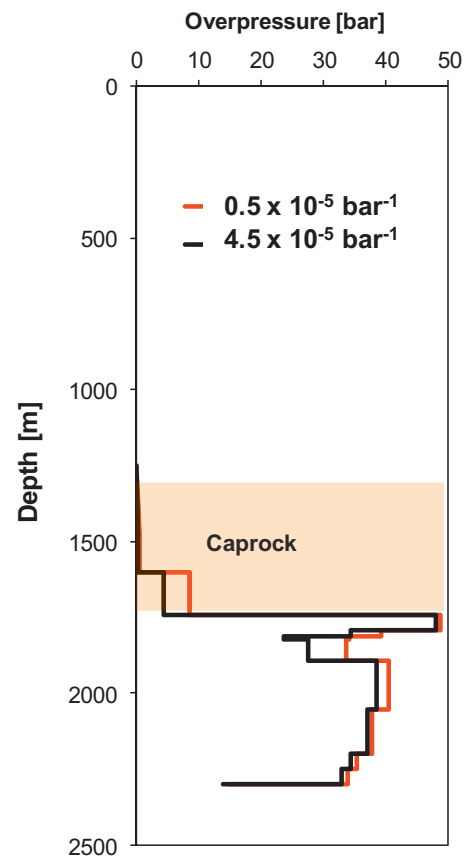

Fig. 12. Vertical profile from the injection cells (Fig. 11) showing overpressure development and vertical transmission from the reservoir to mean sea level for both measured (0.5×10^{-5} bar^{-1}) and standard compressibility (4.5×10^{-5} bar^{-1}) case after 40 years of 60 Mt of CO_2 injection.
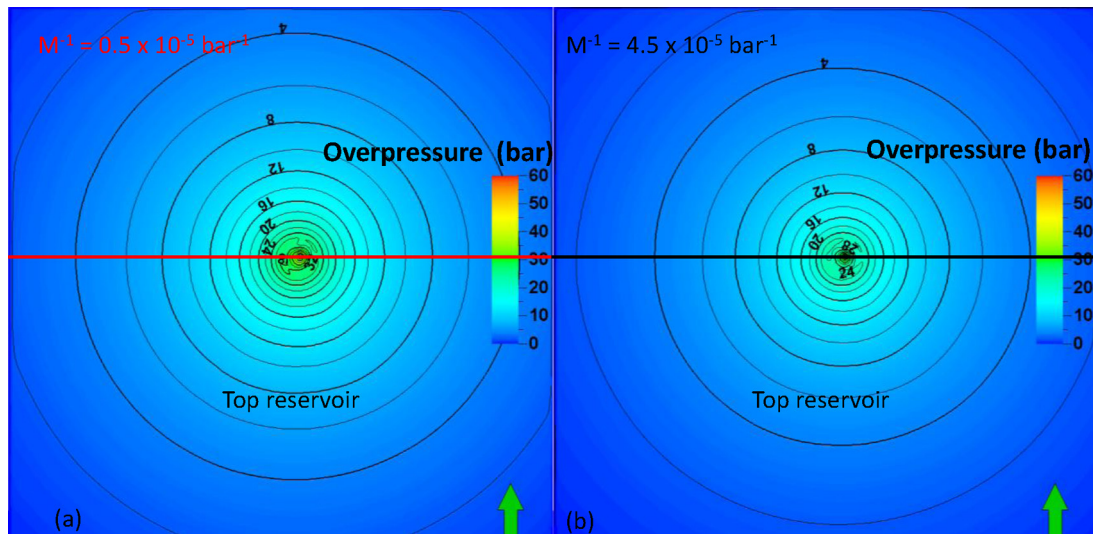
Fig. 13. Map of the top reservoir showing overpressure development from the injection well and lateral transmission after 40 years of 60 Mt CO_2 injection. (a) The case with measured caprock compressibility; (b) the case with standard caprock compressibility. 50 km line indicates the profile across x-direction.

multipliers. The overpressure difference shown in Fig. 14 between the base and standard case is about 5 bar at the reservoir close to the injection cells and about 2 bar through the entire reservoir.

3.3. Permeability and pressure development in Vedsted structure

The permeability of sealing layers plays an important role in lateral and vertical pressure development within the reservoir and the overlying aquifers. In order to evaluate the influence from caprock permeability and the consequences for pressure development in the Vedsted site, there is a need for considering a range of one to two orders of permeability below and above the experimental value. This will give an overview of possible scenarios of overpressure outcome with respect to varying caprock permeability. Fig. 15 shows cross sections of the reservoir interbedded by shale layers and the overlying layers. The caprock permeability is varied by one and two order of magnitudes smaller than and greater than the base value of 0.1 μD and the resulting layers affected by overpressure is seen as light color while the blue

Fig. 14. Pressure profile at top reservoir showing overpressure development and lateral transmission after 40 years of CO_2 injection for the case with measured and standard caprock compressibility.

color is where overpressure development is very minimal or is absent. Pressure buildup is greater in the reservoir layers but minimal or absent within the interbedded shale and shale layers. In order to compare vertical pressure development within the Vedsted structure, a vertical overpressure profile at 0.2 km from the injection cell is shown for the top Triassic unit to the mean sea level in Fig. 16. It is important to assess sensitivity of vertical overpressure development to caprock permeability within the structure and also to compare with the base case permeability. The results in Fig. 16 indicate that the experimentally determined matrix permeability of 0.1 μD for the Fjerritslev Formation does not allow overpressure transmission beyond the lower 0.2 km of the 0.53 km thick caprock layer. Reducing the matrix permeability by one order of magnitude (0.01 μD) gives the same result of vertical overpressure as the experimental value. A further reduction by two orders of magnitude (0.001 μD) resulted in a perfect seal case where there is no overpressure effect in the caprock. On the other hand, increasing the Fjerritslev Formation permeability by one order of magnitude (1.0 μD) causes a 2.0 bar overpressure in the uppermost layer of the formation but still the pressure could not be transmitted to the Haldager Sand Formation which is overlying the caprock. Increasing the Fjerritslev Formation permeability by two orders of magnitude will allow pressure transmission from the Gassum reservoir to the Haldager Sand Formation and the effect is then confined by the Flyvbjerg Formation which forms a secondary seal. In the worst case scenario, where Fjerritslev Formation permeability is increased by two (10 μD) and three (100 μD) orders of magnitude there is still no significant amount of pressure buildup in the shallow fresh water aquifer (Chalk Group). A relatively high permeability in the primary seal allows less pressure buildup in the Gassum Formation as some is transmitted vertically. The magnitude of vertical pressure buildup will also depend on the permeability of the layers above the primary caprock. This result suggests the importance of investigating hydrogeological layers and flow parameters, even at shallower depths.

However, the existence of faults connecting the reservoir and the overlying formations could strongly increase the magnitude of vertical pressure transmission, but this subject is not the scope of this work but will be addressed in subsequent work.

Fig. 17 presents maps of the uppermost layer of Gassum Formation showing pressure buildup and lateral transmission after 40 years of CO_2 injection for different caprock permeabilities. The
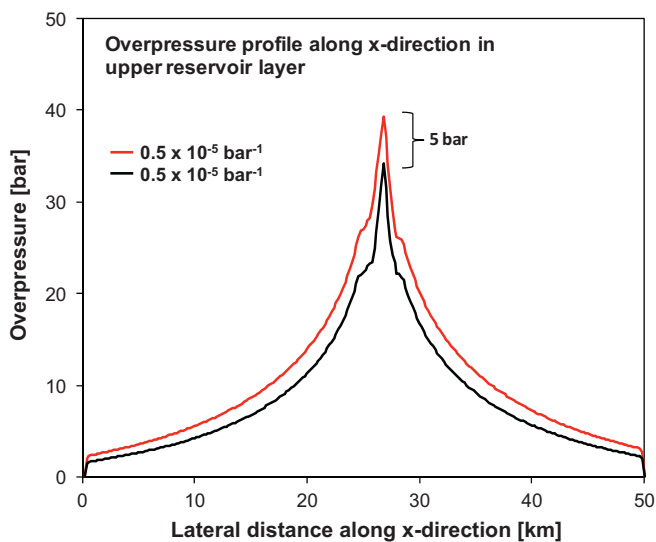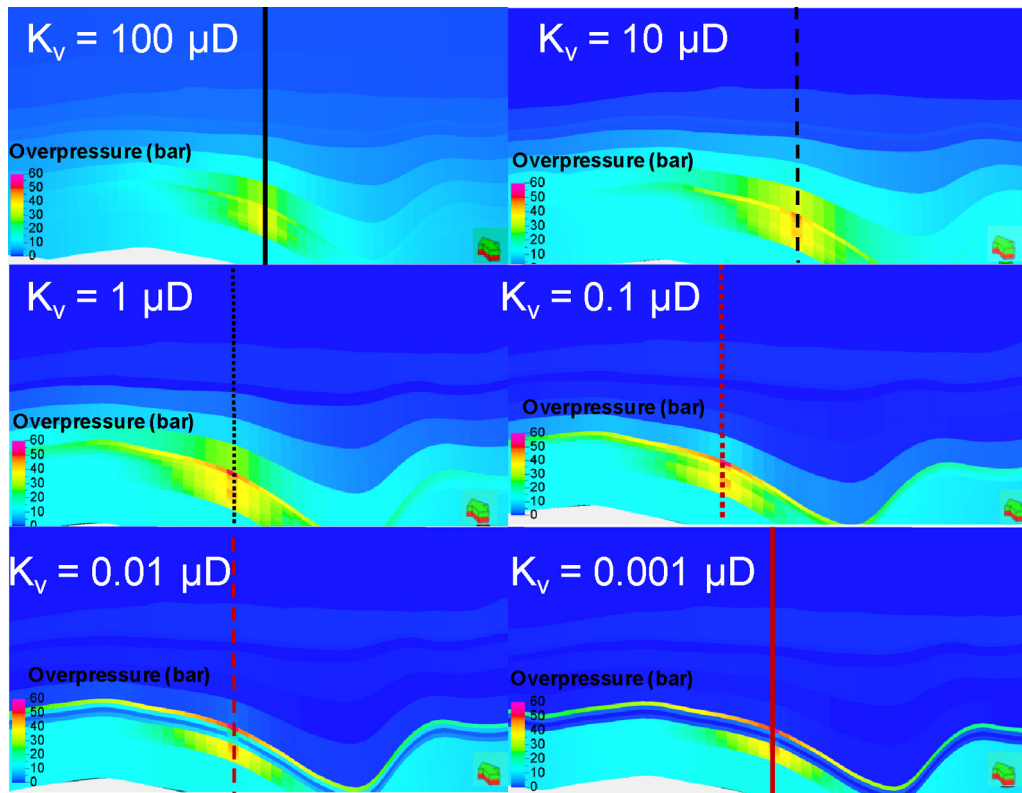
Fig. 15. Cross section of the reservoir and the overlying layers showing overpressure development (in bar) and transmission after 40 years of 60 Mt CO_2 injection for cases with different caprock permeability varied by several order of magnitudes from the measured value of 0.1 μD.
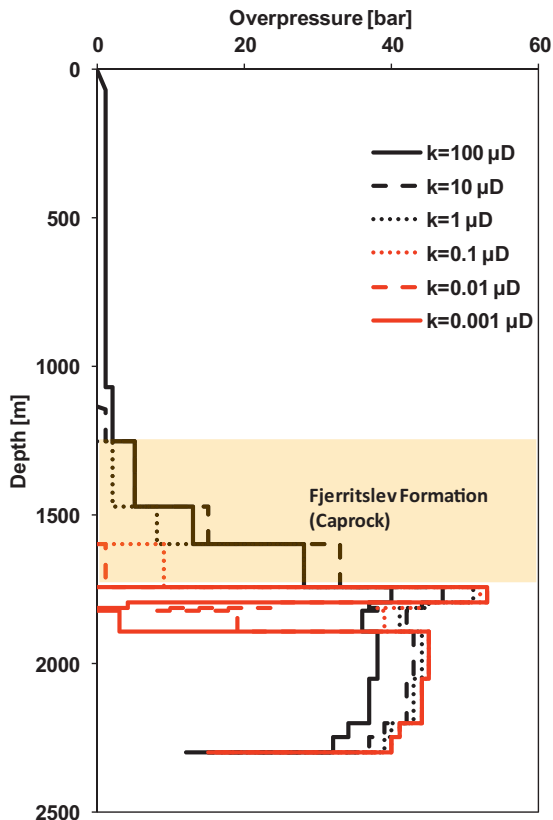

Fig. 16. Vertical profile from the injection cells showing overpressure development and transmission from the reservoir to mean sea level after 40 years of 60 Mt CO_2 injection for different caprock permeabilities.

overpressure maps clearly show that as the Fjerritslev permeability is varied from 100 to 0.001 μD, pressure buildup in the reservoir formation increases and consequently enhances the lateral transmission reaching the boundary of the Vedsted structure for the cases with < 10 μD permeability. Fig. 18 presents profiles showing the magnitude of overpressure along 50 km lateral distance through the injection cell. For the case with higher caprock permeability, the pressure buildup reaches 40 bar and reduces laterally to 0.5 bar, whereas for the lower permeability the pressure buildup reaches 53 bar at the injection point and reduces to 3 bar at the boundary. Fig. 19 presents maps of the uppermost layer of Fjerritslev Formation showing pressure buildup and lateral transmission and Fig. 20 presents profiles showing the magnitude of overpressure along 50 km lateral distance through the injection cell. The cases with higher caprock permeability (100, 10 and 1.0 μD) show pressure buildup of about 5 bar in the area close to the injection point and a reduction laterally to hydrostatic pressure before the project boundary is reached. There is no pressure buildup for the lower permeability cases including the base case. Fig. 20 shows only the profile at the base Chalk Group for the case with caprock permeability of 100 μD where pressure builds up to 1.0 bar and is transmitted laterally over 15 km radius from the center of the base layer. The other case with less than 100 μD permeability shows no pressure builds up at the base of the Chalk Group (Fig. 21).

3.4. Influence of grid effects, relaxation time, and the k_v/k_h ratio on pressure development in the Vedsted structure

3.4.1. Gridding

We are well aware that the rather coarse grid representing the Vedsted model might have some effect on the simulation results and the illustration of their magnitude. The decision about gridding was guided by practical computation time for the work on
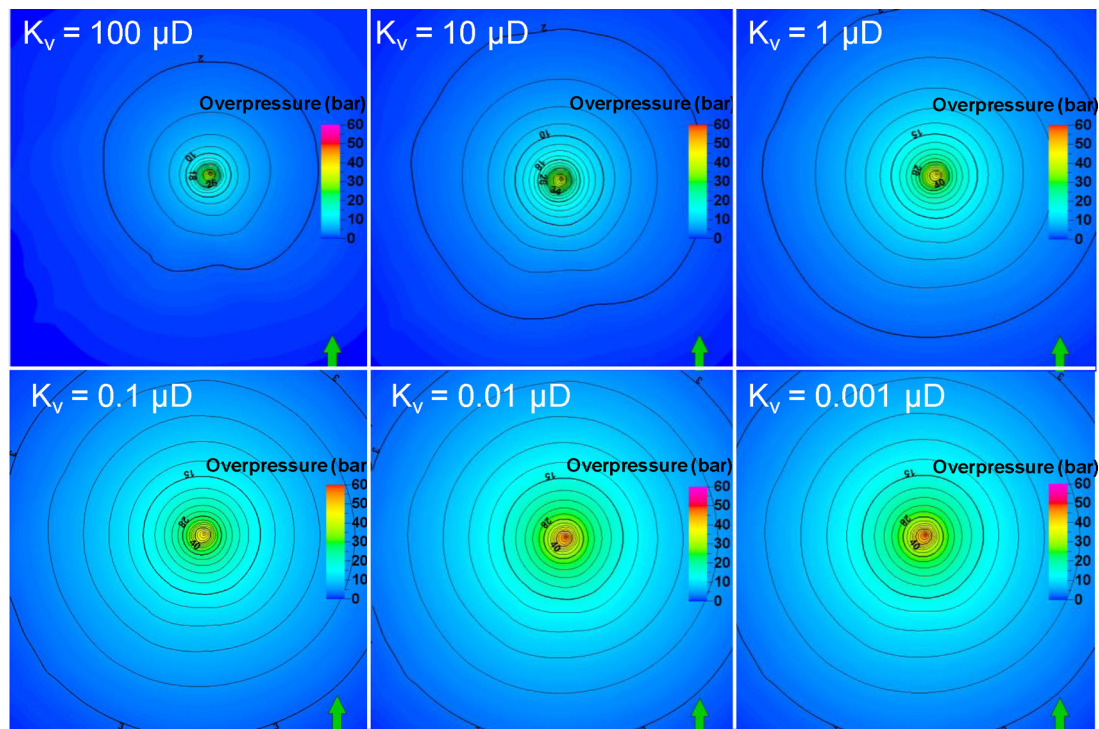
Fig. 17. Map of the uppermost layer of the reservoir showing overpressure development (in bar) from injection well and the lateral transmission after 40 years of 60 Mt CO_2 injection for cases with different vertical caprock permeability varied in order of magnitudes from the measured value of 0.1 μD.

sensitivity analysis requiring multiple simulation runs. We therefore examined the effect of grid resolution on a single example of a simulation run of pressure propagation in order to illustrate the effects. In a grid-refined model, the grid cells within a radius of 2.5 km around the injection well in the reservoir and the base caprock layers were refined vertically to 20 m grid cell thickness as shown in Fig. 22(a). The result is compared with the coarse grid model used in this study (Fig. 22b) with vertical dimension for the grid cells of 125 m and above. We accept that a large grid block size will tend to overestimate the amount of CO_2 dissolution and consequently might underestimate the pressure buildup compared with

the fine grid model version We show the comparison of the results of the simulation by examining the amount of pressure buildup in the reservoir at the base of the caprock at the end of injection at 40 years in Fig. 22(a) and (b). It seems that grid resolution has very little effect on the average pressure buildup in the aquifer and the caprock. The difference between the fine and coarse grid is seen in the details of the extent of the overpressure propagation, but there is no major difference in overpressure at the base of the caprock for the two cases. The effect of grid resolution on pressure was also investigated by Pickup et al. (2010) and their simulation results also showed that grid resolution had little effect on pressure buildup and concluded that coarse grids may be sufficient for initial assessment of storage potential.
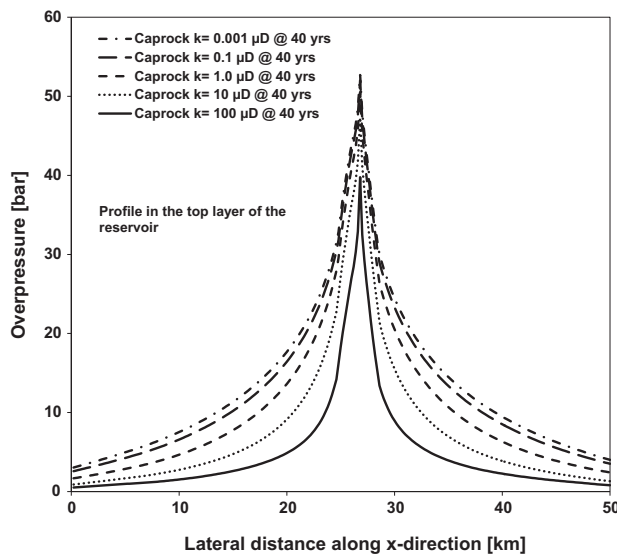
3.4.2. Pressure relaxation after injection stop

Fig. 23 shows the overpressure profile for the upper layer of the Gassum reservoir after 40 years of CO_2 injection (60 Mt) and 100 years after the end of the injection period. At the year 40, the overpressure in the upper layer of the reservoir reaches up to 55 bar. This overpressure declines rapidly in the first 5 years after the injection stops to about 20 bar and continues to decrease steadily 10 years after the end of the injection. After 100 years from the end of CO_2 injection in the Gassum reservoir the overpressure equilibrates close to the hydrostatic pressure in reservoir.

3.4.3. Permeability anisotropy

In our simulations have been used a permeability anisotropy of 0.1, which is a quite normal value for assumption about sub-grid cell layered heterogeneity. As our plug measurements for the shale gave a much smaller value of 0.02, we tested the effect of changing this anisotropy generally for the shale lithologies in the simulation. Fig. 24 compares the result of overpressure development in the base of the caprock after 40 years of CO_2 injection for the measured vertical and horizontal permeability ratio of 0.02 and that of 0.1 used in these simulations. It is seen that using the k_v/k_h ratio of 0.1, the overpressure in the base of the Fjerritslev Formation is

Fig. 18. Pressure profile in the uppermost layer of the reservoir showing overpressure development and lateral transmission after 40 years of 60 Mt CO_2 injection for the cases with different caprock permeability.
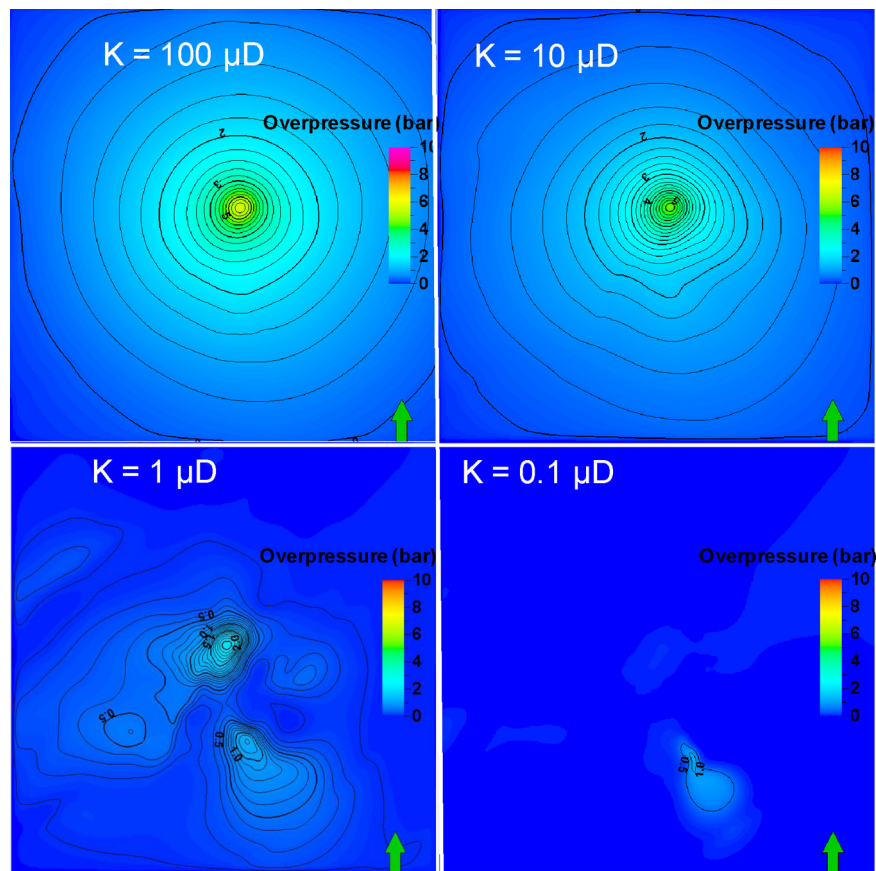
Fig. 19. Map showing overpressure in the uppermost layer of the 530 m thick Fjerritslev caprock after 40 years of 60 Mt CO_2 injection. The irregularities in the maps for the 1 μD and 0.1 μD are interpreted as numerical artifacts.
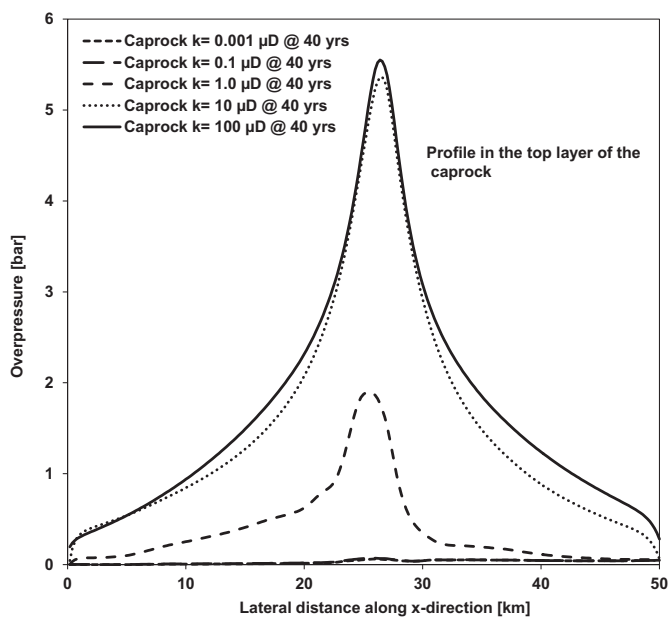
Fig. 20. Pressure profile (Fig. 18 for reference) in the uppermost layer of Fjerritslev Formation Caprock showing overpressure development and lateral transmission after 40 years of 60 Mt of CO_2 injection for the cases with different caprock permeability.

Fig. 21. Pressure profile (Fig. 18 for reference) in the base Chalk Group showing overpressure development and lateral transmission after 40 years of 60 Mt CO_2 injection. The case with 100 μD caprock permeability shows slight overpressure while the other cases show no overpressure in the Base Chalk Group.

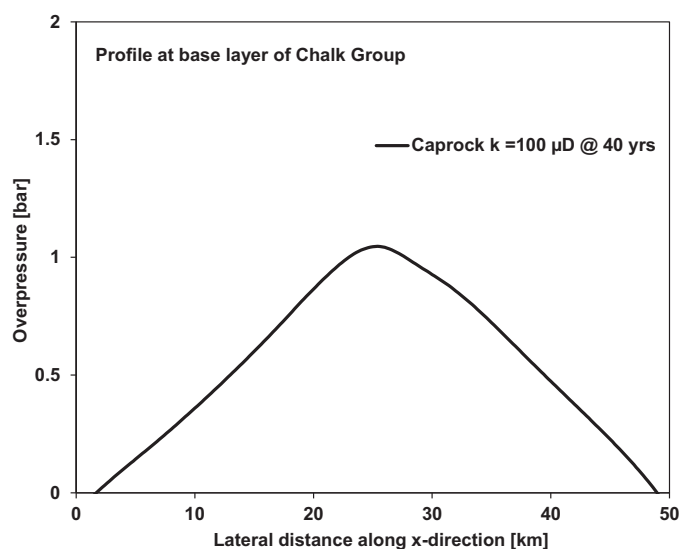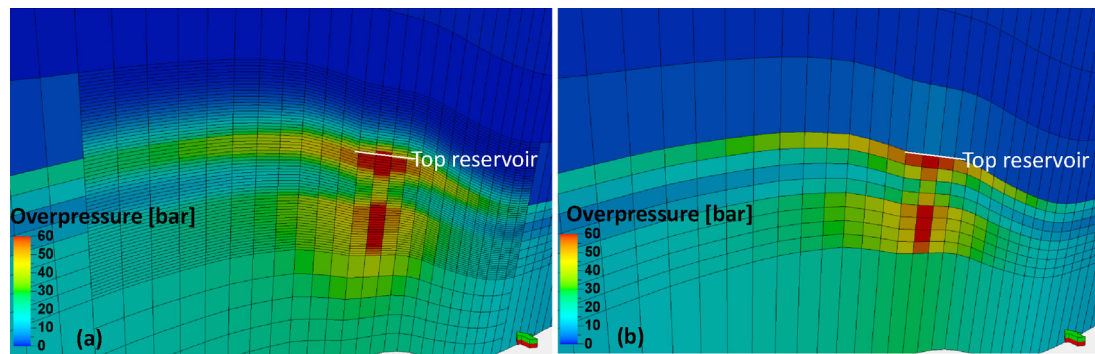**Fig. 22.** The overpressure development for both finer and coarser grids resolution. (a) Vertical grid refinement within the reservoir and the base caprock layers with each cell having vertical dimension of 20 m with the radius of 2.5 km from the injection well. (b) The coarse grid model used in this study and each cell has vertical dimension of 125 m.
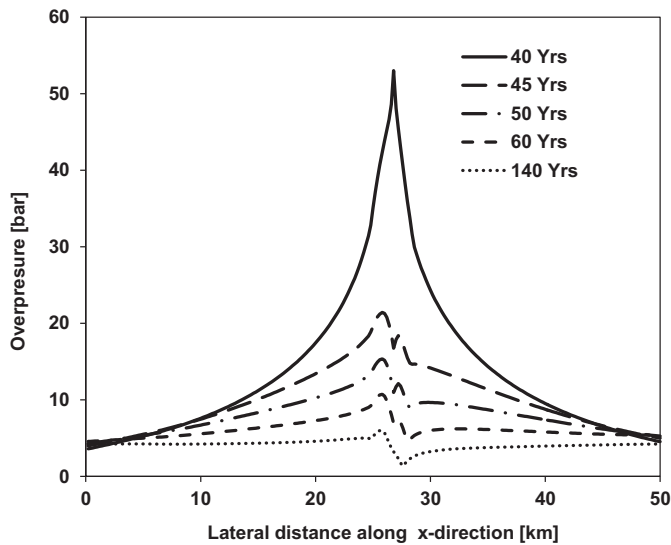

Fig. 23. The overpressure development at after 40 years of 60 Mt of CO_2 injection and 100 years after the stop of injection for the upper layer of Gassum reservoir. The irregularity in the profile peak is numerical artifacts due to the coarse grid used.
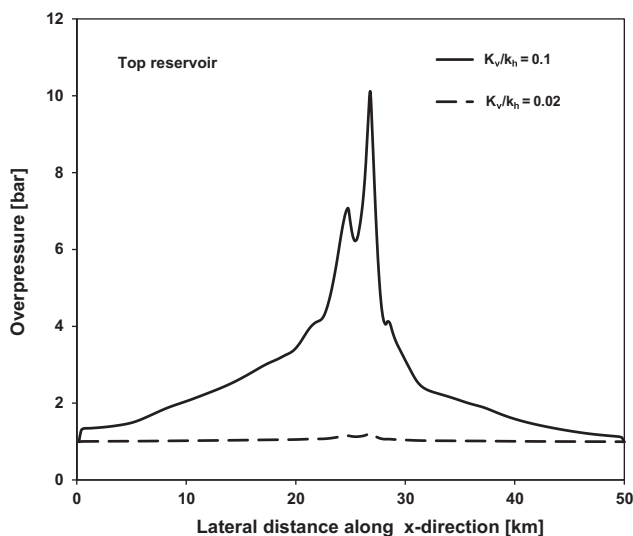

Fig. 24. Comparison of the overpressure development in the base of the caprock after 40 years of 60 Mt of CO_2 injection for measured vertical and horizontal permeability ratio of 0.02 and the value of 0.1 used in this simulations. The irregularity in the profile peak is numerical artifacts due to the coarse grid used.

10 bar higher than with a ratio of 0.02. It therefore has some importance to specify the k_v/k_h ratio of the lithology, or at least perform a sensitivity test when carrying out simulation studies for pressure development.

4. Conclusions

The influence of caprock compressibility and permeability and the consequences for pressure development have been studied for the Vedsted structure. These studies underscore the significance of obtaining valid experimental data for reservoir simulation studies. Laboratory experiments and dynamic sonic velocity data from relevant shale formations in Denmark show that shale compressibility is lower than often assumed for standard reservoir simulation studies and detailed laboratory work on this subjection is presented in the paper by Mbia et al. (2013a,b). The consequences of this low compressibility are investigated in a simulation case study. Laboratory measurements were carried out on centimeter-scale core plug samples from analog onshore wells. The experiments were performed under drained conditions. A series of uniaxially confined loading and unloading stress paths were applied to the in situ stress level to close up the induced unloading fractures. Static compressibility was determined from the loading and unloading stress paths. The loading experiments were undertaken with continuous ultrasonic recording of compressional and shear wave velocities. At reservoir conditions, dynamic compressibility is similar to the static compressibility at the beginning of the unloading stress path corresponding to elastic deformation. The analysis of both data sets indicates that Fjerritslev Formation compressibility is 0.5×10^{-5} bar^{-1} and is one order of magnitude lower than the standard value of 4.5×10^{-5} bar^{-1} normally used for shale compressibility in reservoir simulation studies.

The caprock permeability was measured by a geotechnical method of constant rate of strain (CRS) experiment and the result is compared with modeled permeability data for the same material. We found average vertical permeability of the Fjerritslev Formation (primary caprock) to be 0.1 μD.

The ECLIPSE 100 reservoir simulator has been used to investigate the effect of the measured caprock compressibility and permeability and the consequences for pressure buildup and transmission, vertically and laterally within the Vedsted structure. This has been evaluated when 60 Mt of CO_2 is injected into the Gassum Formation during 40 years.

The pressure buildup in the top of the storage formation is 5 bar higher for the measured caprock compressibility compared with the standard caprock compressibility normally used in reservoir simulation studies. This pressure difference can also play a significant role by increasing the magnitude of the overpressure in

the shallower aquifers in the presence of permeable fractures and faults. Therefore well-designed investigations of formation properties are recommended when carrying out reservoir simulation studies in order to minimize the risk of underestimating or overestimating pressure buildup in CO_2 storage sites.

The sensitivity of the pressure buildup and transmission for varying caprock permeability indicates that when increasing Fjerritslev Formation permeability from 0.1 μD to 1.0 μD, the overpressure could not be transmitted through the 530 m thick caprock, but by increasing further the permeability to 10 and 100 μD, overpressure is transmitted through the caprock and up to the Chalk Group. Reducing the caprock permeability by one or two orders of magnitude further reduces the vertical pressure buildup but increases lateral pressure buildup and the extent within the storage formation. It is also important to note that the ratio of vertical to horizontal permeability has some influence on the vertical pressure transmission.

Acknowledgement

References

Anderson, M.A., Jones, F.O., 1985. A comparison of hydrostatic stress and uniaxial strain pore volume compressibilities using nonlinear elastic theory. In: Proceedings of the 26th US Symposium on Rock Mechanics, pp. 403–410.

Armitage, P.J., Faulkner, D.R., Worden, R.H., Aplin, A.C., Butcher, A.R., Iliffe, J., 2011. Experimental measurement of, and controls on, permeability and permeability anisotropy of caprocks from the CO_2 storage project at the Krechba Field, Algeria. Journal of Geophysical Research 116, B12208, http://dx.doi.org/10.1029/2011JB008385.

Bennion, D.B., Bachu, S., 2006. Supercritical CO_2 and H_2S – brine drainage and imbibition relative permeability relationships for intergranular sandstone and carbonate formations. In: SPE Europec/EAGE Annual Conference and Exhibition, Vienna, Austria, 12–15 June.

Berg, R.R., 1975. Capillary pressures in stratigraphic traps. AAPG Bulletin 59, 939–956.

Berg, R.R., Habeck, M.F., 1982. Abnormal pressures in the lower Vicksburg, McAllen ranch fields, south Texas. Transaction – Gulf Coast Association of Geological Society 32, 247–253.

Bigelow, E.L., 1994. Global occurrences of abnormal pressures. In: Fertl, W.H., Chapman, R.E., Hotz, R.E. (Eds.), Studies in Abnormal Pressures. Elsevier Science, New York, pp. 1–17.

Birkholzer, J.T., Zhou, Q., Tsang, C.F., 2009. Large-scale impact of CO_2 storage in deep saline aquifers: a sensitivity study on pressure response in stratified systems. International Journal of Greenhouse Gas Control 3, 181–194.

Birkholzer, J.T., Zhou, Q., 2009. Basin-scale hydrogeologic impacts of CO_2 storage:capacity and regulatory implications. International Journal of Greenhouse Gas Control 3 (6), 745–756.

Bradley, J.S., 1975. Abnormal formation pressure. AAPG Bulletin 59, 957–973.

Bredehoeft, J.D., Hanshaw, B.B., 1968. On the maintenance of anomalous fluid pressures: I. Thick sedimentary sequences. Geological Society of America Bulletin 79, 1097–1106.

Bredehoeft, J.D., Neuzil, C.E., Milly, P.C.D., U.S. Geological Survey Water Supply Paper 2237 1983. Regional flow in the Dakota aquifer – a study of the role of confining layers., pp. 45.

Buscheck, T.A., Chen, M., Sun, Y., Hao, Y., Elliot, T.R., 2012. Two-stage, integrated, geothermal-CO_2 storage reservoirs: an approach for sustainable energy production, CO_2-sequestration security, and reduced environmental risk. Lawrence Livermore National Laboratory, Contract DE-AC52-07NA27344.

Chapman, R.E., 1972. Clays with abnormal interstitial fluid pressures. American Association Petroleum Geology Bulletin 56, 790–795.

Chapman, R.E., 1994. The geology of abnormal pore pressures. In: Fertl, W.H., Chapman, R.E., Hotz, R.E. (Eds.), Studies in Abnormal Pressures. Elsevier Science, New York, pp. 19–49.

Cheng, C.H., Johnston, D.H., 1981. Dynamic and static moduli. Geophysical Research Letters 8, 39–42.

Christensen, N.P., Dirschauer, W., Gortz, S., 2012. Carbon capture and storage – a pragmatic way to reduce CO_2 emissions. Energy and Environment 23 (2 & 3).

Deming, D., 1994. Factors necessary to define a pressure seal. AAPG Bulletin 78, 1005–1009.

Dewhurst, D.N., Aplin, A.C., Sarda, J.P., 1999. Influence of clay fraction on pore-scale properties and hydraulic conductivity of experimentally compacted mudstones. Journal of Geophysical Research 104 (29), 261–329.

Dewhurst, D.N., Aplin, A.C., Sarda, J.P., Yang, Y., 1998. Compaction driven evolution of porosity and permeability in natural mudstones: an experimental study. Journal of Geophysical Research 103, 651–661.

Dickey, P.A., Shriram, C.R., Paine, W.R., 1968. Abnormal pressures in deep wells of southwestern Louisiana. Science 160, 609–615.

Dickinson, G., 1953. Geological aspects of abnormal reservoir pressures in Gulf Coast Louisiana. American Association Petroleum Geology Bulletin 37, 410–432.

Dzevanshir, R.D., Buryakovskiy, L.A., Chilingarian, G.V., 1986. Simple quantitative evaluation of porosity of argillaceous sediments at various depths of burial. Sedimentary Geology 46, 169–175.

Faulkner, D.R., Rutter, E.H., 2000. Comparisons of water and argon permeability in natural clay-bearing fault gouge under high pressure at 20 °C. Journal of Geophysical Research 105 (16), 415–416, 426.

Fjær, E., 2009. Static and dynamic moduli of weak sandstone. Geophysics 74, 103–112.

Fjær, E., Stroisz, A.M., Holt, R.M., 2012. Combining static and dynamic measurements for evaluation of elastic dispersion. In: American Rock Mechanics Association Proceedings of the 46th US Rock Mechanics/Geomechanics Symposium, Chicago, IL, USA, 24–27 June.

Freed, R.L., Peacor, D.R., 1989. Geopressured shale and sealing effect of smectite to illite transition. American Association Petroleum Geology Bulletin 73, 1223–1232.

Holt, R.M., 2012. Static vs. dynamic behavior of shale. In: American Rock Mechanics Association Proceedings of the 46th US Rock Mechanics/Geomechanics Symposium, Chicago, IL, USA, 24–27 June.

Hossain, Z., Fabricius, I.L., Grattoni, C.A., Solymar, M., 2011. Petrophysical properties of greensand as predicted from NMR measurements. Petroleum Geoscience 17, 111–125.

Hou, Z., Rockhold, M.L., Murray, C.J., 2012. Evaluating the impact of caprock and reservoir properties on potential risk of CO_2 leakage after injection. Environmental Earth Sciences 66, 2403–2415.

Hower, J., Eslinger, E.V., However, M.E., Perry, E.D., 1976. Mechanism of burial metamorphism of argillaceous sediment. I. Mineralogical and chemical evidence. Geological Society of America Bulletin 87, 725–737.

Hunt, J.M., 1990. Generation and migration of petroleum from abnormally pressured fluid compartments. AAPG Bulletin 74, 1–12.

Jin, M., Mackay, E., Quinn, M., Hitchen, K., Akhurst, M., 2012. Evaluation of the CO_2 storage capacity of the captain sandstone formation. In: The EAGE Annual Conference and Exhibition Incorporating SPE Europe, Copenhagen, Denmark, 4–7 June.

Josh, M., Esteban, L., Delle, P., Sarout, C., Dewhurst, J., Clennell, D.N.M.B., 2012. Laboratory characterisation of shale properties. Journal of Petroleum Science and Engineering 88–89, 107–124.

Katsube, T.J., Mudford, B.S., Best, M.E., 1991. Petrophysical characteristics of shale from the Scotian shelf. Geophysics 56, 1681–1689.

Khatchikian, A., 1995. Deriving reservoir pore-volume compressibility from well logs. Society of Petroleum Engineering Advanced Technology Series 4.

Kim, J.W., Bryant, W.R., Watkins, J.S., Tieh, T.T., 1999. Electron microscopic observations of shale diagenesis, offshore Louisiana USA, Gulf of Mexico. Geo-Marine Letter 18, 234–240.

King, M.S., 1970. Static and dynamic moduli of rocks under pressure. Proceedings of the 11th US Symposium on Rock Mechanics, 329–351.

Kozeny, J., 1927. Ueber kapillare Leitung des Wassers im Boden. Sitzungsberichte der Kaiserlichen Akademie der Wissenschaften. Wien 136, 271–306.

Kwon, O., Kroneberg, A.K., Gangi, A.F., Johnson, B., Herbert, B., 2004. Permeability of illite-bearing shale: 1-anisotropy and effects of clay content and loading. Journal of Geophysical Research 109 (B10), B10205.

Kwon, O., Kronenberg, A.K., Gangi, A.F., Johnson, B., 2001. Permeability of Wilcox Shale and its effective pressure law. Journal of Geophysical Research B: Solid Earth and Planets 106, 19339–19353.

Lachance, D.P., Anderson, M.A., 1983. Comparison of uniaxial strain and hydrostatic stress pore-volume compressibilities in the nugget sandstone. In: Paper SPE 11971 Presented at the 58th SPE Annual Technical Conference and Exhibition.

Lee, J.H., Ahn, J.H., Peaco, D., 1985. Textures in layered silicates progressive changes through diagenesis and low temperature metamorphism. Journal of Sedimentary Petrology 55, 532–540.

Lin, W., 1978. Measuring the permeability of Eleana argillite from area 17, Nevada test site, using the transient method. Lawrence Livermore National Laboratory Livermore, pp. 11, California Rep. UCRL-52604.

Magara, K., 1971. Permeability considerations in generation of abnormal pressures. Society of Petroleum Engineering Journal 11, 236–242.

Magara, K., 1975a. Reevaluation of montmorillonite dehydration as cause of abnormal pressure and hydrocarbon migration. AAPG Bulletin 59, 292–302.

Magara, K., 1975b. Importance of aquathermal pressuring effect in Gulf Coast. AAPG Bulletin 59, 2037–2045.

Mbia, E.N., Fabricius, I.L., Oji, C.O., 2013a. Equivalent pore radius and velocity of elastic waves in shale Skjold Flank-1 Well, Danish North Sea. Journal of Petroleum Science and Engineering 109, 280–290.

Mbia, E.N., Fabricius, I.L., Krogsbøll, A., Frykman, P., Dalhoff, F., 2013b. Permeability, compressibility and porosity of Jurassic shale from the Norwegian–Danish Basin. Journal of Petroleum Geosciences.

Mesri, G., Olson, R.E., 1971. Mechanisms controlling the permeability of clays. Clays and Clay Minerals 19, 151–158.

Michelsen, O., Nielsen, L.H., Johannessen, P.N., Andsbjerg, J., Surlyk, F., 2003. Jurassic lithostratigraphy and stratigraphic development onshore and offshore Denmark. In: Ineson, J.R., Surlyk, F. (Eds.), The Jurassic of Denmark

and Greenland. Geological Survey of Denmark and Greenland Bulletin, 1, pp. 147–216.

Moore, D.E., Morrow, C.A., Byerlee, J.D., 1982. Use of swelling clays to reduce permeability and its potential application to nuclear waste repository sealing. Geophysical Research Letter 9, 1009–1012.

Nazmul, M.H., Bjørlykke, K., Jahren, J., Høeg, K., 2007. Experimental mechanical compaction of clay mineral aggregates – changes in physical properties of mudstones during burial. Marine and Petroleum Geology 24, 289–311.

Newman, G.H., 1973. Pore-volume compressibility of consolidated, friable, and unconsolidated reservoir rocks under hydrostatic loading. Journal of Petroleum Technology.

Norrish, K., 1972. Factors in the weathering of mica to vermiculite. In: Serratosa, J.M. (Ed.), Paper Presented at the Proceedings on International Clay Conference. Division de Ciencias, CSIC, Madrid, pp. 417–432.

Olsen, H.W., 1972. Liquid movement through kaolinite under hydraulic, electric, and osmotic gradients. American Association Petroleum Geology Bulletin 56, 2022–2028.

Ong, S., Zheng, Z., Chajlani, R., 2001. Pressure-dependent pore volume compressibility – a cost effective log based approach. In: Paper SPE 72116 Presented at the SPE Asia Pacific Improved Oil Recovery Conference, Kuala Lumpur, Malaysia.

Peltonen, C., Marcussen, Ø., Bjørlykke, K., Jahren, J., 2009. Clay mineral diagenesis and quartz cementation in mudstones: the effects of smectite to illite reaction on rock properties. Marine and Petroleum Geology 26, 887–898.

Peltonen, C., Marcussen, Ø., Bjørlykke, K., Jahren, J., 2008. Mineralogical control on mudstone compaction: a study of Late Cretaceous to Early Tertiary mudstones of the Vøring and Møre basins Norwegian Sea. Petroleum Geosciences 14, 127–138.

Petersen, I.H., Nielsen, H.L., Bojesen-Koefoed, A.J., Mathiesen, A., Kristensen, L., Dalhoff, F., 2008. Evaluation of the quality, thermal maturity and distribution of potential source rocks in the Danish part of the Norwegian–Danish Basin. Geological Survey of Denmark and Greenland Bulletin, 16.

Pickup, G.E., Kiatsakulphan, M., Mills, J.R., 2010. Analysis of grid resolution for simulations of CO$_2$ storage in deep saline aquifers. In: 12th European Conference on the Mathematics of Oil Recovery, Oxford, UK, 6–9 September.

Pruess, K., Garcia, J., Kovscek, T., Oldenburg, C., Rutqvist, J., Steefel, C., Xu, T., 2002. Intercomparison of numerical simulation codes for geologic disposal of CO$_2$. Lawrence Berkeley National Laboratory, Berkeley, CA, LBNL-51813.

Reece, J.S., Flemings, P.B., Dugan, B., Long, H., Germaine, J.T., 2012. Permeability-porosity relationships of shallow mudstones in the Ursa Basin, northern deepwater Gulf of Mexico. Journal of Geophysical Research 117, B12102, http://dx.doi.org/10.1029/2012JB009438.

Revil, A., Cathles III, L.M., 1999. Permeability of shaly sands. Water Resources Research 35, 651–662.

Schmidt, G.W., 1973. Interstitial water composition and geochemistry of deep Gulf Coast shales and sandstones. American Association Petroleum Geology Bulletin 57, 321–337.

Scott, A.D., Smith, S.J., 1966. Susceptibility of interlayer potassium in micas to exchange with sodium. Clays Clay Minerals 14, 69–81.

Simmons, G., Brace, W.F., 1965. Comparison of static and dynamic measurements of compressibility of rocks. Journal of Geophysical Research 70, 5649–5656.

Sparks, D.L., 1995. Environmental Soil Chemistry. Academic Press, San Diego, CA, pp. 267.

Sposito, G., Skipper, N.T., Sutton, R., Park, S.-H., Soper, A.K., Greathouse, J.A., 1999. Surface geochemistry of the clay minerals. Proceedings of National Academy of Science 96, 3358–3364.

Teevu, D., 1971. Prediction of formation compaction from laboratory compressibility data. Society of Petroleum Engineers Journal 21, 263–271.

Thomas, L.K., Katz, D.L., Tek, M.R., 1968. Threshold pressure phenomena in porous media. SPE Journal 8 (2), 174–184.

Tutuncu, A.N., Podio, A.L., Sharma, M.M., 1994. Strain amplitude and stress dependence of static moduli in sandstones and limestones. In: Proceedings from the 34th US Symposium on Rock Mechanics, pp. 489–496.

Van Olphen, H., 1977. An Introduction to Clay Colloid Chemistry, 2nd ed. John Wiley, Hoboken, NJ, pp. 318.

Walsh, J., Brace, W., 1966. Elasticity of rock: a review of some recent theoretical studies. Rock Mechanics and Engineering Geology 4, 283–297.

Walsh, J.B., 1965. The effect of cracks on the uniaxial compression of rocks. Journal of Geophysics Research 70, 399–411.

Whitworth, T.M., Fritz, S.J., 1994. Electrolyte-induced solute permeability effects in compacted smectite membranes. Applied Geochemistry 9, 533–546.

Wissa, A.E.Z., Christian, J.T., Davis, E.H., Heiberg, S., 1971. Consolidation at constant rate of strain. Journal of the Soil Mechanics and Foundation Engineering Division, American Society of Civil Engineers 97, 1393–1413.

Yale, D.P., Nieto, J.A., Austin, S.P., 1995. The effect of cementation on the static and dynamic mechanical properties of the Rotliegendes sandstone. In: Proceedings of the 35th US Symposium on Rock Mechanics, pp. 169–175.

Yi, X., Ong, S.H., Russell, J.E., 2005. Characterizing pore compressibility, reservoir compaction and stress path under uniaxial strain condition for nonlinear elastic rock. In: Presentation at Alaska Rocks 2005. The 40th U.S. Symposium on Rock Mechanics (USRMS): Rock Mechanics for Energy, Mineral and Infrastructure Development in the Northern Regions, Anchorage, Alaska, 25–29 June.

Young, A., Low, P.F., McLatchie, A.S., 1964. Permeability studies of argillaceous rocks. Journal of Geophysical Research 69, 4237–4245.

Zhou, Q., Birkholzer, J.T., Tsang, C.F., Rutqvist, J., 2008. A method for quick assessment of CO$_2$ storage capacity in closed and semi-closed saline formations. International Journal of Greenhouse Gas Control 2, 626–639.

Zhou, X., Zeng, Z., Liu, H., 2010. Laboratory testing on pierre shale for CO$_2$ sequestration under clayey. In: 44th U.S. Rock Mechanics Symposium and 5th U.S.–Canada Rock Mechanics Symposium, Salt Lake City, UT, 27–30 June.

I

Quantifying porosity, compressibility and permeability in Shale

Mbia, E. N., Fabricius, I.L., Frykman, F., Krogsbøll, A., Dalhoff, F.

Introduction

Petrophysical properties of shale such as porosity, compressibility and permeability are important in investigation of pressure propagation through caprocks, predicting well bore stability as well as regional subsidence and fluid movement. Despite their importance, these are less predictable physical properties of shale, permeability being the least predictable. In reality it is not easy to measure shale porosity in the laboratory even with the established standard methods; the fact that samples have been retrieved from their in situ condition can, even with specialized handling procedure, affect the quantification of shale porosity. In this work we will quantify and compare shale porosity from three independent methods comprising helium expansion and mercury immersion (HPMI) test, the mercury injection capillary pressure (MICP) test and the nuclear magnetic resonance (NMR) test.

In situ uniaxial static and dynamic compressibility can be determined simultaneously on core samples. Alternatively compressibility can be obtained from elastic wave propagation data which are routinely recorded during drilling operation and may also be recorded during geotechnical testing. Published studies on shale indicate that compressibility estimated from stress strain data is higher than the one calculated from velocity of elastic waves (Fjær 2009; and Holt 2012). A difference between static and dynamic compressibility in rocks could primarily be due to drainage conditions (Fjær et al. 2012), but also could be due to the procedure used to estimate elasticity from recorded testing data and the condition of the shale (Hendron et al., 1970).

Shale permeability varies widely in order of magnitudes from microdarcy to nanodarcy with values well above and below those required for pressure seals over characteristic geologic and reservoir production times (Dewhurst et al. 1999). Shale permeability has been reported to depend on porosity, clay mineralogy and content, grain size distribution, grain shape, grain packing, as well as specific surface area of the clay (Dewhurst et al.1999; Yang & Aplin 1998, 2007), all of which may change with increasing temperature (Kim et al. 1999). Measuring fluid flow directly from shale to calculate permeability is very difficult and time consuming. An indirect geotechnical approach has been proposed by Wissa et al., (1971) to measure permeability from excess pore pressure and was found to correspond very well with permeability determined from flow through tests (Mondol et al. 2008; Daigle & Hugan 2009). The influence of Biot's coefficient has not been tested in this method and Biot's coefficient is often assumed to be 1.0 even for deeply buried shale that might have undergone some degree of cementation. Besides measuring shale permeability directly from core samples, there exist a variety of capillary tube models that could estimate permeability from more easily measured physical property of porosity and specific surface as by Kozeny's model or void ratio, mercury injection data, and clay content as by Yang and Aplin's empirical formulation, but the key question remains whether these models are applicable to shale with changing mineralogy. In this study we will compare different methods for quantifying shale porosity, compressibility and permeability and seek to explain the discrepancy between them using Jurassic shale samples from the onshore Norwegian-Danish Basin.

Method and theory

Preserved core and cuttings samples were obtained from onshore wells in Denmark. Routine core analysis was carried out on cleaned samples. Mineralogy was determined by XRD, texture was evaluated by scanning electron microscopy of polished sections by applying the backscatter technique (BSEM), grain density analysis was done by He-expansion, grain size distribution was done using the SediGraph method which is based on well established and well-understood physical phenomena of gravitational sedimentation, specific surface area was measured by the BET method, cation-exchange capacity (CEC) was measured by Ba-ion exchange and Inductively Coupled Plasma–Optical Emission Spectrophotometry (ICP-OES). Porosity was determined by HPMI, MICP and NMR. Compressibility was calculated from stress and strain data for static compressibility and from elastic wave velocity obtained during uniaxial consolidation experiments performed under drained conditions. Permeability was calculated from excess pore pressure during constant rate of strain experiments conducted in an oedometer loading frame under room temperature. Some of the oedometer tests were conducted by controlling the pore pressure and stress to calculate Biot's coefficient. Permeability was also modelled from BET specific surface and porosity by Kozeny's equation and from void ration and clay content

using the Yang and Aplin model. The modelled and measured permeabilities are compared in Figure 1 for this study together with published data (Daigle et a., 2011; Mondol et al., 2008; Yang & Aplin., 2007; Dewhurst et al., 1999; Hursrud et al., 1998)

Results

Bulk mineralogical composition of the Jurassic shale as derived from XRD shows that quartz, K-feldspar, plagioclase, calcite, dolomite and pyrite are present in the non-clay fraction with quartz dominating, while illite, kaolinite and chlorite are present in clay fraction with kaolinite dominating.

Porosity results obtained from the three methods differ. For a given sample, the NMR method recorded the highest porosity of 21%, the second-highest porosity of 20% was obtained from HPMI while the MICP method measured the lowest porosity of 11% simply because mercury even at the maximum pressure of 414 MPa could not intrude pores with pore radius less than 2.0 nm, thereby underestimating shale porosity. In principle we expect the NMR porosity to be the same with that of the HPMI method but this is not so probably due to the presence of unloading fractures which was observed by BSEM.

Oedometer tests were carried out on centimetre-scale core plug samples. A series of uniaxial-strain loading and unloading stress paths were applied up to the in situ stress level. Static compressibility was determined from the loading and unloading stress paths. The loading experiments were undertaken with continuous ultrasonic recording of compressional and shear wave velocities. Elastic moduli were calculated from ultrasonic data and Gassmann substitution was used to estimate the corresponding moduli applicable to drained conditions. At reservoir stress and unloading conditions (as during pressure build-up in nature), dynamic compressibility was found to be similar to the static compressibility and in the range of $2–5 \times 10^{-5}$ MPa^{-1}. The compressibility was thus found to be one order of magnitude lower than the standard values of 45×10^{-5} MPa^{-1} used as default in the Eclipse simulation program

Figure 1 compares modelled permeability to measured permeability for both synthetic and natural shale material with kaolinite or smectite dominating the clay fraction. The results show that kaolinite rich shale tend to have higher permeability as estimated by both flow through and constant strain rate experiments, than shales rich in smectite. Kozeny's modelled permeability fall in the same order of magnitude as measured permeability for shale with kaolinite dominating the clay fraction but two to three orders of magnitude higher than measured permeability for shale rich in smectite. Yang and Aplin modelled permeability fall within +/- 1 order of magnitude as the measured permeability.
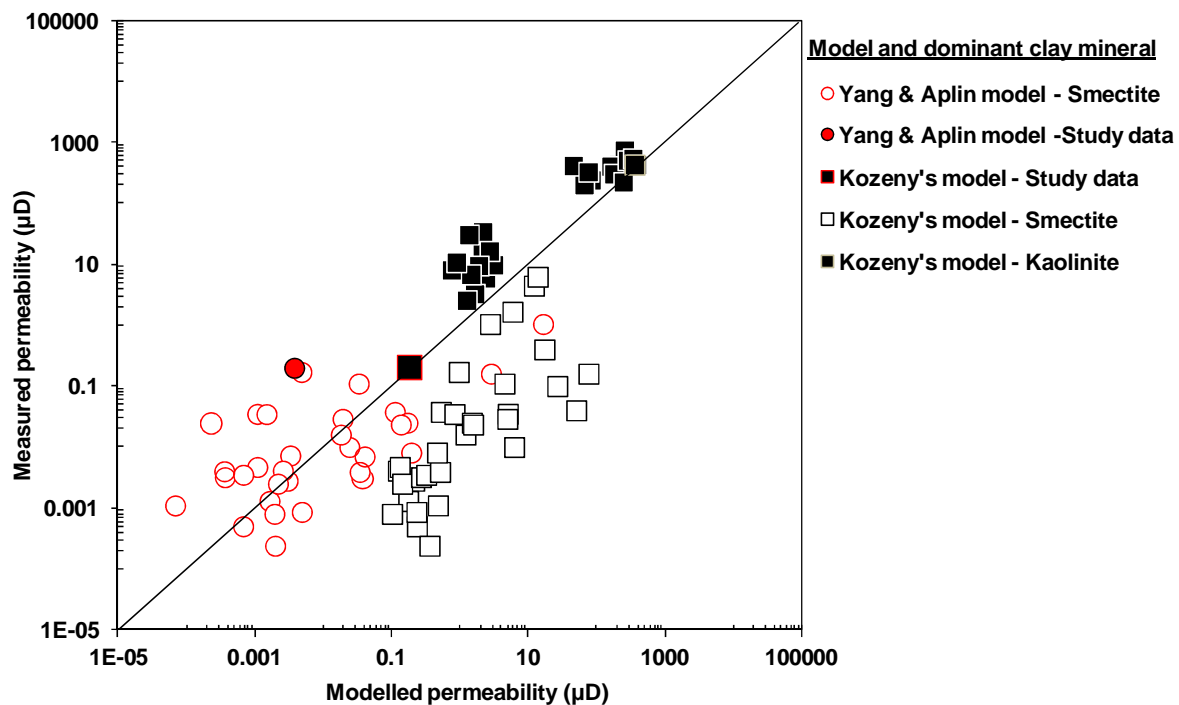
Figure 1 Relationship between predicted permeability from Kozeny's and Yang and Aplin model as compared with measured permeability for both synthetic and natural shale material.

Conclusions

Porosity measured from three independent methods gave different results. The results indicate that a higher porosity is measured by nuclear magnetic resonance method (21%) and helium porosimetry-mercury immersion method (20%) than mercury injection capillary pressure method (11%) for the same samples. It implies that defining shale porosity based on a single method can bias results. The static and dynamic compressibility can be compared based on uniaxial geomechanical testing. We find that the elastic compressibility of the Jurassic shale as measured from uniaxial stress and strain data at in situ stress and the beginning of the unloading stress path correspond with dynamic compressibility data. The compressibility of this shale formation measured from core samples is smaller by a factor of 10 or more than previously published data on shale. The reason is probably a procedure designed for geotechnical purpose used for estimating shale compressibility in earlier studies.

Permeability for the same shale material may range from micro to nanodarcy value depending on the methodology used for the evaluation. We found that Kozeny's modelled permeability fall in the same order of magnitude with measured permeability for shale rich in kaolinite but overestimates permeability by two to three orders of magnitudes for shale with high content of smectite. The empirical Yang and Aplin model gives good permeability estimate comparable to the measured one for shale rich in smectite. This is probably because Yang and Aplin model was calibrated in London clay which is rich in smectite. It is therefore important that any model that is meant to estimate shale permeability should be calibrated on a large amount of data from both synthetic and natural shale samples.

References

Daigle, H., and Dugan, B. 2009. Extending NMR data for permeability estimation in fine-grained sediments. *Marine and Petroleum Geology*, **26**, 1419–1427.

Dewhurst, D. N., Aplin, A. C., Sarda, J. P. & Yang, Y. 1998. Compaction driven evolution of porosity and permeability in natural mudstones: An experimental study: Journal *of Geophysical Research,* **103**, 651–661

Fjær, E. 2009. Static and dynamic moduli of weak sandstone. *Geophysics,* **74**. 103–112.

Fjær, E., Stroisz, A. M., & Holt, R. M. 2012. *Combining static and dynamic measurements for evaluation of elastic dispersion*. American Rock Mechanics Association proceedings of the 46th US Rock Mechanics / Geomechanics Symposium held in Chicago, IL, USA, 24-27 June 2012.

Hendron, Jr., Mesri, G., Gambe, J. C., and Way, G. 1970. '' Compressibility Characteristics of Shales Measured by Laboratory and In Situ Tests,'' Determination of the in Situ Modulus of Deformation of Rock, ASTM STP **477**, *American Society for Testing and Material*, pp. 137–153

Holt, R. M. 2012. *Static vs. Dynamic Behavior of Shale*. American Rock Mechanics Association proceedings of the 46th US Rock Mechanics / Geomechanics Symposium held in Chicago, IL, USA, 24-27 June 2012.

Kim, J.-W., Bryant, W. R., Watkins, J. S. & Tieh, T. T. 1999. Electron microscopic observations of shale diagenesis, offshore Louisiana, USA, Gulf of Mexico. *Geo-Marine Letter*, **18**, 234–240.

Mondol, N.H., Bjørlykke, K., Jahren, J., and Høeg, K. 2008. Experimental compaction of clays: relationship between permeability and petrophysical properties in mudstones. *Petroleum Geoscience*, 14, 319–337

Wissa, A.E.Z., Christian, J.T., Davis, E.H. & Heiberg, S. 1971. Consolidation at constant rate of strain. *Journal of the Soil Mechanics and Foundation Engineering Division, American Society of Civil Engineers*, **97**, 1393–1413.

Yang, Y., & Aplin, A. C. 2007. Permeability and petrophysical properties of 30 natural mudstones. *Journal of Geophysical Research*, 112, pp 14.

II

Caprock compressibility and the consequences for pressure development in CO_2 storage sites

Mbia, E. N., Fabricius, I.L., Frykman, F., Nielsen, C.M, Bernstone, C., Pickup, G.

CAPROCK COMPRESSIBILITY AND THE CONSEQUENCES FOR PRESSURE DEVELOPMENT IN CO$_2$ STORAGE SITES

Ernest N. Mbia[1], Peter Frykman[2], Carsten M. Nielsen[2], Christian Bernstone[1], Ida L. Fabricius[3], Gillian Pickup[4]

[1]Vattenfall A/S
[2] Geological Survey of Denmark and Greenland
[3]Technical University of Denmark
[4] Heriot-Watt University

ernm@byg.dtu.dk

ABSTRACT

The Vedsted structure located in the Northern part of Jutland in Denmark has previously been considered for industrial-scale CO$_2$ storage. The site comprises reservoir sandstone of Upper Triassic - Lower Jurassic age. The site is a domed shaped saline aquifer covering an area of about 12 km x 6 km and at 1.9 km depth; it is bounded by an overlying shaley caprock of 500 m. Laboratory experiments and dynamic sonic velocity data from relevant shale formations in Denmark indicates that shale compressibility might be lower than often assumed for reservoir simulation studies. The consequences of this low compressibility are investigated in a simulation case study. Laboratory measurements were carried out on centimeter-scale core plug samples from analogue onshore wells. The experiments were performed under drained conditions. A series of uniaxially confined loading and unloading stress paths were applied up to the in situ stress level. Static compressibility was determined from the loading and unloading stress paths. The loading experiments were undertaken with continuous ultrasonic recording of compressional and shear wave velocities. At reservoir conditions, dynamic compressibility is similar to the static compressibility at the beginning of the unloading stress path corresponding to elastic deformation. The analysis of both data sets indicate that compressibility might be one order of magnitude lower than the standard values of 4.5 x 10^{-5} bar^{-1} (Buschet et al. 2012; Birkholzer et al. 2009; Zhou et al. 2008 etc) normally used for shale compressibility in reservoir simulation studies. Since the magnitude of overpressure in a CO$_2$ storage site depends on the compressibility, this can have important implications.

The Eclipse reservoir simulator was used to simulate a CO$_2$ injection process with varying values of compressibility between 5 x 10^{-6} bar^{-1} and 4.5 x 10^{-5} bar^{-1} (Table 1). The simulation results show that the lower compressibility (increased stiffness) of the caprock causes a faster upwards propagation of the overpressure caused by the CO$_2$ injection, and it also causes a generally higher level of overpressure throughout the reservoir formation (Fig.1).
The base of the caprock around the injection well shows pressure differences of about 5 bar between the two cases, so that overestimating the compressibility can cause underestimation of the pressure increase in the caprock. This pressure difference can be decisive in a case with highly permeable vertical faults.

Table1. Model setup/caprock properties

Properties/Caprock properties	Proposed case	Standard case
Horizontal permeability, k_h (mD)	1.0×10^{-3}	1.0×10^{-3}
k_v/k_h	1.0×10^{-1}	1.0×10^{-1}
Uniaxial compressibility, M^{-1} (bar^{-1})	**5.0×10^{-6}**	**4.5×10^{-5}**
Porosity	0.11	0.11
Simulated area (km)	50 x 50	50 x 50
CO_2 injection rate (sm^3/day)	2.3×10^6	2.3×10^6
Injection period (years)	40	40
Resrvoir depth from top (km)	1.9	1.9
Number of grid cells	1.2×10^6	1.2×10^6
Grid cell dimension (m)	200 x 200	200 x 200
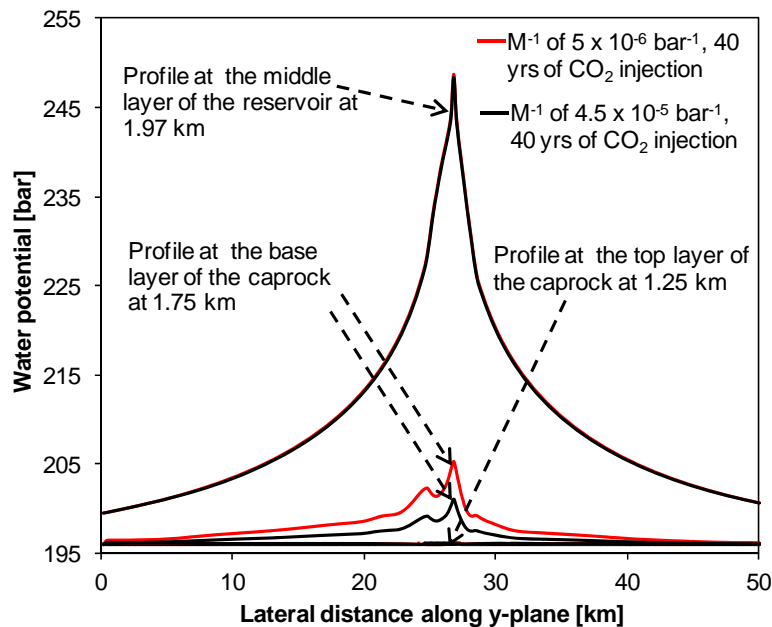
Fig.1. *Water potential versus lateral distance along a y-plane in the middle layer of the reservoir model and the base and top layers of Fjerritslev Formation caprock.*

REFERENCES

Birkholzer, J.T., Zhou, Q., Tsang C.F. 2009. Large-scale impact of CO_2 storage in deep saline aquifers: A sensitivity study on pressure response in stratified systems. *International Journal of Greenhouse Gas control,* **3,** 181–194.

Zhou, Q., Birkholzer, J.T., Tsang, C.-F., Rutqvist, J. 2008. A method for quick assessment of CO_2 storage capacity in closed and semi-closed saline formations. *International Journal of Greenhouse Gas Control*, **2**, 626–639.

Buscheck, T.A., Sun, Y., Chen, M., Hao, Y., Wolery, T.J., et al. 2012. Active CO_2 Reservoir Management for CO_2 Capture, Utilization, and Storage: An Approach to Improve CO_2 Storage Capacity and to Reduce Risk. *Carbon Management Technology Conference, Orlando, Florida, USA, 7–9 February 2012.*

IV

Pore Radius and Permeability Prediction from Sonic Velocity

Mbia, E.N & Fabricius, I.L.

Extended abstract and presentation at the 3rd EAGE Shale Workshop, 23–25 January 2012 in Barcelona, Spain.

Introduction

Several authors have predicted permeability of shales either through laboratory measurements and or from field data using various empirical relations. A critical literature review by Mondol et al., (2008) on available permeability models, concluded that none of the existing models is ideal and all need to be calibrated and validated through a much larger permeability database of well-characterized mudstones. His results on smectite and kaolinite aggregates suggest that the permeability of smectitic clays may be up to five orders of magnitude lower than that of kaolinitic clays with the same porosity, density, velocity or rock mechanical properties. Mari et al., (2011) described a methodology for obtaining a permeability log based on acoustic velocities V_p and V_s, porosity ϕ, P-wave attenuation and frequency, their calculation of the specific surface S of the formation was based on the relationship between porosity ϕ, V_p/V_s and S proposed by Fabricius et al. (2007). Fabricius (2011) indicate that pore radius and thus permeability of shale in the depth interval of mechanical compaction may be predicted from porosity and sonic velocity. In this work we are presenting the empirical equations developed from experimental data that can be used to predict pore radius and permeability of shale from sonic velocity data measured in the field.

Method and Theory

Experimental data from Cenozoic and Jurassic shale of Skjold Flank-1 well (Mbia et al., 2011) and that of kaolinite and smectite aggregates (Mondol et al., 2007) were used. The experimental data used includes porosity ϕ, BET specific surface, grain density ρ_g and sonic velocities (Vp and Vs). Those of Mondol et al., (2007) are given for mixtures of kaolinite or smectite and brine. Bulk density, ρ, for each data point was calculated from ϕ, ρ_g, and ρ_{fl}.

$$\rho = \rho_g\,(1\text{-}\phi) + \rho_{fl}\phi \tag{1}$$

Elastic compressional modulus, M, was calculated as: $\qquad M= \rho V_p^{\,2} \tag{2}$

Elastic shear modulus, G, was calculated as: $\qquad G= \rho V_s^{\,2} \tag{3}$

Elastic bulk modulus, K, was as calculated as: $\qquad K = M - 4/3\ G \tag{4}$

For modeling pore radius, we need information on ϕ, ρ_g, and on specific surface, S_s of the solid.

The pore radius, r, is approximated by: $\qquad r = (2\ \phi)/(S_s\ \rho_g\ (1\text{-}\phi)) = 2/S_p \tag{5}$

Where S_p is the specific surface relative to pore space.

The calculated pore radius r, eqn. (5) together with the moduli eqn. (2) to (4), (Fig. 2a, 2c & 2e) were used to compute the following empirical equations which can predict pore radius r, directly from acoustic data (Fig. 2b, 2d & 2f).

$$r_M = 9 \times 10^{-9} +3.3E\text{-}6.77M^{-2} \tag{6}$$

$$r_G = 19.95E\text{-}9G^{-0.5} \tag{7}$$

$$r_K = 6 \times 10^{-9} +3E\text{-}6.77K^{-2} \tag{8}$$

were moduli are given in GPa and r_M, is pore radius from compressional modulus, r_G, from shear modulus and r_K from bulk modulus.

Permeabilities, k (Fig. 2), were modeled by using eqn. (6) to (8) and Kozeny's relation so that we will have eqn. (9) to (11) as follows:

$$k_M = c(\phi r^2_M/4) \tag{9}$$

$$k_G = c(\phi r^2_G/4) \tag{10}$$

$$k_K = c(\phi r^2_K/4), \tag{11}$$

Where, c is Kozeny's constant and ϕ is porosity.

Results

Experimental data from Cenozoic and Jurassic shales of Skjold Flank-1 well (Mbia et al., 2011) and that of kaolinite and smectite aggregates (Mondol et al, 2007) were used to calculate compressional modulus which vary from 4 to 40 GPa, shear modulus (0.1 – 8 GPa) and bulk modulus (4 – 35 GPa) and pore radius from BET, porosity and grain density (1E-09 –1E-07 m). The cross plots of elastic moduli versus pore radius (Fig. 2.) were used to derived the empirical equations which can be used to predict pore radius and permeability from field data. The cross plots (Fig. 2a, 2c & 2e) show that kaolinite, smectite and Cenozoic (containing kaolinite, interlayered illite/Smectite) blend together with very low elastic moduli and corresponding large pore radius. This is because Cenozoic shale including kaolinite and smectite aggregates are not cemented and in the mechanical compaction zone. The Jurassic samples at greater depth show very high elastic moduli with corresponding small pore radius. The high elastic moduli and small pore radius may indicate that this material has undergone some degree of cementation under chemical compaction. The predicted pore radius from compressional and bulk moduli anyway fits very well in linear scale (5% difference in some few data points) with that calculated from measured BET specific surface, grain density and porosity (Fig. 2b & 2f) but that predicted from shear modulus shows some degree of scattering at higher values.

The empirical equations were used to derive permeability log from field data (Fig. 1) and the predicted permeability matched each other very well and shows the same depth trend from Cenozoic to Jurassic shale for the three equations. The predicted permeability for Cenozoic shale varies from 0.5 to 10 µD while that of Jurassic shale vary from 0.0001 to 0.5 µD. It implies that one can use compressional or shear velocity to predict pore radius and thus permeability.
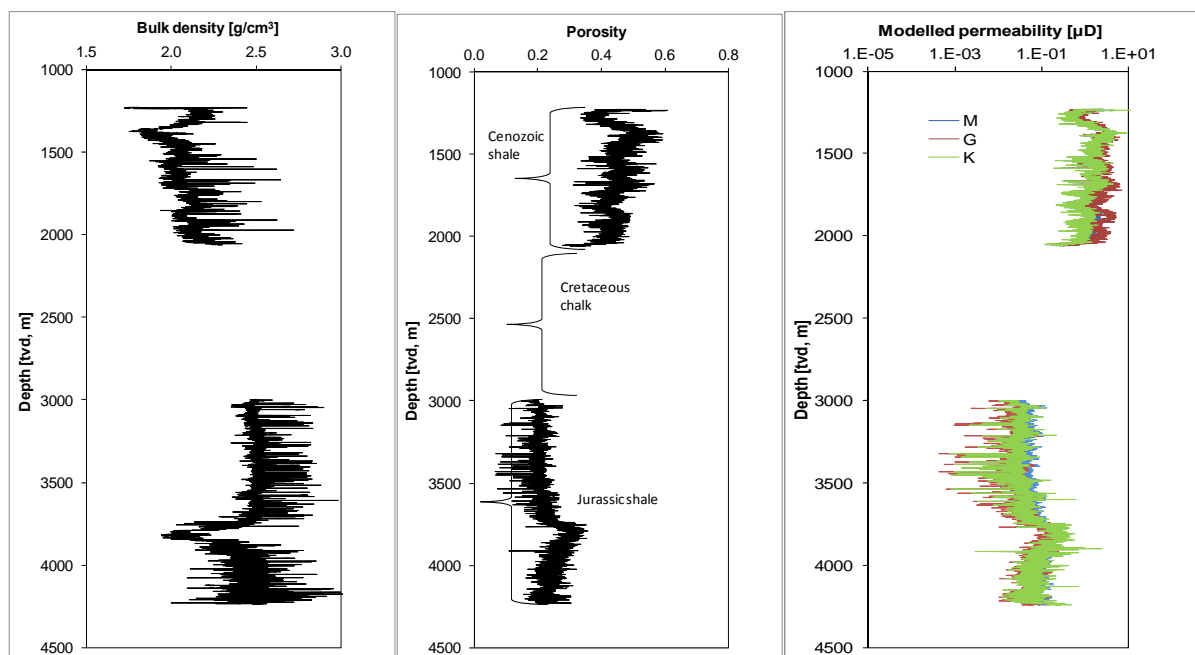
Fig.1. *Depth plot of density, porosity and predicted permeability of shale intervals from of Skjold Flank-1 well.*
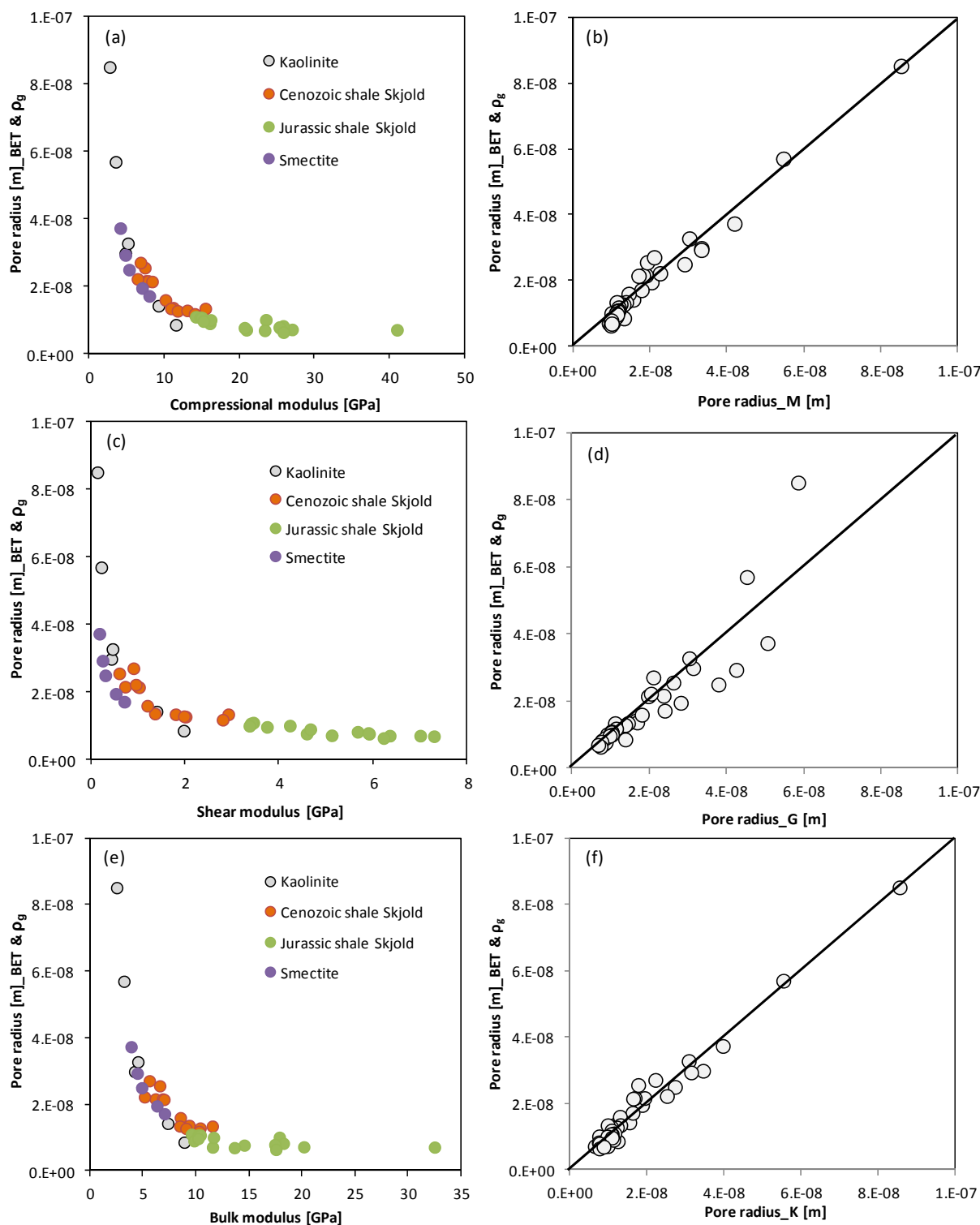
Fig.2. *Cross plots of calculated pore radius versus predicted pore radius and moduli. (a) pore radius calculated from BET specific surface, porosity and grain density versus compressional modulus, (b) calculated pore radius versus the predicted pore radius from M, (c) calculated pore radius versus shear modulus G, (d) calculated pore radius versus pore radius predicted from shear modulus G, (e) calculated pore radius versus bulk modulus K, (f) calculated pore radius versus pore radius predicted from bulk modulus, K.*

Conclusions

The empirical equations developed (eqn. 6 – 11) can be applied to field data to predict pore radius and permeability of shale in the depth interval of mechanical compaction and will give a fair estimate in shale that have underdone degree of cementation at greater depth.

This result is very important for field applications and can be very useful for CO_2 storage and for other engineering applications. It should be noted that in order to validate these findings more experimental work is needed to be done on extensive shale samples from different locations.

Acknowledgement

References

Fabricius, I. L. 2011: Relationship between Elastic Moduli and Pore Radius in Clay Aggregates. 73rd EAGE Conference & Exhibition incorporating SPE EUROPEC 2011 Vienna, Austria, 23-26 May 2011.

Fabricius I. L., Baechle G., Eberli G.P. , Weger R., 2007, Estimating permeability of carbonate rocksfrom porosity and Vp/Vs, Geophysics, **72**, E185-E191.

Kozeny, J. 1927. Uber Kapillare Leitung des Wassers im Boden: Stizurgsberichte. Akademie der Wissenschaften in Wien, 136, 271–306.

Mari J.L., Gaudiani P., Delay J., 2011. Estimating Permeability from Acoustic Attenuation and Porosity - Field Example of a Carbonate Formation. 73rd EAGE Conference & Exhibition incorporating SPE EUROPEC 2011 Vienna, Austria, 23–26 May 2011.

Mavko, G., Mukerji, T., and Dvorkin, J. 2009. The Rock Physics Handbook 2ed. Cambridge U.P. 511pp.

Mbia, E. N., Fabricius, I. L., Oji. C. O. 2011. Petrophysics of Shale Intervals in the Skjold Field, Danish North Sea. 73rd EAGE Conference & Exhibition incorporating SPE EUROPEC 2011 Vienna, Austria, 23-26 May 2011.

Mondol, N.H., Bjørlykke, K., Jahren, J., and Høeg, K. 2007. Experimental mechanical compaction ofclay mineral aggregates –Changes in physical properties of mudstones during burial. Marine and Petroleum Geology **24**, 289-311.

Mondol, N.H., Bjørlykke, K., Jahren, J., and Høeg, K. 2008. Experimental compaction of clays: relationship between permeability and petrophysical properties in mudstones. Petroleum Geoscience, **14**, 319–337

III

Different Methods of Predicting Permeability in Shale

Mbia, E.N & Fabricius, I.L., & Krogsbøll, A

Introduction

Shale permeability prediction is recently gaining a lot of attention due to the growing concern in gas shale, CO_2 and other toxic waste storage. Shale form major cap-rocks in majority of our sedimentary basins around the world and knowing permeability of these rocks is one of the most important parameters in assessing their integrity as potential seals. The two widely accepted models in calculating permeability of porous media are Darcy's and Kozeny's equations. The Darcy equation relates the instantaneous discharge rate through a porous medium, the viscosity of the fluid and the pressure gradient over a given distance, while Kozeny describes permeability in terms of porosity and specific surface area. A majority of authors have concluded that Darcy model gives a more reliable estimate of shale permeability compared with Kozeny's model which often produces discrepancies of many orders of magnitude between predicted and measured permeability in mudstones (Yang & Aplin 1998; Dewhurst et al. 1999a, b; Revil & Cathles 1999). This discrepancy may be due partly to their assumptions that all pores are capillary tubes with the same cross-sectional area, which means equal pore diameters (Mondol et al, 2008). In reality, mudstone pores have a wide range of diameters (Olsen 1962; Griffiths & Joshi 1989; Katsube & Williamson 1994; Dewhurst et al. 1999b; Yang & Aplin 2007). In this work we are going to address how to estimate permeability in shale from constant rate of strain testing (Wissa et al, 1971) since it is very difficult to drain a shale sample and then compare the result with predicted permeability values from Kozeny's model. This will be done using core and cuttings samples of Fjerritslev shale formation from Stenlille and Vedsted on-shore wells of Danish basin.

Method and Theory

Thirteen Fjerritslev Formation shale cuttings and two core trim samples were taken from the Jurassic section of Stenlille-2, 5 and Vedsted-1 on-shore wells of Danish Basin at depths between 1222 and 1740 m. Mineralogy, porosity, grain density, BET specific surface and cation exchange capacity were measured in the laboratory using the procedure described by Mbia et al., (2011) and the results is shown in table 1. All experiments were performed at room temperature between 20^0C and 23^0C. Permeability (k) is predicted using the Kozeny relation as described by Mortensen et al., (1998) as follows;

$$k = c\frac{\phi^3}{S^2}, k = c\frac{\phi^3}{(1-\phi)^2 \bullet S_s^2}, k = c\frac{\phi^3 \bullet d^2}{(1-\phi)^2 \bullet 6^2}, \dots\dots\dots\dots\dots\dots\dots\dots\dots\dots (1)$$

where k is the liquid permeability, ϕ is porosity, S is grain-specific surface area per bulk volume, S_s is specific surface (grain-surface area per grain volume), and d is equivalent spherical diameter and is determined by combining for the grain-surface area $A = \pi*d^2$ and grain volume $V = 1/6* \pi d^3$ into the expression $S_s = A/V = 6/d$. Kozeny's constant and is given by;

$$c = \left(4\cos\left(\frac{1}{3}\arccos\left(\phi\frac{8^2}{\pi^3}-1\right)+\frac{4}{3}\pi\right)+4\right)^{-1}$$

$$\dots\dots\dots\dots\dots\dots\dots\dots\dots\dots\dots\dots (2)$$

Consolidation tests (Oedometer tests); Experimental compaction measurements on two natural shale samples of Fjerritslev Formation obtained at depth of 1483–1484 m from Stenlille-2 well, were performed at Danish Geotechnical Institute (GEO). The core material has been well preserved to maintain in-situ saturation of the shale sample (recovered at about 98% to 99.5 %). The salinity of the pore water varies between 100.000 ppm and 150.000 ppm (TDS). The shale samples were plugged normal to bedding with diameter of 25 mm and height of 13.76 mm. The compaction tests were performed by running constant rate of strain tests in the high stress oedometer cell. The samples were loaded up to 17.5 and 100 MPa, at rate of 0.013 mm/h and then switched at 17.5 MPa from 0.013 mm/h to 0.056 mm/h to 33 MPa all at controlled pore pressure (Figure 1a). The data obtained directly from the test include the average strain rate, the pore pressure at the top and at the bottom of the sample, and the total stress at the top of the sample. The difference in effective stress at the bottom

and top of the sample can be computed. The ratio of excess pore pressure at the bottom to effective vertical stress was controlled at ± 30%. The sample is drained towards the top and excess pore pressure is measured at the bottom, µh. The hydraulic conductivity (ƙ) of these shale samples was calculated at time intervals of 21 minutes from the excess pressure at the bottom of the sample and the average strain rate as time increases (Δt). The estimated errors in measurements are, load ± 0.090 kN, deformation ± 1% and pore pressure 0.006 MPa and by using the approach described by Wissa et al., (1971), the hydraulic conductivity ƙ (m/s) of the sample can be calculated as;

$$\mathcal{k} = 0.5(\mathcal{E}_r H^2 Y_w / \mu h) \dots\dots\dots\dots\dots\dots\dots\dots\dots\dots\dots\dots\dots\dots\dots\dots\dots\dots\dots\dots\dots\dots\dots\dots\dots. (3)$$

where; $\mathcal{E}_r$ is the strain rate, $\mathcal{E}_r = \Delta\mathcal{E}_d/\Delta t$ where $\Delta\mathcal{E}_d = \Delta H/H$. uh is excess pore pressure,
$Y_w = g \times g_w$ (g is the gravitational acceleration and g_w is density of brine)

Permeability (k), m^2 from Darcy can be calculated knowing the hydraulic conductivity (3) as;

$$k = \mathcal{k}(\mu/\rho g) \dots\dots\dots\dots\dots\dots\dots\dots\dots\dots\dots\dots\dots\dots\dots\dots\dots\dots\dots\dots\dots\dots\dots\dots\dots\dots\dots\dots (4)$$

Where µ is the dynamic viscosity, kg/(m.s)
Equation (4) now becomes,

$$k = 0.5(\mathcal{E}_r H^2 \mu / uh) \dots\dots\dots\dots\dots\dots\dots\dots\dots\dots\dots\dots\dots\dots\dots\dots\dots\dots\dots\dots\dots\dots (5)$$

Results

The XRD analysis of cuttings and core trim samples is shown in table 1. These samples contain clay minerals including illite (8–40%), kaolinite (4–28%), Smectite (1–7%) and chlorite (1–10%). The non-clay minerals include quartz (35-70%), calcite (1-14%), K-feldspar (0–8%), plagioclase (0–5%) and dolomite (0–2%). The calculated permeability from specific surface vary from 90 to 48530 nD while that calculated from consolidation test at different time interval vary from 100 nD at a low vertical effective stress to 9 nD at high vertical effective stress of 100 MPa. Permeability estimated from Kozeny's model depend on the specific surface, porosity and the degree of the homogeneity of the material express by Kozeny's constant. The samples from Vedsted well contain high content of non-clay minerals (55–76%) compared with Stenlille well samples which is reflected on their relatively low specific surface and high estimated permeability by Kozeny's model (table.1). The permeability values estimated from consolidation test at higher vertical effective stresses above 40 MPa fall in the same range of magnitude as those calculated from the specific surface and porosity data of samples from Vedsted well. On the other hand the permeability is two to four orders of magnitude higher than Stenlille shale samples and three to five orders of magnitude higher than the core trim samples at the same depth at lower vertical effective stress below 40 MPa. This imply that Kozeny's permeability model is sensitive to heterogeneity of the shale material with high clay content above 30% as shown in table 1.

Permeability values determined from consolidation tests at increasing vertical effective stress is also sensitive to the type of pore fluid express by viscosity and the development of the pore pressure. Fig.1(a) show the vertical effective stress versus the vertical strain of two the samples from Stenlille from very low stress to 33 MPa and 100 MPa and Figure.1 (b) show corresponding permeability versus vertical effective stress. The two sample show similarity in higher permeability values of about 1000 nD at low stress level at the same strain rate but permeability falls rapidly as the strain rate is increased in sample 2. The increased strain rate probably increases compaction and causes pore pressure to build up at the bottom resulting in lower permeability values at the same vertical effective stress in the two samples (Figure 1b).

Table 1. *Cuttings data from Fjerritslev shale formation; Clay and non-clay fractions determined by XRD, ρ_{grain} is grain density, ϕ is mercury porosity, BET is specific surface by N_2 adsorption, CEC is cation exchange capacity. Experimental errors are; for $\rho_{grain} < 3$ g/cm^3; for $\phi < 2$ p.u; for BET < 0.3 m^2/g; for CEC < 5%.*

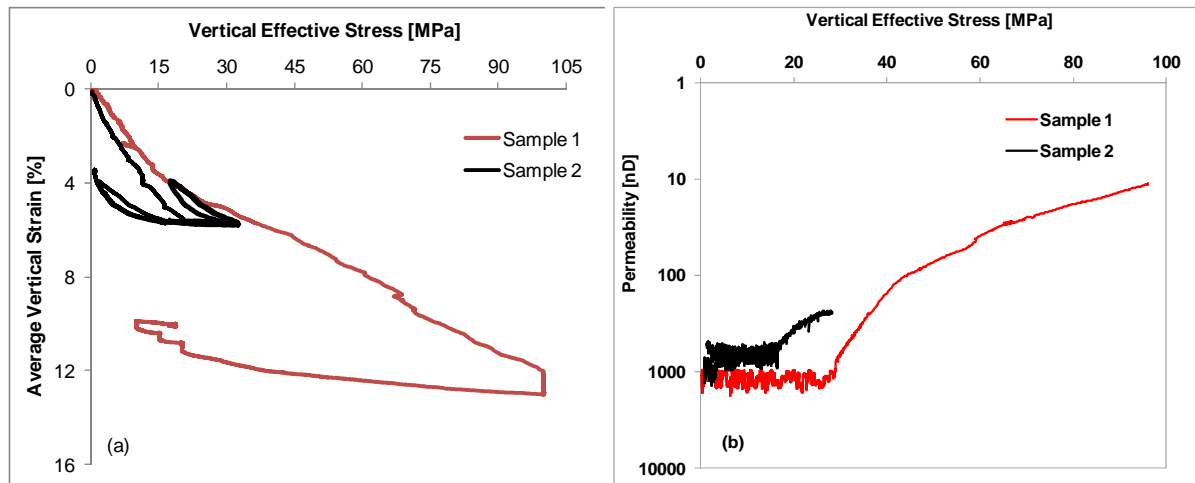| Depth (m)	Well	Formation	Clay (%)	Non-Clay %	ϕ (p.u.)	ρ_grain g/cm^3	CEC mEq/100g	BET (m^2/g)
1222	Vedsted-1	Fjerritslev	24	76	44	2.64	21	13.71
1255			24	76	53	2.69	31	22.00
1350			46	54	50	2.64	36	37.87
1445			53	53	41	2.71	28	31.30
1515			39	61	32	2.77	29	26.71
1585			34	66	44	2.77	36	27.16
1675			45	55	35	2.68	25	31.70
1740			28	72	42	2.70	33	28.32
1745			44	56	42	2.71	28	17.78
1419	Stenlille 5		53	47	25	2.67	19	42.64
1422			58	42	26	2.67	24	43.70
1527			56	44	33	2.66	12	42.83
1530			48	52	26	2.64	33	42.01
1475	Stenlille 2		55	45	22	2.66	25	46.27
1483-84			65	35	17	2.63	34	48.34

Figure1. *(a) Cross plots of vertical effective stress versus vertical strain for two shale samples loaded up to 100 and 33 MPa. (b) Cross plots of indirect permeability data calculated at time interval of 21 minutes versus vertical effective stress of two shale samples obtained from 1483 m and 1484 m intervals.*

Conclusions

The indirect permeability calculated from consolidation tests falls in the same magnitude at higher vertical effective stress, above 40 MPa, as that of the Kozeny model for shale samples with high non-clay content ≥ 70% but are higher by two to five orders of magnitudes at lower vertical effective stress below 40 MPa as the content of clay minerals increases causing heterogeneity in shale material. This imply that Kozeny's model may be applicable to estimate maximum permeability values in shale with high content of non-clay minerals above 30 % but become less applicable with increasing clay content.

Indirect permeability from consolidation testing is very useful in estimating the maximum and minimum values of shale permeability required when simulating fluid flow in caprocks. Permeability is seen to be higher at lower vertical effective stress where the pore pressure is still very low and

reduces to lower values as the stress increases. The degree to which permeability reduces with vertical effective stress also depends on the strain rate during which the material is loaded which will give different permeability values at the same vertical effective stress.

Acknowledgement

References

Dewhurst, D.N., Aplin, A.C. & Sarda, J.P. 1999*a*. Influence of clay fraction on pore-scale properties and hydraulic conductivity of experimentally compacted mudstones. *Journal of Geophysical Research*, **104**, 29261–29274.

Dewhurst, D.N., Yang, Y. & Aplin, A.C. 1999*b*. Permeability and fluid flow in natural mudstones. *In:* Aplin, A.C., Fleet, A.J. & Macquaker, J.H.S. (eds) *Muds and Mudstone: Physical and Fluid-flow Properties*. Geological Society, London, Special Publications, **158**, 23–43.

Griffiths, F.J. & Joshi, R.C. 1989. Change in pore size distribution due to consolidation of clays. *Géotechnique*, **39**, 159–167.

Katsube, T.J. & Williamson, M.A. 1994. Effects of diagenesis on clay nanopore structure and implications for sealing capacity. *Clay minerals*, **29**, 451–461.

Kozeny, J. 1927. Uber Kapillare Leitung des Wassers im Boden: Stizurgsberichte. Akademie der Wissenschaften in Wien, **136**, 271–306.

Mbia, E. N., Fabricius, I. L., Oji. C. O. 2011. Petrophysics of Shale Intervals in the Skjold Field, Danish North Sea. *73rd EAGE Conference & Exhibition incorporating SPE EUROPEC 2011 Vienna, Austria*, 23-26 May 2011.

Mondol, N.H., Bjørlykke, K., Jahren, J., and Høeg, K. 2007. Experimental mechanical compaction of clay mineral aggregates –Changes in physical properties of mudstones during burial. *Marine and Petroleum Geology* **24**, 289-311.

Mondol, N.H., Bjørlykke, K., Jahren, J., and Høeg, K. 2008. Experimental compaction of clays: relationship between permeability and petrophysical properties in mudstones. *Petroleum Geoscience*, **14**, 319–337

Mortensen, J., Engstrøm, F. & Lind, I. 1998. The relation among porosity, permeability, and specific surface of chalk from the Gorm field, Danish North Sea. *SPE Reservoir Evaluation & Engineering,* **1**, 245 – 251

Olsen, H.W. 1962. Hydraulic flow through saturated clays. *In:* Ingerson, E. (ed.) *Clays and Clay Minerals. Proceedings – Ninth National Conference on Clays and Clay Minerals*, **9**, 131–161.

Revil, A. & Cathles, L.M. III. 1999. Permeability of shaly sands. *Water Resources Research*, **35**, 651–662

Wissa, A.E.Z., Christian, J.T., Davis, E.H. & Heiberg, S. 1971. Consolidation at constant rate of strain. *Journal of the Soil Mechanics and Foundation Engineering Division, American Society of Civil Engineers*, **97**, 1393–1413.

Yang, Y. & Aplin, A.C. 1998. Influence of lithology and compaction on the pore size distribution and modelled permeability of some mudstones from the Norwegian margin. *Marine and Petroleum Geology*, **15**, 163–175.

Yang, Y. & Aplin, A.C. 2007. Permeability and petrophysical properties of 30 natural mudstones. *Journal of Geophysical Research*, **112**, B03206.

V

Petrophysics of shale intervals in the Skjold Field, Danish North Sea

Mbia, E.N & Fabricius, I.L.

Extended abstract and presentation at the 73rd EAGE Conference & Exhibition incorporating SPE EUROPEC, 23–26 May 2011 in Vienna Austria.

D018

Petrophysics of Shale Intervals in the Skjold Field, Danish North Sea

E.N. Mbia* (Technical University of Denmark), I.L. Fabricius (Technical University of Denmark) & C.O. Oji (Technical University of Denmark)

SUMMARY

Stratigraphical variation of shale petrophysical properties in the Central North Sea was studied by laboratory analysis of cuttings samples and compared to wireline logging data obtained from Skjold Flank-1 well, Skjold field in the Danish North Sea. The logged section is split into six depth intervals based on wireline log pattern, and with reference to the mud log, cuttings samples were selected. The shallowest intervals (1–3) are silty shale. Interval 2 is rich in organic material. Interval 4 comprises of chalk and underlying calcareous shale. Interval 5 is shale with sand stringers; whereas interval 6 is mainly shale. X-ray diffraction analysis reveals the dominance of inter-layered smectite/illite in interval 1–3 and upper part of interval 4, whereas illite dominates interval 5 and 6. Other minerals include kaolinite, chlorite, quartz, calcite, Opal-CT, dolomite and plagioclase. Mineralogical variation is reflected in cation exchange capacity, BET specific surface, and grain density. Shales vary in total organic carbon, radioactivity, carbonate content, porosity and modeled permeability. Cross plots of logging data splits intervals according to mineralogy, porosity, modeled permeability, and induration. The most effective of intervals splitting is obtained by cross-plotting shear velocity and gamma ray.

Introduction

The stratigraphical variation of shale petrophysical properties in the Central North Sea can be studied by laboratory analysis of cuttings samples as compared to wireline logging data. Shale typically has clay content in excess of about 40% (Shaw & Weaver, 1965), and is the most common and abundant sedimentary rock. It has characteristic physical and chemical properties and due to its low permeability it may act as a seal to hydrocarbon accumulation. When shale has a high content of organic material (high TOC) it may act as a source rock. In the last decade shale has increasingly been seen as a possible reservoir rock.

The purpose of this study is to examine mineralogical variation and variation in petrophysical parameters (TOC, grain density, radioactivity, porosity, Cation Exchange Capacity (CEC), Carbonate content, specific surface by BET and modeled permeability) in Cenozoic, Cretaceous and Jurassic shales, and to show how these properties are reflected in wireline logging results. Our study is based on cuttings samples and logging data from the Skjold Flank-1 well, in the Skjold field, Danish North Sea.

Methods

Geophysical logs

The following well logs from Skjold Flank-1 were used; mud log, caliper, gamma ray, density, neutron, resistivity, as well as P-wave and S-wave velocity logs. The mud log was compiled during drilling operation and records the lithology. It was used for selecting samples from the operator's store. Six depth intervals were defined from the log pattern. Interval 1(1200-1487m) is slightly silty shales, 2 (1487-1792m) is organically rich shales, 3 (1793-2095m) is silty shales. Intervals 1–3 are of Cenozoic age. Interval 4 (2095-3008m) is Cretaceous chalk and shale. Interval 5 (3008-3917m) is Jurassic shale with sand stringers. Interval 6 (3917-4474m) is Jurassic shale with few stringers.

Cuttings-data

Thirty one shale cuttings samples were collected from Skjold Flank-1 well. The samples were carefully cleaned and each sample was handpicked for cavings. The following procedures were then followed; determination of porosity by mercury immersion, BET specific surface by nitrogen adsorption according to the method developed by Brunauer, Emmet and Teller (1938), Permeability was modeled by Kozeny's equation according to Mortensen et al. (1998), The concentrations of U, Th and K were measured on powdered samples by a NaI-crystal gamma spectrometer. Carbonate content was obtained by means of titration and the total organic carbon (TOC) was measured by combustion in a LECO (CS-200) Carbon/Sulfur Analyzer-oven, CEC was measured by Ba-ion exchange followed by Inductively Coupled Plasma-Optical Emission Spectrophotometry (ICP-OES). Mineralogy was determined through X-ray diffractometry. We did not measure the TOC and the concentration of U, Th and K on 8 Cretaceous samples with high carbonate content.

Results and Discussion

The six shale intervals show variation in petrophysical properties from Cenozoic to deeper Jurassic shales as shown in Table 1. XRD results reveal that quartz, calcite, plagioclase, and Opal CT are present as the non-clay minerals while mixed-layered smectite/illite, illite, kaolinite and chlorite are present among the clay minerals.

Solid phase

A high content of smectite and relatively low content of illite in the inter-layered smectite/illite in intervals 1, 2 and 3 of Cenozoic shales is associated with low grain densities and high measured porosity which corresponds very well with the high neutron porosity (Figure 1a) and contributes

Table 1: *Cuttings data from well Skjold Flank-1; ρ$_{grain}$ is grain density , φ is mercury porosity, BET is specific surface by N$_2$ adsorption, k is calculated permeability by Kozeny's model, TOC is total organic carbon, CEC is cation exchange capacity, Th is Thorium, U is uranium and K is potassium identified by spectral gamma radiometry. Experimental errors are; for ρ$_{grain}$ < 3 g/cm^3; for φ <7 p.u; for BET < 0.3 m^2/g.; for k< 12%; for TOC < 8%; for CEC < 15%; for U: < 0.2 ppm., Th: < 0.5 ppm., K: < 0.02%,*

| Age	Interval	Depth (m, tvd)	ρ$_{grain}$ (g/cm^3)	BET (m^2/g)	φ (p.u)	Calc.k (µD)	CEC (mEq/100g)	CaCO$_3$ (%)	TOC (%)	Spectral Gamma Ray Th (ppm)	U (ppm)	K (%)
CENOZOIC	Int. 1	552	2,65	31	32	1,99	38	5,88	0,57	14,40	4,98	1,87
		707	2,54	26	26	1,47	26	5,65	0,91	12,90	4,38	1,74
		863	2,66	31	30	2,20	22	4,03	1,10	11,60	4,58	1,63
		872	2,58	32	33	2,17	27	4,84	1,12	12,90	5,38	1,68
		1009	2,61	26	26	1,77	36	3,85	0,93	13,90	4,38	1,66
		1164	2,62	30	28	1,70	48	3,62	0,87	12,80	5,88	1,81
	Int. 2	1338	2,85	23	30	2,82	55	1,58	0,83	9,40	5,98	1,77
		1484	2,74	22	32	3,75	46	2,55	2,58	8,10	3,58	1,90
		1622	2,51	19	32	3,40	43	2,25	3,52	7,40	6,48	1,85
	Int. 3	1768	2,75	26	29	2,52	48	3,51	1,36	7,30	5,68	2,22
		1923	2,78	42	32	0,96	29	1,55	1,00	xx	xx	xx
		2070	2,77	43	30	0,74	39	5,00	0,71	xx	xx	xx
CRETACEOUS	Int. 4	2691	2,79	12	31	24,51	9	55,69	xx	xx	xx	xx
		2719	2,82	37	24	0,76	22	27,20	xx	xx	xx	xx
		2746	2,77	18	21	2,00	7	72,29	xx	xx	xx	xx
		2774	2,70	10	21	9,68	8	44,20	xx	xx	xx	xx
		2807	2,64	18	27	3,18	15	51,58	xx	2,30	4,68	0,69
		2829	2,73	13	25	7,60	10	66,04	xx	xx	xx	xx
		2850	2,71	28	28	1,84	22	9,96	xx	xx	xx	xx
		2871	2,63	19	33	5,20	20	10,50	xx	xx	xx	xx
JURASSIC	Int. 5	3051	2,66	15	22	5,05	9	27,68	1,99	7,70	4,68	1,86
		3200	2,83	13	36	15,36	14	14,69	2,39	4,70	3,48	1,42
		3353	2,81	14	32	9,27	17	12,64	2,48	7,10	2,38	1,34
		3520	2,75	16	37	11,55	14	13,35	2,32	xx	xx	xx
		3658	2,82	16	27	5,55	12	11,09	2,36	7,80	2,88	1,68
		3810	2,80	23	33	3,56	13	6,57	2,58	xx	xx	xx
	Int. 6	3959	2,83	19	17	1,39	15	5,28	1,39	9,60	3,68	1,78
		4115	2,81	22	10	0,45	14	7,22	1,41	9,00	4,98	2,17
		4270	2,75	29	15	0,57	15	6,30	1,69	8,20	5,18	2,15
		4420	2,79	26	13	0,29	13	5,65	2,20	xx	xx	xx
		4572	2,79	22	19	1,17	16	5,25	1,24	10,30	4,38	1,94
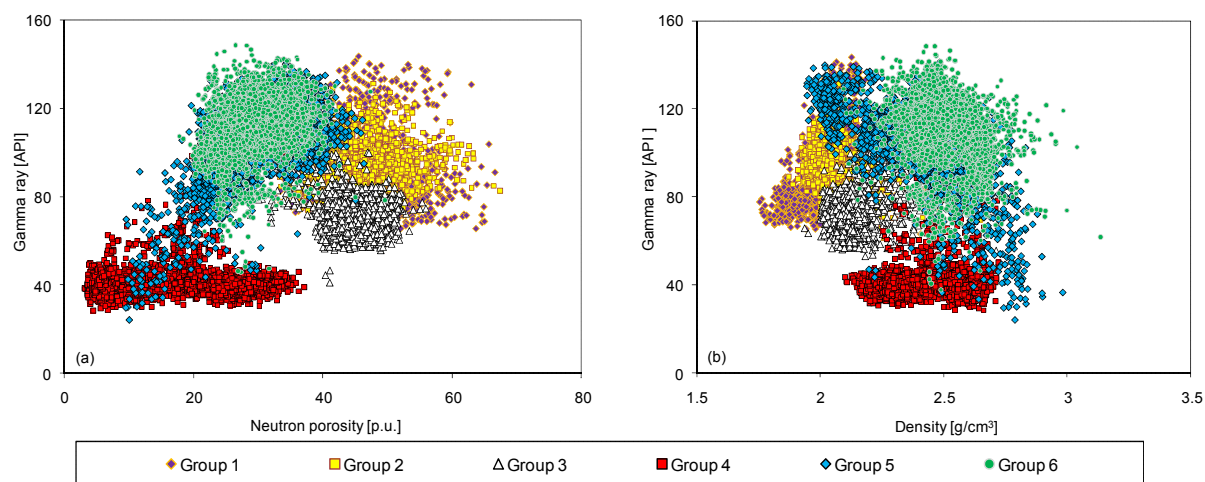
Figure 1: *Cross plots of gamma log versus (a) neutron porosity and (b) density*

the low bulk density seen in these shales (Figure 1b). Cenozoic intervals with high content of smectite splits from the Cretaceous chalk rich in calcite and Cretaceous and Jurassic shale intervals rich in illite and Kaolinite as shown in Figure 1a. Variation in the concentration of Th, U and K with depth is reflected in the variable gamma radioactivity seen in the Cenozoic and Jurassic shale intervals (Table 1).
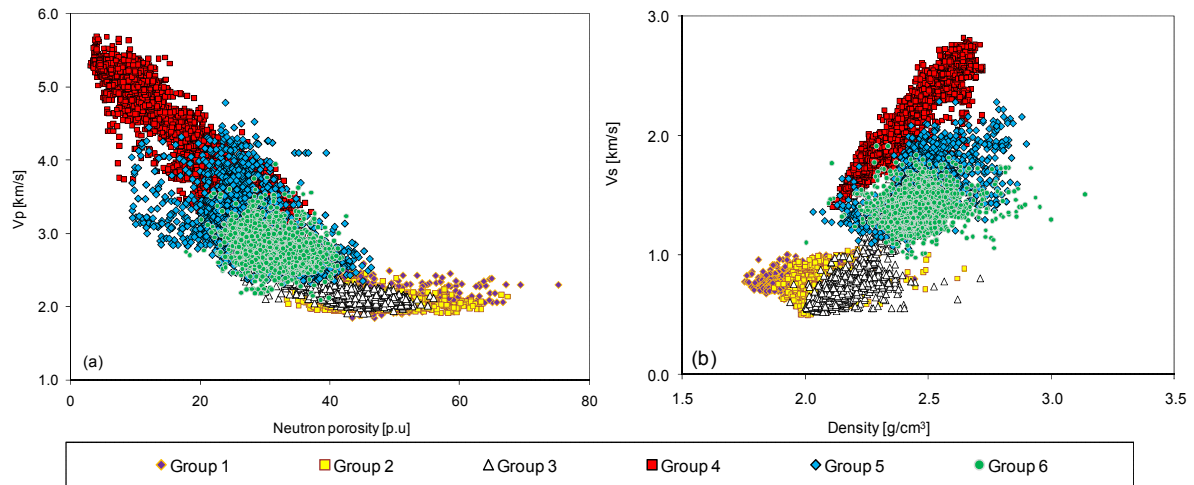
Reservoir properties

Figure 2: *Cross plots of (a) P-wave velocity versus neutron porosity and (b) S-wave velocity versus density. S-wave velocities versus density show a positive correlation for all the intervals while P-wave velocity versus neutron porosity shows a common trend with L-shaped curve.*

There is a significant variation in porosity, bulk density and induration of shales with depth from interval 1 to 6 as shown by the cross plots of sonic velocities versus neutron porosity and bulk density. P-wave velocity (Figure 2a) versus neutron porosity gives a very good slope with a negative correlation for the Cretaceous and Jurassic intervals while the Cenozoic intervals have near constant Vp with high porosity and low velocity as a result of high content of smectite.

Plot of S-wave velocity versus density (Figure 2b) gives a general positive correlation with a break in slope between Cenozoic and Cretaceous shales. Cretaceous chalk splits out from the Cretaceous and Jurassic shale unlike in Figure 2a despite having the same range of bulk densities. The split is caused by cementation and stiffening in Cretaceous chalk.

Elastic properties

The boundary where smectite is completely transformed to illite (at about $55 - 65^0$ C) is easily visible in the plot of shear modulus versus average porosity (Figure 3a). This plot gives negative slope with L-shape similar to the plot of P-wave velocity versus neutron porosity (Figure 2a), except in this case, interval 4, 5 and 6 with high content of illite and kaolinite, separates from the chalk group with high cementation and stiffness. The plot of acoustic impedance versus ratio of P-wave and S-wave velocity (Figure 3b) gives three distinct trends as a result of change in the content of illite, kaolinite and smectite.

Plots of gamma ray versus Vp-impedance (Figure 3c) and Vs-impedance (Figure 3d) also result in three different trends but gamma ray versus Vs-impedance gives a better split between Cenozoic intervals, Cretaceous chalk, and shales of interval 4, 5 and 6 as a result of change in the content of clay minerals.
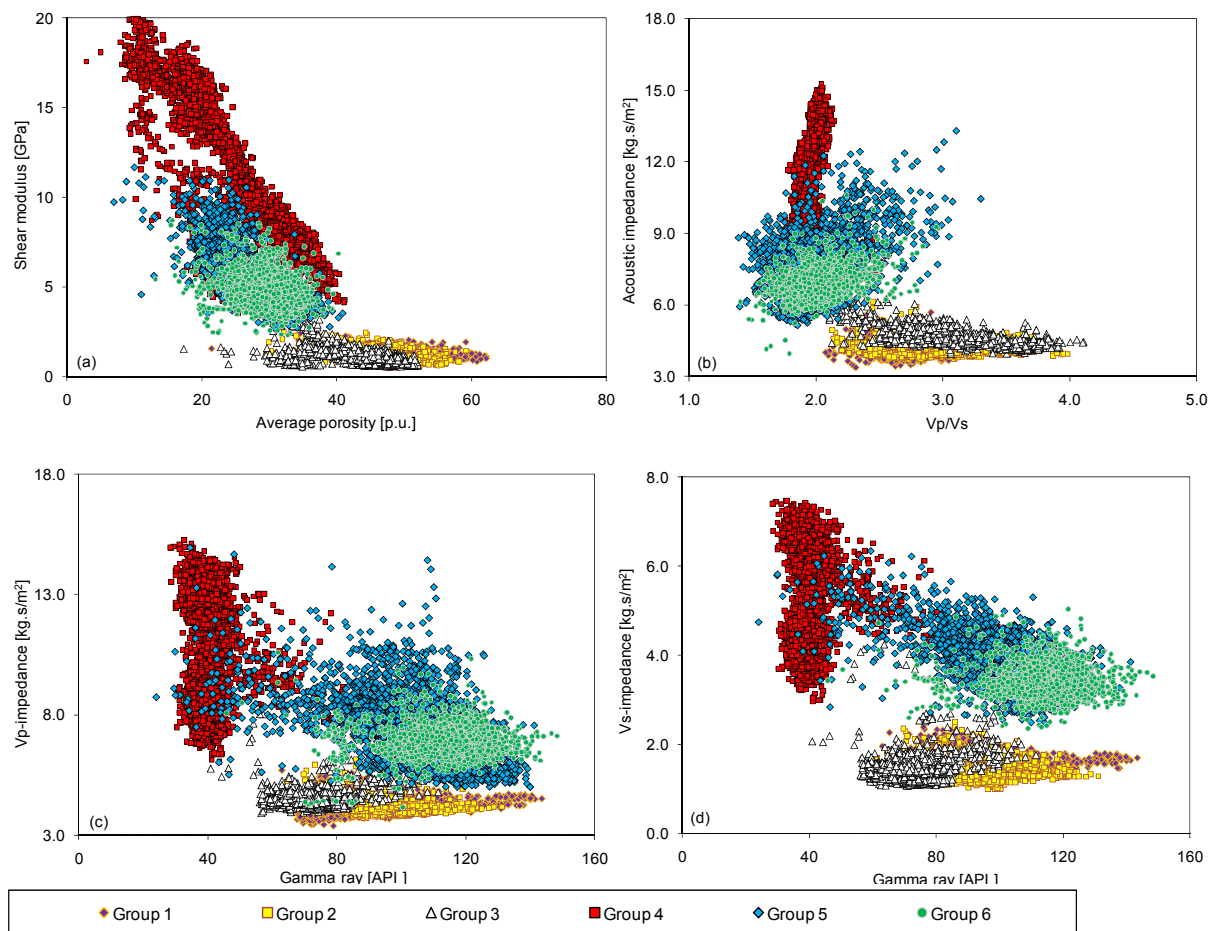
Figure 3: *Cross plots of shear modulus versus average porosity (a), acoustic impedance versus Vp/Vs ratio (b) and that of gamma ray versus sonic wave impedance (c and d).*

Conclusions

Detailed interpretation of logging data could be done or supplemented by integrating petrophysical analysis of core data obtained from laboratory measurements. In most wells we often lack core materials for shale intervals and studies have used cuttings materials to determine mineralogy of shales. In this study we have shown that cuttings analysis can also supplement logging data in providing us with additional petrophysical information which is useful in borehole formation evaluation.

Acknowledgement

We thank Mærsk Oil and Gas AS for data and cuttings material.

References

Brunauer, S., Emmett, P. H. & Teller, E. 1938. Adsorption of gases in multimolecular layers. Journal of the American Chemical Society, **60**, 309-319.

Mortensen, J., Engstrøm, F., & Lind, I. 1998. The relation among porosity, permeability, and specific surface of chalk from the Gorm field, Danish North Sea. SPE Reservoir Evaluation & Engineering, **1**, 245-251.

Shaw, D. B. & Weaver, C. E. 1965. The mineralogical composition of shales. Journal of Sedimentary Petrology, **35**, 213-222.

Pressure propagation in Vedsted structure due to CO2 has been investigated through simulation study. Caprock properties of the Fjerritslev Formation sealing Gassum reservoir have been studied through experimental work on core and cuttings samples. The experimental data of caprock permeability and compressibility and literature data of fault permeability have been used as input properties to investigate their sensitivity pressure buildup in the reservoir and transmission to the overburden layers. This investigation quantifies pressure in Vedsted structure after storing 60 million tons of CO2 for 40 years which is important in investigating brine water movement that may affect fresh water quality residing in the Chalk Group approximately 300 m below the surface.

Pressure propagation in Vedsted structure due to CO2 has been investigated through simulation study. Caprock properties of the Fjerritslev Formation sealing Gassum reservoir have been studied through experimental work on core and cuttings samples. The experimental data of caprock permeability and compressibility and literature data of fault permeability have been used as input properties to investigate their sensitivity pressure buildup in the reservoir and transmission to the overburden layers. This investigation quantifies pressure in Vedsted structure after storing 60 million tons of CO2 for 40 years which is important in investigating brine water movement that may affect fresh water quality residing in the Chalk Group approximately 300 m below the surface.